UNIVERSITY OF OXFORD

DEPARTMENT OF ENGINEERING SCIENCE

---

# TWO-PHOTON POLYMERISATION DIRECT LASER WRITING FOR LIQUID CRYSTAL PHOTONICS

---

JOHN SANDFORD O’NEILL

Wolfson College

A thesis submitted for the degree of

*Doctor of Philosophy*

2021

# *Abstract*

## TWO-PHOTON POLYMERISATION DIRECT LASER WRITING FOR LIQUID CRYSTAL PHOTONICS

by JOHN SANDFORD O'NEILL

This thesis investigates the use of two-photon polymerisation direct laser writing (2PP-DLW) in liquid crystal materials, with an emphasis on the development of applications in photonics. 2PP-DLW is a 3D printing technique employed in the fabrication of multi-dimensional structures with micro- and nano-scale dimensions. As a maskless microfabrication method, it is typically used as a rapid-prototyping tool for solid polymer objects. However, there is increasing interest in the technique as a way to manufacture functional materials and devices that cannot be produced via other means. Crucial to this effort is the development of smart resins, whereby the physical properties of a resin can be varied and controlled in-situ during the fabrication process. In this thesis, liquid crystal mixtures containing reactive mesogens are shown to be a promising smart resin material due to their anisotropic physical properties and ability to respond to external electric fields.

Stabilisation of the voltage-dependent states of the nematic Fréedericksz cell via the fabrication of polymer micropillars with 2PP-DLW is described and analysed. The polymer structures are studied with polarised optical microscopy and an electrically-tunable visibility phenomenon is characterised and explained. By synchronising the fabrication of polymer features with the application of different voltages, reconfigurable images are inscribed into liquid crystal devices. Potential applications are explored with a demonstration of a prototype anti-counterfeiting security marking.

Topological defects in nematic liquid crystal pi-cells are fabricated and electrically-controlled via the fabrication of topologically discontinuous polymer structures using 2PP-DLW. A control system for electrical-tuning of defects is developed and advanced concepts for confinement of disclination lines are demonstrated. The transport of a microparticle by a defect is presented with the potential for applications in defect templates for micro/nano assembly.

Switchable diffractive optical elements (DOEs) are fabricated with 2PP-DLW in liquid crystals and their diffractive behaviour is characterised. A model of a laser-written diffraction grating is developed using a continuum theory approach to director simulations and a wave-optics approach to the diffraction of light. The 3D capabilities of 2PP-DLW are exploited to fabricate switchable bilayer DOEs and computer-generated holograms.

This work in this thesis has important technological implications in both the development of smart resins for 2PP-DLW as well as in the development of advanced alignment and control techniques for liquid crystal devices.

# *Acknowledgements*

There are not enough effusive words in the English language to adequately express my deep thanks and affection for my incredible supervisors Stephen Morris and Steve Elston, for their unfailing support and kindness in the course of my DPhil. The Steves have been endlessly reassuring and positive about my work, giving me the boost I needed at the times I did not believe in it. Thank you Steve M for supporting me unconditionally from the moment I joined the Soft Matter Photonics group. Your wise belief that the DPhil is an expansive educational experience that is about more than the grind for results in the lab has allowed me to explore widely, to travel all over the world, and to enjoy some of the very best years of my life. Thank you Steve E for the numerous evenings in the Wine Cafe, Ecclesiastes 1:9, music recommendations, and our meandering chats that often encompass just about every topic except science. I am truly grateful for our utter inability to concentrate on talking about work and I am so lucky to have had a supervisor equally as willing to spend a lunchtime at MOMA as you are talking about the minutiae of liquid crystal modelling. Thank your for all your time, your patience and your brilliant teaching and guidance.

Thank you to Patrick Salter for your company during hours spent in the fabrication lab, your generosity, and your support during all the projects we worked on together. Thank you Martin Booth for your enthusiasm and support, and to the whole of the Dynamic Optics and Photonics group for enjoyable chats, away-days and Christmas parties.

Thank you to all the members of the Soft Matter Photonics group. In particular to Chloe, Ellis, David, Taimoor, Serena, Konrad and Julian, who made me feel so welcome when I started my DPhil. Thanks also to SMP's newer members Waqas, Yihan and Lake. It has been a pleasure to get to know you all, as I made the slow transition from the most junior to the most senior member of the group over the past 4 years. To Jia-De, thank you for your incredible kindness and having such a positive impact on the group. We still miss you. To Hassan, thank you for working so hard in your 4YP and being such a pleasure to supervise. This year, a whole new generation of brilliant students have joined the SMP powerhouse and I thank Zimo and Bohan for working with me so diligently on the DOEs project over the past few months.

To Chloe, thank you for persuading me to join the group. It all began with you. As you often say these days, everything happens for a reason and, looking back, it all makes sense now. I feel so lucky to have met a kindred spirit in you, and I deeply treasure our open and honest friendship. Ellis, you are one of the most inspiring people I have ever met and our trip to California will always remain an absolute highlight of my DPhil. Thank you for encouraging me to be the best person I can be and for showing me the joys of a balanced approach to DPhil life. David, thank you for the chats, the drinks and the yoga sessions. I could not have got through the DPhil without you. To Taimoor, thank you for your incredible warmth and kindness, and for teaching me 'you have to go to the well'.

There are many others who have helped me during my DPhil: Andy Acreman, Grahame Faulkner, Greg Cook, Dave Ilsley, Paul Giraud, John Hong, Jason Brown, Mike Hird and Nathan Smith. Thanks also to Jure Aplinc, Ziga Kos and Miha Ravnik at the University of Ljubljana for their fruitful collaboration.

I am fortunate to be a member of Wolfson College, unquestionably the best graduate college in Oxford! It feels strange to thank an institution, so instead I thank the college staff and all members past and present for making Wolfson such an extraordinary place to live and work. Many of my most treasured memories at Oxford were formed at Wolfson dinners, balls, bops and cèilidhs. Thank you to Adam Mahdi, my college advisor for always being a willing ear and a supportive influence. The friends I met at Wolfson are too numerous to list here, but I thank each and every one of you. Thank you to Amy, Kerstin and David for inviting me to sit on the Wolfson Winter Ball Committee. The 2018 Winter Ball was undoubtedly one of my proudest achievements at Oxford. Thanks also to David for encouraging me to start DJing, which has reminded me of the joy of performing and opened up surprising and brilliant opportunities over the past few years.

To my dear friends who I've met at Oxford; Rav, Cam, Flo, Dan, Laura, Jay, Sam, Leo, Fig, James, Laurynas, Louise, Joe and Maddie, thank you for countless brilliant days and evenings with so much laughter it gave me eye wrinkles. And thank you to my old friends from UCL; Kasia, Rainbow and Mark for continuing to be an unparalleled collective of supportive ears. Thank you to Cathy, Andy and Hywel for your friendship, the BBQs and boardgames. Thank you to Kerstin for our therapeutic lunchtime walks around Uni Parks and to Mizu for your support and enthusiasm. Thank you Steph for your wise and kind counsel and your incisive ability to get to the heart of any issue I face. To my oldest friends Peter, Oska, Daniel, Joe and Nick, thank you for all the drinks, parties, festivals, raves, birthdays and holidays. To my rave buddies and friends Sam, Marieke, Morgan and Lisa, thank you for the euphoric times we spent dancing together. To Alistair, I cannot thank you enough for your unconditional, uncomplicated and steadfast friendship. I am so glad our paths crossed in that Diamond Summer. Wolfson lunches, punting, May Day, Magdalen dinners, so many good memories. Chogm. And thank you Tash for brightening up these dark lockdown days, making me believe in myself and making me laugh every single day.

Thanks to the EPSRC and Merck for sponsoring my DPhil. Special thanks also to the IET, the European Forum Alpbach and Hong Kong Baptist University for awarding me with scholarships and providing me with genuinely life-changing opportunities over the course of my DPhil.

Finally, my deepest thanks goes to my incredible family. You are the solid rock in my life and I could not have done this without your love and support. Thank you Mum, Dad, Ellen and Roisin. I dedicate this thesis to you.

# Publications

**Sandford O'Neill, J. J.**, Salter, P. S., Zhao, Z., Chen, B., Daginawalla, H., Booth, M. J., Elston, S. J., Morris, S. M., "3D switchable diffractive optical elements with two-photon polymerization." *In submission.*

**Sandford O'Neill, J. J.**, Salter, P. S., Booth, M. J., Elston, S. J., Morris, S. M., "Electrically-tunable positioning of topological defects in liquid crystals." *Nature Communications*, **11**, 2203 (2020).

**Sandford O'Neill, J. J.**, Fells, J. A. J., Welch, C., Mehl, G., Yip, W. C., Wilkinson, T. D., Booth, M. J., Elston, S. J., Morris, S. M., "Robust measurement of flexoelectro-optic switching with different surface alignments." *Journal of Applied Physics*, **125**, 093104 (2019).

Tartan, C. C., **Sandford O'Neill, J. J.**, Salter, P. S., Aplinc, J., Booth, M. J., Ravnik, M., Morris, S. M., Elston, S. J., "Read on demand images in laser-written polymerizable liquid crystal devices." *Advanced Optical Materials*, **6**, 1800515 (2018).

# Conference presentations

**Gordon Research Conference on Liquid Crystals**
Boston, USA – July 2019 (Poster)
"Read-On-Demand Images in Liquid Crystal Devices"

**University of Oxford Photonics Day**
Oxford - April 2019 (Invited Oral & Poster)
"Photonics Engineering with Ultrafast Laser Microfabrication in Liquid Crystal Materials"

**University of Oxford Department of Engineering Science Researchers Conference**
Oxford – March 2019 (Poster)
"Read-On-Demand Images in Liquid Crystal Devices"

**University of Oxford Photonics Day**
Oxford – April 2018 (Poster)
"Optical Cloaking in Liquid Crystal Devices"
(awarded 1st place in the poster competition)

**Merck CASE conference**
Southampton – April 2018 (Oral)
“Voltage-Induced Optical Cloaking in Liquid Crystal Devices”

**Emerging Liquid Crystal Technologies, Photonics West**
San Francisco, USA – January 2018 (Invited Oral)
“Reconfigurable Optical Patterns in Polymerizable Liquid Crystals Using Aberration Corrected Direct Laser Writing”

**British Liquid Crystal Society Young Researchers Conference**
Durham - September 2017 (Oral)
“3-Dimensional Structures in Polymerizable Liquid Crystals Using Aberration-Corrected Direct Laser Writing”

# Awards

Institution of Engineering and Technology (IET) Leslie H. Paddle Scholarship 2019

European Foundation Alpbach Scholarship 2019

HKBU Innovation & Entrepreneurship Summer School Scholarship 2019

Institute of Physics (IOP) CR Barber Trust Travel Grant

Oxford Photonics Day 2018 Best Poster Prize

SPIE Photonics West Travel Award 2018

# Patents

**Sandford O’Neill, J. J.**, Salter, P. S., Booth, M. J., Elston, S. J., Morris, S. M. “Switchable Diffractive Optical Elements in Liquid Crystal Devices.” *Filing in progress.*

Tartan, C. C., **Sandford O’Neill, J. J.**, Salter, P. S., Morris, S. M., Ravnik, M., Booth, M. J., Elston, S. J. “Method and Apparatus for Optical Cloaking” WO2019211582. Filed: 2019-04-25

# Contents

# Chapter 1

# Introduction

This chapter serves as an introduction to this thesis, giving a brief outline of the key results that are presented in each chapter and also an explanation of how this interdisciplinary work fits into the existing research landscape.

*"All of this has happened before, and all of this will happen again."*

**Leoben Conoy, Battlestar Galactica**

## 1.1 Introduction

The work described in this DPhil thesis was conducted on a new research interface between soft matter photonics and ultrafast laser nanoprinting. Since its conception in 1997, two-photon polymerisation direct laser writing (2PP-DLW) has emerged as a key microfabrication technique for engineering of 3-dimensional microscale structures and is now considered part of the rapidly-growing field of 3D additive manufacturing. The method exploits the physics of two-photon absorption to crosslink polymer monomers in a photoresist, forming solid structures from the liquid state. As this chemical change only occurs in a very small volume, termed a "voxel" in analogy with the two-dimensional pixel, architectures with incredibly fine features can be constructed by scanning the laser focus through the resist in 3D. Remarkably, it is even possible to achieve a resolution below the diffraction limit of light, as the photoresist materials behave in a highly nonlinear manner with respect to two-photon absorption. The flexible nature of this technique has led to applications in bioengineering, photonics and metamaterials.

Three key goals now exist in the development of 2PP-DLW: (i) finer features, (ii) faster fabrication and (iii) functional/smart resins[1]. This thesis directly addresses the third goal, by using tunable resins derived from liquid crystal materials to enable new technologies and applications in photonics and beyond.

Liquid crystals (LCs) are an unusual class of materials that can be understood as an interesting hybrid between the conventional solid and liquid states-of-matter. Their crystalline nature is manifest in their anisotropic physical properties, which emerge from the anisotropy in their chemical structures[2].

This thesis concerns the use of ‘calamitic’ LCs which have a rod-like shape and thus possess uniaxial birefringence. This optical property makes them ideally suited for optoelectronic applications and, indeed, all high-resolution LC displays are based on these materials. More generally, LCs can be considered to be stimuli-responsive materials, i.e. their properties can be tuned by exposing them to external stimuli such as variations in temperature and electric or magnetic fields[3].

This thesis explores new technologies and applications that are enabled by direct laser writing in liquid crystalline resins. The existing research in this area has been quite limited, largely concentrating on the fabrication of structures consisting of conventional photoresists that are subsequently infiltrated with an LC[4–6]. In contrast, the approach described here offers the possibility of single-step fabrication, starting with an LC cell and finishing with a more sophisticated device consisting of multiple alignment structures embedded within and comprised of LC. During fabrication, the electric field applied to the resin can be tuned, allowing fabrication of microscale polymer structures with a controllable molecular orientation and order. In this way, multiple material properties can be engineered from the use of a single resist. This approach enables novel applications and advanced molecular alignments that are impossible or very challenging to achieve with conventional LC technologies.

## 1.2 Thesis Outline

Chapter 2 provides an introduction to LC science and technology such that the results that follow in the rest of this thesis can be appreciated in the broader context of LC research.

Chapter 3 begins by explaining the physics of two-photon absorption and how this applies to the two-photon polymerisation microfabrication method, before reviewing the limited existing research on direct laser writing in LC materials.

Chapter 4 details the experimental methods that were frequently used throughout this thesis including LC device characterisation, mixture preparation, polarised optical microscopy and 3D printing. The second half of the chapter goes on to report technical details of the design and build of a two-photon polymerisation direct laser writing system tailored to fabrication in LC materials.

Chapter 5 explores the use of 2PP-DLW in the fabrication of microscale read-on-demand images employing voltage-induced refractive index matching. This chapter introduces the concept of "locking-in" voltage-dependent LC alignments with the formation of polymer structures inside a device. By carefully synchronising the application of different voltages with the fabrication of polymer structures via the microfabrication system, complex images can be inscribed into an LC device and switched on and off with the application of a uniform voltage post-fabrication. A "microbicycle" structure, inspired by stop-frame animation and a microscopic switchable QR code are demonstrated which may find use in anti-counterfeiting and authentication applications. The work described in this chapter has been published in *Advanced Optical Materials* in a paper titled "Read on demand images in laser-written polymerizable LC devices"[7].

Chapter 6 extends the microscale "locking-in" concept to LC states that have topological discontinuities known as defects. Even though their name implies some kind of deficiency, defects are in fact of great interest in emerging applications for LCs in the manipulation of soft matter and nanomaterials. In this chapter, the use of 2PP-DLW in stabilising and controlling defects is shown and electrical control of the position of a defect is also demonstrated. The potential for these electrically-controllable defects to manipulate other materials is proven with a demonstration of the cargo-towing of microparticles doped into an LC mixture. The work described in this chapter has been published in *Nature Communications* in a paper titled "Electrically-tunable positioning of topological defects in liquid crystals"[8].

Chapter 7 explores the use of 2PP-DLW in the fabrication of switchable LC diffractive optical elements (DOEs). The unique capabilities of the fabrication method are used to manufacture DOEs that would be extremely challenging or impossible to create by other methods. 1D switchable diffraction gratings are demonstrated, as well as the fabrication of 3D bilayer switchable gratings and computer-generated holograms. A model of an LC diffraction grating is demonstrated, which links the switching behaviour of the LC in the grating to the diffraction pattern produced by the grating, and shows a good match with the experimental data.

Chapter 8 provides an overall summary of this thesis, details some potential areas of future work and offers some concluding remarks.

# Chapter 2

# Liquid Crystals

This chapter gives the relevant theory and background to liquid crystal science and technology that is required to understand the work presented in this thesis. Nematic ordering and continuum theory are explained and an overview of the dielectric and optical properties of liquid crystals is given. Also discussed are approaches for modelling liquid crystals, the architecture of liquid crystal devices, and polymer stabilisation using reactive mesogens.

> *"Life is a partial, continuous, progressive, multiform and conditionally interactive, self-realisation of the potentialities of atomic electron states."*
>
> **John Desmond Bernal**

## 2.1 Introduction to Liquid Crystals

The interesting properties of liquid crystals (LCs) are a result of the anisotropy of their molecular structure. Due to their molecular anisotropy they exhibit the ability to self-organise, assembling into complex period structures on the molecular scale. Liquid crystal molecules come in many different structures and physical shapes but always have a significant difference in one of their linear dimensions. This anisotropy is reflected in the macroscopic physical properties of an LC material, such as electrical and optical properties, having a crystal-like anisotropy[2].

As the name suggests, LCs also possess liquid-like properties such as viscosity and the ability to flow and fill a container. It is this combination of solid and liquid properties that has led to great scientific interest in LCs, as well as their now ubiquitous use as a switchable material in optoelectronic devices including high resolution flat panel displays.

The LC phase, as a state of matter in between solids and liquids is classed as a mesophase (from the Greek *mesos* meaning 'middle') and LC molecules themselves are referred to as mesogens. LCs can be subdivided into the thermotropics, which exhibit phase transitions that depend on temperature, and lyotropics, which exhibit phase transitions dependent on the concentration of the material in a solvent.

As the temperature of a thermotropic nematic LC is increased, it goes through a number of phase transitions that affect the microscopic order (Figure 2.1). Below the melting point of the material, it exists as a crystalline solid with regular, periodic positional and orientational order. As the temperature is increased, it melts into the nematic phase where the majority of molecules point in a preferred direction. Above another critical temperature known as the clearing point, the LC transitions into

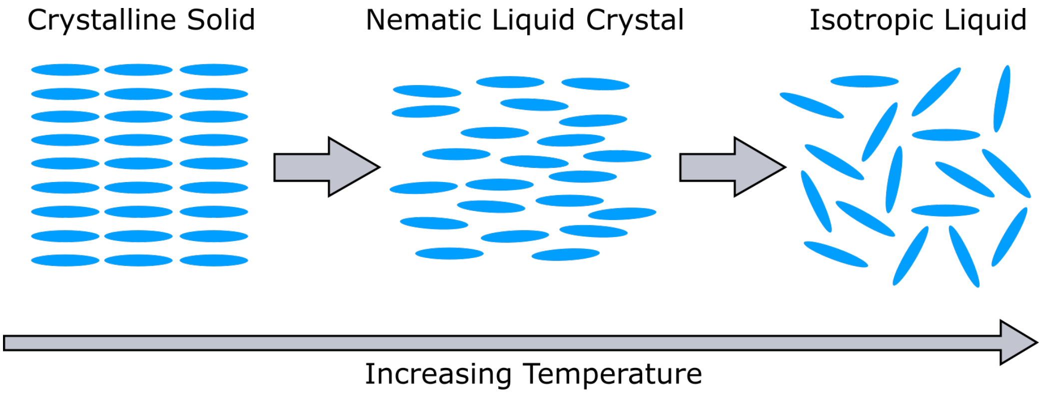

FIGURE 2.1: The influence of temperature on the order in a thermotropic nematic liquid crystal. As the temperature is increased, the order decreases and the LC passes through a phase transition from crystalline solid to nematic liquid crystal and from nematic liquid crystal to isotropic liquid.

the isotropic liquid phase, where there is no positional or orientational order. It should be noted that other mesophases can exist in LCs, most notably the smectic phase, where LC molecules self-organise to form ordered layers. However, smectic LC materials are not used in this thesis and are not discussed further.

## 2.2 A Brief History of Liquid Crystals

Liquid Crystals were first observed in the 1880s by Friedrich Reinitzer, an Austrian botanist, while he was investigating the properties of cholesteryl benzoate, a material found naturally in carrots. In collaboration with the German physicist Otto Lehmann, who had designed and built a polarising microscope, Reinitzer confirmed his observations of a new phase of matter, existing in between the solid and liquid phases[9]. Although the discovery was viewed with some interest at first, it was generally overlooked and considered to be a niche scientific curiosity for some 80 years.

In the late 1940s research on LCs slowly intensified, with research groups in Europe turning their attention to chemical synthesis of LC molecules as they began to understand the structure-property relationships governing anisotropic organic molecules. The first international conference on LCs was held at Kent State University, Ohio, in 1965 and marks the start of the modern era for LC science, with applications of LCs in display technology quickly emerging over the following few years. In 1991, the significance of the field was affirmed by the awarding of the Nobel Prize in Physics to Pierre-Gilles de Gennes for his work studying the theoretical underpinnings of the ordering of LCs[10].

The birth of the liquid crystal display (LCD) was a hugely significant moment in the history of information display, spawning a multi-billion dollar industry and realising the first ever high resolution flat-panel display technology. In 2007, sales of LCDs surpassed cathode ray tubes (CRTs) for the first time, rendering the CRT obselete as the LCD became ubiquitous in homes and offices across the world. The reader can find a complete history of LC science and technology in Dunmur and Slukin[9].

In recent years, LCDs have faced stiff competition as emerging display technologies have come to market. Nowadays, organic light-emitting diode (OLED) and microLED displays can be found in high-end consumer products and have led in the development of flexible displays. This has intensified the search for new applications of LCs and their reframing in the literature as a stimuli-responsive material, rather than exclusively an opto-electronic material. Enabled by advanced manufacturing techniques such as direct laser writing and drop-on-demand inkjet printing, new potential applications of LCs have been found in nanophotonics, microrobotics and bioengineering[11].

## 2.3 Nematic Ordering

Calamitic nematic LCs, which are defined by their rod-like shape, are the subject of this thesis. They are the most commonly studied type of LC and have found the most use in technological applications. Due to their shape anisotropy they exhibit a phenomenon termed nematic ordering, meaning that there is a long-range orientational order but no positional order.

An example of a nematic LC molecule, 5CB, is illustrated in Figure 2.2. Due to the rigid structure of the two phenyl rings and the long carbon backbone, the volume the organic molecule occupies can be approximated as an ellipsoid. LC molecules are commonly illustrated as ellipsoids in order to explain experimental phenomena.

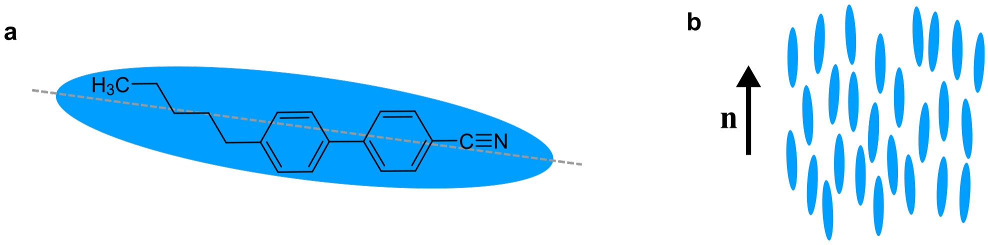

FIGURE 2.2: (a) The chemical structure of 5CB, a common cyanobiphenyl liquid crystal. The long axis of the molecule is indicated by a dashed line. (b) Nematic order, which is where the LC molecules tend to point in a direction given by the director **n**.

We define a unit vector called the director, **n**, which describes the average orientation of the long axes of the LC molecules. In the nematic phase, LCs preferentially orient along this direction. To quantify the degree of ordering along the director, a scalar order parameter, $S$, is defined. For an ensemble of LC molecules, the scalar order parameter is given by the second order Legendre polynomial[12],

$$S = \frac{1}{2}\left\langle 3\cos^2\theta - 1\right\rangle \tag{2.1}$$

where $\theta$ is the angle between the long axis of a molecule and the director and $\langle\rangle$ indicates the spatial and temporal average. For an isotropic liquid,

$S = 0$ and for the completely ordered case, $S = 1$, while a nematic LC will have an order parameter of $0.3 < S < 0.8$.

As the order parameter provides us with a quantified measure of the order in an LC, it must have a temperature dependence. As the temperature rises in an LC, the molecules have greater kinetic energy and therefore spend a greater proportion of their time deviated from the director. This loss of orientational order is expressed by a decrease in the order parameter as the temperature increases (Figure 2.3). Above the clearing point, $T_c$, the temperature above which the LC enters the isotropic phase, the order parameter drops discontinuously to 0.

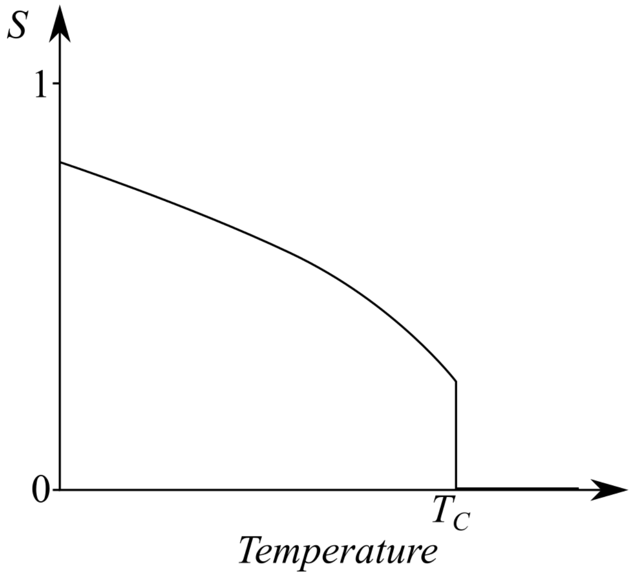

FIGURE 2.3: An example of the temperature dependence of the scalar order parameter of nematic LCs.

## 2.4 Elastic Energy and Continuum Theory

The behaviour of LCs can be described with continuum theory, developed by the physicist Sir Charles Frank in the 1950s[13], building on the work of Oseen[14] and Zocher[15] published in 1933. Frank constructed a description of the elastic free energy density of a LC by considering the myriad ways in which a nematic LC can be deformed.

As discussed previously, nematic LC molecules in thermodynamic equilibrium and unconstrained tend to align parallel to each other, in a direction described by a vector called the director, **n**. In other words, in the ground state, the LC director field, **n**, is non-varying throughout space. Frank reduced the possible deformations away from this lowest-energy state to three fundamental distortions: splay, twist and bend, to which all possible distortions can be reduced. The three deformation modes are visualised in Figure 2.4. According to Oseen-Frank theory, deviations from equilibrium are analogous to changes in the length of a spring from its equilibrium length. Therefore, the distortion free energy density is given by,

$$f_d = \underbrace{\frac{1}{2}K_{11}(\nabla \cdot \mathbf{n})^2}_{\text{splay}} + \underbrace{\frac{1}{2}K_{22}(\mathbf{n} \cdot (\nabla \times \mathbf{n}))^2}_{\text{twist}} + \underbrace{\frac{1}{2}K_{33}|\mathbf{n} \times (\nabla \times \mathbf{n})|^2}_{\text{bend}} \tag{2.2}$$

where $\mathbf{n} = (n_x, n_y, n_z)$ and $K_{11}$, $K_{22}$, $K_{33}$ are the Frank splay, twist and bend elastic constants with units of [N], analogous with the spring constant. In general, the Frank elastic constants have values on the order of 10pN and in most LCs, $K_{33} > K_{11} > K_{22}$, meaning that bend distortions are penalised more than splay and twist distortions.

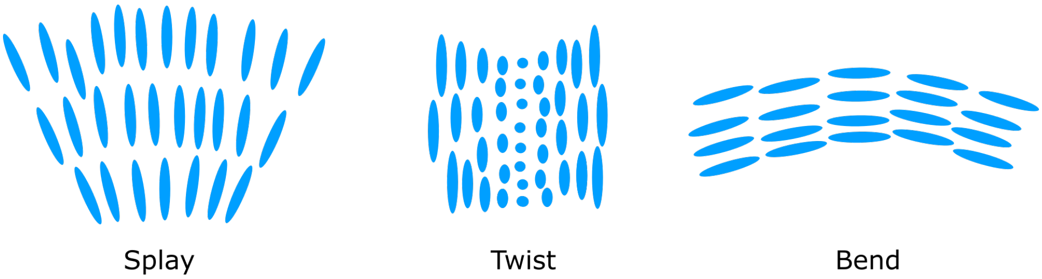

FIGURE 2.4: The three fundamental distortion modes that exist in liquid crystals according to continuum theory.

The form of the three distortion mode terms in equation 2.2 can be understood by considering the nature of the director field for each distortion mode. For splay distortions, the director points outwards radially from a point, which is described by a non-zero divergence

($\nabla \cdot \mathbf{n} \neq 0$). For twist distortions, curl($\mathbf{n}$) is parallel to the director ($\mathbf{n} \cdot (\nabla \times \mathbf{n}) \neq 0$) while for bend distortions, curl($\mathbf{n}$) is perpendicular to the director ($\mathbf{n} \times (\nabla \times \mathbf{n}) \neq 0$).

In continuum theory, this distortion free energy density expression describes the elastic energy density cost associated with deformations away from the equilibrium state (with all the molecules lying parallel to each other). As this is a free energy, the director field can be calculated by minimising this expression and solving the resulting differential equation.

However, in practice there are many cases where equation 2.2 is too complex to solve analytically and so a simplifying assumption is made that $K_{11} = K_{22} = K_{33} = K$. This leads us, via some vector algebra, to the one-constant elastic free energy density due to distortion,

$$f_d = \frac{1}{2}K\left[(\nabla \cdot \mathbf{n})^2 + |\nabla \times \mathbf{n}|^2\right]. \tag{2.3}$$

## 2.5 Electrical Properties

### 2.5.1 Dielectric Coupling

Liquid crystals are dielectric materials, meaning that the application of an electric field induces dipole moments in the molecules that oppose the applied electric field. The combined action of these dipole moments is described by the polarisation density field **P**. The electric susceptibility, $\chi_e$, of a material quantifies the polarizability of a material and in LCs it can be a tensor quantity, as the susceptibility can vary depending on the direction of the applied field. The electric susceptibility determines the electric permittivity of a material and therefore affects many electrical and optical properties. The equation for the polarisation density of a dielectric

$\mathbf{P}$ under an applied field $\mathbf{E}$ is given by

$$\mathbf{P} = \varepsilon_0 \chi_e \mathbf{E} \tag{2.4}$$

where $\varepsilon_0 = 8.85 \times 10^{-12}\ \mathrm{C}^2/\mathrm{Nm}^2$, the permittivity of free space.

Assuming a director fixed in one direction in a uniaxial material there are, in general, two values for the electric susceptibility. For an electric field applied parallel to the director, the susceptibility is denoted $\chi_{\parallel}$ and for a field applied perpendicular to the director, the susceptibility is denoted $\chi_{\perp}$. It is therefore convenient to express the electric susceptibility as a tensor and this would take the following form for a director aligned along the $z$-axis.

$$\chi_e = \begin{pmatrix} \chi_{\perp} & 0 & 0 \\ 0 & \chi_{\perp} & 0 \\ 0 & 0 & \chi_{\parallel} \end{pmatrix} \tag{2.5}$$

In a dielectric material, the electric displacement field, $\mathbf{D}$, expresses the distribution of electric charges resulting from the application of an electric field and includes the induced polarisation. It is given by

$$\mathbf{D} = \varepsilon_0 \mathbf{E} + \mathbf{P} = \varepsilon_0 (1 + \chi_e) \mathbf{E} = \varepsilon_0 \varepsilon_r \mathbf{E} \tag{2.6}$$

where $\varepsilon_r$ is the relative permittivity and is related to the electric susceptibility by $\varepsilon_r = 1 + \chi_e$. In anisotropic materials $\varepsilon_r$ is therefore also a tensor and is given by

$$\varepsilon_r = \begin{pmatrix} \varepsilon_{\perp} & 0 & 0 \\ 0 & \varepsilon_{\perp} & 0 \\ 0 & 0 & \varepsilon_{\parallel} \end{pmatrix} \tag{2.7}$$

where $\varepsilon_{\perp}$ and $\varepsilon_{\parallel}$ are the electric permittivities perpendicular and parallel to the director arbitrarily oriented along the $z$-axis. We can define a dielectric anisotropy as $\Delta\varepsilon = \varepsilon_{\parallel} - \varepsilon_{\perp}$ and write the electric displacement field as,

$$\mathbf{D} = \varepsilon_0 \begin{pmatrix} \varepsilon_{\perp} & 0 & 0 \\ 0 & \varepsilon_{\perp} & 0 \\ 0 & 0 & \varepsilon_{\parallel} \end{pmatrix} \begin{pmatrix} E_x \\ E_y \\ E_z \end{pmatrix} \tag{2.8}$$

or,

$$\mathbf{D} = \varepsilon_0 \left[ \varepsilon_{\perp} \begin{pmatrix} 1 & 0 & 0 \\ 0 & 1 & 0 \\ 0 & 0 & 1 \end{pmatrix} \begin{pmatrix} E_x \\ E_y \\ E_z \end{pmatrix} + \begin{pmatrix} 0 & 0 & 0 \\ 0 & 0 & 0 \\ 0 & 0 & \Delta\varepsilon \end{pmatrix} \begin{pmatrix} E_x \\ E_y \\ E_z \end{pmatrix} \right] \tag{2.9}$$

which can be written as,

$$\mathbf{D} = \varepsilon_0 \varepsilon_{\perp} \mathbf{E} + \varepsilon_0 \Delta\varepsilon (\mathbf{n} \cdot \mathbf{E}) \mathbf{n} \tag{2.10}$$

since $\mathbf{n} = (0, 0, 1)$.

To evaluate the free energy density due to dielectric coupling we use the standard equation for the electrostatic energy density inside a dielectric medium,

$$f_e = -\frac{1}{2} \mathbf{D} \cdot \mathbf{E}. \tag{2.11}$$

Substituting in the equation for the electric displacement (Eqn. 2.10) yields,

$$f_e = -\frac{1}{2} \varepsilon_0 \varepsilon_{\perp} E^2 - \frac{1}{2} \varepsilon_0 \Delta\varepsilon (\mathbf{n} \cdot \mathbf{E})^2. \tag{2.12}$$

As only the second term is dependent on the orientation of the director, the first term is omitted when expressing the free energy density. Therefore, the free energy density associated with an applied electric field can be reduced to

$$f_e = -\frac{1}{2} \varepsilon_0 \Delta\varepsilon (\mathbf{n} \cdot \mathbf{E})^2. \tag{2.13}$$

Examining this equation reveals that the free energy is minimised when the director is parallel to the electric field for positive $\Delta\varepsilon$ materials. Conversely, for negative $\Delta\varepsilon$ materials the free energy is minimised when the director is perpendicular to the electric field. As physical systems always behave in such a way as to minimise their free energy, this means that an electric field can be used to reorient the LC director.

To derive a full description of LC behaviour we must add an additional dielectric term of the form of equation 2.13 to the expression for the one-constant distortion free energy density presented in Section 2.4. The overall free energy density is then given by,

$$F = f_d + f_e \tag{2.14}$$

$$F = \frac{1}{2}K\left[(\nabla \cdot \mathbf{n})^2 + |\nabla \times \mathbf{n}|^2\right] - \frac{1}{2}\Delta\varepsilon\varepsilon_0(\mathbf{n} \cdot \mathbf{E})^2. \tag{2.15}$$

### 2.5.2 Fréedericksz Threshold

As shown in the previous section, LCs exhibit reorientation in an applied electric field. However, due to the elasticity of the LC, there is a critical field below which reorientation will not occur, known as the Fréedericksz threshold[2]. This is given by,

$$E_c = \frac{\pi}{d}\sqrt{\frac{K}{\Delta\varepsilon\varepsilon_0}}. \tag{2.16}$$

This equation can be recast to give a threshold in terms of an applied voltage, which is independent of the device thickness,

$$V_c = \pi\sqrt{\frac{K}{\Delta\varepsilon\varepsilon_0}}. \tag{2.17}$$

As this equation only depends on the material parameters $K$ and $\Delta\varepsilon$, the Fréedericksz threshold for a given material is not dependent on the thickness of the LC layer in the device. The existence of the threshold can be understood as the minimum dielectric coupling required to compensate for the elastic energy cost incurred by switching the LC into a distorted state.

## 2.6 Director Modelling

### 2.6.1 Director Modelling in COMSOL

In Chapter 7 the finite element modelling (FEM) software COMSOL Multiphysics is used to build a model linking the orientation of the LC director in a diffraction grating to the propagation of light through the grating. In this section, the equations that describe the equilibrium configuration of the director are derived and formulated in a manner suitable for input into COMSOL.

The equilibrium configuration of the director, **n**, can be established by minimising the free energy density with respect to $n_x$, $n_y$ and $n_z$, the components of the director **n** in cartesian coordinates. This can be performed by applying the Euler-Lagrange equation, a standard result from the calculus of variations which states that a function of the form,

$$F\left(y, \frac{\partial y}{\partial x_i}, x_i\right) \tag{2.18}$$

can be minimised by,

$$0 = \frac{\partial F}{\partial y} - \sum_i^n \frac{\partial}{\partial x_i}\left(\frac{\partial F}{\partial\left(\frac{\partial y}{\partial x_i}\right)}\right). \tag{2.19}$$

Therefore, minimisation of the free energy density is performed by substituting equation 2.15 for the distortion free energy density into equation 2.19. This needs to be performed three times, once each for $n_x$, $n_y$ and $n_z$. Let us first consider the minimisation with respect to the $x$ component of the director, $n_x$, which is given by,

$$0 = \frac{\partial F}{\partial n_x} - \frac{\partial}{\partial x}\left(\frac{\partial F}{\partial\left(\frac{\partial n_x}{\partial x}\right)}\right) - \frac{\partial}{\partial y}\left(\frac{\partial F}{\partial\left(\frac{\partial n_x}{\partial y}\right)}\right) - \frac{\partial}{\partial z}\left(\frac{\partial F}{\partial\left(\frac{\partial n_x}{\partial z}\right)}\right). \tag{2.20}$$

Substituting equation 2.15 into equation 2.20 yields

$$0 = K\left(-\frac{\partial^2 n_x}{\partial x^2} - \frac{\partial^2 n_x}{\partial y^2} - \frac{\partial^2 n_x}{\partial z^2}\right) - \Delta\varepsilon\varepsilon_0 n_x E_x^2. \tag{2.21}$$

In order to model dynamic behaviour, we then equate this to a viscous dissipation term, giving the following time-dependent PDE for $n_x$,

$$-\gamma\frac{\partial n_x}{\partial t} = K\left(-\frac{\partial^2 n_x}{\partial x^2} - \frac{\partial^2 n_x}{\partial y^2} - \frac{\partial^2 n_x}{\partial z^2}\right) - \Delta\varepsilon\varepsilon_0 n_x E_x^2 \tag{2.22}$$

where $\gamma$ is the rotational viscosity of the LC. Following the same minimisation procedure for $n_y$ and $n_z$ gives us a system of three coupled PDEs that govern the equilibrium configuration of the director $\mathbf{n}$:

$$-\gamma\frac{\partial n_x}{\partial t} = -K\nabla^2 n_x - \Delta\varepsilon\varepsilon_0 n_x E_x^2 \tag{2.23}$$

$$-\gamma\frac{\partial n_y}{\partial t} = -K\nabla^2 n_y - \Delta\varepsilon\varepsilon_0 n_y E_y^2 \tag{2.24}$$

$$-\gamma\frac{\partial n_z}{\partial t} = -K\nabla^2 n_z - \Delta\varepsilon\varepsilon_0 n_z E_z^2 \tag{2.25}$$

where $\nabla^2 = \left(\frac{\partial^2}{\partial x^2} + \frac{\partial^2}{\partial y^2} + \frac{\partial^2}{\partial z^2}\right)$ is the Laplacian operator.

Due to the requirement that $|\mathbf{n}| = 1$, we add another term to the free energy density expression (equation 2.15) that penalises any deviation away from $|\mathbf{n}| = 1$. The form of this term is,

$$f_\mu = \frac{\mu}{4}(n_x^2 + n_y^2 + n_z^2 - 1)^2 \tag{2.26}$$

where $\mu$ is a constant with a sufficiently large magnitude to suppress any solutions where the condition $|\mathbf{n}| = 1$ is not satisfied. In practice, the value of this constant is set to the highest possible value that still provides stable results from the FEM solver.

When this term is added to the free energy density, the system of three coupled PDEs derived by Euler-Lagrange minimisation become:

$$-\gamma\frac{\partial n_x}{\partial t} = -K\nabla^2 n_x - \Delta\varepsilon\varepsilon_0 n_x E_x^2 + \mu(n_x^2 + n_y^2 + n_z^2 - 1)n_x \tag{2.27}$$

$$-\gamma\frac{\partial n_y}{\partial t} = -K\nabla^2 n_y - \Delta\varepsilon\varepsilon_0 n_y E_y^2 + \mu(n_x^2 + n_y^2 + n_z^2 - 1)n_y \tag{2.28}$$

$$-\gamma\frac{\partial n_z}{\partial t} = -K\nabla^2 n_z - \Delta\varepsilon\varepsilon_0 n_z E_z^2 + \mu(n_x^2 + n_y^2 + n_z^2 - 1)n_z \tag{2.29}$$

In order to solve a system of PDEs in COMSOL, they must be expressed in a standard form that can be interpreted by the COMSOL FEM solver. The standard form of a PDE in COMSOL is given as,

$$e_a\frac{\partial^2\mathbf{u}}{\partial t^2} + d_a\frac{\partial\mathbf{u}}{\partial t} + \nabla\cdot(-c\nabla\mathbf{u} - \alpha\mathbf{u} + \gamma) + \beta\cdot\nabla\mathbf{u} + a\mathbf{u} = f \tag{2.30}$$

where $\mathbf{u}$ is the dependent variable to be solved for. This $\mathbf{u}$ can be a scalar quantity, in which case equation 2.30 describes a system consisting of a single PDE. Alternatively, $\mathbf{u}$ can be a vector of dependent variables, in which case equation 2.30 becomes a vector equation expressing a system of coupled PDEs. Note that the notation $\nabla\mathbf{u}$ is equivalent to taking the tensor product $\nabla\otimes\mathbf{u}$.

By inspection, we can express the three coupled PDEs for $n_x$, $n_y$ and $n_z$ in this form by allowing $\mathbf{u} = \mathbf{n} = (n_x, n_y, n_z)$ and setting the coefficients $e_a = \alpha = \gamma = \beta = 0$ while $c = K$ (the elastic constant), $d_a = \gamma$ (the rotational viscosity), $a = \mu(n_x^2 + n_y^2 + n_z^2 - 1)$ and $f$ is the source term, which expresses the dielectric energy in this case. Thus our system of PDEs is now expressed in COMSOL form as,

$$\gamma \frac{\partial \mathbf{n}}{\partial t} - \nabla \cdot \mathbf{K} \nabla \mathbf{n} + \mathbf{a}\mathbf{n} = f \tag{2.31}$$

where

$$\mathbf{K} = \begin{pmatrix} K & 0 & 0 \\ 0 & K & 0 \\ 0 & 0 & K \end{pmatrix}$$

$$\gamma = \begin{pmatrix} \gamma & 0 & 0 \\ 0 & \gamma & 0 \\ 0 & 0 & \gamma \end{pmatrix}$$

$$\boldsymbol{a} = \begin{pmatrix} \mu(n_x^2 + n_y^2 + n_z^2 - 1) & 0 & 0 \\ 0 & \mu(n_x^2 + n_y^2 + n_z^2 - 1) & 0 \\ 0 & 0 & \mu(n_x^2 + n_y^2 + n_z^2 - 1) \end{pmatrix}$$

$$\boldsymbol{f} = \begin{pmatrix} \Delta\varepsilon\varepsilon_0 n_x E_x^2 \\ \Delta\varepsilon\varepsilon_0 n_y E_y^2 \\ \Delta\varepsilon\varepsilon_0 n_z E_z^2 \end{pmatrix}$$

and use is made of the identity $\nabla^2 \mathbf{n} = (\nabla \cdot \nabla)\mathbf{n}$. Note that $\mathbf{K}$ commutes here as it is a scalar matrix (a multiple of the identity matrix $\mathbf{I}$).

### 2.6.2 Director Modelling with the Finite Difference Method

A simpler method for simulating the LC director is using a numerical finite difference method (FDM). In this method, a one-dimensional model of a LC device is formulated, where the plane of the cell is defined to be the $xy$-plane and the $z$ axis is normal to the cell substrates. The director is represented as a function of a tilt angle, $\theta$, measured from the $x$-axis. In this simple 1D model, the tilt angle $\theta$ is a function of the $z$ coordinate axis. The model geometry is illustrated in Figure 2.5.

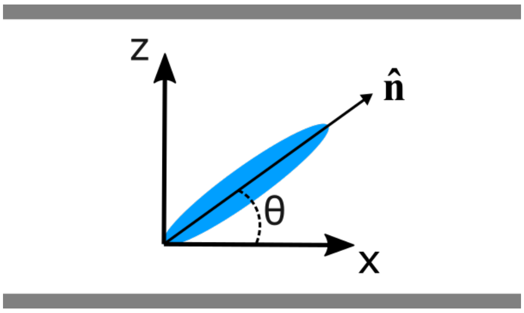

FIGURE 2.5: Illustration of the geometry of a one-dimensional FDM model of the director in an LC device.

In this description, the director, **n** is defined as,

$$\mathbf{n} = \begin{pmatrix} \cos\theta \\ 0 \\ \sin\theta \end{pmatrix} \tag{2.32}$$

Similar to the FEM approach described in Section 2.6.1, equation 2.15 for the distortion free energy must be minimised by using the Euler-Lagrange equation. In this FDM model, however, there is only one spatial dimension and the minimisation is performed with respect to $\theta$. Therefore, the Euler-Lagrange equation is,

$$0 = \frac{\partial F}{\partial \theta} - \frac{\partial}{\partial z}\left(\frac{\partial F}{\partial\left(\frac{\partial \theta}{\partial z}\right)}\right). \tag{2.33}$$

which gives a PDE of the form,

$$-\gamma\frac{\partial \theta}{\partial t} = -K\frac{\partial^2 \theta}{\partial z^2} - \Delta\varepsilon\varepsilon_0 E_z^2 \sin 2\theta \tag{2.34}$$

Finite difference methods are a class of numerical analysis techniques that allow a PDE to be transformed into a system of linear equations to be solved iteratively by an algorithm. The method relies on the discretization of space and time, approximating continuous spatial functions as a grid of discrete points and approximating time-dependent functions as a finite series of time-steps. The partial derivatives with respect to $z$ are given by the following finite-difference approximations:

$$\left.\frac{\partial\theta}{\partial z}\right|_i \approx \frac{\theta_{i+1} - \theta_{i-1}}{2\Delta} \tag{2.35}$$

$$\left.\frac{\partial^2\theta}{\partial z^2}\right|_i \approx \frac{\theta_{i+1} - 2\theta_i + \theta_{i-1}}{\Delta^2} \tag{2.36}$$

where $i$ is the point on the discretized grid that the derivative is to be evaluated and $\Delta$ is the grid-spacing defined in the model.

To solve the resulting equations, an iterative relaxation method is employed, where an effective torque is calculated for each point and the tilt angle is adjusted by an amount proportional to the torque and a relaxation parameter. The process repeats until there is no change in the director field.

After the solution to the director has been found, optical modelling is performed by using a Jones matrix method. This allows the director profile to be related to experimentally-measurable quantities such as the transmission of light through a device. The approach proceeds by dividing the director structure into a finite number of birefringent slices, where the number of slices is defined by the spatial-discretization of the director field from the FDM model of the director. Thereafter, the Jones matrix for each slice is defined and then used with an input polarisation vector to calculate the transmission. Section 2.7.2 describes the general formulation of the Jones matrix method.

## 2.7 Optical Properties

### 2.7.1 Birefringence

The propagation of light through a non-magnetic material is characterised by a dimensionless number called the refractive index. For an isotropic material with relative permittivity $\varepsilon_r$, the refractive index is,

$$n = \sqrt{\varepsilon_r} \tag{2.37}$$

The refractive index governs the speed and wavelength of light in a medium via the following relations,

$$v = \frac{c}{n} \tag{2.38}$$

$$\lambda = \frac{\lambda_0}{n} \tag{2.39}$$

where $\lambda_0$ is the wavelength of light in a vacuum.

Calamitic nematic LCs are uniaxially birefringent, possessing an extraordinary refractive index, $n_e$, which dictates the propagation of light polarised parallel to the long axes of the molecules and an ordinary refractive index, $n_o$, which dictates the propagation of light polarised perpendicular to the long axes. This phenomenon is manifest due to the anisotropy in the relative permittivity of a birefringent material and, in the case of LCs, is due to the conjugation of $\pi$-orbitals along the long-axis of the molecules. Figure 2.6 illustrates the optical indicatrix for an uniaxial LC. The birefringence or optical anisotropy of an LC is defined as,

$$\Delta n = n_e - n_o \tag{2.40}$$

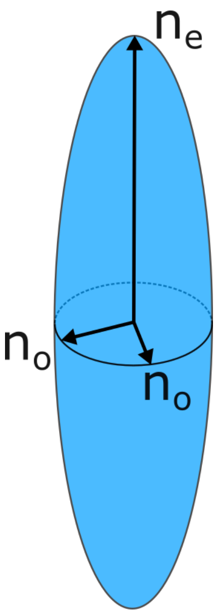

FIGURE 2.6: Optical indicatrix of a uniaxially birefringent LC with $n_e > n_o$.

Due to the anisotropy in the refractive index, polarisation components of light travelling through an LC sample parallel and perpendicular to the long-axis of the LC will travel at different velocities. Thus a phase-lag between polarisation components can develop, resulting in a change in the overall polarisation state of the light. This phenomenon is called optical retardation and allows LCs to be used as electrically-switchable waveplates. The retardance is proportional to the thickness of the LC layer and the birefringence of the LC and, as in most waveplates, is a wavelength-dependent effect. It is optical retardation that is responsible for the panoply of colours that can be seen when studying birefringent samples with polarised light microscopy (see Section 4.1.2).

The indices of refraction in an LC have a strong temperature dependence, resulting from the decrease in order observed with increasing temperature as explained in Section 2.3. Figure 2.7 illustrates a typical example of this temperature dependence.

### 2.7.2 Jones Matrices

In Section 2.6.2 a finite difference method for numerically simulating the director field in a LC device was introduced. To calculate experimentally

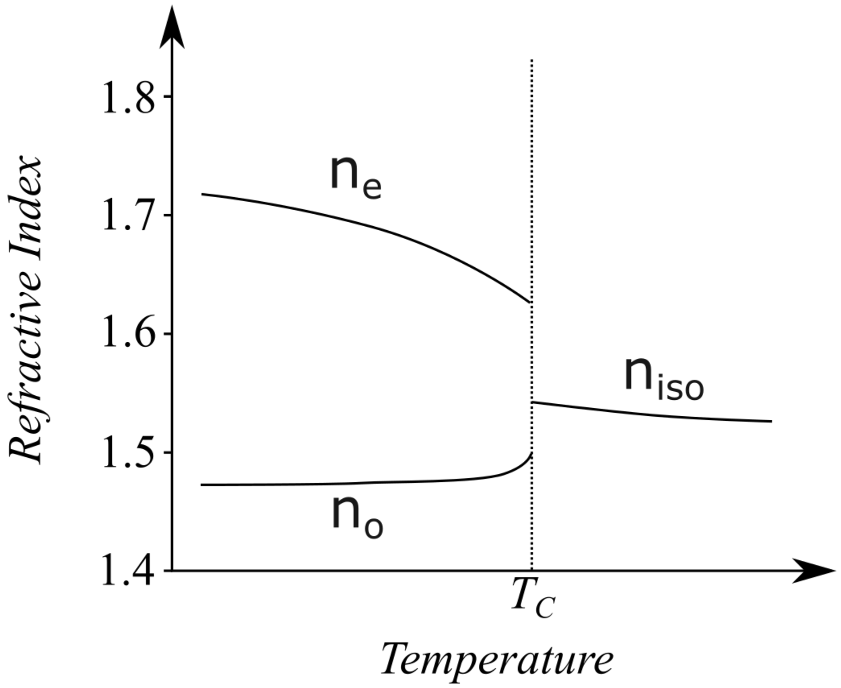

FIGURE 2.7: Temperature dependence of indices of refraction in a nematic liquid crystal.

observable optical properties of an LC device, the simulated director field can be used in conjunction with the Jones matrix method. This section provides a short introduction to the Jones approach as applied to LCs, and a complete description can be found elsewhere[16].

The Jones matrix method is a simple way of calculating the change in the polarisation state of light caused by optical materials[17]. In this formulation, light is represented as a $2 \times 1$ complex vector, **J**, with two elements corresponding to the orthogonal components of the electric field. The Jones vector for linearly polarised light with an orientation at an angle $\Psi$ measured from the $x$-axis is given by,

$$\mathbf{J} = \begin{pmatrix} \cos\Psi \\ \sin\Psi \end{pmatrix} \tag{2.41}$$

Some special cases of linearly polarised states are given by,

$$\mathbf{J}_{horizontal} = \begin{pmatrix} 1 \\ 0 \end{pmatrix} \qquad \mathbf{J}_{vertical} = \begin{pmatrix} 0 \\ 1 \end{pmatrix} \tag{2.42}$$

$$\mathbf{J}_{\Psi=+45^\circ} = \frac{1}{\sqrt{2}} \begin{pmatrix} 1 \\ 1 \end{pmatrix} \qquad \mathbf{J}_{\Psi=-45^\circ} = \frac{1}{\sqrt{2}} \begin{pmatrix} 1 \\ -1 \end{pmatrix} \tag{2.43}$$

whereas circularly polarised light is expressed as,

$$\mathbf{J}_{RCP} = \frac{1}{\sqrt{2}} \begin{pmatrix} 1 \\ -i \end{pmatrix} \qquad \mathbf{J}_{LCP} = \frac{1}{\sqrt{2}} \begin{pmatrix} 1 \\ i \end{pmatrix}. \tag{2.44}$$

In the Jones method, optical components such as polarisers and waveplates are represented as 2 × 2 matrices, which, when they are multiplied with a Jones vector representing the input light, will produce an output vector that describes the polarisation state resulting from transmission through the optical component(s). Therefore, for polarised light passing through one optical component with a Jones matrix $\mathbf{M}$, the Jones vector output is given by $\mathbf{J}_{out} = \mathbf{M}\,\mathbf{J}_{in}$. The intensity of the transmitted light can be calculated multiplying $\mathbf{J}_{out}$ by its complex conjugate. The Jones matrices for polarisers with transmission axes oriented horizontally and vertically are given below,

$$\mathbf{M}_{H\_polariser} = \begin{pmatrix} 1 & 0 \\ 0 & 0 \end{pmatrix} \qquad \mathbf{M}_{V\_polariser} = \begin{pmatrix} 0 & 0 \\ 0 & 1 \end{pmatrix} \tag{2.45}$$

An LC device is represented in the Jones method as a variable waveplate or optical retarder. For a waveplate made of birefringent material of thickness $d$ with a phase retardance, $\Gamma = \frac{2\pi}{\lambda}\Delta n_{eff}\, d$, with its optic axis oriented at an angle 45° with respect to the $x$-axis, the Jones matrix is given by,

$$\mathbf{M}_{waveplate} = \begin{pmatrix} \cos\frac{\Gamma}{2} & -i\sin\frac{\Gamma}{2} \\ -i\sin\frac{\Gamma}{2} & \cos\frac{\Gamma}{2} \end{pmatrix} \tag{2.46}$$

An example of an LC optics experiment that can be modelled with the Jones method is the situation of an LC device located in between a pair of crossed (orthogonal) polarisers, with the optic axis of the LC at 45° to the polariser axis. The experiment can be described with Jones matrices as follows,

$$\mathbf{J}_{out} = \begin{pmatrix} 1 & 0 \\ 0 & 0 \end{pmatrix} \begin{pmatrix} \cos\frac{\Gamma}{2} & -i\sin\frac{\Gamma}{2} \\ -i\sin\frac{\Gamma}{2} & \cos\frac{\Gamma}{2} \end{pmatrix} \frac{1}{\sqrt{2}} \begin{pmatrix} 0 \\ 1 \end{pmatrix} = \frac{-i}{\sqrt{2}} \begin{pmatrix} \sin\frac{\Gamma}{2} \\ 0 \end{pmatrix} \tag{2.47}$$

The first matrix represents the analyser, while the second matrix represents the birefringent LC device. The third term, represents the input polarisation after passing through the first polariser. Note that we have assumed the input light is unpolarised and has a magnitude equal to 1, such that only half of the light intensity passes through the first polariser.

This experimental arrangement, with an LC device between crossed polarisers is commonly found in LC technology. Thus it is useful to understand the transmission through the device to explain observations of a cell on a polarising optical microscope or the operation of a liquid crystal display. The transmission can be found by taking the dot product of the output Jones vector with its complex conjugate, which gives,

$$T = \frac{1}{2}\sin^2\left(\frac{\pi\Delta n_{eff}\, d}{\lambda}\right) \tag{2.48}$$

This approach can be extended to the more-complex situation where the LC device is oriented such that its optic axis is at an arbitrary angle, $\chi$, to the polariser axis. It can then be shown that the transmission is[16],

$$T = \frac{1}{2}\sin^2(2\chi) sin^2\left(\frac{\pi \Delta n_{eff}\, d}{\lambda}\right) \tag{2.49}$$

Therefore, the effective birefringence of the LC, $\Delta n_{eff}$, which can be controlled with an applied electric field, leads to the alteration of the polarisation state of the input light, leading to transmission through the analyser. However, if the director of the LC is aligned parallel to either the polariser or analyser ($\Psi = 0°$ or $90°$), no transmission occurs. Furthermore, if the effective birefringence is reduced to zero, no transmission will occur. This condition is met in an LC device where the director is aligned along the light propagation direction, as the light would only experience the ordinary refractive index.

The strength of the Jones approach is that it can be easily extended to light passing through multiple polarisation-altering elements. For light passing through $N$ optical elements, $\mathbf{J}_{out} = \mathbf{M}_N \ldots \mathbf{M}_3\, \mathbf{M}_2\, \mathbf{M}_1\, \mathbf{J}_{in}$. Therefore, for light passing through an LC device with a complex director distribution, the LC can be divided into a finite number of birefringent slices and the overall transmission calculated by multiplying the Jones matrices representing each slice.

## 2.8 Liquid Crystal Devices

### 2.8.1 Description of LC Devices

In order to take advantage of the useful electro-optic properties exhibited by liquid crystals, these materials are usually filled into glass cells. These devices consist of two glass substrates which are placed very close together, such that there exists a gap of only a few microns between the substrates. The cell gap is normally maintained with a spacing material, most commonly silica or plastic beads of a fixed diameter of 2 - 20 µm. Spacer beads can either be dissolved into the glue that holds the substrates together or dispersed throughout the cell to provide greater uniformity in the cell thickness. To complete the device assembly, an LC is used to fill the cell, such that it forms a thin layer with a uniform thickness in the cell gap.

The glass substrates comprising an LC cell are often augmented with additional functional layers to enable electrical control of the LC director and to encourage a particular alignment. Schematics of the layers comprising an LC device can be seen in Figure 2.8. A transparent conducting material, often indium tin oxide (ITO), is used to coat the glass substrates with electrodes so that a voltage can be applied to the cell. Typically, an alignment layer is deposited on top of the ITO layers and is used to fix the orientation of the LC director at the surface interface.

There are two main types of surface alignment used in LC devices: homogeneous (or planar) where the director lies in the plane of the substrates, and homeotropic, where the director is perpendicular to the substrates. Homeotropic cells, where the director is oriented perpendicular to the glass substrates comprising the cell, can be manufactured with surfactants that are coated onto the cell substrates and promote vertical alignment in the adjacent LC molecules. Egg lecithin is a suitable alignment material in such cases and can be utilised by spin coating an IPA solution of lecithin onto the glass substrates of the cell. However, homeotropic devices are not used in this thesis and will not be discussed further.

Homogeneous planar alignment layers have the effect of fixing the director to lie in the plane of the device substrates and generally consist

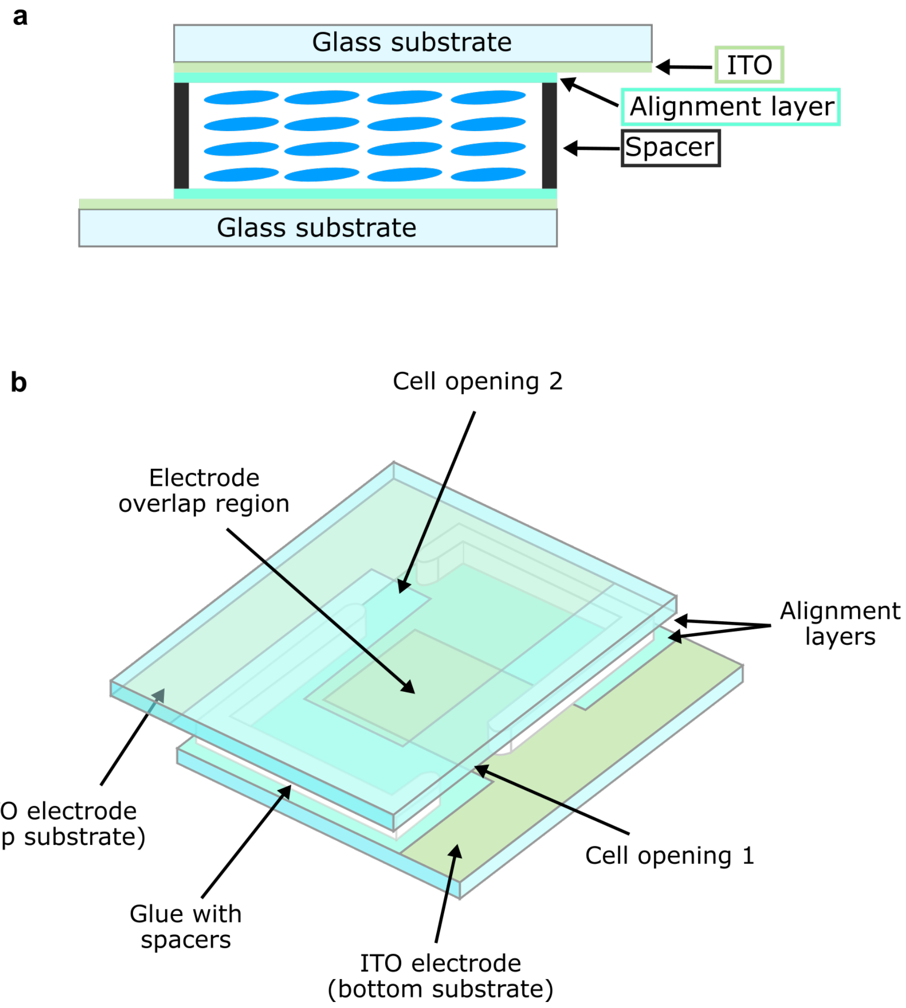

FIGURE 2.8: LC device architecture in (a) 2D and (b) 3D views.

of a polyimide layer that has been mechanically rubbed in one direction. The LC director will lie in the direction dictated by this rubbing direction. In practice, however, there is usually a small pretilt of 1 - 10°, such that the director does not lie perfectly parallel to the device substrates.

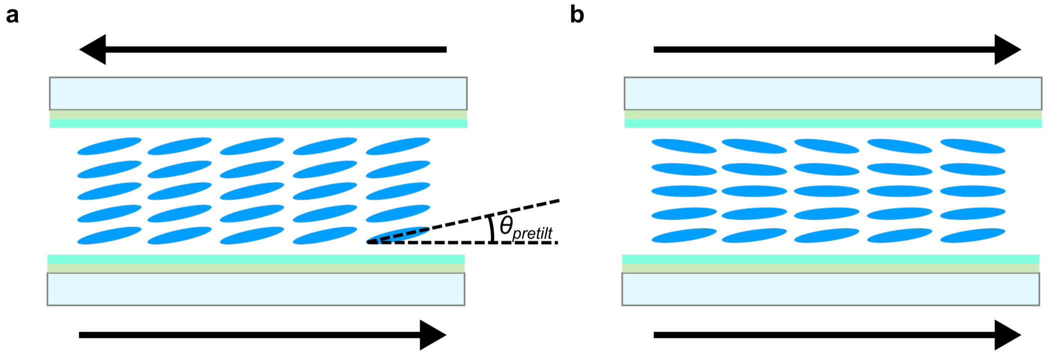

FIGURE 2.9: Schematic illustrations of two different types of planar aligned LC cells, with the substrate rubbing directions indicated by black arrows. (a) A Fréedericksz device formed with substrates with anti-parallel rubbing directions. (b) A pi-cell device formed with substrates with parallel rubbing directions, inducing a uniform splay state across the device. The pretilt angle is indicated in the figure with $\theta_{pretilt}$.

The relative orientation of the rubbing direction of the two substrates has a significant impact on the properties of a device. Figure 2.9 illustrates two different cell types that are distinguished by whether the rubbing directions are parallel or anti-parallel. Fréedericksz devices are assembled such that the rubbing directions are anti-parallel which produces a uniform director profile across the device. In contrast, pi-cells are assembled such that the rubbing directions of the two substrates are parallel and, due to the pretilt of the layers, this creates a uniform splay state across the device. Despite the similarity of these devices, the way in which a nematic LC behaves in response to an applied electric field is dramatically different. The interesting topological-discontinuities in the director field that result from applying an electric field to pi-cells are discussed further in Chapter 6.

### 2.8.2 Alignment Technologies

The standard method of LC alignment is to create an LC cell with thin layers of mechanically rubbed polyimide on the inner surfaces. This encourages the LC molecules to align parallel to the direction in which the polymer has been rubbed. The exact mechanism behind the alignment effect is not fully understood, but it is known that the rubbing process causes the formation of microgrooves oriented parallel to the rubbing direction. The LC molecules are thought to orient parallel to the grooves to reduce their elastic energy, as any other orientation will result in elastic deformations in the LC. Furthermore, the rubbing process is known to orient the polymer chains of the polyimide, such that intermolecular interactions between the LC and the polymer chains also favour a parallel alignment[12]. The rubbing process also produces a unidirectional tilt in the dangling bonds or side chains on the surface of the polyimide layer, which are thought to control the pretilt[18].

The rubbed polyimide technique suffers from a number of significant problems: difficulty in obtaining even rubbing pressure, problems with dust and static charging and, crucially, the inability to obtain multiple alignment domains. For many applications in photonics, it is critical that LC alignment can be performed with microscopic control and high uniformity. As the properties of an LC device depend so strongly on the alignment, a high degree of alignment control may lead to the discovery of new electro-optic phenomena and new applications of LCs.

Consequently, in recent years there have been many reports of more complex alignment technologies that are able to create different alignment domains within the same device. The probe of an atomic force microscope (AFM) can be used to inscribe a polyimide layer and create a micropatterned surface alignment[19–21]. The resolution of such a technique is inherently in the nanoscale regime, however the nature of AFM raster scanning makes it very slow and so it is unlikely that the process could be scaled-up for manufacturing.

Photoalignment is a versatile non-contact method for fabricating LC alignment surfaces[22, 23]. It was first described by Ichimura et al. who coated a substrate with a light-sensitive material which underwent orientational ordering when exposed to polarized light[24]. This process can be performed on individual substrates or in fully-assembled cells, even when they are filled with LC[25]. It took two decades for the process to be refined to the point where it was industrially relevant; in 2009 SHARP Corporation announced a Generation 10 LCD with improved contrast ratios and response times that was fabricated with a photoalignment process[26].

Patterning photoalignment layers can be used to create complex optical elements like q-plates[27], diffraction gratings[28] and switchable Fresnel lenses[29]. Generally, these studies have used holography to create an image of a mask in the plane of a sample, but it is also possible to use single-photon DLW[30, 31]. A clever solution to the patterning of azimuthal and radial alignments has been found with the use of rotating substrates and polarizers in combination with photomasks[27, 32, 33]. However, despite the considerable advances in LC photonics enabled by photoalignment, the technology is limited to patterning of the surfaces that bound a volume of LC.

A key disadvantage of the advanced alignment techniques described in this section is that they can only induce alignment through surface modification and so are limited to fabrication in two dimensions. Whereas, through the use of 2PP-DLW, 3D alignment control can be accomplished, opening up new applications for LCs in photonic technologies. The following section discusses the polymer materials used in 2PP-DLW and Chapter 3 discusses the fabrication process itself.

## 2.9 Polymer Stabilisation and Reactive Mesogens

The incorporation of polymeric constituents into LC mixtures has become an important sub-field of research in LCs[34, 35]. The pioneering work in this field was conducted by Broer and Hikmet who found that the orientational order of an LC phase could be 'locked-in' (or 'frozen-in') through the creation of a polymer network via in-situ photopolymerisation with mesogenic molecules possessing acrylate functional groups[36, 37]. These polymerisable LC monomers are referred to as reactive mesogens (RMs) and, when doped into a host LC, they adopt the molecular orientation of the host.

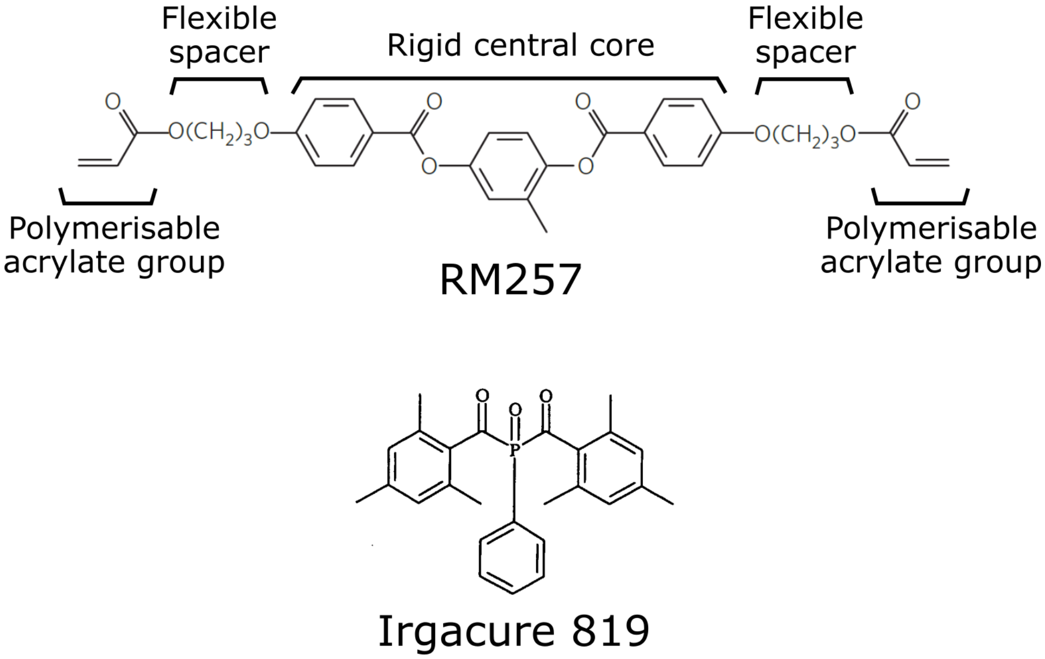

FIGURE 2.10: Chemical structures of a typical diacrylate reactive mesogen, RM257 and a photoinitiator, Irgacure 819.

When UV light is shone on a sample of diacrylate reactive mesogens and photoinitiator dissolved in a non-reactive LC, a polymer network that stabilises the alignment is created via free-radical polymerisation[38]. The chemical structures of typical reactive mesogen and photoinitiator molecules are shown in Figure 2.10. The polymerisation process results in the formation of a bi-continuous composite material where a continuous polymer network permeates a continuous LC phase[39]. The formation of a polymer-stabilised liquid crystal (PSLC) network in an LC device is illustrated in Figure 2.11. The self-assembled order of the liquid crystalline phase is transferred onto the polymer network and the LC is stabilised by elastic interactions between the network and the LC[40]. In practice this means much higher voltages are required for realignment of the LC trapped within the network, the switching response time is reduced and there is a much improved thermal stability of the mesophase[41]. These composite materials are commonly referred to as polymer-stabilised liquid crystals (PSLCs) or anisotropic gels, due to their consistency and mechanical properties.

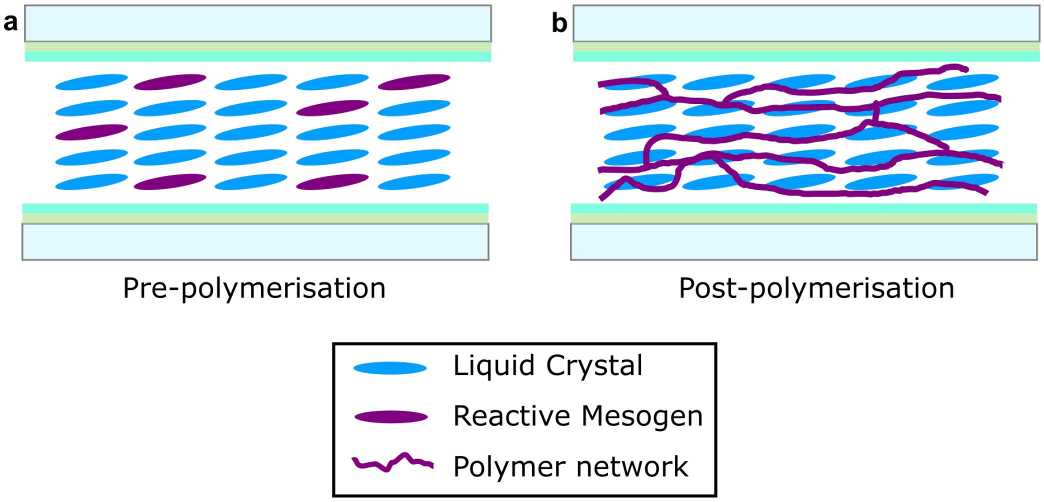

FIGURE 2.11: Formation of a polymer stabilised liquid crystal (PSLC) device. (a) Before polymerisation the device contains a mixture of LC, reactive mesogen and photonitiator (not illustrated). (b) After polymerisation the reactive mesogen has formed a polymer network that stabilises the alignment of the LC. Adapted from [40].

The free-radical polymerisation process that forms a polymer network can be described by three equations, corresponding to (i) initiation, (ii) propagation and (iii) termination. During initiation, photoinitiators enter an excited state after the absorption of a high energy photon, and become a highly reactive free-radical (a chemical species with an unpaired valence electron),

$$\mathrm{I} \xrightarrow{h\nu} \mathrm{I}\bullet \tag{2.50}$$

where $\bullet$ denotes a radical species. Following this, the free-radicals attack the polymer monomers (M) to produce monomer radicals, which go on to attack other monomers and form radical polymer chains.

$$\mathrm{I}\bullet + \mathrm{M} \longrightarrow \mathrm{M}\bullet \tag{2.51}$$

$$\mathrm{M_n}\bullet + \mathrm{M} \longrightarrow \mathrm{M_{n+1}}\bullet \tag{2.52}$$

In the termination process, two monomer radical chains combine together and the polymerisation process is terminated,

$$\mathrm{M_n}\bullet + \mathrm{M_m}\bullet \longrightarrow \mathrm{M_{n+m}} \tag{2.53}$$

There are other potential reactions that can occur during the free-radical polymerisation process, known as side-reactions. For example, a radical monomer chain can terminate by joining the two ends of its chain together. However, these reactions occur much less frequently than the reactions above, and the polymerisation process is therefore largely described by the above equations.

Since their invention in the early 90s, reactive mesogens have found use in a wide range of applications including optical compensation films for LCDs[42], elastomeric polymer networks for actuators[43] and broadband switchable reflective mirrors[44]. Combining photoalignment surface patterning with reactive mesogens has led to the creation of stable anisotropic polymer films[45] that can be used as smart materials for self-cleaning coatings[46] and artificial muscles[47].

# Chapter 3

# Two-Photon Polymerisation Direct Laser Writing

This chapter gives the theory and background to two-photon polymerisation direct laser writing (2PP-DLW), the fabrication technique that was used in most of the results presented in this thesis. The physics of two-photon absorption is explained and the resolution and speed of direct laser writing is discussed. The advantages of including adaptive optical elements and galvanometers into 2PP-DLW systems are examined, and previous work on the use of liquid crystal materials in 2PP-DLW is reviewed.

> *"A laser is a solution seeking a problem."*
>
> **Theodore Maiman**

## 3.1 Introduction to 2PP-DLW

Two-Photon Polymerisation Direct Laser Writing (2PP-DLW) has emerged as a powerful laser-processing technique that can be used to fabricate polymer structures on the micro/nanoscale[48–50]. It is often classed as an advanced additive manufacturing or 3D printing technique[51] and the terms "nanoprinting" and "3D two-photon printing" are sometimes used synonymously with 2PP-DLW. High intensity ultrafast pulses from a femtosecond laser are focused into a polymerisable resin, whereupon the light is absorbed by photoinitiators that trigger a free-radical polymerisation process, crosslinking the monomers in the resin. It offers an advantage compared to conventional focussed UV laser/LED systems because the absorption occurs in a smaller volume (termed a “voxel”) due to the nonlinear light-matter interaction that occurs as a result of the high intensity in each ultrafast laser pulse. By translating the sample with respect to the focus of the laser, fine structures can be fabricated in 3D, with the possibility of achieving a resolution below the optical diffraction limit[52, 53].

## 3.2 Two-Photon Absorption

The extraordinary capabilities of 2PP-DLW stem from the physics of two-photon absorption (2PA), a nonlinear optical process that only occurs when matter is exposed to light of a very high intensity. The phenomenon was first described theoretically by Goppert-Meyer in 1931[54] and, enabled by the invention of the laser, was experimentally demonstrated 30 years later by Kaiser and Garett[55].

In conventional photolithography processes, a photoresist absorbs a single photon in the UV wavelength range, triggering a change in the chemical structure of the photoresist. For positive resists this is typically a bond-cleaving reaction, and the exposed portion of the resist becomes soluble to a developer. Whereas, for negative resists, the exposed area typically undergoes a crosslinking reaction and becomes insoluble to a developer.

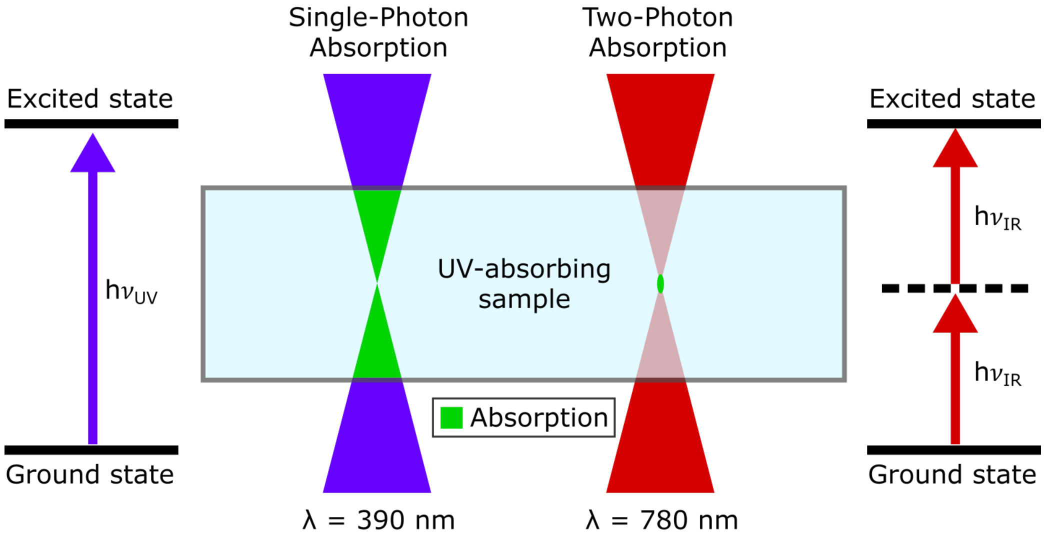

FIGURE 3.1: Schematic illustration of single-photon and two-photon absorption in a sample that is sensitive to UV light.

In a two-photon absorption event, a molecule sensitive to UV light can absorb two photons of near-IR light in quick succession, each of which has half the energy required for excitation. A comparison of single-photon and two-photon absorption is shown in Figure 3.1. The probability of a nonlinear multiphoton process with $N$ photons is $\propto I^N$, where $I$ is the intensity of the incident radiation. Therefore, for 2PA the absorption rate is proportional to the square of the photon density within the resist. In practice, this means that 2PA will only occur in a small volume in the focus of an ultrafast laser that has been focussed with a high-quality microscope objective lens with high NA (numerical aperture). There is no absorption along the path of the beam except for at the focus, because the materials used are transparent to near-IR light and 2PA will only occur when the light intensity is extremely high.

## 3.3 Two-Photon Polymerisation Direct Laser Writing

By translating a photopolymerisable sample (sometimes known as a resin) in a controlled manner relative to the high NA focus of a femtosecond laser, 3D structures can be built up from polymerised voxels (the 3D analogy of pixels) formed via free-radical polymerisation. A schematic illustration of this process is shown in Figure 3.2. By subsequently developing this photopolymerisable resin in a solvent or developer, the unpolymerised material is removed and solid free-standing polymer structures result. Positive photoresist processes have also been demonstrated whereby voids can be created instead of solid structures; having particular use in the fabrication of microfluidic components[56].

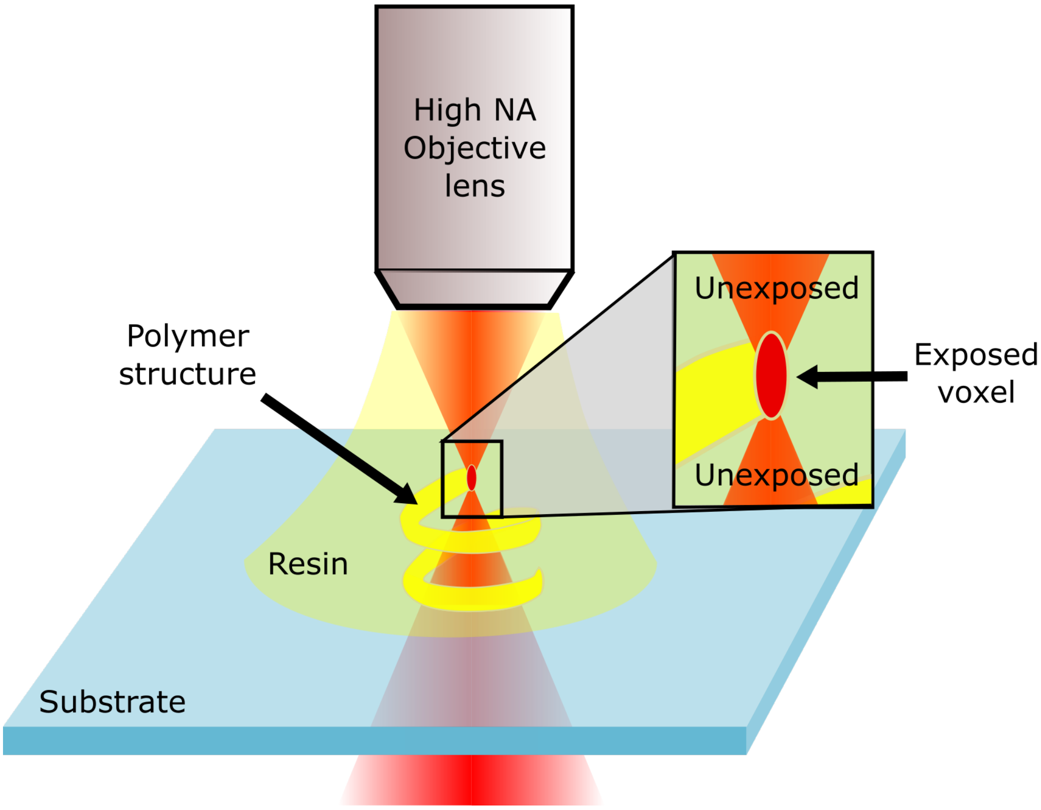

FIGURE 3.2: Schematic illustration of two-photon polymerisation direct laser writing. A 3D structure can be fabricated by scanning the position of the laser focus inside a polymerisable resin. Due to 2PA, the polymerisation reaction only occurs in a small volume in the focus of the laser where the light intensity is high enough to initiate 2PA. This polymerised volume is termed a voxel.

2PP-DLW was first described in 1997 by Maruo et al.[57] since which there has been intense research activity across a number of areas and it is now possible to buy commercial fabrication systems[58, 59]. Applications of 2PP-DLW range from nano- and micro-photonics[60] to metamaterials[61–63] and biomedical engineering[64].

The resolution of 2PP-DLW depends strongly on the NA of the objective lens used to focus the ultrafast laser inside the photosensitive resin, with smaller features being achievable with higher NA. The minimum feature (voxel) size in the lateral ($\Delta r$) and axial ($\Delta z$) directions can be estimated by the following expressions[65, 66],

$$\Delta r \approx \frac{0.61\lambda}{\mathrm{NA}} \qquad \Delta z \approx \frac{2n\lambda}{\mathrm{NA}^2} \tag{3.1}$$

where $\lambda$ is the wavelength of the laser, $n$ is the refractive index of the resin and NA is the numerical aperture of the focussing objective lens.

There is an aspect ratio of 2.5 - 3 in the voxel dimensions even under aberration-free focussing at the very highest NA of 1.25 - 1.4, due to the nature of the light intensity distribution in the focus of a Gaussian beam[65]. Voxels thus have an elongated ellipsoidal shape. In practice, the voxel size in 2PP-DLW depends on numerous factors, such as the absorption properties and concentration of the photoinitiator; the diffusion properties of the radicalised monomers and the exposure time and power of the laser. A comprehensive review of the scaling laws relating to the voxel size in 2PP-DLW can be found in reference [67].

The NA of the focussing objective is clearly a critical parameter for 2PP-DLW, with fabrication of the smallest possible polymer features usually conducted with NA = 1.4 oil-immersion objectives. However, use of the highest NA objective is not necessarily advisable due to the dramatic increase in total fabrication time that results. One of the drawbacks of

2PP-DLW is its extremely low-throughput when working at the highest possible resolutions with high NA objective lenses.

A simple estimate of the total fabrication time of a polymer structure can be obtained by evaluating the following expression[48],

$$t = \frac{xyzF}{Rv} \tag{3.2}$$

where $x$, $y$ and $z$ are the width, length and height of the structure, $R$ is the voxel volume, $v$ is the scanning speed, and $F$ is the fill factor (ratio of polymerised volume to unpolymerised volume in the structure design). As an example, for a typical mesoscale structure with dimensions of 500 µm × 500 µm × 100 µm, with a fill factor of 50%, a voxel volume of 0.14 $\mu m^3$ with NA = 1.4 and a scanning speed of 100 µm/s, the fabrication time is 892857 s (over 248 hours). Using an objective lens with NA = 0.5 to fabricate a structure of the same design gives a fabrication time of 12500 s (approximately 3.5 hours). However, the smallest feature size in the structure also needs to be considered when selecting an appropriate NA and analysed in terms of the minimum voxel size given by equation 3.1.

## 3.4 Advanced Components in Two-Photon Polymerisation Systems

The capabilities of 2PP-DLW go well beyond that offered by conventional lithographic processes, as the technique provides true 3D structuring rather than 2D layer-by-layer fabrication. It also allows rapid prototyping and maskless conversion from 3D design to 3D microstructure, as well as the remarkable ability to create sub-diffraction limited polymer features[68]. However, there are significant challenges in improving the scalability and speed of the technique, which currently inhibits its use as a mass-production fabrication method.

In this section, some advanced DLW technologies which can be used to enhance the performance of 2PP-DLW systems are described. DLW systems are commercially available but are associated with a large cost of >$250K and are typically basic instruments tailored to the fabrication of free-standing microstructures in proprietary negative photoresists. In this thesis, a custom-built 2PP-DLW system was designed and built to allow more control over the system design, and specifically to tailor it to fabrication in LC materials. This system is described in detail in Section 4.2.

The functionality and capabilities of 2PP-DLW systems can be augmented by incorporating adaptive optical elements into the system design[69]. Such devices can correct for spherical aberration[70] occurring due to focussing the laser through a refractive-index mismatch, which is of particular importance for LC devices due to the requirement for a LC device to have two glass substrates to obtain alignment in a thin LC layer. Furthermore, spatial light modulators (SLMs) can also address concerns over scalability and fabrication time associated with 2PP-DLW by creating multiple foci to pattern larger regular arrays with increased efficiency and throughput[71, 72] and by altering the beam-profile[73].

The simplest method of increasing the throughput of 2PP-DLW is to increase the sample translation speed. However, this is limited to ~100 µm/s for commonly-used piezoelectric translation stages and to ~500 mm/s for direct-drive linear stages.

Up to two orders of magnitude improvement in fabrication time can be achieved by using galvanometer scanning mirrors, which move the laser focus inside the sample at speeds on the order of several metres per second. Furthermore, galvanometer scanning mirrors enable 3D structuring with nanometer-precision at a much lower cost than nanopositioning direct-drive linear stages[65].

The key disadvantage of galvanometer scanning is that the writing-field is much smaller (∼100 × 100 µm, depending on the NA of the objective) and thus stitching is required to build up larger structures. Stitching errors are extremely challenging to avoid, although the severity of this problem depends on the resolution of the fabricated structures and the performance of the translation stages[65]. An alternative to stitching is the use of 'infinite field-of-view' technology, where the scanning of the galvanometer mirrors is synchronised closely with the motion of the translation stages[74, 75]. However, the computational difficulty, both in terms of the coordination/timing of multiple hardware components, as well as software development overheads, makes this quite challenging to implement.

## 3.5 Liquid Crystal Resins for Direct Laser Writing

In this thesis, the use of LC materials as functional resins in 2PP-DLW is investigated. This section provides some background on the state-of-the-art in this area of research. Existing reports of microfabrication using 2PP-DLW in LCs can be divided into two categories: (i) microstructuring of polymer surfaces/lattices that are infiltrated with LC after fabrication, and (ii) in-situ laser writing of a polymerisable LC mixture to form crosslinked LC-polymer networks.

It is well known that LCs align when they are in contact with micro-scale grooves or gratings on a polymer surface[18, 76]. Xie et al.

first reported the fabrication of such periodic structures with 2PP-DLW in PMMA (a positive photoresist) for the purposes of aligning nematic LCs[77] and Lee et al. reported the fabrication of similar structures in a commercial negative photoresist[78]. A number of studies since then have successfully used 2PP-DLW to create microgratings for planar alignment before fabricating more complex polymer microstructures on top of the micrograting. A slightly different approach to create polymer alignment surfaces was demonstrated by Ji et al. where polymer walls were written in a negative photoresist which subsequently caused alignment of the LC director parallel to the wall direction[79].

A number of groups have extended this 2D alignment capability by creating 3D polymer microstructures that function as LC alignment surfaces. Serra et al. fabricated a simple cubic microlattice using a negative resist that was subsequently functionalised with a homeotropic alignment agent and then infiltrated with LC[6]. This created a complex frustrated director profile inside each cubic void in the lattice. Applying a voltage caused some of these pixels to become dark under polarised optical microscopy, due to the director becoming uniformly aligned with the field. There was some degree of 'memory' associated with this process, whereby the number of pixels that stayed dark after the voltage was removed depended on the strength of the voltage initially applied. Woodpile photonic crystal structures have also been fabricated from negative photoresist before being infiltrated with LC. Ho et al. showed that light diffraction through such a structure can be tuned by tuning the degree of order in the LC through changes in temperature[5].

Recently, Lee et al. have reported the fabrication of a fast, polarisation-independent LC phase modulator created via 2PP-DLW fabrication of polymer shelf structures to partition the cell gap in LC devices[80]. The polymer shelf effectively splits the liquid crystal cell in two and, as the response time is quadratically dependent on the cell thickness, a decrease in the response time results[4].

It is clear that interesting and novel phenomena have been demonstrated with LC-infiltrated polymer structures. However, it is not possible to exert direct control over the alignment at every point in the bulk of the LC using this method. The alignment is communicated to the bulk of the LC molecules by the bounding surfaces, and the director profile is thereafter dependent on the elastic energy and cannot be directly controlled or modified during the fabrication.

2PP-DLW in polymerisable LCs follows a different methodology to the examples described above. A mixture of a host LC and reactive mesogen and photoinitiator resin can be injected into a LC cell and used in a 2PP-DLW system in order to fabricate 3D polymer-stabilised LC structures in-situ within the device. The photoinitiators absorb the light through 2PA and generate free radicals that transfer electrons to the reactive diacrylate molecules which cause them to cross-link and form a PSLC network. Here, the photopolymerisable resin is itself liquid crystalline, which means that the polymer structures possess a molecular anisotropy that depends on the alignment at the moment of fabrication (Section 2.9). This presents significant new opportunities for creating novel electro-optic effects and functional LC-polymer composites, as the orientation (and thus birefringence) of LC molecules embedded in the polymer can be controlled microscopically during laser-writing by dictating the alignment with external fields.

The first reports on 2PP-DLW of LC-polymer structures fabricated in-situ were described by Yoshida et al. who polymerised a chiral nematic monomer mixture in a spatially-selective manner to leave an unpolymerised layer of chiral LC in the centre of an LC device[81, 82].

This had the effect of creating a photonic defect mode which could be exploited when the chiral nematic structure was used as a cavity for an LC laser[83]. Subsequently, Ito et al. fabricated microcylinders using 2PP-DLW with a photopolymerisable nematic liquid crystal mixture aligned in a simple rubbed polyimide cell[84]. These studies demonstrated the use of 2PP-DLW in creating intricate polymer structures inside a liquid crystal device, but the alignments were uniform and were not actively controlled during fabrication.

In contrast, Tartan et al. showed the advantages of localised and controlled polymer stabilisation of different voltage-dependent alignments inside an LC device using 2PP-DLW[85]. The technique was employed to form homeotropically-aligned polymer walls by applying a voltage with a magnitude sufficiently high to unwind the helix in a chiral nematic LC device. The periodic polymer walls had the ability to stabilise the uniform-lying helix electro-optic switching mode[86] which is challenging to align and tends to be unstable[87].

## 3.6 Summary

In summary, 2PP-DLW is a powerful and versatile technique for fabricating LC-polymer composite materials with microscale feature sizes. Furthermore, alignment control is of paramount importance in LC technology and, as new LC photonic devices have been demonstrated by controlling the alignment with a microscale precision; there is a compelling opportunity to use the reactive mesogen and photoinitiator molecules described in Section 2.9 as a resin material for 2PP-DLW microfabrication. As this process can be conducted inside a fully-assembled LC cell, an electric field can be applied during fabrication, allowing highly-localised polymer stabilisation of voltage-dependent director profiles. This is a largely unexplored area for advanced microfabrication of functional structures in LCs and is the key subject of this thesis.

# Chapter 4

# Experimental Methods

This chapter details the experimental methods frequently used in this thesis, including liquid crystal device characterisation, mixture preparation, polarised optical microscopy and 3D printing. The latter half of the chapter describes the design and build of a bespoke 2PP-DLW system for microfabrication in liquid crystals.

> *"Published papers may omit important steps and the memory of men of science, even the greatest, is sadly fallible."*
>
> **John Desmond Bernal**

## 4.1 Liquid Crystal Devices and Characterisation

To avoid repetition in subsequent chapters, this section describes some of the methods commonly used throughout this thesis, including mixture preparation, cell filling and polarised optical microscopy. Other methods that were specific to particular experiments are described in full in the relevant chapters.

### 4.1.1 Fabrication of Liquid Crystal Devices and Cells

Typically, the photoresists used in 2PP-DLW form isotropic polymers where there is no molecular ordering to the crosslinked polymer chains and the functionality of the materials is controlled solely by the micro/nanostructure of the 3D design. In contrast, throughout this thesis, the resin used is a polymerisable liquid crystalline mixture, allowing tuning of the properties of the resin itself by altering the molecular alignment and order with external fields during fabrication.

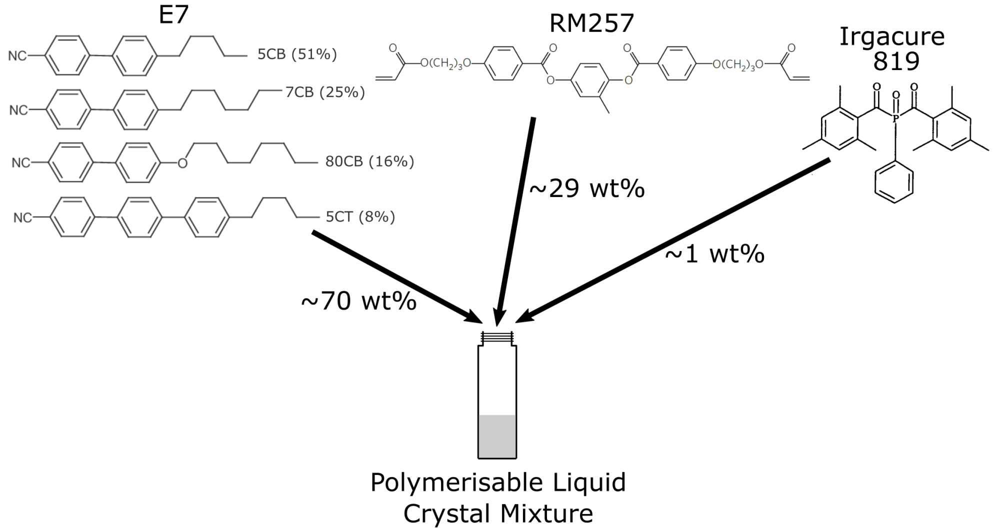

FIGURE 4.1: Schematic illustration of the mixture preparation process. E7, RM257 and Irgacure 819 are mixed together in a ratio by weight of approximately 70:29:1 to form a polymerisable liquid crystal mixture suitable for curing via UV and two-photon polymerisation.

The constituents of the polymerisable resin are a host LC, a reactive mesogen and a photoinitiator which are mixed together in a 70:29:1 ratio by weight, following the method of Tartan et al.[85]. The chemical structures of the three constituents are shown along with their respective weight fractions in Figure 4.1. Throughout this thesis, the host LC used is E7, a well-characterised commercial mixture of cyanobi- and tri-phenyls with a clearing temperature of 58°C. The reactive mesogen used is RM257, a common RM material that exists as a solid at room temperature and has a nematic range of 86 - 116°C. The refractive indices of polymerised RM257 are $n_o = 1.53$ and $n_e = 1.66$[34]. It is important to employ an RM with refractive indices that are close to that of the host material E7 ($n_o = 1.5, n_e = 1.69$), to avoid scattering caused by a large mismatch in the refractive indices between the host and the RM. After polymerisation, the polymer network formed will not be exclusively formed of RM257 and will additionally contain E7 embedded in the network and E7 phase-separated in micrometer-sized pockets within in the network. Unpolymerised regions will contain E7 and unreacted monomer and photoinitiator.

The smallest component by weight of the mixture is Irgacure 819 (Chemical name phenylbis(2,4,6-trimethylbenzoyl)phosphineoxide), a commonly used photoinitiator for free-radical polymerisation, with strong absorption from 360 - 410 nm. This photoinitiator was chosen due to its absorption peak at 390 nm, which is half of the wavelength of the fabrication laser used to initiate two-photon polymerisation.

To completely mix the constituents of the polymerisable mixture, the sample vial is placed in an oven for 24 hours at a temperature of 70°C. This temperature was chosen as the mixture is observed to have a clearing point of $\sim$69°C and it is important to completely mix the components in the isotropic phase. After this, the mixture can be filled into an LC cell in

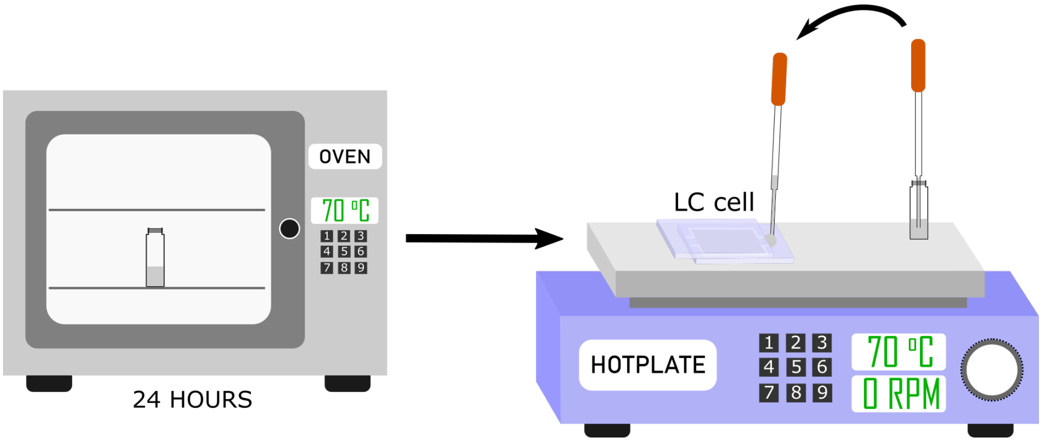

FIGURE 4.2: Schematic illustration of the process of cell filling. First the mixture is placed in an oven at 70°C for 24 hours to completely mix in the isotropic phase. The cell to be filled is placed on a hotplate and then filled via capillary action with the hotplate set to 70°C to ensure filling takes place in the isotropic phase. The cell is then allowed to cool before being polymerised.

readiness for photopolymerisation.

Cell-filling proceeds by first placing an LC cell on a hotplate set to 70°C. The mixture is rapidly transferred from the oven to the hotplate to ensure it remains in the isotropic phase. A Pasteur pipette is then used to transfer a small droplet from the vial onto one of the openings of the cell, after which it infiltrates the cell via capillary action. After the cell is completely filled, the temperature is slowly reduced to room temperature so that the LC will relax into the most thermodynamically stable alignment within the device.

### 4.1.2 Polarised Optical Microscopy

There is considerable use of polarised optical microscopy (POM) throughout this thesis to observe the microstructure of LC devices engineered with 2PP-DLW. Microscopy was conducted using an Olympus BX51 microscope with a QImaging Retiga R6 6.0 megapixel CCD camera attached to the phototube. A schematic illustration of the microscope setup is shown in Figure 4.3. In transmission mode, the illumination is provided by a halogen light bulb that first passes through a condenser lens and a linear polariser before reaching the sample plane. A long-pass filter with a cut-off wavelength of 550 nm was inserted before the sample to avoid causing any polymerisation in devices that still contained unreacted monomer.

An objective lens turret allows for convenient switching of the magnification and a rotatable analyser (a second linear polariser) can be inserted before the eyepieces/phototube to observe the interference colours exhibited by birefringent samples. In general, the analyser is rotated such that is it "crossed" with respect to the first polariser, a configuration where the transmission axis of the analyser is perpendicular to the first polariser. Under these conditions, isotropic samples appear black (extinction), whereas birefringent samples generally exhibit bright interference colours described by the Michel-Levy chart[88]. However, if a birefringent sample is mounted such that its optic axis is parallel to the microscope axis, it will also appear black between crossed polarisers. In LCs, this condition is met when an LC device is aligned homeotropically, that is, where the director is perpendicular to the glass substrates of the device.

The sample stage could be rotated to allow observation at a range of angles with respect to the crossed polarisers. To aid with positioning of the sample, the stage was fitted with an adaptor to allow lateral translation of the sample with manual thumbscrews. Olympus objective lenses were used with the cover slip correction collar set to the thickness of the glass slides comprising the LC device, in order to improve the quality of the microscope images by reducing spherical aberration.

Throughout this thesis, LC cells were investigated with POM at a range of voltage amplitudes in order to study the switching behaviour. To increase the efficiency of these measurements, MATLAB scripts were

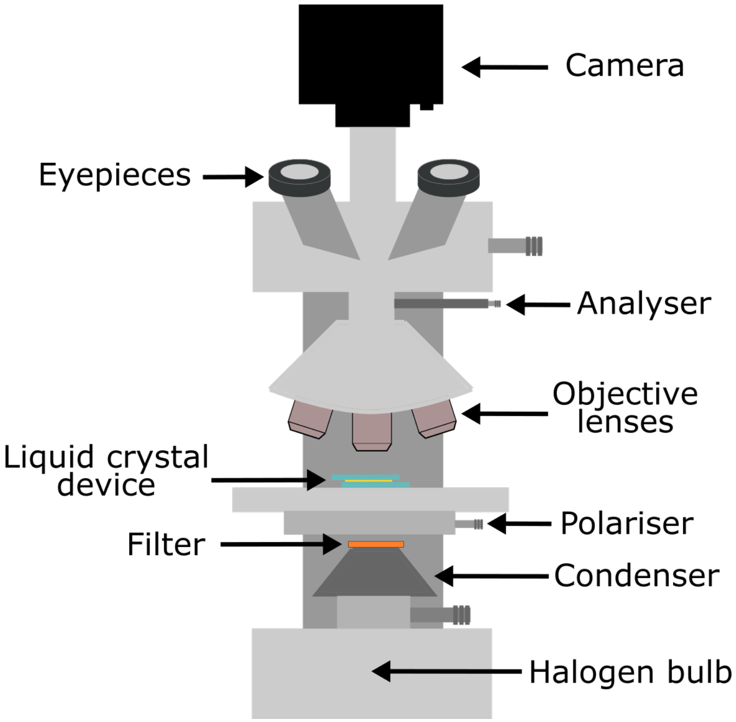

FIGURE 4.3: Schematic illustration of the polarising optical microscope used in this thesis with optical components labelled.

written to automate the process of obtaining microscope images at different voltage amplitudes. This was done both to increase speed and reduce the likelihood of the sample being inadvertently repositioned between measurements.

### 4.1.3 3D printing

3D printing was frequently used to rapidly manufacture adaptors and connectors used in experimental setups. These components were made with PLA (polylactic acid) filament and fabricated by a Makerbot Replicator+ 3D printer. The printer heats the filament to 220°C before extruding it mechanically by forcing the filament through the nozzle of an extruder. By translating the extruder around the build plate with stepper motors, a solid plastic part can be built up in a layer-by-layer fashion.

The design process began by building a 3D model of the component in the Solidworks 3D CAD software before exporting the file as an .STL (stereolithography) file. The .STL file was imported into Makerbot Print, a software package that controlled the 3D printer and allowed remote monitoring of the printing process. The position of the component on the build plate could be adjusted in order to optimise the printing process. In general, components should be oriented to minimise overhangs, as additional support material is required to support overhanging sections of a printed part, and the build quality usually decreases in these cases.

The settings for the print depended on the quality of the part required, the desired printing speed and the footprint of the part on the build plate. There is a trade-off between quality and fabrication time such that setting a low "minimum layer height" (effectively the resolution of the print) of 0.02 mm would lead to a high quality print but a very long fabrication time.

A common problem found in 3D printing was with components peeling off the build plate as the part was printed. This was a particularly prominent issue in parts with a large footprint, and results from the cooling of the PLA plastic after it is extruded from the nozzle. To combat this, the build plate could be covered in an adhesive tape to improve the adhesion of the part as the plastic cooled down. Alternatively, the Makerbot Print software could be instructed to print a "raft", which is a thin 3D-printed bed onto which the part is printed, and this generally improves the adhesion to the build plate.

## 4.2 Design and Build of Liquid Crystal Direct Laser Writing System

The microfabrication of polymer structures in LC materials that is described in this thesis was conducted using two different two-photon polymerisation direct laser writing systems. The work described in Chapters 5 and 6 was conducted using a laser machining system developed by Dr. Patrick Salter and colleagues in the Dynamic Optics and Photonics Group in the Department of Engineering Science at the University of Oxford[89]. This system was initially designed to explore the potential of using adaptive optics in laser micromachining systems[70] and has been used extensively for fabrication inside diamond[90] and silica glass[73]. The configuration of this system was adapted for two-photon polymerisation in LC devices and is described in the experimental methods sections of Chapters 5 and 6.

As part of the DPhil project described in this thesis, a separate 2PP-DLW system was designed and built which was tailored for fabrication in LC materials. This resulted in a bespoke 2PP-DLW system that was designed solely for the requirements of fabrication in LCs. The fabrication of the diffractive optical elements described in Chapter 7 was conducted using this apparatus. This section describes the design of the system, as well as detailing some ideas for further development that will enhance its future capabilities.

### 4.2.1 Overview of System Design

A 2PP-DLW system is a complex optical setup with multiple subsystems that perform various functions including optical power control, beam diagnostics, beam gating, beam conditioning, sample positioning and in-situ imaging.

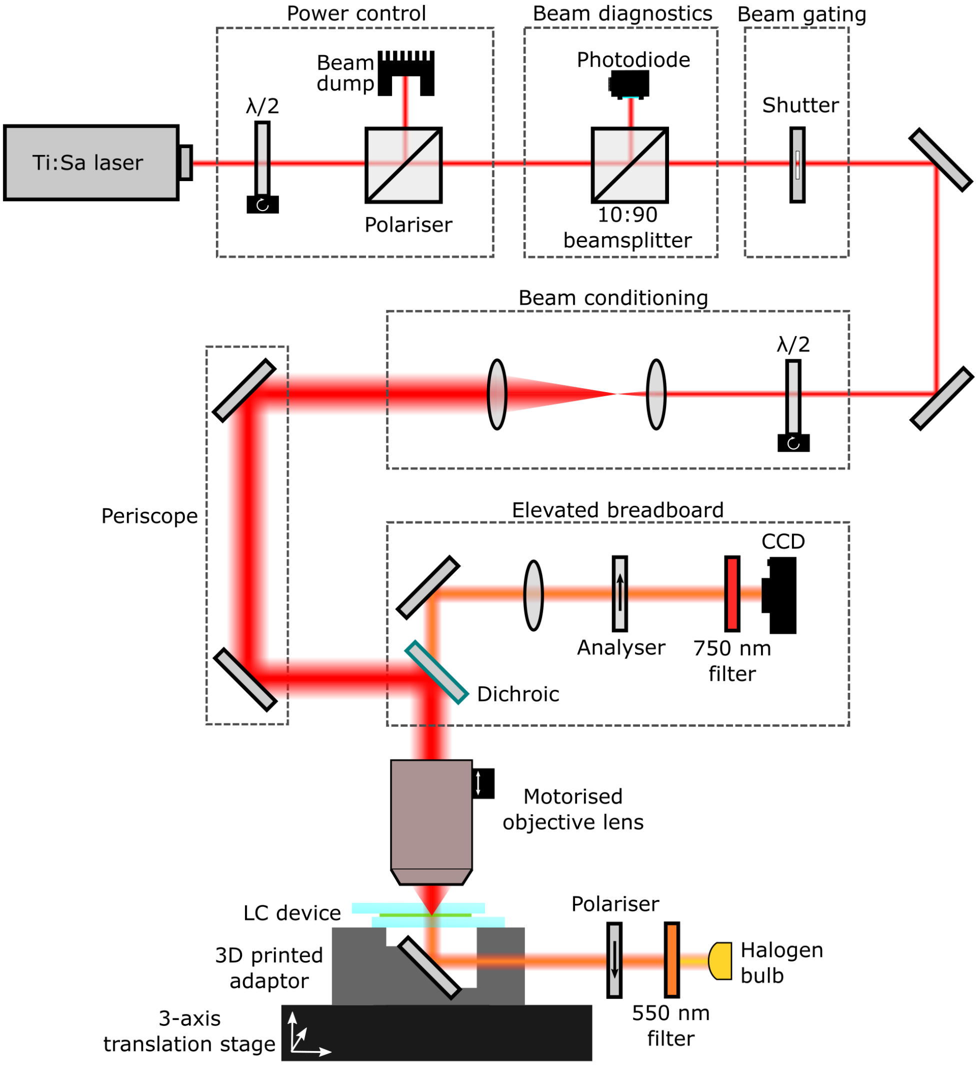

FIGURE 4.4: Schematic of the optical layout of the two-photon polymerisation direct laser writing system with key optical subsystems highlighted. The red lines show the path of the 780 nm femtosecond laser, while the orange lines show the path of the sample illumination subsystem.

A schematic of the direct laser writing system design is shown in Figure 4.4. The laser source is a mode-locked Titanium:Sapphire femtosecond laser (Spectra-Physics Tsunami) at 780 nm, emitting 100 fs pulses at a repetition rate of 80 MHz. The beam is first passed through the power control system, consisting of a half-waveplate and polariser, where the waveplate is mounted on an electronically-controlled rotation stage in order to vary the optical power.

The beam then passes through a beam diagnostics subsystem which consists of a 10:90 non-polarising beamsplitter and a photodiode (Thorlabs S120C) connected to a digital optical power meter. The beamsplitter taps 10% of the power of the main beam so that its optical power can be ascertained without losing a large proportion of the power delivered to the sample.

For beam gating, a fast (20 ms) mechanical beam shutter (Thorlabs SH05) is mounted immediately after the beamsplitter and allows for a modulated laser power that can be synchronised with the motion of the stages. Mounting the shutter in this position, after the beam diagnostics subsystem, is useful as the power of the beam can be measured and adjusted without any radiation reaching the sample plane.

The beam conditioning subsystem follows after the optical shutter and consists of a half-waveplate on a manual rotation stage and lenses for beam expansion. It was important to have control over the polarisation of the laser with respect to the sample orientation, as aberrations are dependent on the polarisation when a laser is focussed through a birefringent material. The half-waveplate therefore allowed rotation of the linear polarisation of the femtosecond laser.

To fill the rear focal plane of the objective lens, the beam must be expanded. The expansion required depends on the pupil diameter of the objective lens being used for the fabrication and is given by, $\varnothing = 2\text{NA}\, f$, where $f$ is the focal length of the objective. This is given by $f = 180/M$, where $M$ is the magnification for an infinity-corrected objective with a tube length of 180 mm.

In this thesis, two Olympus infinity-corrected objective lenses of magnifications 10X and 20X were used which had NA = 0.3 and 0.5. The pupil diameters are therefore 10.8 mm and 9 mm, respectively. At the output of the laser, the beam is approximately 2 mm in diameter and therefore required expansion by a factor of $\sim$5.5 for the 0.3 NA lens and $\sim$4.5 for the 0.5 NA lens. The magnification was performed by a pair of lenses in a telescope configuration with a 50 mm, 300 mm pair used for the 0.3 NA lens and a 80 mm, 300 mm pair used for the 0.5 NA lens.

The beam is then deflected upwards with the use of a mirror and deflected again by a second mirror to bring the beam into the plane of an elevated optical breadboard. The beam is then deflected downwards by a shortpass dichroic mirror onto the back aperture of the objective lens mounted underneath the breadboard. The objective lens itself is mounted on a piezo scanner with a range of 100 µm (PI PIFOC) so that its position can be adjusted independently of the sample. It was useful to have an independent method for adjusting the depth of focus in a sample, as this allowed the depth of focus to be changed while automated fabrication routines were running.

The sample positioning subsystem consists of a three-axis stack of translation stages (Aerotech ANT95XY-050 and ANT95V-3) with a positioning resolution of 1 nm onto which the sample is mounted. An adaptor to hold the sample was designed in 3D CAD software and printed using the 3D printer described in Section 4.1.3. A photograph of the objective lens and sample-mounting system is shown in Figure 4.5.

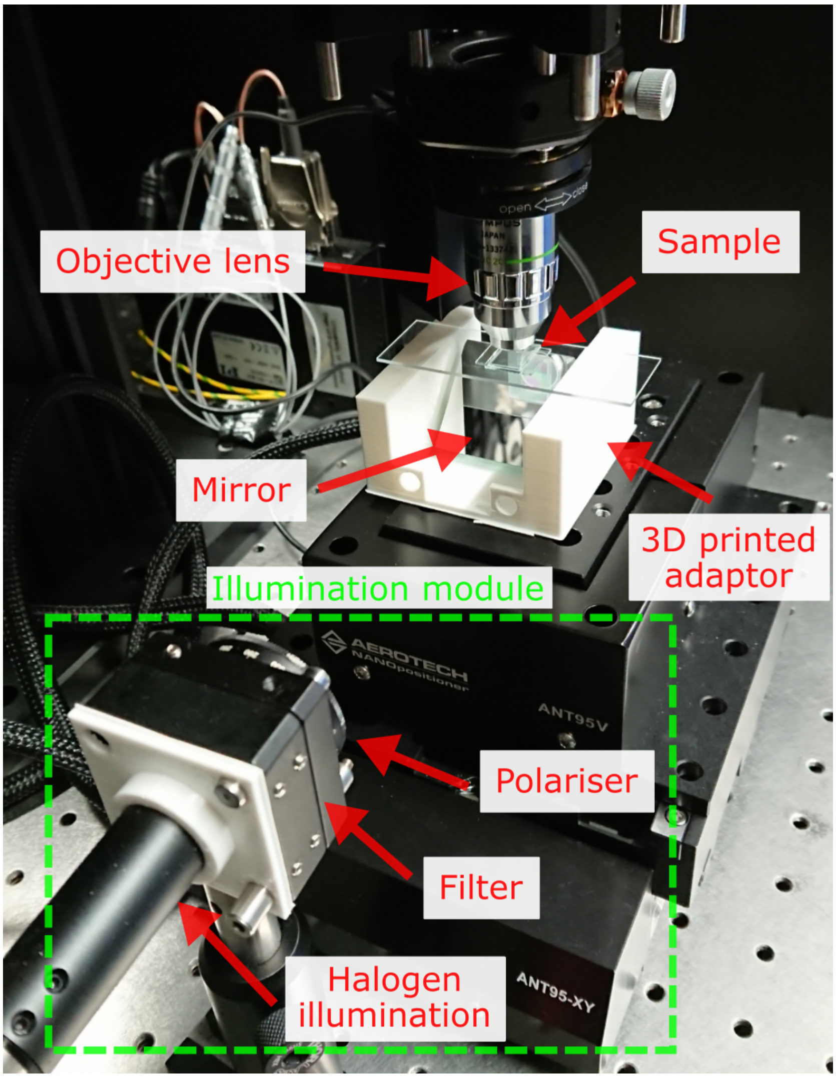

FIGURE 4.5: Photograph of the sample-mounting arrangement in the DLW setup. The illumination module for the imaging subsystem is shown in a dashed green box.

The in-situ imaging subsystem was designed to allow microscopic observation of the sample between crossed polarisers in real-time. The subsystem consists of a halogen illumination source (Thorlabs OSL2) which is coupled into a multi-mode optical fibre and collimated by an adaptor at the output of the fibre. The white light first passes through a 550 nm longpass optical filter, which blocks any light that could be absorbed by the photoinitiator in the sample. Then it passes through a film polariser before reflecting off a mirror mounted at 45° in the 3D printed adaptor underneath the sample. This mirror deflects the light upwards through the sample and towards the objective. The light then encounters the shortpass dichroic mirror which has a cutoff wavelength of 650 nm, allowing any light below 650 nm to be transmitted through the dichroic mirror. It then reflects off another mirror which brings the path of the light into the plane of the elevated breadboard before being focussed by a lens and passing through an analyser onto a colour CCD camera (Thorlabs DCU224C). There is an additional 750 nm shortpass filter mounted onto the front of the CCD camera, as it was found that the dichroic mirror could not completely suppress the 780 nm laser which caused saturation of the CCD.

### 4.2.2 Beam Diagnostics Subsystem Power Calibration

It was necessary to calibrate the beam diagnostics subsystem so that the power measured in the beam tapped off the main beam by the 10:90 beamsplitter could be related to the power received at the sample plane. This subsystem was important to the design, as it allows the power received by the sample to be measured without disrupting the mounting of the sample.

The calibration was performed by using a thermal optical power sensor (Thorlabs S350C) placed in the sample plane and simultaneously

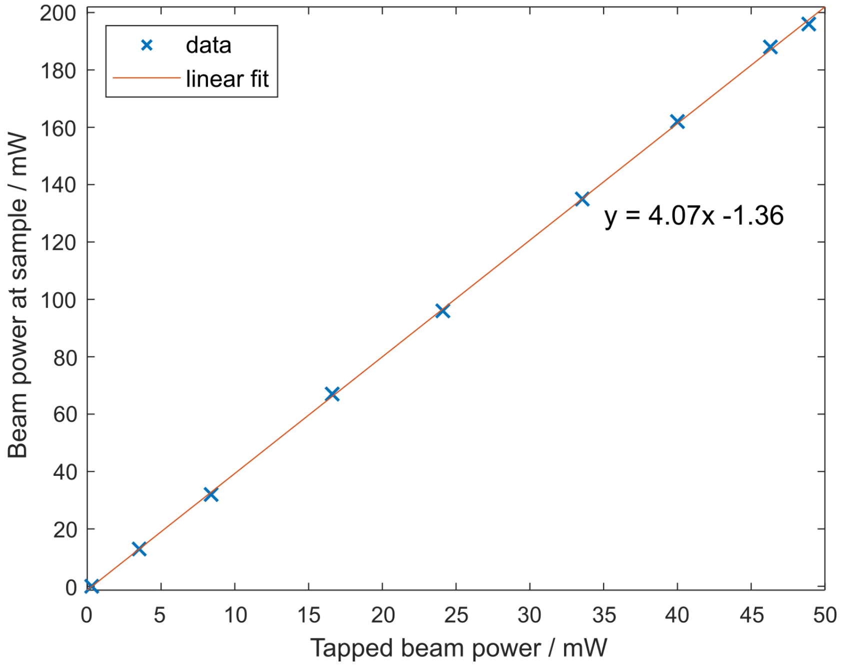

FIGURE 4.6: Calibration for the beam diagnostics subsystem. The power of the tapped beam from the 10:90 beamsplitter is displayed on the x-axis and the power measured at the sample plane is displayed on the y-axis. A linear fit gives a calibration factor of 4.07.

measuring the power of the tapped beam at a range of input powers. By varying the angle of the waveplate in the power control subsystem, the optical power input to the DLW system could be easily adjusted. The calibration is shown in Figure 4.6, where a linear fit to the data has been performed, giving a calibration factor of 4.07. To obtain the optical power at the sample, the power measured in the tapped beam from the 10:90 beamsplitter simply needs to be multiplied by this calibration factor.

### 4.2.3 Software

The direct laser writing system was controlled with various software packages. This section explains the purpose of each piece of software and how it interacted with the hardware of the DLW system.

The Thorlabs Kinesis motion control package was used to control the angle of the rotation stage to which the half-waveplate for power control was mounted. The optical power of the tapped beam measured by the photodiode was displayed with the Thorlabs Optical Power Meter program. Use of these two pieces of software in tandem allowed the power to be adjusted and monitored in real-time.

The piezo-stage to which the objective lens was mounted was controlled by PI Nanocapture. This allowed the position of the objective to be adjusted over a range of 100 µm with a resolution of 1 nm.

The CCD in the imaging subsystem was controlled with Thorlabs ThorCam which allowed both real-time monitoring and adjustment of the camera settings including exposure and gain. It was also occasionally useful to mark the image of the device with annotations for reference. This was used frequently to mark the position of the laser spot in the sample, such that the user would be able to anticipate where a fabrication would begin.

The fabrication process itself was controlled by the Aerotech Ensemble Motion Composer. This software allows for writing and testing of AeroBasic code (see following section) which dictates the motion of the translation stages and controls the laser shutter. It also allows for editing of various control parameters for the stages and tuning of the stage PID control loops.

### 4.2.4 AeroBasic Translation Stage Commands

The high-resolution Aerotech translation stages can be controlled with a G-code derived programming language called AeroBasic. The language is comprised of commands that instruct the stages how to move and is supplemented with other commands that can be used to trigger auxiliary outputs and interface with other equipment. In the context of this thesis, an AeroBasic script is often referred to as a "fabrication script", as it is used to control the pattern that is fabricated into a polymerisable LC device.

The most common command used in fabrication scripts is the `linear` command which instructs the stages to move to a new position at a constant speed. An example of a linear command is:

```
linear X 0.20 Y 0.50 Z 0.00 F 0.10
```

The letters `X`, `Y` and `Z` refer to the axes of the 3-axis translation stage stack and the numbers after each letter give the distance the axis should move. The letter `F` refers to the movement speed. The units used in AeroBasic are millimetres and seconds. Therefore, this command is instructing the stages to move by 0.2 mm in the `X` axis and 0.5 mm in the `Y` axis at a speed of 0.1 mm/s.

Another frequently used command was the `DOUT` command which controlled one of the auxiliary digital outputs of the stage controller. This output was connected to the optical shutter placed in the path of the fabrication laser so that the laser could be gated and synchronised with the movement of the stages.

AeroBasic scripts were very rarely written manually in the course of this thesis. With the exception of brief test runs, the standard process involved writing a script in MATLAB to generate the AeroBasic fabrication script. As fabrication processes often involved repetitive movements, this was the most efficient way to produce AeroBasic code. In addition, for some fabrication processes, the desired polymer structure was based on a particular design image. In these instances, the input to the MATLAB generation script was an image of the design and this was read and interpreted by the script in order to produce an AeroBasic fabrication script.

### 4.2.5 Future System Development

As described in Section 3.4, the inclusion of adaptive optics into a two-photon polymerisation system confers a number of benefits including improved feature resolution, parallel processing, and beam shaping. The DLW system described in this chapter was designed such that a spatial light modulator could be inserted into the setup at a later date.

As the phase of the SLM needs to be conjugate with the back focal plane of the objective, it requires a 4f lens system between the SLM and the objective. This could be accomplished with two 400 mm lenses placed in between the beam expander and the objective lens. To facilitate this, a distance of 1600 mm from the objective was measured and this position was reserved for a future SLM.

As also described in Section 3.4, galvanometer mirrors could be used to improve the fabrication speed while preserving the quality of the fabrication process. With some adjustments to the path of the beam on the optical table, galvanometer mirrors could be inserted into the system. This would require an additional 4f lens pair to image the plane of the galvos onto the SLM.

This 2PP-DLW system is designed to be specifically tailored to microfabrication in LC devices. To extend its capabilities in this area, a calibrated hot stage, mounted to the translation stages, could enable fabrication in materials with LC phases that do not exist at room temperature. This would also introduce another degree-of-freedom to the fabrication process, whereby the temperature could be adjusted during fabrication, so the nematic order of fabricated polymer features could be tuned. In addition, it would enable fabrication in LC materials while they are in an isotropic phase above the clearing point of the material.

Finally, control software could be designed in LabVIEW or

MATLAB that unifies the individual software packages used to control the hardware elements of the DLW system. This would increase efficiency and ease-of-use, and may enable the development of more complex fabrication procedures that synchronise the motion of galvanometer mirrors and translation stages to rapidly manufacture polymer structures over a large area.

# Chapter 5

# Voltage-Induced Refractive Index Matching for Read-On-Demand Images

This chapter describes how 2PP-DLW can be used to fabricate microscale polymer structures that stabilise the voltage-dependent states of a nematic liquid crystal cell. This capability enables complex patterns to be inscribed and hidden in an LC device and made invisible or visible depending on the voltage applied to the device after fabrication. By reading a device with the same voltage amplitude that is used to write the polymer structures, features can be made to disappear as the director profile becomes homogeneous with the surrounding regions. It is shown how this process can be used to create microscale reconfigurable emoticons and QR codes within a fully assembled LC device, with potential use in authentication and identification applications.

*"The pages are still blank, but there is a miraculous feeling of the words being there, written in invisible ink and clamouring to become visible"*

**Vladimir Nabokov**

## 5.1 Introduction and Background

### 5.1.1 Refractive Index Matching in LC/polymer devices

Refractive index matching of polymer binders with liquid crystalline materials has been explored in considerable depth over many years, particularly in the context of polymer dispersed liquid crystals (PDLCs), where the mismatch between the refractive indices of a polymer matrix with embedded LC droplets leads to light scattering. PDLC devices are electrically switchable, where the scattering can be turned off by matching the ordinary refractive index of the LC to that of the polymer using an applied voltage[91–97]. This phenomenon has been exploited in LC privacy windows that switch between transparent and opaque/translucent states[98, 99] and PDLCs have also found use in a range of other optical devices including light shutters[100], displays[101], and diffractive optical elements[102].

PDLCs are usually composed of 40 – 60 wt% LC, with the rest of the mixture made up by isotropic polymer monomers and a small concentration of photoinitiator. A simple PDLC film is usually fabricated by using UV light to initiate a photopolymerisation-induced phase separation (PIPS) process across the bulk of a sample. This leads to the formation of approximately spherical or prolate domains of LC, randomly suspended in a polymer matrix[103, 104], as illustrated in Figure 5.1a. In the LC droplets, the director alignment is generally bipolar or radial[105], but the net orientation of the director in each droplet is random and this causes incident light to be scattered as it passes through the device, due to the mismatch between the refractive index of each droplet and the polymer[106]. A PDLC device can be switched to a non-scattering transparent state with the application of an electric field that aligns the director within the droplets to be parallel to the field (Fig. 5.1b).

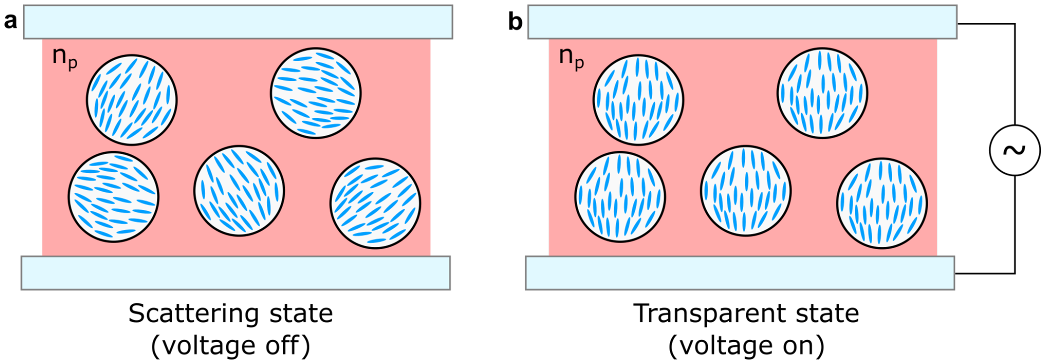

FIGURE 5.1: A schematic of a PDLC film (a) with no applied voltage in a scattering state and (b) with an applied voltage that reorients the director in the LC droplets and switches the device to a transparent state. For index-matching to occur, the polymer matrix must have refractive index $n_p = n_o$ where $n_o$ is the ordinary refractive index of the LC.

A key disadvantage of the PDLC approach to switchable refractive index matching stems from an inability to exert direct control over the phase separation process. PDLC fabrication techniques usually produce a polydispersity in LC droplet sizes, which negatively impacts the electro-optic characteristics of a device by introducing inter-droplet scattering[107, 108]. There is therefore a potential advantage in new index-matching technologies that allow precise and direct control over the size and morphology of LC polymer network structures.

As discussed in Chapter 3, advanced fabrication techniques such as direct laser writing (DLW) offer new ways to structure and manipulate LC/polymer composite materials. This enables more-complex device designs to be realised and greater control over the morphology of polymer structures as compared to conventional photopolymerisation techniques such as those employed in PDLCs.

This chapter describes how 2PP-DLW can be used to precisely fabricate microscale polymer pillars directly inside electrically addressable LC devices. These embedded features function as 3D alignment surfaces, imposing a boundary condition on the LC at the surface of the polymer structures. The orientation of the LC/reactive mesogen mixture at the moment of fabrication is stabilised inside the polymer structures and additionally influences the unpolymerised LC surrounding the structures. By applying a series of different voltages during fabrication, it is possible to stabilise distinct director profiles over the area of the device.

After fabrication, when applying a voltage to the device that matches the voltage applied during fabrication, the LC layer is brought into harmony with the boundary conditions imposed by the polymer features and produces a uniform refractive index profile. Thereby removing scattering and masking the objects in the presence of both polarised and unpolarised light. This chapter examines and analyses this voltage-induced “invisibility” and demonstrates some application concepts which exploit this interesting behaviour.

### 5.1.2 Microscale Authentication Technologies

Authentication and anti-counterfeiting technologies are a crucial part of life in the modern world, most commonly seen on banknotes and coins to deter and prevent the counterfeiting of money. However, an increasing number of industries now suffer from counterfeiting of manufactured goods including pharmaceuticals[109], electronics[110] and mass-produced high-value consumer goods such as beverages, perfumes and cigarettes[111]. Analysis published in a landmark OECD (Organisation for Economic Co-operation and Development) report on counterfeiting published in 2007 estimated that trade in counterfeit products was worth up to $200 billion in 2005[111] and is forecast to reach up to $991 billion by 2022[112].

Numerous anti-counterfeiting methods have been developed to combat the economic losses associated with counterfeit goods. In general, anti-counterfeiting technologies use some form of security marking that is challenging to copy or reproduce and can be attached securely to a product[113–117]. Better still is when the security marking can be embedded within a product and an additional level of security is provided when these markings are covert and not easily detected by the naked eye.

Microscale authentication technologies are particularly powerful because (i) the fabrication is not straightforward, requiring complex equipment to reproduce the covert feature and (ii) the markings are challenging to detect, being comprised of microscopic features[118]. In this chapter, the fabrication of a switchable microscopic quick-response (QR) code embedded within a polymerisable LC device is demonstrated. This type of security marking is particularly suited for authentication applications, as the QR code can only be read when a voltage is applied to the device, adding another step to the authentication procedure.

## 5.2 Experimental Procedure

### 5.2.1 Fabrication of Polymer Micropillars

Polymer micropillars were fabricated inside LC devices by employing 2PP-DLW to selectively polymerise a device containing reactive mesogen and photo-initiator that had been dispersed into an LC host. The mixture consisted of the nematic LC mixture E7 (70.7 wt%) (Synthon), reactive mesogen RM257 (Merck) (28.5 wt%) and Irgacure 819 (Merck) (0.8 w%) and was produced following the procedure described in Section 4.1.1.

The mixture was capillary filled in the isotropic phase into 20 µm-thick LC cells manufactured by Instec Inc. using a hotplate held at 70°C. The cells consisted of two glass substrates which were coated with indium tin oxide (ITO), and anti-parallel rubbed polyimide alignment layers. After cooling to room temperature, the LC device was mounted onto the translation stage stack in a 2PP-DLW system and connected to a function generator (Tektronix AFG 3022) so that a 1 kHz AC electric field could be applied to the device during fabrication.

The results in this chapter were obtained prior to the design and build of the bespoke 2PP-DLW system tailored to LC device fabrication described in Section 4.2. Instead, an existing laser microfabrication system based in the Dynamic Optics and Photonics group was adapted for two-photon polymerisation in LCs and its configuration is described below.

Femtosecond laser pulses of duration 100 fs from a Spectra-Physics Mai-Tai titanium-sapphire oscillator emitting at 790 nm with a repetition rate of 80 MHz were focussed with a 0.3 NA objective lens into the LC layer. The power of the fabrication laser prior to the objective was 24 mW. A phase-only spatial light modulator (Hamamatsu X10468-02) was imaged onto the pupil plane of the objective lens in a 4f configuration to correct for spherical aberrations introduced when focusing inside the LC device.

Liquid crystal devices were mounted onto a stack of high-resolution air-bearing translation stages (Aerotech ABL1000) that allowed the sample to be moved relative to the laser focus with a precision of ± 1 nm. A 630 nm red LED was used to provide transmission illumination of the device so that the fabrication could be monitored in-situ with a monochrome CCD without interfering with the photopolymerisation process.

After the devices had been filled, they were exposed to bursts of tightly focussed femtosecond laser pulses using the 2PP-DLW system. An illustration of the fabrication of the laser fabrication of polymer micropillars is presented in Figure 5.2. Each polymer pillar was fabricated with a single 60 ms exposure to the laser and polymer walls were fabricated by moving the sample at a speed of 100 μm/s under continuous exposure to the pulsed laser beam.

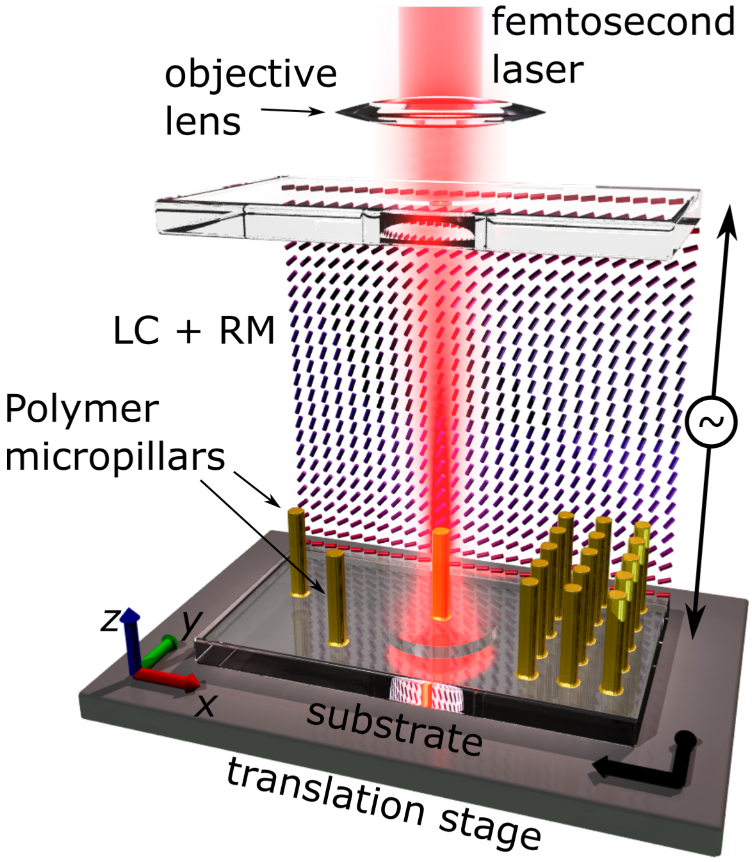

FIGURE 5.2: Schematic illustration of the fabrication of polymer micropillars inside a LC device using 2PP-DLW. The beam from a Ti-Sa femtosecond laser is focussed with an objective lens into a 20 μm thick device filled with a polymerisable LC mixture. The polymer micropillars are fabricated tethered to the bottom substrate of the device, to ensure structural integrity and stability of the pillars. A voltage can applied to the device during fabrication to change the director profile of the device and fix the LC director within and immediately surrounding the pillars in a particular orientation. This image was rendered by Jure Aplinc (University of Ljubljana) using the ray-tracing software POVRAY.

When the ultrafast laser is focussed into the device, two-photon absorption by the photoinitiator triggers cross-linking of the reactive mesogen molecules, resulting in the creation of a micropillar structure of polymer network. After polymerisation, the unreacted LC will still contain a considerable portion of RM257 monomer as only a small amount is consumed in the formation of a polymer pillar. The focus depth of the laser was configured such that the micropillars were tethered to the bottom substrate of the device and had a height of ~5 μm within the

20 µm-thick cell. This process locks-in the LC director profile at the moment of exposure to the laser beam and forms a microscale polymer-stabilised liquid crystal (PSLC) structure. This director profile defines the alignment of the LC director within and at the surfaces of the polymer pillar, irrespective of the voltage that is applied after fabrication.

Throughout this chapter, the term "write-voltage" ($V_w$) is used to mean the voltage applied to the LC device during the fabrication of a polymer structure, while the term "read-voltage" ($V_r$) is used to mean the voltage applied to the device after fabrication. Polymer structures were often written at a particular write-voltage before being characterised at a range of read-voltages.

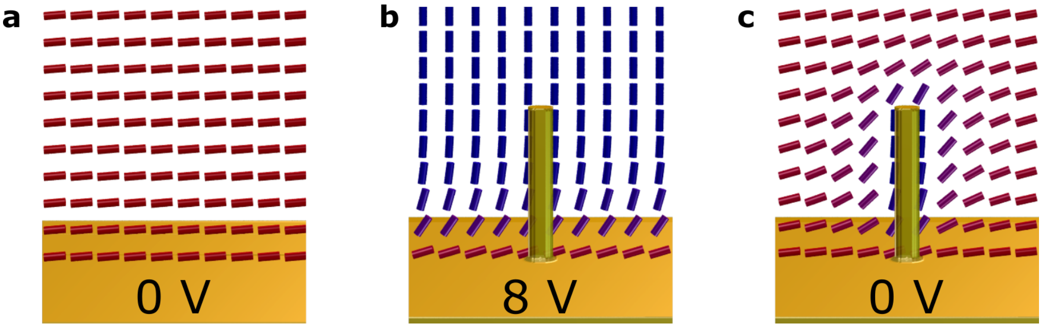

FIGURE 5.3: Simulated director profiles in a nematic LC before, during and after fabrication of a polymer micropillar at a write-voltage of 8 V. (a) Director profile in the absence of an applied voltage, (b) a polymer micropillar is fabricated in the device with a write-voltage of $V_w$ = 8 V applied to the device and, (c) following the removal of the voltage. The simulations assume that the director profile at the write-voltage is preserved within and on the surface of the micropillar. Director simulations were performed by Jure Aplinc (University of Ljubljana).

Figure 5.3 depicts LC director simulations showing the fabrication of a polymer micropillar with 2PP-DLW at a write-voltage of 8 V. Details on the numerical modelling and calculations of the LC director are provided in Section 5.2.2. In the absence of an applied voltage, the nematic LC assumes a planar-alignment, as shown in Figure 5.3a. A voltage of 8 V is then applied to the device, causing the LC to align with the electric field before a single polymer micropillar is fabricated from a 60 ms exposure to the focussed femtosecond laser (Fig. 5.3b).

The locked-in director field is confined solely to the sufaces and volume of the polymer micropillar. The unpolymerised surrounding bulk material remains free to realign in the presence of an applied voltage post-fabrication, while the alignment within and at the surface of the pillars is fixed, as dictated by the strong surface anchoring conditions. This behaviour is illustrated in the director simulation in Figure 5.3c, which shows the resultant director field at a read-voltage of 0 V. At this voltage, the bulk of the device has relaxed back to its equilibrium ground state upon removal of the applied voltage but the influence of the surface anchoring on the polymer pillar is plainly visible in the distortion in the LC surrounding the pillar.

Since the polymer pillars preserve the orientational order of the LC director at the point of fabrication, they possess a birefringence that depends on the applied write-voltage and they also influence the alignment of the neighbouring LC director in the surrounding unpolymerised regions. Different LC alignments can therefore be locked-in to the pillars by electrically switching the device to different voltage amplitudes during the 2PP-DLW procedure.

### 5.2.2 Numerical Modelling

The numerical modelling in this chapter was performed by Professor Miha Ravnik and Dr. Jure Aplinc of the Physics of Soft and Partially Ordered Matter group at the University of Ljubljana, Slovenia[119]. It is appropriate to give a brief description of their modelling approach in this section and a detailed review of the method used can be found in reference [120].

The simulation of the LC director in cells containing polymer micropillars relies upon a continuum theory model that uses the Landau-de Gennes (LdG) free-energy minimisation approach[2, 121]. This method takes into account the orientation of the director, the orientation of any possible biaxial ordering relative to the director and the nematic degree of order. A tensor order parameter, **Q**, fully describes the orientational order of the LC director and can be used to construct an expression for the total free energy[121], including both the bulk and surface free-energies to account for the anchoring on both the substrate surfaces and the polymer pillar/bulk LC interface. The total free-energy functional, $F$, is given by,

$$\begin{aligned}
F = & \int_{LC} \left\{ \frac{A}{2} Q_{ij} Q_{ji} + \frac{B}{3} Q_{ij} Q_{jk} Q_{ki} + \frac{C}{4} (Q_{ij} Q_{ji})^2 \right\} dV \\
& + \int_{LC} \left\{ \frac{L_1}{2} \frac{\partial Q_{ij}}{\partial x_k} \frac{\partial Q_{ij}}{\partial x_k} + \frac{L_2}{2} \frac{\partial Q_{ij}}{\partial x_j} \frac{\partial Q_{ik}}{\partial x_k} + \frac{L_3}{2} Q_{ij} \frac{\partial Q_{kl}}{\partial x_i} \frac{\partial Q_{kl}}{\partial x_j} \right\} dV \\
& - \int_{LC} \left\{ \frac{1}{2} \epsilon_0 \left( \bar{\epsilon} E_i^2 + \frac{2}{3} \epsilon_a^{mol} Q_{ij} E_i E_j \right) \right\} dV \\
& + \int_{Surf} \left\{ \frac{W}{2} \left( Q_{ij} - Q_{ij}^{(0)} \right) \left( Q_{ij} - Q_{ij}^{(0)} \right) \right\} dS
\end{aligned}$$

where $LC$ denotes integration over the bulk of the LC and $Surf$ is integration over the surfaces of the pillars. The first term accounts for the variation in the nematic degree of order whereby $A$, $B$ and $C$ are material parameters. The second term penalises elastic distortions, where $L_i$ are the elastic constants. The third term represents the dielectric coupling, where $\epsilon_0$ is the vacuum permittivity, $\bar{\epsilon}$ is the average LC permittivity, $\epsilon_a^{mol}$ is the molecular dielectric anisotropy, and $E_i$ is the external electric field. The final term accounts for the interaction of the LC with the surfaces, where $W$ is the anchoring strength. Homogeneous planar anchoring was assumed for the substrate surfaces, while the anchoring on polymer pillars was spatially dependent. To calculate the equilibrium director field, the total free energy $F$ was minimised numerically using an explicit finite difference relaxation scheme.

Numerical simulations were performed in two consecutive stages in order to mimic the laser writing process of locking-in spatially dependent director fields and creating arbitrarily complex anchoring within the bulk of the device. For the first stage of the process, the director profile was calculated in a planar-aligned nematic cell without the presence of the polymeric structure for a given write-voltage. For the second stage, the full geometry of the cell with the polymer pillar structures included was simulated, where the calculated nematic profile from the first stage was used as the surface-imposed spatially-dependent alignment direction at the pillar surfaces and as the fixed bulk birefringent profile within the pillars.

Director profile simulations of the devices were performed on a cubic grid consisting of $260 \times 260 \times 410$ simulation points (for a single pillar). Cylindrical polymer pillars consisted of 20 points in diameter and 100 in height. Numerical calculations were performed with the following material parameters for E7: $K_{11} = 10.7$ pN, $K_{22} = 6.5$ pN, $K_{33} = 16.2$ pN, $A = -0.172\ \mathrm{MJ/m^3}$, $B = -2.12\ \mathrm{MJ/m^3}$, $C = 1.73\ \mathrm{MJ/m^3}$, strength of the surface anchoring $W = 10^{-2}\ \mathrm{J/m^2}$, birefringence $\Delta n = 0.219$ and the dielectric anisotropy $\Delta\epsilon = 13.7$.

Simulated polarised optical microscopy images were calculated via the Jones $2 \times 2$ matrix method introduced in Section 2.7.2, using ray optics and taking into account the colour spectrum of the microscope illumination used in experiments. By dividing the model geometry into multiple birefringent layers and multiplying the respective Jones matrices for each layer, simulations of transmission polarising micrographs were calculated.

### 5.2.3 Scanning Electron Microscopy

Scanning electron microscopy (SEM) was used to confirm the dimensions of the micropillars fabricated with 2PP-DLW. Devices were immersed in a bath of acetone for 24 hours in order to remove any unreacted liquid crystalline material. The substrate and superstrate were then disassembled and coated in a 27.5 nm-thick gold layer for SEM imaging using a secondary electron detector. A 20 kV electron beam voltage was used at a working distance of 11.5 mm.

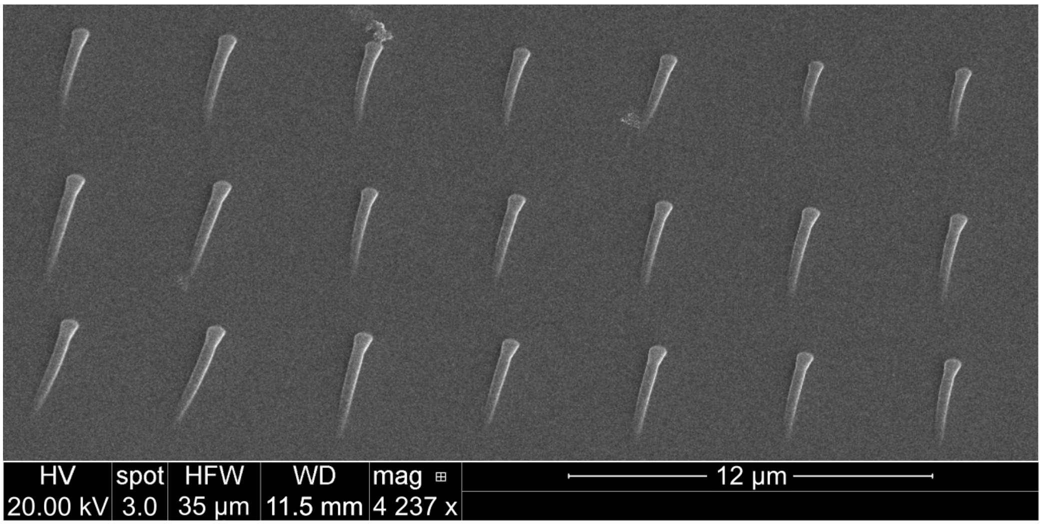

FIGURE 5.4: SEM image of a micropillar array with 5 μm spacing. This image was recorded by Dr. Chloe Tartan.

Figure 5.4 shows an SEM image of a pillar array with a 5 μm array spacing, captured using the method described above. The dimensions of each pillar are found to be ∼1 μm in diameter and ∼5 μm in height. However, it should be noted that SEM observation of liquid crystal polymer networks is very challenging, as opening the cell and removing the unreacted material with a solvent can damage the fragile polymer network structure, causing shrinkage and distortion[40]. Therefore, the SEM image in Figure 5.4 may not be a true representation of the structure of the micropillars while they are still immersed in the bulk LC within a device. In particular, the polymer pillars are observed to have fallen over and are therefore no longer lying perpendicular to the surface of the substrate after the SEM preparation process. The aforementioned challenges of SEM imaging of polymer network structures are likely to account for the lack of uniformity in the pillar structures across the image in Figure 5.4. However, SEM still provides a reasonable estimate for the dimensions of the micropillars which is concordance with observations of micropillars performed using a polarising optical microscope.

## 5.3 Results and Discussion

### 5.3.1 Image Analysis of Polymer Micropillar Invisibility

To demonstrate the ability to match the refractive indices and hide polymer micropillars under specific voltage conditions, Figure 5.5 shows the experimental and simulation results for a single polymer pillar that has been fabricated at a write-voltage of $V_w = 4$ V and is subsequently read at six different applied voltages after fabrication ($V_r = 0 - 5$ V). As can be seen in the POM images in the top row, for voltages where $V_r \neq V_w$, the micropillar is clearly visible against the background LC. At these voltages, the birefringence of the polymer pillar is different from the surrounding regions of LC, which in turn leads to differences in the phase of light transmitted through the device and the features are distinguishable against the LC background.

Conversely, when the read-voltage, $V_r$, applied to the device matches the write-voltage, $V_w$, (in this case $V_r = V_w = 4$ V), the director field in the regions surrounding the pillars and within the pillars themselves merge almost seamlessly into the background, thereby resulting in the object being hidden. It should be noted that at a writing voltage of $V_w = 4$ V, the contrast between the polymer pillar and the unpolymerised LC is most significant at low read-voltages because the elastic distortion around the pillars becomes most pronounced below the

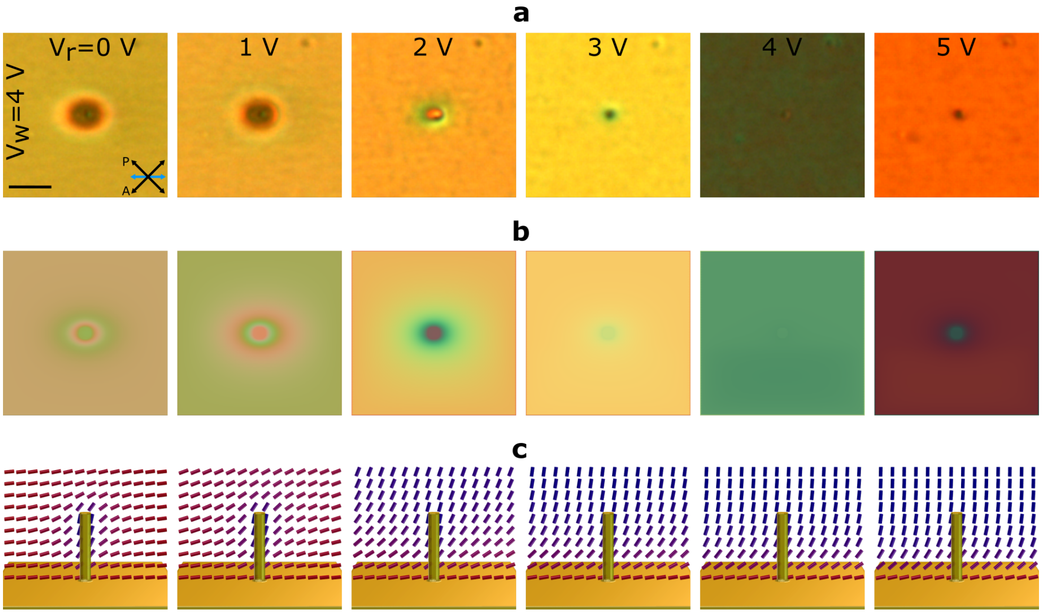

FIGURE 5.5: Voltage-induced refractive index matching of a single polymer micropillar in a LC device. (a) POM images of a polymer micropillar fabricated at a write voltage of $V_w$ = 4 V and subsequently imaged at six different read-voltages ($V_r$ = 0 – 5 V). The orientation of the crossed polarisers is indicated by the black arrows and the optic axis of the nematic phase are indicated by the blue arrow. Scale bar is 10 µm. (b) Simulated POM images for the same sequence of voltages, showing the micropillar becoming invisible at a read-voltage of 4 V and (c) the associated simulated director profiles. The results highlight the effective homogeneity in the director alignment when the read and write voltages are equivalent ($V_r$ = $V_w$) and the resulting invisibility of the polymer pillar. Simulation results in (b) and (c) were obtained by Jure Aplinc.

Fréedericksz threshold of the device ($V_{th}$ $\sim$0.9 V). Below the threshold, the planar alignment in the bulk LC is more distinct compared to the hybrid alignment locked-in at the surface of the polymer pillar, leading to greater director distortion surrounding the pillar and increased visibility.

The simulated microscope images in Figure 5.5b are found to be in good agreement with the experimental results, confirming the structure of the pillar, the interaction with the bulk unpolymerised LC, and the voltage-dependent visibility of the pillar. The corresponding director profile simulations presented in Figure 5.5c show that when the polymer pillar is formed at a write-voltage of $V_w$ = 4 V, the locked-in LC director at the pillar surface assumes a tilted orientation, leading to elastic distortion when $V_r \neq V_w$. The distortion in the director profile is only lifted when the read-voltage ($V_r$) is equal to the write-voltage ($V_w$), which leads to a uniform director profile across the device, thereby hiding the fabricated polymer micropillar under this voltage condition.

From an applications perspective, having the polymer structures vanish when examined with both polarised and unpolarised light would be highly desirable. Figure 5.6 demonstrates the concept of voltage-induced visibility in a polymer pillar array imaged at read-voltages of 0 – 5 V for both polarised (Fig. 5.6a) and unpolarised (Fig. 5.6b) light. Each column of pillars in the array, going from left to right, was written at voltages ranging from 0 V to 5 V in 1 V increments.

Image analysis was performed to quantify the visibility of the pillars for both polarised and unpolarised light (Figure 5.7). MATLAB® was used for the analysis by first cropping an image of each pillar at each read-voltage. These images of individual pillars were extracted from the images of the pillar array in Figure 5.6. The images were then converted from RGB to greyscale format before the standard deviation

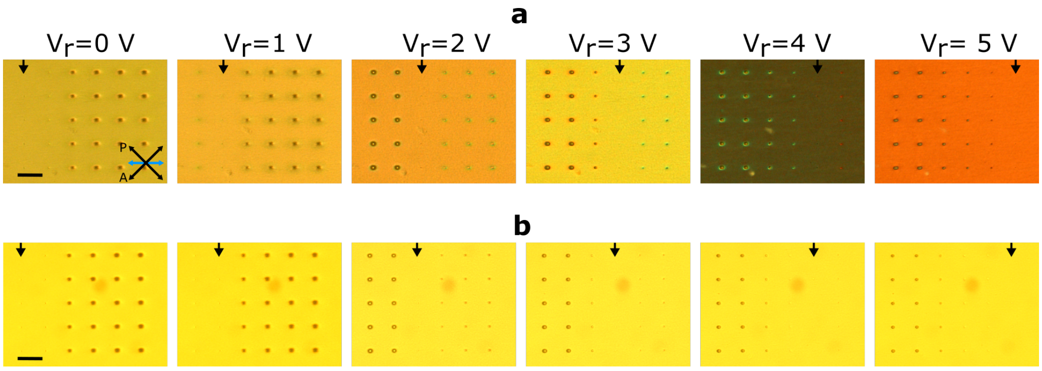

FIGURE 5.6: Refractive index matching of an array of polymer micropillars examined with both (a) polarised and (b) unpolarised light. Each column of micropillars in the array, from left to right, was written at voltages from $V_w$ = 0 V to 5 V in 1 V steps. Transmission microscope images of a 5 × 6 array of polymer micropillars with a 40 µm lattice spacing for (a) crossed polarisers and (b) unpolarised light. The same read and write voltages were used as those presented in Figure 5.5. The orientation of the crossed polarisers and the optic axis of the nematic phase are indicated by the black and blue arrows in (a), respectively. The small black arrows at the top of each image indicate the column of micropillars that has become invisible due to the refractive index matching. Scale bars are 40 µm

of each image was determined. This standard deviation data was then plotted in greyscale colourmap charts according to the write-voltage and the read-voltage, such that low values of standard deviation are denoted by the black squares and high values of standard deviation are denoted by the white squares.

For both polarised and unpolarised microscopy, it can be seen that there is a clear minimum in visibility along the diagonal lines where $V_w = V_r$. Furthermore, the greyscale charts show the significant impact of the Fréedericksz threshold ($V_{th}$ ~0.9 V) on the visibility of the pillars, especially for unpolarised light where the pillars written above the threshold voltage ($V_w > V_{th}$) all have a similar visibility when the read-voltage is also above this threshold ($V_r > V_{th}$) (and vice versa for pillars written below the threshold).

Additional polarised microscope images, along with simulated microscope images and director profiles, are presented in Figure 5.8 for an array of pillars that further elucidate why the micropillars in each column vanish when the $V_r = V_w$ condition is satisfied. When the surrounding

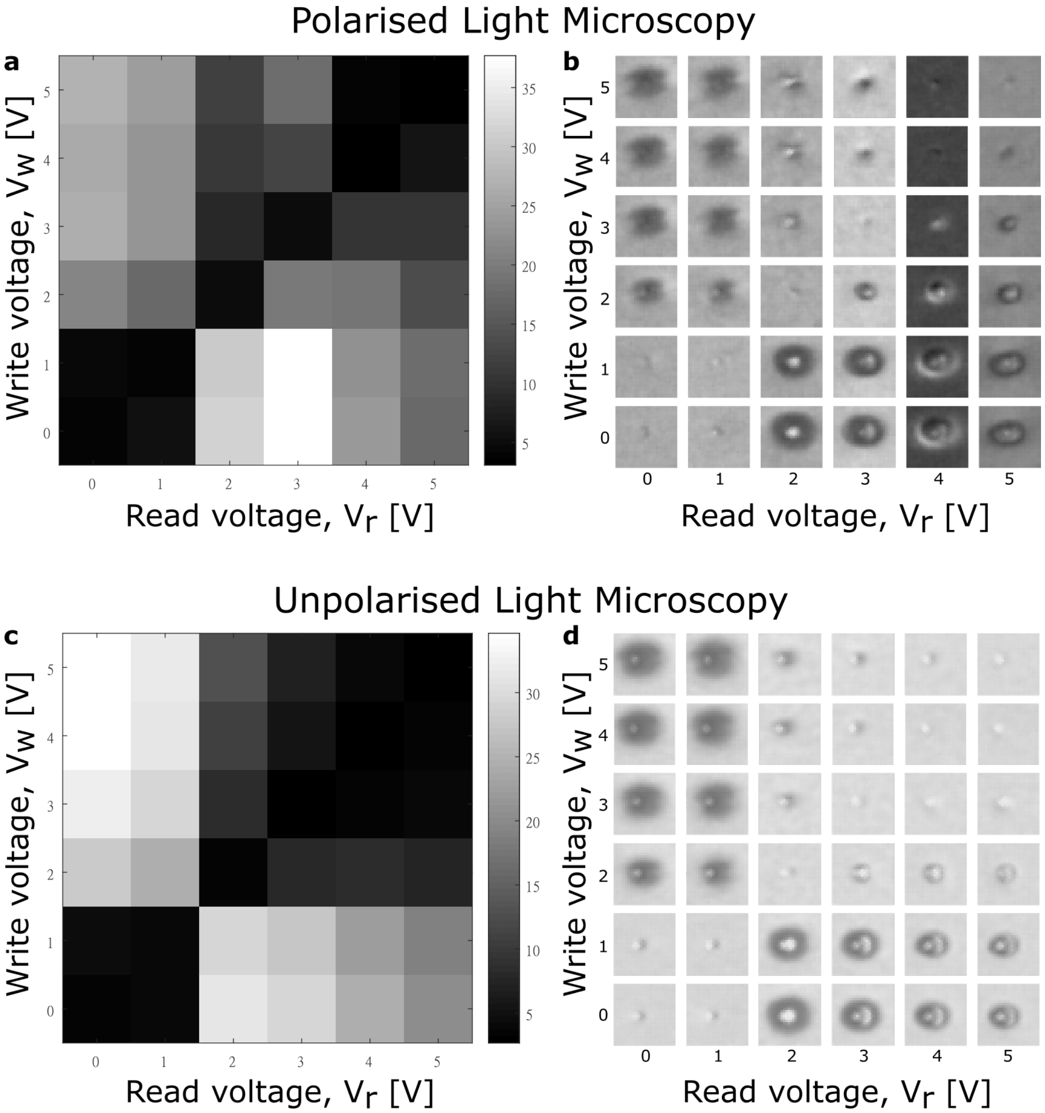

FIGURE 5.7: Grayscale charts summarising the results of image analysis of a polymer micropillar array for polarised (a and b) and unpolarised (c and d) light. Individual micropillars from the images of the pillar array in Figure 5.6 were cropped and placed in a matrix according to their read and write voltage (b and d). The standard deviation of each pillar image was evaluated to quantify the degree of visibility and plotted in the greyscale charts (a and c). A minimum in visibility is present along the diagonal where $V_w = V_r$, for both polarised and unpolarised light, satisfying the condition for refractive index matching.

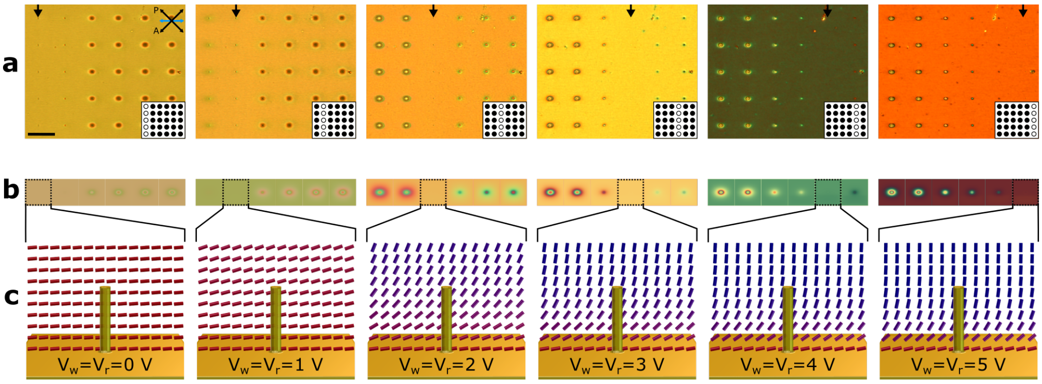

FIGURE 5.8: Electrically-induced invisibility of a polymer micropillar array via refractive-index matching. (a) POM images of pillars in a 40 µm-spaced array whereby each column was written in the presence of a different applied voltage (from left to right the columns of pillars in the array were written with $V_w$ = 0 - 5 V in 1 V increments). The arrows and insets highlight the column of pillars that vanishes at that specific read-voltage ($V_r = V_w$). Scale bar is 40 µm. (b) Simulated POM images confirm that the polymer pillars become invisible when $V_r = V_w$. (c) Simulated director profiles for the case when both the read and write voltages are equivalent, illustrating that invisibility occurs when the LC alignment imposed by the surface of the polymer pillars seamlessly joins with the director profile in the bulk of the LC. Simulation results in (b) and (c) were obtained by Jure Aplinc.

director field matches the director profile that is imposed by the anchoring at the surface of the polymer pillar, there is no distortion surrounding the pillar and it therefore becomes invisible. Simulated POM images shown in Figure 5.8b for the varying read-voltages match well with the experimental POM of the micropillar array. Figure 5.8c shows simulated director profiles for the pillar that vanishes at each read-voltage (i.e. the pillar that satisfies the condition $V_r = V_w$). It can be seen that the director profiles exhibit homogeneity in the alignment between the pillar and the bulk LC, with no director distortion surrounding the structure, thereby rendering it invisible.

### 5.3.2 Reconfigurable Optical Elements

By tailoring the write-voltages of a polymer micropillar, it has been shown that it is possible to make the objects appear and disappear in the surrounding LC host as the applied voltage is varied. Extending this principle, and exploiting the flexible patterning capabilities of 2PP-DLW, it is possible to fabricate reconfigurable structures where different features or patterns emerge at different read-voltages. This section presents examples of microscopic read-on-demand images that illustrate this approach and constitute proof-of-concepts for applications exploiting this phenomenon.

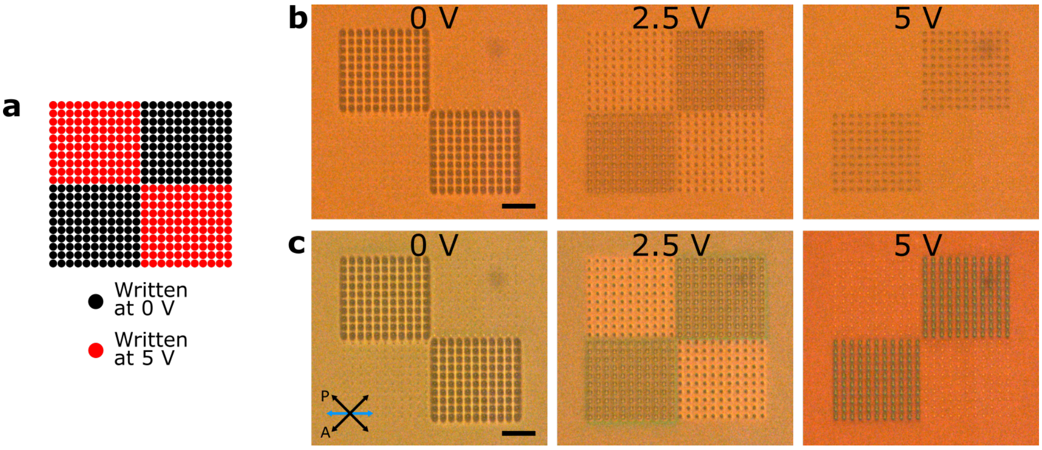

FIGURE 5.9: A switchable checkerboard fabricated in an LC device with 2PP-DLW. (a) Schematic of the design of the switchable checkerboard comprising of arrays of polymer micropillars which are written at either 0 V or 5 V. (b) Micrographs at read-voltages 0 V, 2.5 V and 5 V of the structure examined with unpolarised light. (c) POM images of the structure at read-voltages 0 V, 2.5 V and 5 V. The orientation of the crossed polarisers are indicated by the black arrows and the optic axis of the nematic phase is indicated by the blue arrow. Scale bar is 40 µm.

Firstly, Figure 5.9 shows an example of a relatively simple structure where polymer micropillars were written at two different voltages to produce a recognisable image. The structure is a 220 µm × 220 µm switchable checkerboard where one set of squares was written at $V_w = 0$ V and the other set of squares was written at $V_w = 5$ V. A schematic design of the structure is shown in Figure 5.9a and imaging is performed for both unpolarised (Fig. 5.9b) and polarised (Fig. 5.9c) light.

At a read-voltage of $V_r = 2.5$ V both sets of micropillars are visible in the images, but at either $V_r = 0$ V or 5 V, one set of micropillars disappears and the effect is clearly shown to work for both polarised and unpolarised microscopy. This simple switchable checkerboard shows that recognisable images can be fabricated from pillars that have a voltage-dependent visibility. Furthermore, the image appearance can be dramatically modified with the application of a read-voltage that matches the write-voltage of some of the polymer structures comprising the image.

Extending this principle further, Figure 5.10 demonstrates a 'micro-bicycle' fabricated with 2PP-DLW inside a polymerisable LC device. It was created by writing each spoke of the wheels as a line of polymer pillars at different voltages ranging from $V_w = 2 - 4.5$ V, while the frame was written as a continuous polymer line at $V_w = 0$ V. A schematic design of the structure with the write-voltages used is shown in Figure 5.10a.

POM images of the micro-bicycle at read-voltages of $V_r = 2$, 2.5, 3, 3.5, 4 and 4.5 V are shown in Figure 5.10b, where the spoke with the corresponding write-voltage disappears, highlighting the reconfigurable nature of the structure. The micro-bicycle design was inspired by stop-frame animation, where rapidly displaying a series of images with slight differences between each frame can create an illusion of motion to the human eye. Sequentially stitching together the images in Figure 5.10b to create an animation induces a convincing illusion-of-motion due to the successive disappearance of the spokes of the wheels.

### 5.3.3 Switchable QR Code

Finally, Figure 5.11 demonstrates a arrangement of pillars that represent a 75 × 75 µm 'quick-response' (QR) code that links to the website of the Soft Matter Photonics research group[122]. The design of the QR code is shown in Figure 5.11a and unpolarised microscope images of the structure at $V_r = 0$ V and 5 V are shown in Figure 5.11b and c. By writing the pillars in the absence of an applied voltage (i.e. $V_w = 0$ V), the QR code is

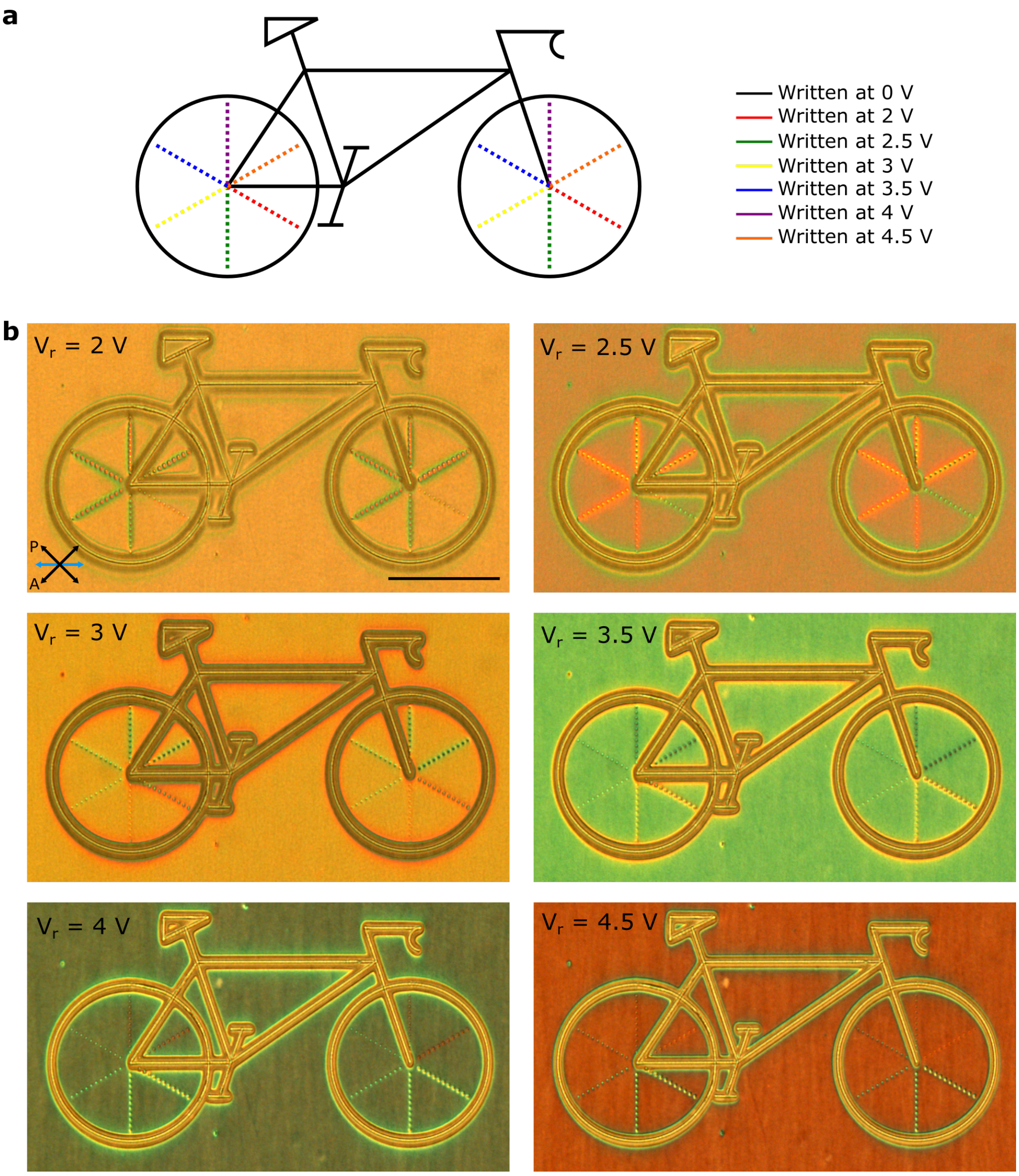

FIGURE 5.10: A micro-bicycle fabricated in an LC device with 2PP-DLW. (a) A schematic illustration showing the write-voltages used to construct the micro-bicycle from a series of polymer walls and micropillars. (b) POM images of the micro-bicycle structure at read-voltages of 2 V, 2.5 V, 3 V, 3.5 V, 4 V, 4.5 V. When the read-voltage matches the write-voltage used to write a series of micropillars, those micropillars disappear. By stitching this sequence of images together to create a stop-frame animation, it is possible to observe the illusion of motion in the wheels of the micro-bicycle as each successive spoke becomes invisible. The orientation of the crossed polarisers is indicated by the black arrows and the optic axis of the nematic phase is indicated by the blue arrow. Scale bar is 100 µm.

invisible at a read-voltage of $V_r = 0$ V and cannot be read by a smartphone QR code reader. In order to produce enough contrast between the pillars and the unpolymerised regions to read the QR code, a voltage above the Fréedericksz threshold has to be applied to the device. This causes the pillars to become visible against the background and switches the code to be readable by a standard QR code reader.

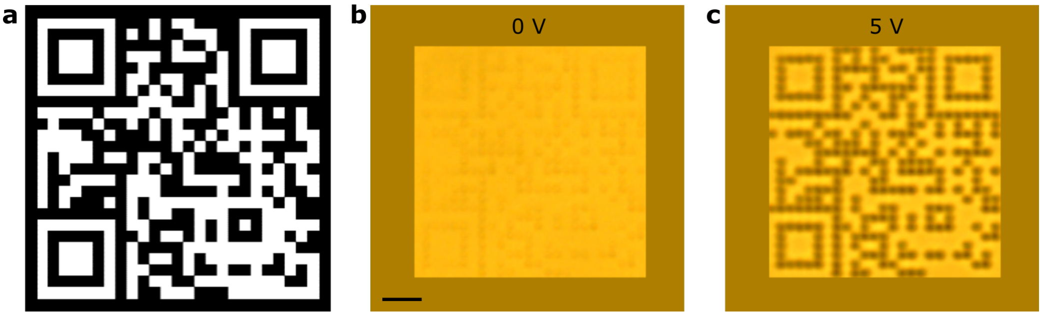

FIGURE 5.11: A 75 × 75 µm quick response (QR) code written into a LC device at a write-voltage of 0 V with a spacing of 3 µm between each micropillar. (a) The QR code design which links to the URL of the Soft Matter Photonics research group website. Microscope images (unpolarised) of the QR code at read-voltages of (b) 0 V and (c) 5 V. An artificial border has been added to the images to aid with reading the QR code. At a read-voltage of 0 V, is it not possible to successfully scan the QR code and it can only be successfully scanned with a smart phone when a voltage above the Fréedericksz threshold is applied to the LC device. Scale bar is 15 µm.

Due to limitations in the algorithm that reads QR codes on most smartphone applications, an artificial border was added to the images in Figure 5.11b and c with a colour that matches the polymer pillars comprising the QR code. This allows the code to be read reliably as the algorithm can successfully identify the edges of the structure. This limitation could be corrected in a straightforward manner in future designs by writing an additional series of polymer pillars around the edge of the QR code.

A QR code made with polymer-stabilised cholesteric LCs has been previously reported[123], but it was a fixed structure with no switchability or tunability and was considerably larger, occupying an area of 3600 × 3600 µm. In contrast, if the QR code demonstrated here was hidden in a security label attached to a consumer product, it could be used as part of a sophisticated authentication procedure where an AC voltage source would need to be connected to electrodes on the label in order to render the QR code readable. The extra step of applying a voltage to the security label would potentially increase the rigour of the authentication process. Furthermore, as discussed in Section 5.1.2, it is advantageous for security markings to be of a small size, as the marking would be challenging to clone and can be effectively hidden. Therefore, the reading device would need to be reasonably sophisticated and effectively function as a simple digital microscope in order to see this QR code. Due to its favourable security characteristics, this switchable QR code therefore successfully demonstrates the potential in exploiting the concept of voltage-dependent visibility of microscale polymer structures in authentication applications.

## 5.4 Summary and Conclusions

In conclusion, an approach to refractive index matching has been demonstrated using 2PP-DLW in polymerisable LC cells, whereby polymer structures can be made to disappear with the application of a voltage that matches the voltage applied during the fabrication procedure. When the read-voltage is equal to the write-voltage, there exists an undistorted director profile between the bulk alignment of the LC and the surface anchoring conditions imposed by the polymer structures. The resultant homogeneity in the alignment reduces the elastic distortion around the polymer network to match the birefringence between the polymer and the bulk LC, such that the pillars are no longer clearly visible.

In this chapter it has been shown that applying different voltages during fabrication of the polymer objects causes the polymer network to 'memorise' the local orientation of the director at the precise moment of laser writing, allowing different patterns to be encoded within the device at different voltage amplitudes. By carefully tailoring the write-voltages, it has been possible to create a number of demonstrations that highlight the potential of this effect; including a reconfigurable checkerboard, a micro-bicycle that exhibits the illusion of motion and a switchable QR code.

Following the demonstration of the switchable QR code, it is envisaged that this approach could be used in the fabrication of high-value covert security features that confirm the authenticity of a consumer product, helping to combat counterfeiting and fraud. The small size of the QR code, having dimensions of just 75 × 75 µm, suggests that it would be extremely challenging to locate or indeed clone such a security feature. Furthermore, the need to apply a specific voltage to the LC in order to make the QR code readable represents another authentication step, further complicating any attempts to clone the microscopic feature.

To conclude, this chapter has demonstrated the potential of using 2PP-DLW to stabilise electrically-dependent director states in a nematic Fréedericksz device, where the applied voltage influences the tilt of the director in the cell. The next chapter takes this further and explores using 2PP-DLW in more-complex LC devices which transition to topologically discontinuous director states upon the application of a voltage, resulting in the formation of topological defects.

# Chapter 6

# Electrically-Tunable Topological Defects

This chapter describes the stabilisation of topologically discontinuous director states in a liquid crystal pi-cell device by creating micron-scale polymer structures with 2PP-DLW. The fabrication of polymer walls which lock-in a topological discontinuity in the director field causes the formation of disclination lines adjacent to the walls in the device. Subsequently applying a voltage to the cell alters the elastic energy of the director states and causes the defects to move in a controlled manner. A control system is designed and built to demonstrate automatic control of the position of a defect, and confinement of disclination lines is explored with the fabrication of polymer channels with 2PP-DLW. The results described in this chapter represents an unprecedented level of control and tunability over the normally random process of defect nucleation and growth in LC pi-cells.

> *"Use your faults, use your defects; then you're going to be a star."*
>
> **Edith Piaf**

## 6.1 Introduction and Background

### 6.1.1 Topological Defects

Topological defects have long been of interest to theoreticians and experimentalists alike due to their ubiquity in ordered physical systems and more-recently due to their emerging use in practical applications. In condensed matter physics, topological considerations play a crucial role in explaining the properties of a wide range of materials including superfluids[124], superconductors[125] and topological insulators[126]. In particle physics and cosmology, topological defects have been studied as a candidate for explaining the density-fluctuations in the early universe that led to structure-formation and consequently, the existence of galaxies, stars and planets[127]. It has been crucial to the development of understanding in the topology of materials that the mathematics used to describe the formation and evolution of topological defects can be transferred across different length-scales and between different disciplines. To this end, defects in liquid crystals have been investigated as highly-analogous laboratory systems for studying both superconductivity[125] and the evolution of the early universe[128].

As we have seen in Chapter 2, self-organisation in LCs is governed by the free energy density associated with the possible arrangements of the anisotropic molecules in space[2]. In certain cases, LCs can self-organise into structures which contain singularities (points of discontinuous order) in the director field that describes the orientation of the LC director in space. Such a situation can occur due to the strong anchoring of the LC director adjacent to a surface, establishing boundary conditions that make it impossible to have a continuously varying director field throughout the LC. Helpfully, LC defects can be imaged with optical microscopy, and indeed the nematic mesophase derives its name from the thread-like defects seen in nematic LCs under a microscope (from the Greek nematos, meaning 'thread').

Early mathematical descriptions of nematic defects were devised by Friedel who suggested that they are regions where the director is disordered and changes its direction discontinuously[129]. Frank was later responsible for coining the term disclination, in analogy with dislocations in solid crystals, to describe these characteristic nematic threads[13]. Disclinations in liquid crystals can be located on a single point (point disclination), on a line (line disclination) or on a surface (sheet disclination). However, in practice, sheet disclinations are highly unstable and will always collapse to a series of line disclinations[2].

Defects are further classified by their topological strength (or charge), a description of the nature of the distortion surrounding the defect. To find the strength of a defect, we draw an anticlockwise line around a defect core and consider the rotation of the director along the line. Taking the example in Figure 6.1a, we see that the director rotates a full $2\pi$ along such a line drawn around the defect and so this defect is of strength $s = +1$. Around any given defect, the director rotates by $2\pi s$. If s is negative, the director rotates clockwise when traversing the anti-clockwise path around the defect. When two defects of equal and opposite strength (charge) meet, they annihilate, leaving behind a region of continuous director orientation.

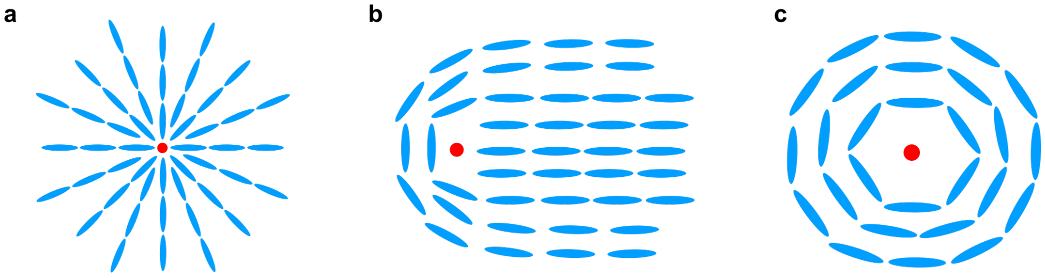

FIGURE 6.1: Liquid crystal alignments that possess topological defects. The red dot indicates the location of the defect and blue rods show the orientation of the liquid crystal director. The topological strength for these example defects are (a) $s = +1$, (b) $s = +1/2$ and (c) $s = +1$.

Defects in LCs are of interest both from a fundamental perspective and due to their potential to be used in a multitude of applications[130]. Most attention in the literature has been directed to the use of defects in the fabrication of nanomaterials. It has been observed that nanoparticle inclusions tend to migrate to defects in LCs as this minimises the overall elastic energy of a LC-colloid composite system. Consequently, topological defect networks have been proposed as templates for the self-assembly of nanoparticles[3, 131–133], allowing intricate structure formation without the need for top-down lithographic approaches.

By changing the nature of the colloidal particles, enhanced functionality can be introduced in LC defect networks. For example, by doping an LC defect system with self-propelled swimming bacteria, it has been found that the presence of defects controls and influences the normally-chaotic swimming behaviour of the bacteria[134]. Furthermore, the use of plasmonic or metallic particles as colloidal dopants in LCs has led to the exploration of tunable metamaterials and plasmonic materials[11, 135, 136].

An emerging area of LC defect research is in advanced spatial light modulators (SLMs) for controlling polarisation and phase singularities in optical fields[137]. Marrucci et al. described an optical spin-to-orbital angular momentum conversion process occurring in laser light passing through a liquid crystal cell with an alignment similar to Figure 6.1c. The process leads to the generation of helical light modes from gaussian beams where the helicity is dependent on the input polarisation[138]. Brasselet subsequently introduced a proof-of-concept switchable SLM comprising of electrically-switchable topological pixels able to generate phase singularities in light across the visible spectrum[139].

Crucially, for these advanced applications, reliable methods of controllably generating and stabilising defects must be developed to enable the engineering of functional defect patterns and networks. Recently reported methods have typically been limited to substrate patterning, typically with photoalignment techniques[140] or by employing electrically-induced nematic flows[141]. Using these methods, the creation of large-scale arrays of defect lines has been demonstrated[142] but these have typically been static networks with a limited degree of tunability.

In this chapter, we will see that 2PP-DLW allows the precise generation, stabilisation and electrical-control of defects in a single-step process over a large area. Furthermore, a number of concepts will be explored that demonstrate the use of tunable defects in microparticle transport and advanced electro-optic devices.

### 6.1.2 Pi-Cells

Nematic pi-cell devices (first introduced in Section 2.8.1) were originally conceived of by Philip Bos in 1984 as a fast-switching display device[143]. He observed the fast electro-optic response of a nematic LC aligned between parallel rubbed substrates, as well as favourable viewing angle characteristics and suggested the devices would find use in fast field-sequential colour displays. In this chapter, pi-cells are used because, in contrast with anti-parallel rubbed cells, it is possible to induce different topologies in the LC by applying a low-voltage electric field across the device to generate director profiles that are topologically distinct.

The pi-cell consists of two glass substrates coated with parallel-rubbed alignment layers, sandwiching a layer of LC a few microns thick. In the ground state, with no applied voltage, the LC director adopts

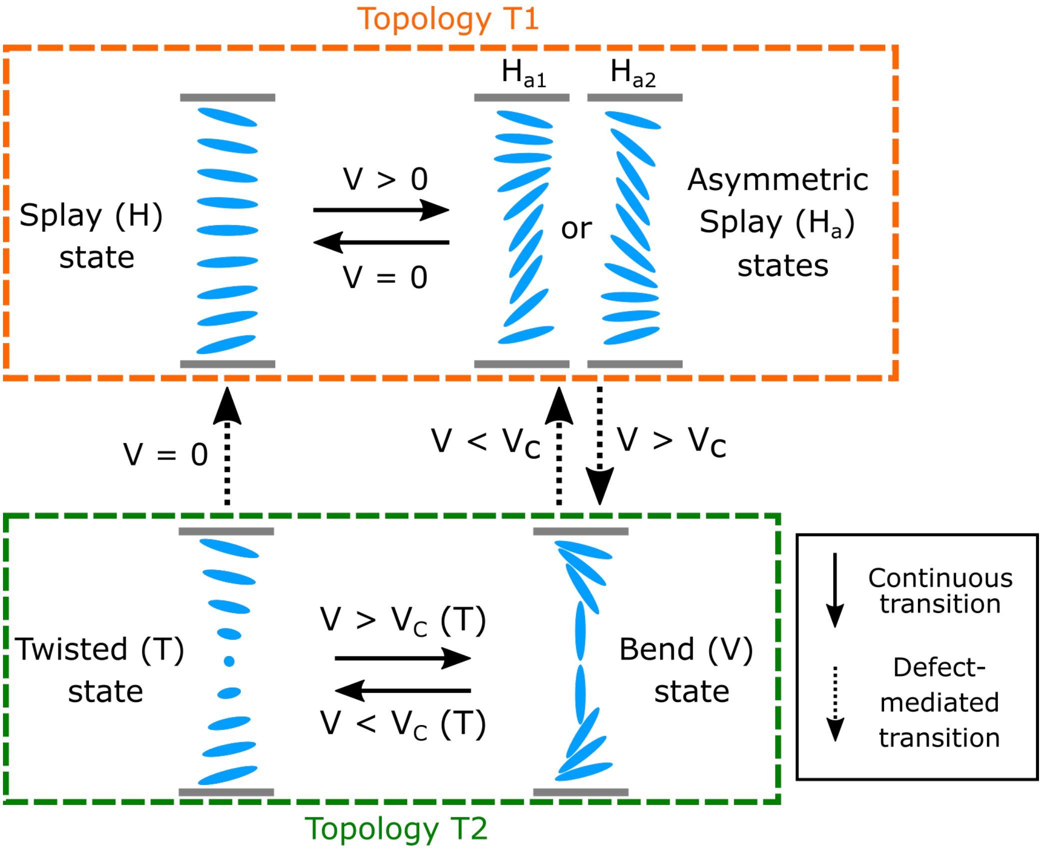

FIGURE 6.2: Director profiles of the different director states possible in LC pi-cells. Transitions between states with topology T1 and topology T2 are defect-mediated.

a homogeneous splay state (or H-state) across the device (Figure 6.2). Applying a voltage initially causes the alignment to distort, forming first an asymmetric H-state ($H_a$-state) and, as the voltage is increased above a critical voltage, $V_c$, the bend state (or V-state). The V-state is topologically distinct from the H-states and grows slowly after nucleation, forming a domain that is bounded by a strength ±½ disclination loop, as long as the voltage remains above $V_c$[144]. If the voltage is reduced below $V_c$, the H-state nucleates and grows, slowly consuming the entire device over a period of 3-5 minutes (at room temperature) via the discontinuous transition back to the ground state. Reducing the voltage further to $\lesssim V_c/2$ results in the bend-state collapsing to a 180° ($\pi$) twisted state (or T-state). The threshold voltage at which this occurs is labelled $V_c(T)$ in Figure 6.2 and is equal to $\sim V_c/2$.

The complete-picture of pi-cell behaviour is evidently complex,

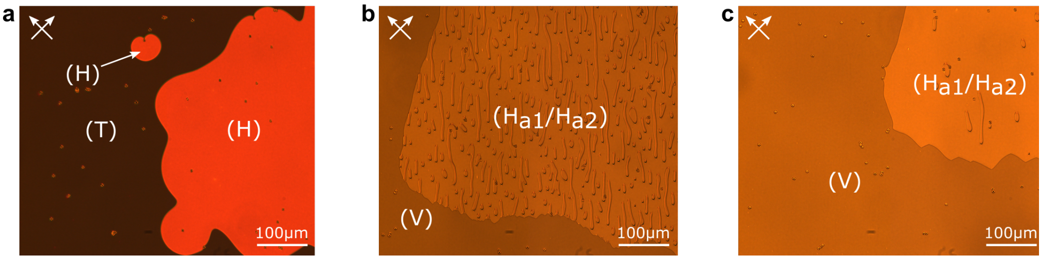

FIGURE 6.3: Defect formation and random nucleation of topologically discontinuous director states in a standard LC pi-cell without any fabricated polymer structures. (a) Random nucleation of the H state at zero applied voltage. The device was initially driven into the V-state by applying a voltage $V > V_c$, before the voltage was removed to allow the cell to relax to the ground state. Nucleation of the H-state occurs randomly and can be seen to originate from the spacer beads in the cell, which cause a strong director distortion in their vicinity. (b) Growth of the V-state and transition into the asymmetric H-states. A voltage, $V > V_c$ is applied to the cell, allowing domain growth of the V-state to occur randomly. The disclination line between the V-state and the H-states has an irregular morphology that depends on where the V-state randomly nucleated in the cell. The H-state region transitions into a mixture of the two asymmetric H-states, with thread-like loops marking the boundaries between the $H_a$ states. (c) The V-state domain has grown, and the asymmetric H-state region has largely collapsed into one of the two asymmetric H-states via $H_{a1}/H_{a2}$ domain wall annihilation.

but it is only important for the understanding of this chapter to note that the V and T states are topologically distinct from the H-states and thus can only exist in the same device with a disclination line separating the states. Thus we can group the pi-cell states by their topology: designating the H and Ha states as topology T1, and the V and T states as topology T2. Furthermore, it should be noted that the nucleation and growth of the topologically discontinuous states in a conventional pi-cell is a random process (Figure 6.3) and this is a key factor preventing pi-cells from finding use in applications[144]. All of these topologically distinct director states and the disclination lines themselves can be observed and identified in a straightforward manner with a polarising optical microscope.

## 6.2 Fabrication Procedure

### 6.2.1 Polymerisable Mixture Preparation

The polymerisable mixture used in this study consisted of the nematic LC mixture, E7 (70.7 wt%), reactive mesogen RM257 (Merck) (28.5 wt%)

and photoinitiator Irgacure 819 (Merck) (0.8 wt%) which was prepared according to the procedure described in Section 4.1.1. The mixture was then capillary filled, using a hotplate at 70°C, into 5 µm thick pi-cells manufactured by Samsung Electronics Co., Ltd. The cells consisted of two ITO coated glass slides, rubbed parallel and separated by 5 µm spherical spacer beads, with a pre-tilt of 4 - 6°. After filling, the cells were allowed to cool to room temperature and prepared for processing on either a custom-built 2PP-DLW system or a UV LED curing system.

### 6.2.2 Bulk Curing with UV LED

Initial experiments were performed with a 365 nm UV LED (Thorlabs High Power UV Curing System CS2010) used to cross-link the reactive mesogen molecules and create polymer networks. Polymerised regions were sequentially polymerised with an intensity of 0.3 mW/cm$^2$ for 30 seconds, using a series of photomasks placed on the outer surface of the device glass substrates. The photomasks were made from black vinyl and cut to the required design by a Roland STIKA SV-8 vinyl cutting machine configured using Roland CutStudio software.

### 6.2.3 Direct Laser Writing

Femtosecond laser pulses of duration 100 fs from a Spectra-Physics Mai-Tai titanium-sapphire oscillator emitting at 790 nm with a repetition rate of 80 MHz were focussed with a Zeiss 0.5 NA objective lens into the LC layer of the cell. This numerical aperture was chosen such that the focus would be longer than the device thickness, ensuring fabrication across the full thickness of the device. The power of the fabrication laser after the objective was 23 mW. A Hamamatsu X10468-02 phase-only SLM was imaged onto the pupil plane of the objective lens in a 4f configuration to correct for spherical aberrations introduced when focusing inside the

LC device. A red LED was used to provide transmission illumination of the device so that the fabrication could be monitored in-situ with a monochrome CCD without affecting the photocuring process.

Pi-cell devices were mounted onto a stack of high-resolution air-bearing translation stages (Aerotech ABL1000) that allowed the sample to be moved relative to the laser focus with high precision and accuracy. Polymer walls were fabricated by moving the sample under continuous exposure to the laser beam at a speed of 100 µm/s. The devices were connected to a Tektronix AFG 3022 function generator so that the 1 kHz voltage applied to the device could be varied during fabrication.

## 6.3 Results and Discussion

### 6.3.1 Electrically-Tunable Disclination Lines

#### Defect Stabilisation with UV Photolithography

Initial experiments were conducted using the UV LED system described above (Section 6.2.2) to create relatively large polymer stabilised regions within pi-cell devices. These experiments were performed to gain an understanding of the behaviour of the pi-cells in order to prepare for more advanced experiments involving 2PP-DLW. A schematic of the fabrication process can be seen in Figure 6.4, where the sequential application of photomasks and two exposures is used to create an uncured channel 540 µm wide in between large regions stabilised in the V- and H- states.

In order to create the two regions, three separate vinyl masks are required: two larger masks that occupy just over half of the device area and a thin strip mask which ensures there is a narrow unpolymerised region in the device (Figure 6.4a). Firstly, the thin mask is placed in the centre of the device (Figure 6.4b) after which the first of the larger masks

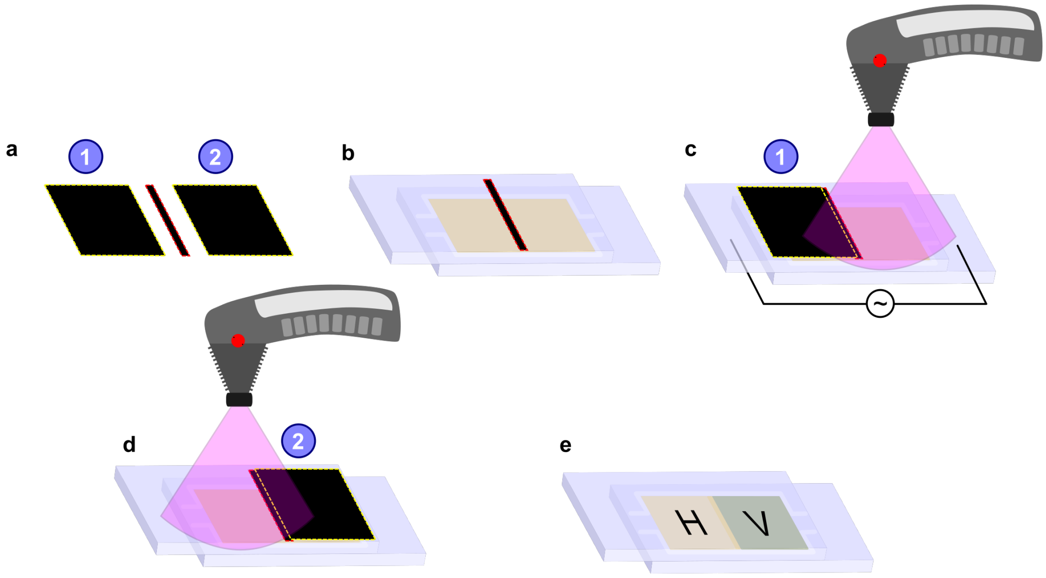

FIGURE 6.4: Fabrication of a tunable disclination line using bulk UV curing. (a) The three black vinyl masks used in the fabrication procedure. (b) Placing of the thin mask in the centre of the device. (c) The first exposure while applying a voltage to the device, resulting in the stabilisation of the V-state. (d) The second exposure with no applied voltage to stabilise the H-state. (e) The final configuration of the device with large regions stabilised in the H and V states and a narrow uncured channel in the centre of the device.

is placed on one side of the device, slightly overlapping with the thin mask. Then a 1 kHz AC square-wave voltage of 10 V is applied to the cell electrodes which causes the entire device to transition to the V-state. The UV LED curing system is then used to polymerise the reactive mesogen in the exposed area, locking-in the V-state (Figure 6.4c). Then, the first of the larger masks is removed and the device is disconnected from the voltage source and allowed to relax to the H-state over a period of several minutes. For the final exposure, the second large vinyl mask is placed on the other half of the device, slightly overlapping with the initial thin mask (Figure 6.4d). Polymerisation proceeds with the same UV curing conditions used in the first exposure, locking-in the H-state in the other half of the device. Finally, all the masks are removed from the device, leaving a device with large regions stabilised in the H and V states with a narrow uncured channel in the centre, in between the two regions (Figure 6.4e).

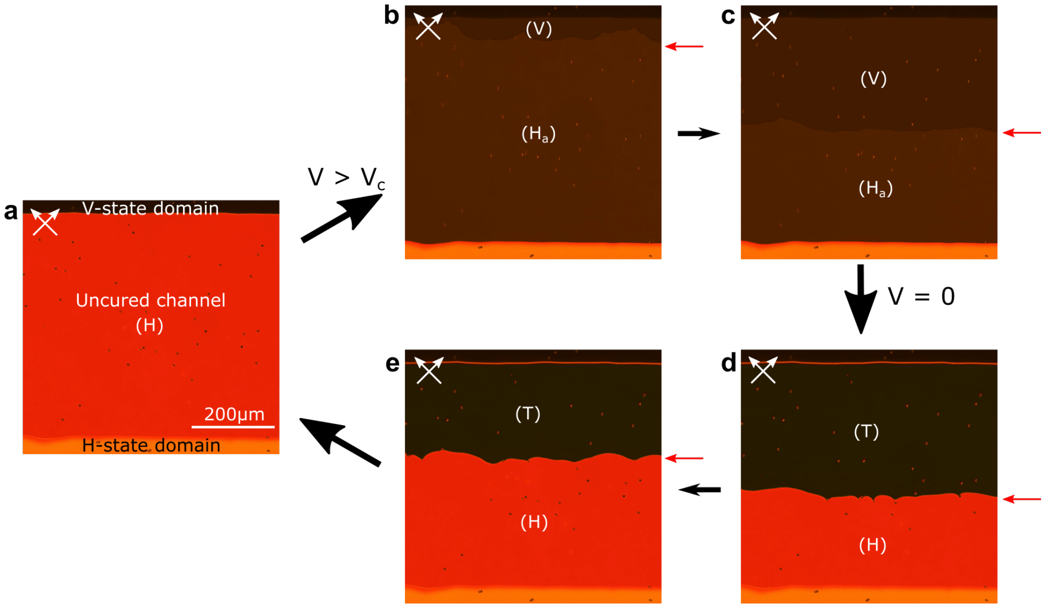

FIGURE 6.5: Polarised optical microscopy (POM) images of a tunable disclination line fabricated with UV photolithography. The red arrows indicate the position of the defect. (a) the structure with no applied voltage. The uncured region in the centre of the image is in the H-state. (b) a 6 V ramp over 5 s is applied to the cell, resulting in the growth of the V-state and (c) the movement of the defect across the cell. (d) the voltage is switched-off, causing the H-state to grow and the V-state to collapse to the T-state. (e) the defect moves back across the cell in the absence of an applied voltage towards the V-state domain.

Polarised optical microscopy was used to investigate the voltage-dependent dynamic behaviour of the device and micrographs showing this can be seen in Figure 6.5. By stabilising the H-state and V-state either side of an uncured channel, a disclination line can be moved across the gap between the cured regions with the application of a voltage across the LC device.

Without an applied voltage, the uncured channel is in the H-state, the ground state of the pi-cell (Figure 6.5a). As the two stabilised states are topologically discontinuous, there is a disclination line adjacent to the polymer-stabilised V-state region. Applying a voltage above $V_c$ causes the V-state to grow across the uncured channel, with the growth originating from the polymer stabilised V-state region (Figure 6.5b). Due to the coupling between the voltage and the positive dielectric anisotropy of the liquid crystalline material, the V-state becomes the state with the lowest free-energy and thus the V-state domain will grow. Because this transition from the H to V states is a topologically discontinuous transition from topology T1 to topology T2 (see director profiles in Figure 6.2), this process causes the translation of the disclination line at the frontier of the growing domain.

The disclination line moves along the channel (Figure 6.5c) until it reaches the H-state polymer stabilised region, which halts the progress of the defect. Switching-off the voltage causes the V-state in the unpolymerised channel to collapse over a period of a few seconds into the T-state (Figure 6.5d). The H-state, with its lower elastic energy, then grows from the H-state domain, moving the defect back across the channel (Figure 6.5e) until it reaches the V-state domain.

This dynamic behaviour is broadly repeatable, however, the nucleation of the V-state under an applied voltage is not uniform and results in a defect line that is not straight and has a zig-zag like appearance. This is likely to be due to variation in the polymer network morphology along the boundary of the polymerised region.

The fabrication of more-complex polymer structures with this UV photolithography method is extremely challenging, due to the need to perform multiple exposures and accurately register a series of photomasks. In addition, creating true micron-scale features would require the projection of an image of the photomask into the LC layer within the glass cell, to prevent the shadowing effect that arises from placing a photomask on the surface of the outer substrates[145].

The above drawbacks of using conventional UV photolithography in the generation and stabilisation of defects in pi-cells demonstrates the need for more sophisticated fabrication techniques. As discussed in Chapter 3, 2PP-DLW can provide the desired micro-scale resolution and allows rapid-prototyping of fabricated structures. In the remainder of this chapter we will see the results of fabricating defects in LCs using this laser microfabrication technique.

### Defect Stabilisation with 2PP-DLW

A schematic illustration of the fabrication of a tunable disclination line with 2PP-DLW is shown in Figure 6.6. The fabrication process is conceptually similar to the bulk curing process illustrated in Figure 6.4 but here the polymerisation occurs due to exposure to a tightly-focussed femtosecond laser beam, rather than a UV LED.

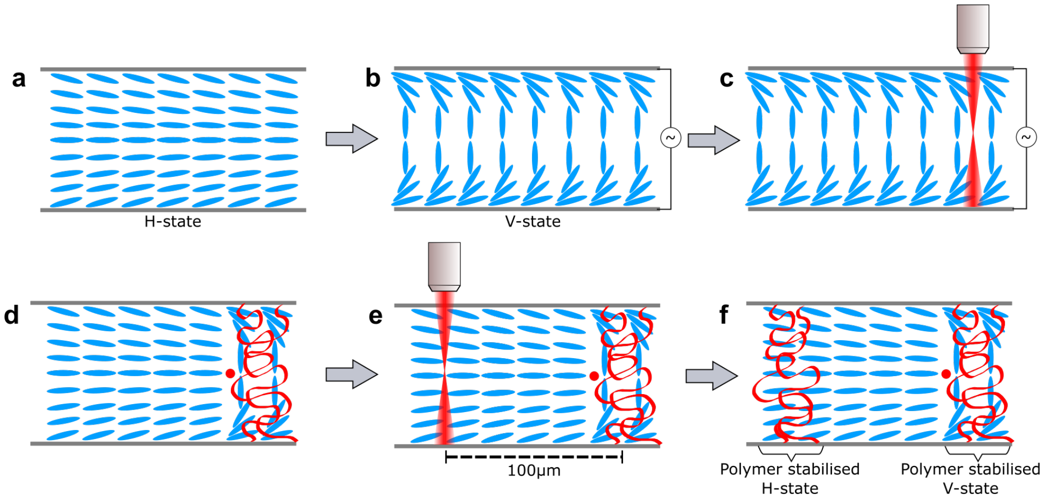

FIGURE 6.6: Schematic illustration showing the cross-section of a pi-cell during fabrication of a tunable disclination line with 2PP-DLW. Blue rods are LC molecules, red ribbons are polymer network and red dots are defects.

The director profile of a pi-cell device in the absence of an applied voltage is shown in Figure 6.6a where the molecules adopt a slightly-splayed homogeneous configuration between the parallel-rubbed substrates. The fabrication process begins by applying a voltage above $V_c$, the critical voltage for formation of the V-state (Figure 6.6b), and translating the device under exposure to the laser (Figure 6.6c) as described in detail in Section 6.2.3. This results in the fabrication of a polymer network (represented by red ribbons in the figure) in the form of a thin polymer wall across the full thickness of the device. This polymer wall is stabilised in the V-state as this is the state the device was in at the moment of fabrication.

The H-state is allowed to form by switching-off the voltage and waiting a few minutes for the whole device to relax to the ground state (Figure 6.6d). As the H-state is topologically discontinuous from the V-state, a defect exists at the interface between the V-state wall and the bulk of the device. The last step is to fabricate a polymer wall stabilised in the H-state, parallel to and at a distance of 100 µm from the V-state wall (Figure 6.6e). The final configuration of the fabricated device is shown in Figure 6.6f, with a 100 µm wide unpolymerised channel bounded by a pair of parallel walls written in the H and V states.

Polarised optical microscopy (POM) images of the fabricated device are shown in Figure 6.7 where each micrograph is paired with a drawing of the director profile corresponding to the POM image. Similar to the bulk-cured device in Figure 6.5, in the off-state of this laser-fabricated structure, the uncured channel is in the H-state and the disclination line is adjacent to the V-state polymer wall (Figure 6.7a). Upon application of a voltage > $V_c$, the unpolymerised channel transitions rapidly from the H-state to the $H_a$ state and the V-state begins to nucleate from the V-state polymer wall (Figure 6.7b). The V-state grows, moving the disclination line separating the topologically discontinuous director states across the channel (Figure 6.7c) until it reaches the H-state polymer wall (Figure 6.7d). It is not possible for the defect to continue beyond the H-state polymer wall as the wall is fixed in the H-state, which is topologically discontinuous from the growing V-state.

Switching-off the voltage causes the V-state to collapse over a period of a few seconds into the T-state (Figure 6.7e). As the voltage has been reduced below $V_c$, the lowest energy state is now the H-state,

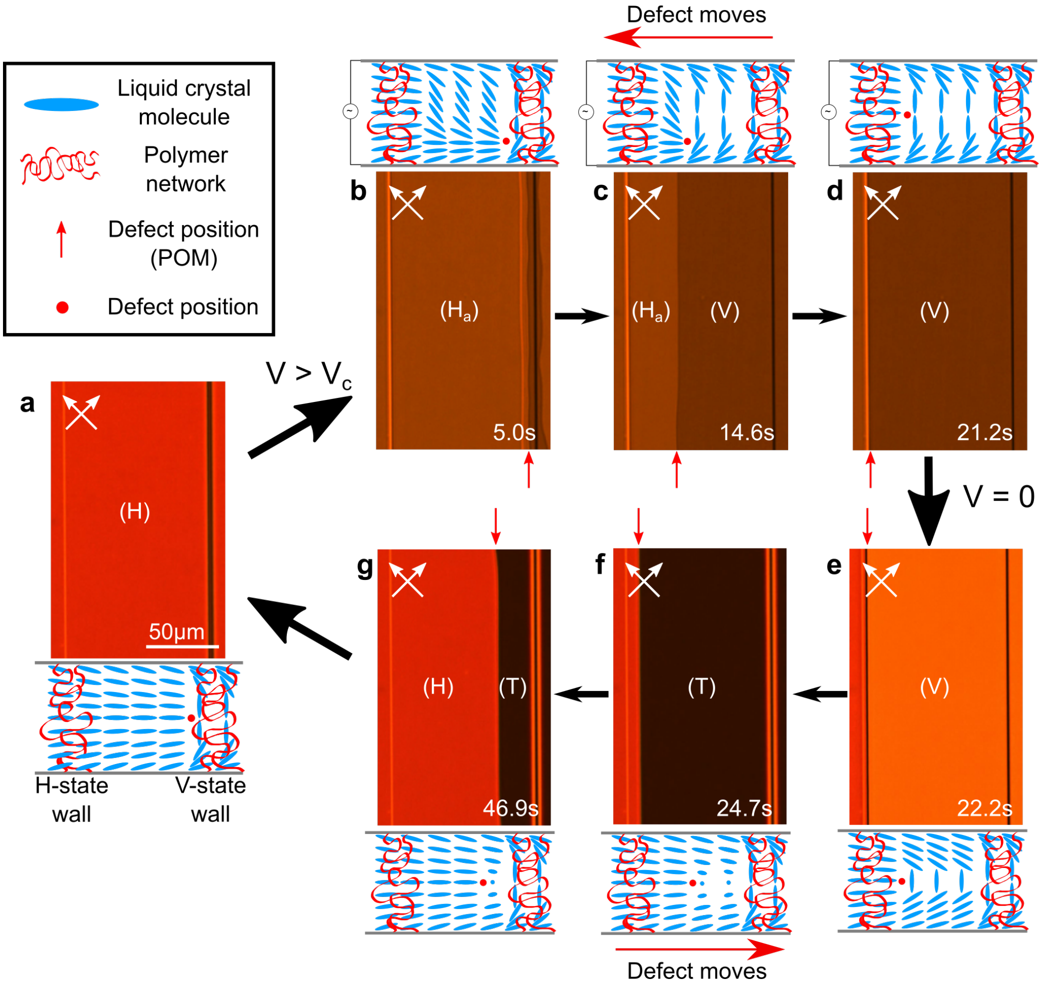

FIGURE 6.7: Polarised optical microscopy (POM) images and director profiles showing the dynamics of a tunable disclination line under an applied voltage. Red arrows highlight the position of the defect line in each POM image. (a) With no voltage applied, the bulk of the device is in the H-state and the defect is adjacent to the V-state wall. (b - d) A voltage above V$_c$ is applied to the device and the defect begins to move across the channel until it meets the H-state wall. (e - g) Removing the voltage causes the V-state to relax into a 180° twisted state (T-state), and the defect moves back across the channel. The H-state grows and moves across the channel with the disclination line at the frontier of the growing domain, until it is impeded by the polymer-stabilised V-state wall.

the ground state of the system. However, as the H-state is topologically discontinuous from the V and T states, it can only grow by a defect-mediated nucleation and growth process. This can be seen in Figure 6.7f, where the H-state has begun to grow, with the growth originating from the H-state polymer wall. The domain continues to grow, moving the disclination line separating the distinct topologies back across the channel (Figure 6.7g). After the device has been reset by returning to the ground state with no applied voltage, the process can be restarted and is highly repeatable.

In contrast with the bulk-cured device shown in Figure 6.5, the morphology of the defect line is very straight, matching the straightness of the laser-fabricated polymer walls. The nucleation of the states from the polymer walls is highly uniform and regular, leading to straight defect lines. This demonstrates that 2PP-DLW can be used to design and engineer these defects with a high degree of precision and control.

There is another detail of note that is revealed when studying the dynamic behaviour of this structure. Looking closely at the POM image in Figure 6.7b, a faint orange thread-like line can be seen adjacent to the V-state polymer wall. This is a domain wall that separates different states.

Referring back to Figure 6.2, it can be seen that there are two subtly different asymmetric H-states named $H_{a1}$ and $H_{a2}$. These states are optically identical and possess the same elastic energy (in a perfect system), differing only by which substrate the elastic distortion is closest to. In reality, however, these states can have slightly different elastic energies due to asymmetries in the exact pretilt angle over the area of the device. This can result in some areas of a given pi-cell consistently switching to one $H_a$ state each time a voltage is applied. In other areas of the device, a mixture of $H_a$ states can form, with the states separated by thread-like domain walls that can be easily seen with polarised microscopy. An example of this phenomenon is shown previously in Figure 6.3b where a region with a mixture of the two $H_a$ states can be seen.

If a voltage is suddenly applied to a pi-cell, a mixture of the two states will form due to the random thermal fluctuations in the molecular orientation at the instant the voltage is switched-on. Whereas if a voltage is applied with a slow ramp over a period of a few seconds, as is the case in Figures 6.5 and 6.7, the LC director will adopt the most thermodynamically stable configuration, and the distribution of the $H_a$ states is governed by the asymmetries in the pretilt angle over the area of the device.

The tunable disclination line structures in Figures 6.5 and 6.7 were deliberately fabricated in regions where only one $H_a$ state forms when a voltage ramp is applied. However, it can be seen that a $H_{a1}/H_{a2}$ domain wall is visible in Figure 6.7b, immediately adjacent to the V-state polymer wall. Therefore, it appears that the energetically unfavourable $H_a$ state has been induced by the V-state wall, forming in a region of the device where it would not normally form. However, this does not affect the behaviour of the disclination line that subsequently propagates from the V-state wall.

In this section we have seen how a tunable disclination line can be fabricated with simple bulk curing methods but that this results in non-uniform nucleation of topologically discontinuous director states and zig-zag like disclination lines. In contrast, employing 2PP-DLW allows controlled and precise fabrication of uniform polymer structures that induce uniform state nucleation behaviour. In other words, topologically discontinuous director states will nucleate at the same instant along the length of the boundary of a polymer structure, resulting in the formation of straight disclination lines.

These disclination lines are tunable, that is, their position can be changed by applying a voltage to the device. Changing the amplitude of the voltage allows the defect to be moved either forwards or backwards. This concept will be developed in the following sections that describe: (i) how the defect behaviour depends on the orientation of the polymer structures with respect to the rubbing direction; before exploring potential applications by demonstrating (ii) computer-control of disclination lines, (iii) defect-mediated microparticle cargo transport and (iv) complex polymer structures for advanced disclination line control.

### 6.3.2 Anisotropic Defect Behaviour

The tunable disclination line structures introduced in the above section were fabricated such that the rubbing direction of the device was parallel to the polymer walls. As the orientation of the defects is dictated by nucleation from the laser-written polymer walls this also means that the defects are parallel to the rubbing direction.

Defects in pi-cells have different natures depending on their orientation. Figure 6.8 shows director profiles for the possible defect types. Splay-bend type defects, where the distortion surrounding the defect is of a splay and bend nature, occur when the disclination line is perpendicular to the rubbing direction of the device. Conversely, twist type defects occur when the disclination line is parallel to the rubbing direction and the defect has a twisted nature[146].

Figure 6.8a shows a 3D schematic director profile of a V-state domain surrounded by an H-state domain. The red line represents the defect loop separating the two topologically discontinuous states. The

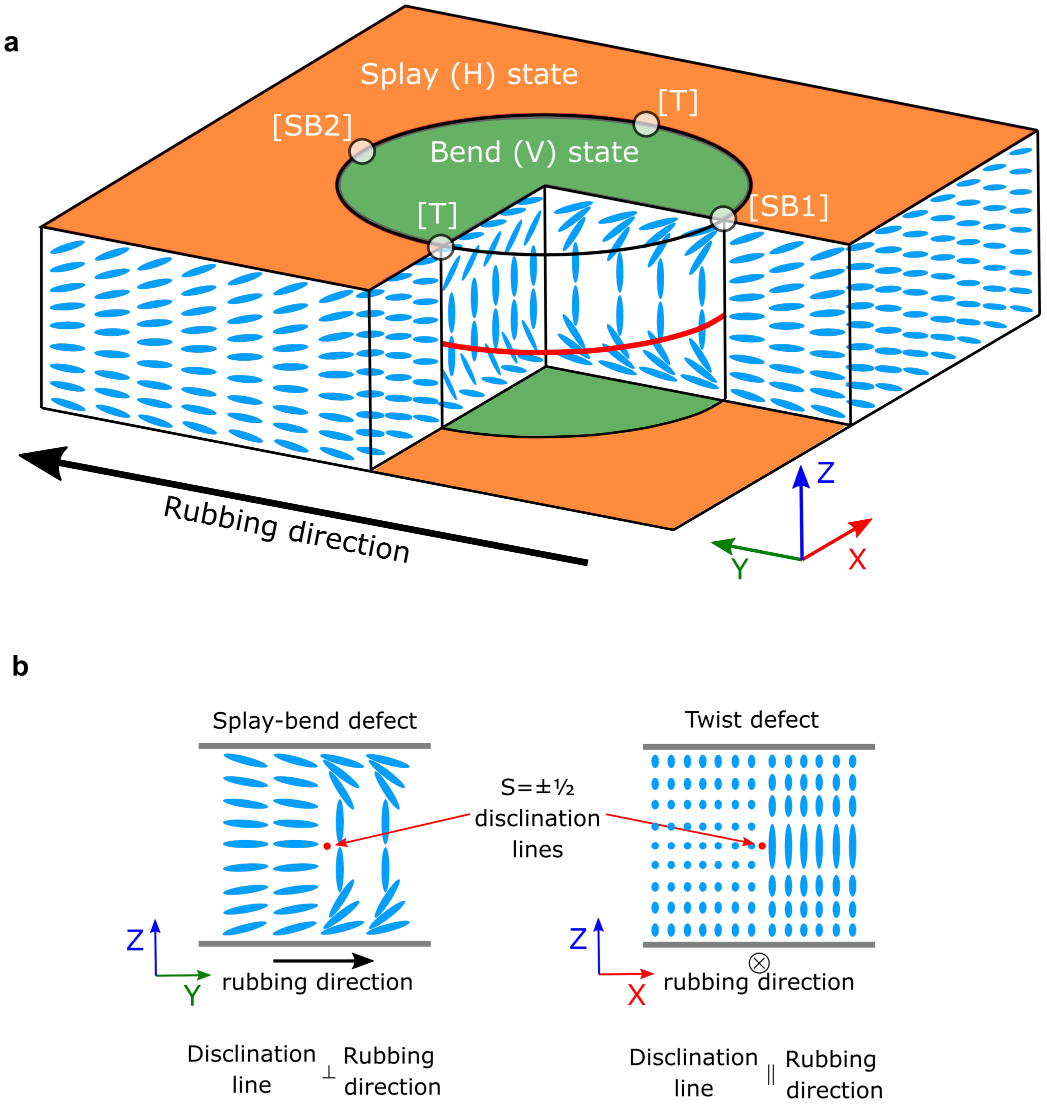

FIGURE 6.8: (a) 3D schematic director profile of a V-state domain surrounded by an H-state domain. The red line represents the defect loop separating the two topologically discontinuous domains. The rubbing direction is along the Y-axis. (b) 2D projections of the different types of defect that exist in pi-cells. Adapted from [146].

rubbing direction is along the Y-axis and the 2D projections in Figure 6.8b correspond to the same geometry. The nature of the disclination varies along the length of the defect loop: at the positions marked [SB1] and [SB2] the defect has a splay-bend nature whereas, at the points marked [T], the defect has a twisted nature. The 2D projections in Figure 6.8b provide a visualisation of the distortion at the points [SB1] and [T].

There is a lower elastic energy cost associated with twist deformations in LCs as compared to splay and bend deformations (this is expressed in the values of the elastic constants, where usually $K_{22} < K_{11}$, $K_{22}$) and thus twist defects have a lower elastic energy and higher stability than splay-bend defects. In reality this means that splay-bend defects have a tendency to distort, forming zig-zag structures to become more parallel to the rubbing direction, such that the defect obtains a partially twisted nature and lowers its elastic energy. This phenomenon can be seen in Figure 6.9 which shows POM images for a tunable disclination line where the polymer walls were written perpendicular to the rubbing direction. Looking closely at Figure 6.9b and c, the characteristic zig-zag structure of the splay-bend type disclination line can be observed. The disclination line behaves in this way to lower its degree of splay-bend distortion, increasing its twist distortion and lowering its elastic energy cost.

It was observed that the magnitude of the applied voltage influences the translation speed of the tunable disclination lines introduced in the above section. At higher voltages, the defects travel faster, as the free energy density of the V-state decreases with increasing voltage, making it energetically favourable for the V-state to grow at a faster rate. The measured relationship between defect speed and voltage is shown in Figure 6.10a for the different types of defect in the pi-cell.

Figure 6.10b shows a POM image of the different defect types.

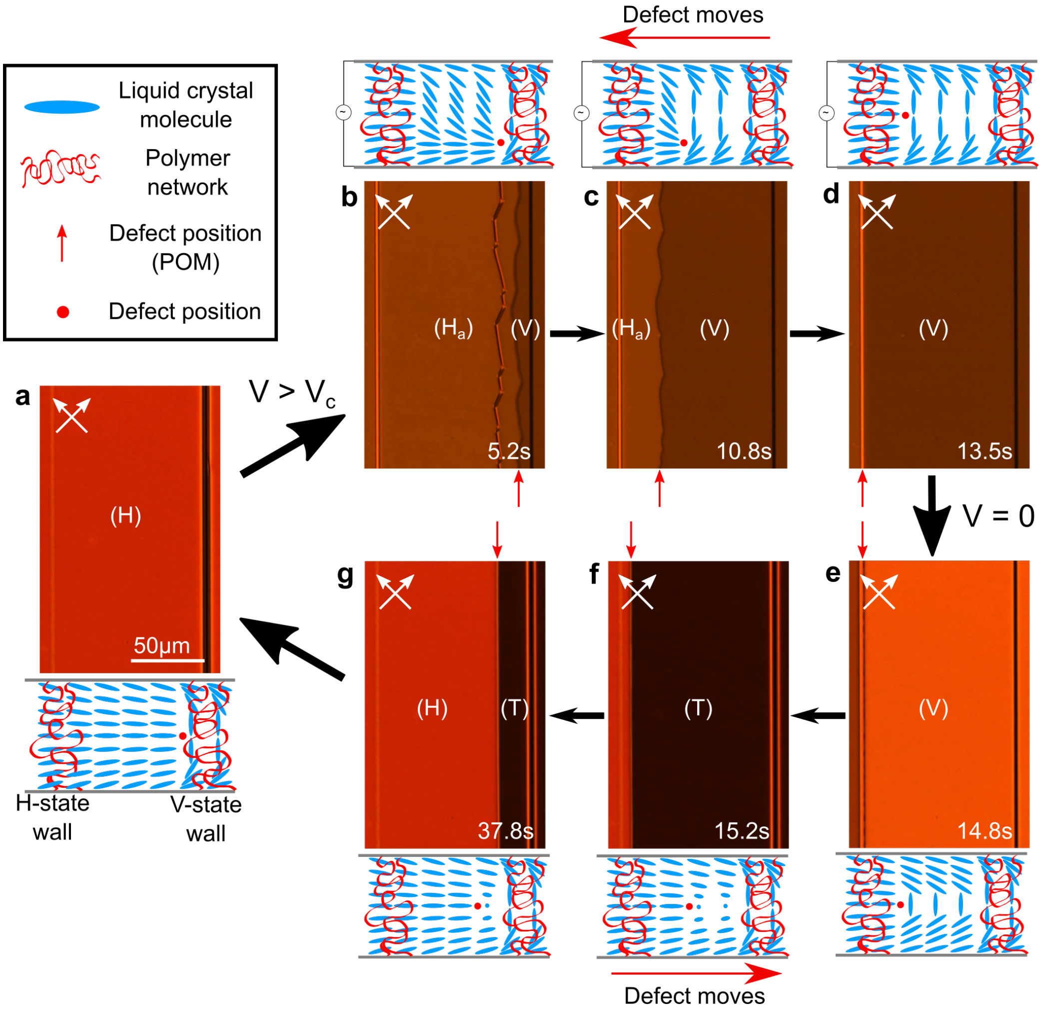

FIGURE 6.9: Polarised optical microscopy (POM) images and director profiles showing the dynamics of a tunable disclination line written perpendicular to the device rubbing direction. Red arrows highlight the position of the defect line in each POM image.

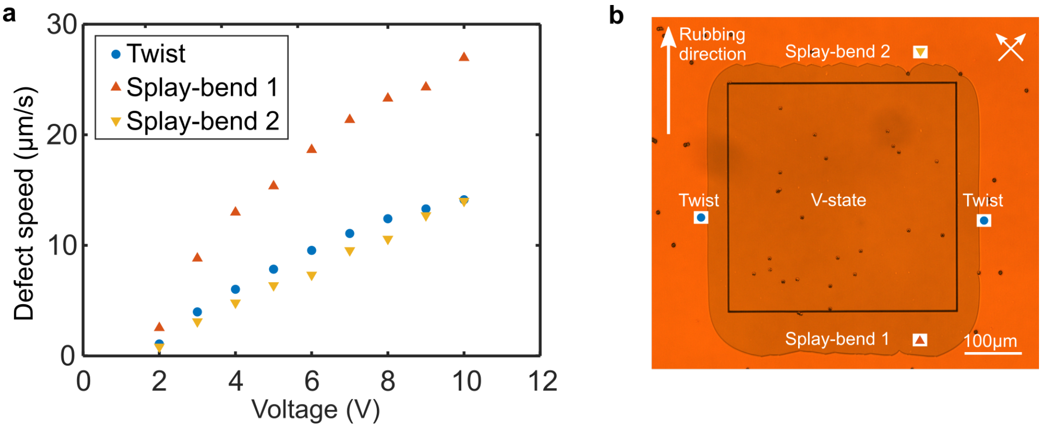

FIGURE 6.10: (a) Disclination line speeds as a function of voltage at 25°C for different defect orientations with respect to the device rubbing direction. (b) POM image of the different types of defect that exist in pi-cells containing the polymerisable mixture used in this study. A voltage V > $V_c$ has been applied to the device, causing the V-state to grow and the defects to move away from the V-state polymer walls. Twist-type defects correspond to the case where disclination lines are parallel to the rubbing direction and splay-bend type defects exist when disclination lines are perpendicular to the rubbing direction. We can observe the zig-zag distortion of the splay-bend defects.

The polymer walls were fabricated to create the outline of a square, in order to force the defects into a particular orientation. At this snapshot, taken a few seconds after the voltage is switched-on, the V-state is growing, and the ‘splay-bend 1’ type defect is growing faster than the other defect types. The image also shows the zig-zag instability observed in the splay-bend type defects.

Due to the inherent asymmetry of the pi-cell resulting from the parallel-rubbed substrates, we can see that disclination lines oriented perpendicular to the rubbing direction (splay-bend type) have a speed versus voltage relationship that depends on the direction in which they travel. Splay-bend type defects that are growing in a direction anti-parallel to the rubbing direction grow at a rate approximately double that of both twist type defects and splay-bend type defects growing parallel to the rubbing direction (Figure 6.10a). This dependence of the rubbing direction on defect mobility is in accordance with previously observed experimental[147] and numerical studies[146] of pi-cells that have shown that the defect behaviour is governed by anisotropic hydrodynamics and flow.

### 6.3.3 Disclination Line Control System

This section describes the creation of a disclination line control system which demonstrates precise control of the position and speed of a tunable disclination line using a control loop to regulate the magnitude of the voltage applied to the device. If nematic defects are to find applications in tunable/switchable electro-optic devices, it is essential that they can be precisely controlled. The disclination line control system described in this section represents a proof-of-concept for switchable electro-optic devices employing tunable defects.

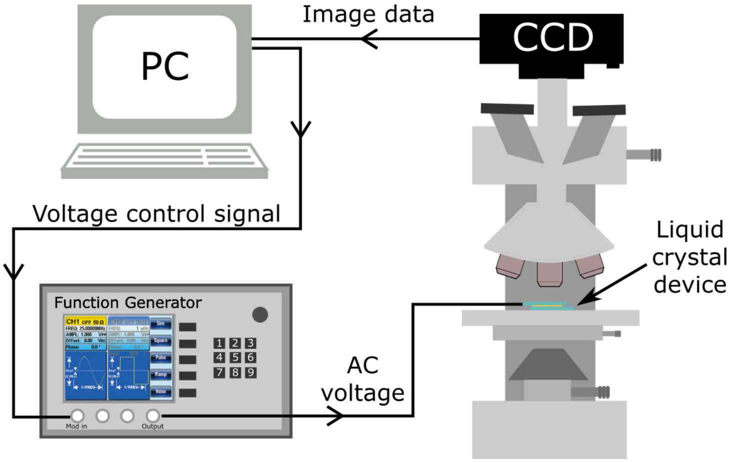

FIGURE 6.11: Schematic diagram of the elements of the control system. The microscope CCD sends images of the device to the control system program running in MATLAB®. The program adjusts the voltage applied to the device via the function generator in order to move the defect to the set position specified by the user.

A schematic showing the elements of the control system is presented in Figure 6.11. The control system receives a real-time video feed from a camera (QImaging Retiga R6 6.0) attached to a microscope (Olympus BX51) imaging the LC device and performs image analysis to determine the position of the defect line. The voltage output from a function generator (Tektronix AFG 3022) is regulated by the system to move the defect to the desired position.

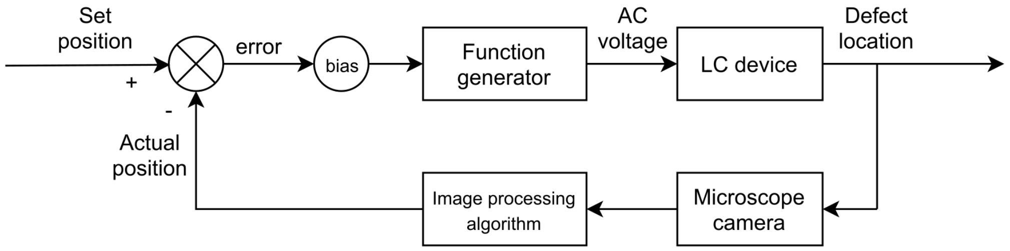

FIGURE 6.12: Control loop block diagram. The position of the defect is detected with an image recognition algorithm and compared with the set position. This voltage output by a function generator connected to the device is made proportional to this error signal in order to control the position of the defect.

A control loop diagram for the system is shown in Figure 6.12. The program was implemented in MATLAB® and used both the Image Acquisition and Instrument Control Toolboxes. Frames from a CCD camera were analysed in a loop running at 10 iterations (or frames) per second. The position of the defect was determined by taking line-sections across the image and using an in-built function findchangepts to find abrupt changes in a signal which correspond to the position of the defect. The position can be detected with an accuracy of ±1 µm, limited by the optical diffraction limit and the resolution of the camera. This position is compared with a set position to produce an error value for each iteration of the loop $(error\ value) = (set\ position) - (current\ position)$. The voltage output from a function generator producing a 1 kHz square wave is made proportional to this error signal.

A GUI was created with a live view of the device (Figure 6.13) to allow the control loop parameters to be tuned during operation and the set position to be adjusted manually. The voltage required to hold the disclination line in place (when the H and V-states are of equal free energy) was found experimentally. The control loop was configured with a bias/offset so that the function generator output this experimentally determined hold voltage when the error signal was equal to zero.

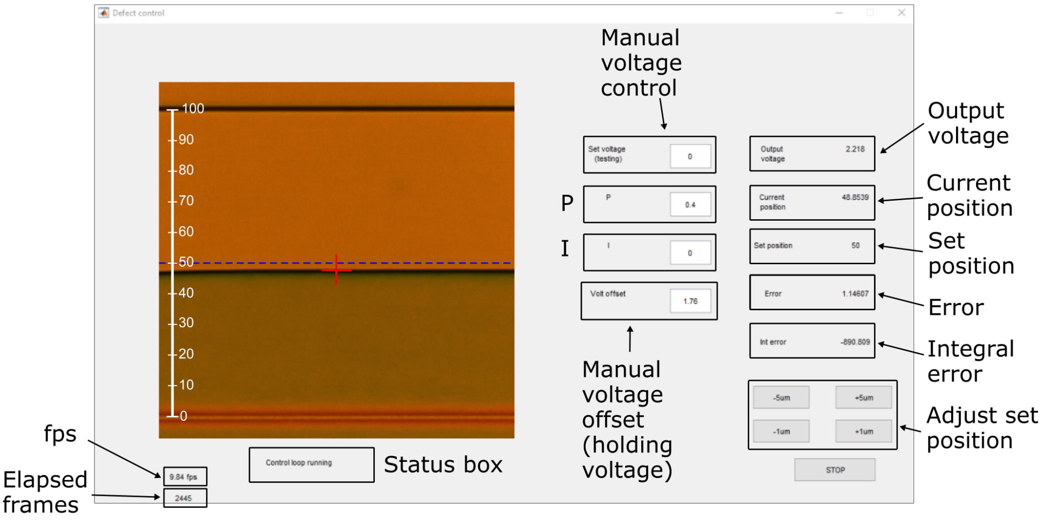
Set voltage (testing) 0
P 0.4
I 0
Volt offset 1.76
Output voltage 2.218
Current position 48.8539
Set position 50
Error 1.14607
Int error -890.809
Control loop running
9.84 fps
2445

FIGURE 6.13: Screenshot of disclination line control system GUI. Parameters in white boxes can be adjusted while the control system is running for the purposes of control loop tuning, debugging and testing. The set position is indicated with a dashed blue line and the current position of the defect is indicated with a red cross. The scale on the left-hand side is in microns.

The optimal configuration was found to be a P-only control loop, such that the voltage output of the function generator is directly proportional to the error signal. A more complex PI control loop was also implemented during development, where the error after each iteration is summed to produce an integral error. However, it was found that this leads to very unstable behaviour, and ultimately the P-only control loop with a linear offset to account for the hold-voltage produced the best performance.

In initial versions of the system, the voltage output of the function generator was controlled by sending SCPI commands (Standard Commands for Programmable Instruments) directly to the instrument via a USB interface. Unfortunately this was found to produce instability in the control loop, resulting from voltage-spikes when the function generator automatically changes its range setting.

A number of voltage modulation solutions were trialed and the most successful was to use a National Instruments USB DAQ (NI USB-6008) to modulate the voltage output of the function generator. In amplitude modulation (AM) mode, the function generator will adjust its output amplitude according to a DC voltage received at the mod-in input. A further complication was that a modulation input voltage of -1 to +1 V corresponded to an output of 0 – 10 V. As the NI USB DAQ was only able to produce positive voltages of 0 – 5 V, a benchtop power supply was used to offset the output voltage by -1 V, such that a 0 – 2 V output from the DAQ actually produced a -1 to 1 V input to the function generator.

Figure 6.14a shows the position of the disclination line in response to a series of changes in the set position. A POM image showing the live-feed from the microscope camera can be seen in Figure 6.14b, with an overlay to show the defect position, the set position and a measurement scale. The tunable disclination line structure is identical to that shown in

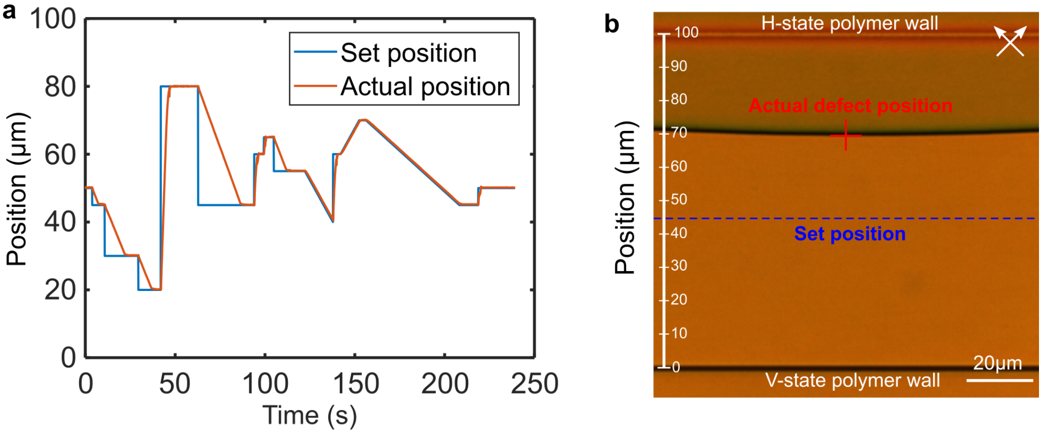

FIGURE 6.14: (a) A disclination line control system responding to an arbitrary series of changes in set position. (b) Snapshot POM image of the control system in operation. The set position is indicated with the dotted blue line and the red cross indicates the actual position of the defect as determined by the image recognition algorithm.

Figure 6.7 and described in the above sections.

Positive changes in the set position correspond to the V-state growing under an applied voltage. Negative changes in the set position correspond to the H-state growing and, as this is a relaxation process, the system responds more slowly when moving in this direction.

By implementing this proof-of-concept of feedback-based control, the position of a disclination line can be stabilised indefinitely and controlled programmatically. In addition to the fabrication and stabilisation of defects shown in the previous section, this section has demonstrated that it is possible to precisely tune the defect position with an applied voltage.

### 6.3.4 Defect-Mediated Microparticle Transport

LC defect networks have been proposed as soft templates for the self-assembly of nano/micro-particles. The reason for this is two-fold: 1) colloidal inclusions in LC hosts tend to become localised and trapped at defect cores and, 2) LC mesophases have the ability to self-organise into complex macroscopic structures[131, 133, 148, 149]. Furthermore, doping of colloidal particles into an LC host can result in new physical properties and functionality that are not intrinsic to the LC material. In addition, LCs can be employed as a tunable medium to influence the properties of the nano/micro-particles[132, 150].

Typically, the defect networks that have been designed in previous studies have been relatively static, with a limited degree of tunability. In contrast, in this section we will see that by doping a polymerisable LC mixture with functionalised 1 µm silica microspheres, defects can be used to pick-up and re-position particles, as a proof-of-concept for disclination-mediated cargo-transport.

Silica beads with a diameter of 0.9 µm (Bangs Laboratories) were functionalised with the homeotropic alignment agent dimethyloctadecyl[3-(trimethoxysilyl) propyl]ammonium (DMOAP) (Sigma-Aldrich). DMOAP was supplied as a 42 wt% solution in methanol. Deionised water was then added to the solution, and the methanol evaporated at 65°C to form a 1 wt% solution of DMOAP in water. 30 mg of the silica beads were added to 200 µL of the 1 wt% DMOAP solution and sonicated for 1 hour at room temperature. The dispersion was then centrifuged at 3000 RPM for 5 minutes to sediment the particles. A pipette was used to extract the excess DMOAP solution, before deionised water was added to the vial. This process of centrifugation and replacement of the excess DMOAP solution with water was repeated 5 times.

Finally, the water was evaporated at 105°C on a hotplate. A mixture was made of 5.5 wt% DMOAP-functionalised silica beads, E7 (Merck) (64.4 wt%), RM257 (Merck) (31.5 wt%) and Irgacure 819 (Merck) (1.5 wt%). This mixture was capillary filled into 5 µm thick pi-cells, as described in Section 6.2.1. On examination with a microscope, the microspheres were seen to be dispersed throughout the device.

Using 2PP-DLW, a tunable disclination line structure was created in the cell, with parallel H and V state polymer walls separated by 100 µm, similar to the devices described above in Section 6.3.1. The cell was examined in-situ during fabrication so that the polymer wall structures could be fabricated either side of a silica microsphere.

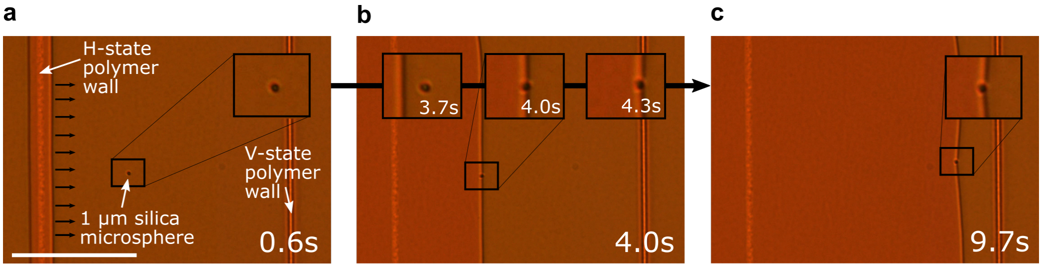

FIGURE 6.15: (a) A 1 µm silica microsphere is towed by a disclination line across the gap between topologically discontinuous polymer walls upon removal of a voltage V > $V_c$ at t = 0. (b) When the disclination line encounters the microparticle (c) it carries it across the channel to the polymer-stabilised V-state wall. Scale bar is 50 µm.

Figure 6.15 shows the microsphere being dragged by the disclination line across the 100 µm wide channel separating the topologically discontinuous polymer walls. The device, which is initially driven into the V-state with an applied voltage above $V_c$, is switched-off at t = 0, causing the H-state to nucleate from the polymer wall on the left hand side. The H-state grows, moving the defect from left to right. When the defect reaches the microparticle it traps it and transports it across the channel. The voltage can be adjusted to tune the position of the defect and thus the location of the particle trapped in the defect.

Controlling the motion of microparticles suspended in an LC in this manner opens up new possibilities for research and technologies that exploit LC colloids. As discussed previously in Section 6.1.1, the inclusion of colloidal particles in LCs is a vast area of research, with applications spanning self-assembly of nanoparticles, metamaterials, and tunable plasmonics. One of the significant advantages of this approach, as opposed to DC voltage-based electrophoresis of dispersed particles, is the use of an AC driving voltage. Developing methods for voltage-induced micro/nano-particle transport with AC driving schemes is of significant interest, as it avoids unwanted electrochemical reactions that can occur when using DC fields[151].

### 6.3.5 Defect Confinement and Control

The laser-written structures presented in the above sections are relatively basic, consisting of simple pairs of polymer walls written in topologically discontinuous states. With the capabilities offered by 2PP-DLW, including the ability to fabricate polymer structures to arbitrary designs, it is possible to engineer much more complex behaviour in the stabilised defects. This section explores several concepts for defect confinement and control of defect dynamics.

For example, it is possible to permanently stabilise topology T2 (the V and T states) within a device over relatively large areas by forming enclosed square wells with 2PP-DLW (Figure 6.16). This is of technological interest because the V-state is the fast-switching state used in display applications of pi-cells, and the slow transition from the H-state to the V-state leads to a significant priming time (time taken for the device to reach an operational state after being switched-on) for such devices[152].

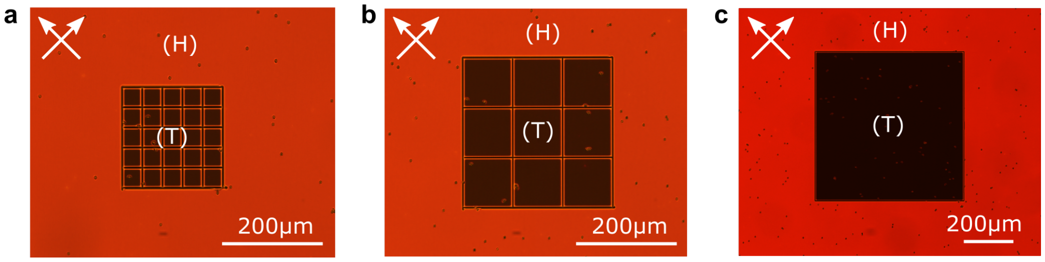

FIGURE 6.16: POM images of a (a) 40 µm, (b) 100 µm and (c) 600 µm pitch bend-state square polymer lattices in the absence of an applied field. The V-state polymer walls stabilise the higher energy bend-state, preventing the relaxation to the splay-state within the square wells. Without an applied voltage the region inside the wells relaxes to the T-state but does not relax to the H-state.

The device was driven into the V-state by applying a voltage above $V_c$ and the square lattices were fabricated in this state. Upon removal of the voltage, the bulk of the device will relax slowly back to the H-state, while the regions confined by the V-state polymer walls relax into the T-state and remain in this state indefinitely.

Surprisingly, this stabilisation phenomenon persists even at very large lattice spacings. Figure 6.16c shows a 600 × 600 µm square fabricated in the V-state. After removal of the applied voltage, the region within the square relaxes to the T-state but will not further relax to the H-state. This phenomenon persists indefinitely, with the devices unchanged after being left for many months. Topology T2 has been permanently stabilised within the square region defined by the laser-written polymer walls.

This can be understood by considering the nature of the transition between states with topology T2 and T1. For a device to relax from topology T2 to T1, the lower energy T1 state must nucleate from a given point. In a normal pi-cell, such as the one shown in Figure 6.3, nucleation occurs at points in the cell which have a large elastic distortion such as clusters of spacer beads and near electrode edges. In these laser-stabilised devices there are no such points within the square lattices and accordingly there are no nucleation points for the H-state to form. Although the rest of the device has relaxed to the H-state, the director reorientation that has propagated across the device cannot penetrate the topologically-discontinuous V-state polymer walls, preserving the state within the square.

Applying a voltage to these stabilised devices causes the T-state to rapidly switch to the V-state, as there is no topological discontinuity between these two states. Conventionally, pi-cells have a long priming time due to the slow transition from the H-state at zero applied voltage, to the technologically useful V-state. This result shows that it is possible to employ 2PP-DLW to engineer a pi-cell device without the slow H-to-V state transition step, thus overcoming a fundamental limitation that has prevented pi-cells from finding technological applications.

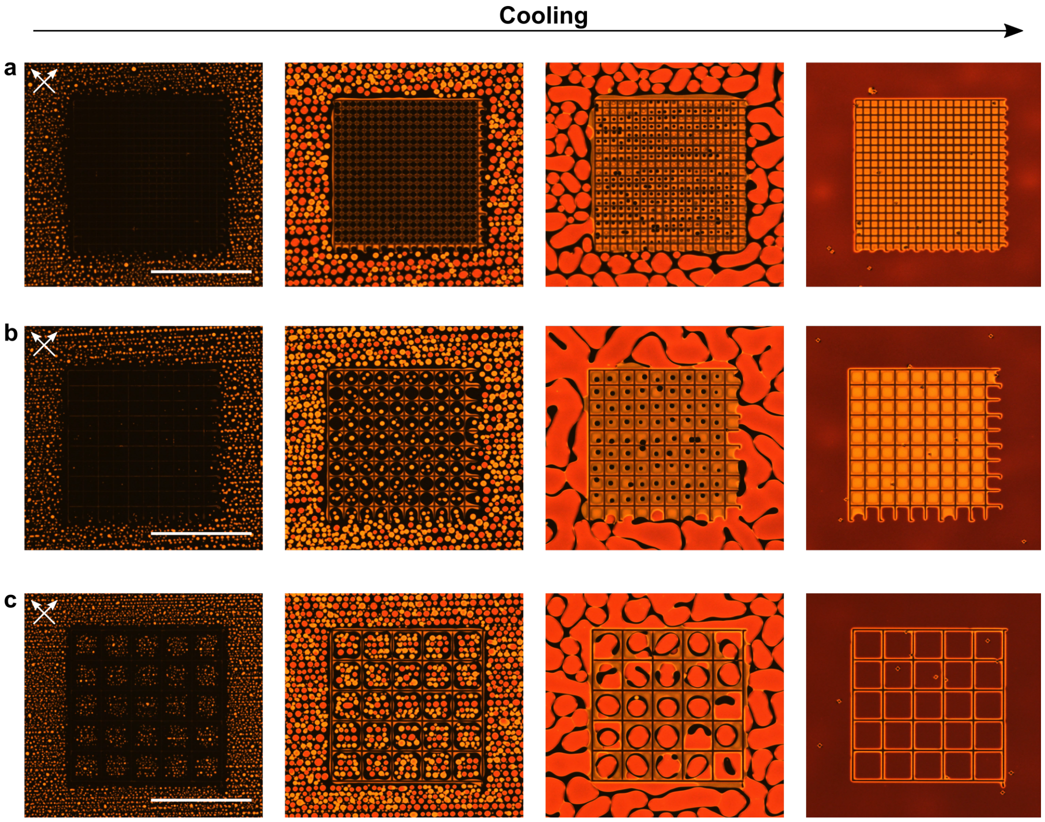

FIGURE 6.17: POM images of cooling V-state square polymer lattices with pitches (a) 10 µm, (b) 20 µm, (c) 30 µm, written with 2PP-DLW in a pi-cell. The device is first heated to the isotropic phase in all cases. As the device cools, small domains of both H- and V-state will form (red and yellow droplets, respectively). The polymer walls encourage the V-state to form in their immediate vicinity. For the smaller pitches (a) and (b), the V-state ultimately dominates and persists inside the lattice as the device is cooled. Scale bars are 100 µm.

Furthermore, V-state polymer lattices with a small pitch cause the V-state to spontaneously form when cooling the device from the isotropic phase. This represents a significant step towards ruggedisation for pi-cell devices. Ordinarily, cooling a pi-cell device from the isotropic phase in the absence of an applied voltage will first result in the formation of small domains of both H- and V-state before finally the H-state dominates, as it is the ground state of the system. However, in Figure 6.17 it can be seen that the V-state is encouraged to form as the device cools by the presence of the polymer walls. For the 10 and 20 µm pitch cases, the V-state will ultimately dominate and persist within the lattices as the device is cooled to room temperature.

Figure 6.18 shows defect rings formed by circular polymer walls laser-written in the H-state. When the device is driven to the V-state and subsequently switched-off, the defect will grow from the circular H-state polymer wall. When the defect lines meet, they annihilate, forming a continuous H-state domain as the state continues to grow.

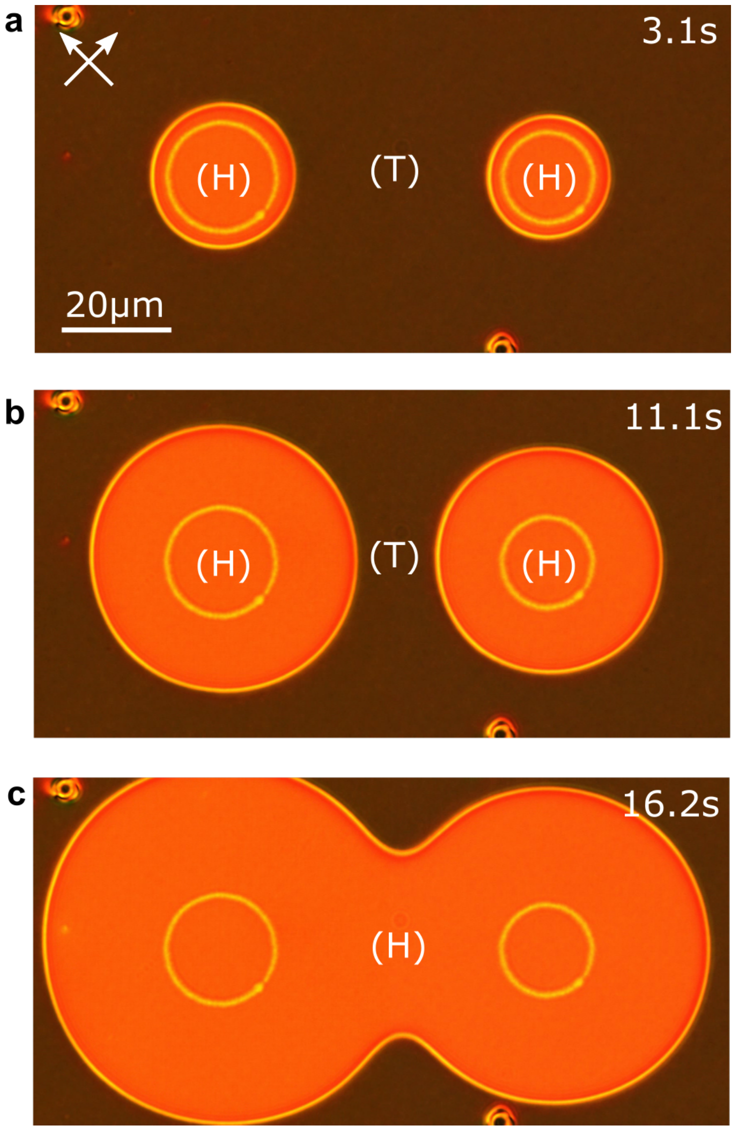

FIGURE 6.18: Polarised optical microscopy (POM) images of circular disclination lines growing as the device relaxes to the ground state. The device is initially in the V-state with a voltage applied. The voltage is switched off at t = 0.

It should also be noted that the H-state is stabilised within the circular regions defined by the polymer walls. Therefore, even when a voltage in excess of $V_c$ is applied to the device, these regions do not switch into the V-state. The growth of the V-state throughout the device is halted by the polymer walls written in the topologically discontinuous H-state.

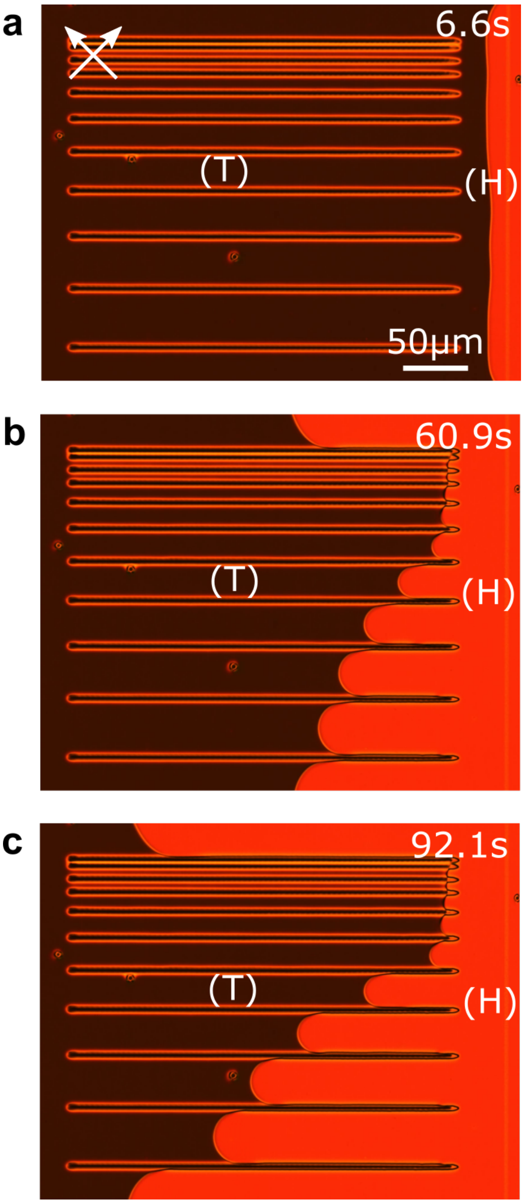

FIGURE 6.19: Polarised optical microscopy images of parallel confining V-state channels. Varying the spacing between adjacent laser-written channels affects the speed of propagation of the H-state as it grows. In the channels with smallest width, the splay-state cannot penetrate the channels. The device is initially in the V-state and at t = 0 the voltage is switched off.

The polymer structure in shown in Figure 6.19 demonstrates that the speed of a disclination line is influenced by confinement with topologically discontinuous polymer walls. A schematic illustration of the

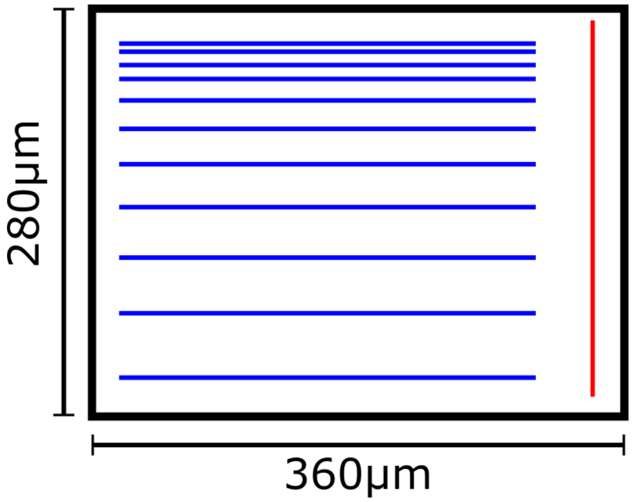

FIGURE 6.20: Schematic illustration of the laser written polymer wall design for the parallel confining V-state channel structure in Figure 6.19. The red line represents an H-state polymer wall and the blue lines represent V-state polymer walls.

device design is shown in Figure 6.20. The structure consists of a series of parallel polymer walls written in the V-state, with an increasingly large gap between each wall. When the applied voltage is switched-off, the H-state nucleates from the H-state polymer wall on the right (Figure 6.19a), and the disclination line separating the topologically discontinuous states begins to travel across the device. When the disclination line meets the confining channels that were written in the V-state, the motion is impeded and the degree to which the defect slows-down clearly depends on the width of the gap between the walls. For the narrowest channels, the H-state is unable to penetrate between the polymer walls as it would be energetically unfavourable to have such a strong degree of distortion in the narrow channel width.

Figure 6.21 shows a bifurcated channel structure inspired by recent developments in microfluidics technology. This represents a totally new approach to LC microfluidics where the ‘flow’ is a wave of director reorientation in the form of a propagating disclination line, rather than conventional fluid-flow through a channel with microscale dimensions. The bifurcated channel is designed to guide the disclination separating the H and V states as the device transitions from one state to another.

The structure consists of a series of polymer walls written in the V-state which define the edges of the channel, and a single H-state polymer wall fabricated in the widest part of the channel.

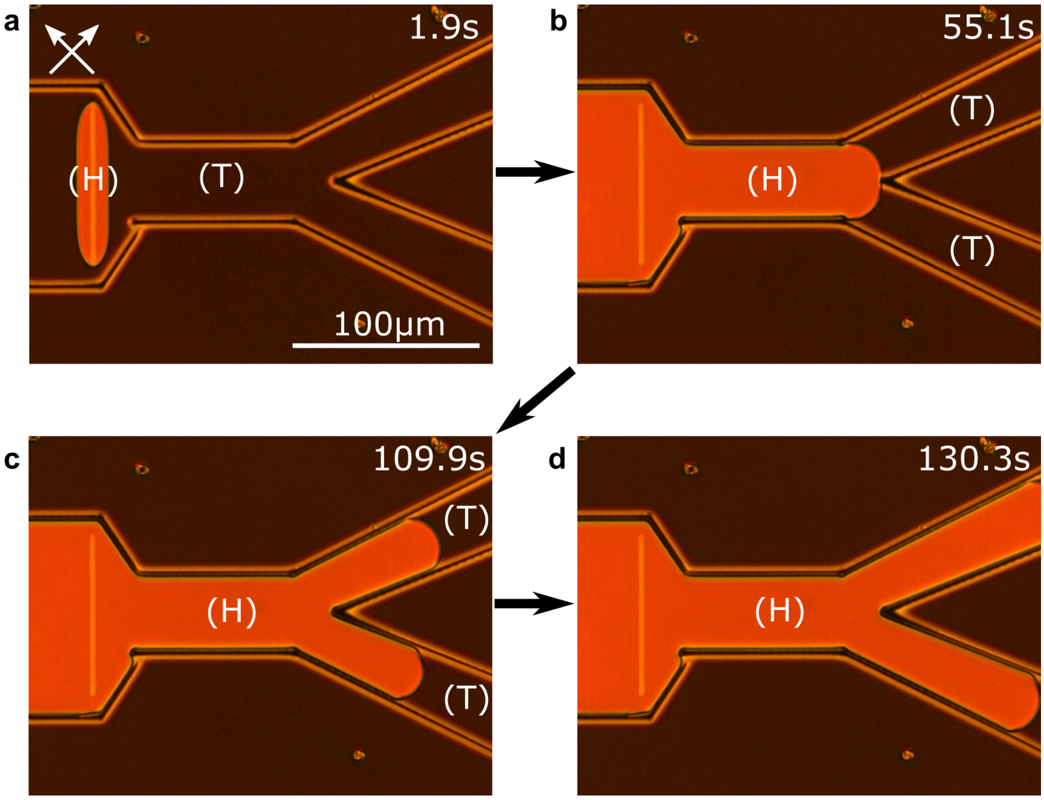

FIGURE 6.21: POM images of a microfluidics-inspired bifurcated defect channel. The walls defining the channel were laser-written in the V-state while, inside the channel, a wall was written in the H-state. When the voltage is switched off at t = 0, the H-state nucleates from this wall and a defect travels down the channels.

The device is first switched into the V-state with the application of a voltage above $V_c$. Then, at t = 0, the voltage is switched-off and the H-state nucleates from the polymer wall written in the H-state (Figure 6.21a) before propagating along the channel (Figure 6.21b). The H-state is unable to penetrate through the V-state polymer walls that define the channel boundary, as they have been stabilised in a topologically discontinuous state (structure design is shown in Figure 6.22). When the propagating disclination line separating the two states reaches the junction to the two separate channels, it is forced to move along these narrower channels (Figure 6.21c and d). In accordance with the result shown in Figure 6.19,

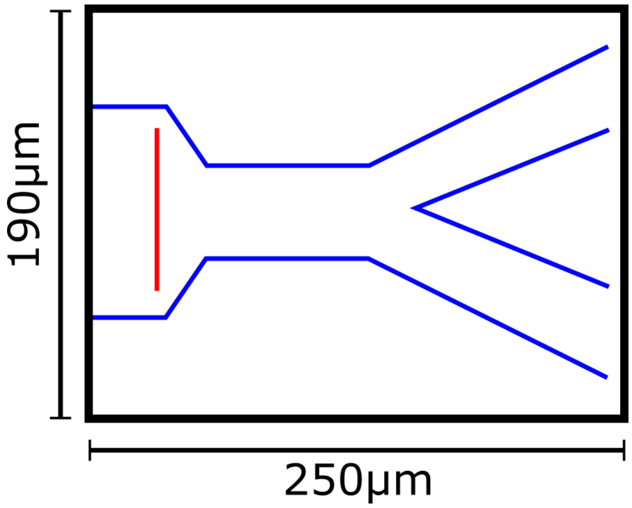

FIGURE 6.22: Schematic illustration of the laser written polymer wall design for the bifurcated channel structure in Figure 6.21. The red line represents an H-state polymer wall and the blue lines represent V-state polymer walls.

the speed of the defect depends on the confining channel width, and thus the defect travels much more slowly in the narrower channels.

## 6.4 Summary and Conclusions

Ordinarily, topologically discontinuous states nucleate randomly across a pi-cell device, forming approximately spherical domains that are bounded by disclination lines. In this chapter, we have seen that using 2PP-DLW to precisely polymerise different topologically discontinuous states within a pi-cell allows control of this nucleation process, leading to engineering of the dynamic behaviour and morphology of the defect lines. By carefully tailoring the shape of the polymer structures, it is possible to pre-configure/program the motion of the disclination lines that respond when the voltage applied to the device is altered. Thereby bringing order to the usually-random and disordered process of defect nucleation and growth in LC devices.

As seen in Chapter 5, polymerisation of a tunable LC resin creates polymer features with a controllable alignment, which function as 3D alignment surfaces for neighbouring LC molecules. Using this method, different molecular alignments and topologies can be polymerised in the same device with resolution on the microscale. This chapter has exploited this capability in order to stabilise topologically discontinuous states and disclination lines inside an electrically-addressable pi-cell device.

Laser-written defects were found to have a completely reversible tunability, and the velocity of the disclination lines has been shown to depend on the magnitude of the applied voltage and the orientation of the defect with respect to the device rubbing direction. The morphology of defect lines was found to depend on the device rubbing direction, with defects written perpendicular to the rubbing direction possessing zig-zag instabilities.

In addition to studying the fundamentals of the tunable defect behaviour via simple structures consisting of parallel topologically discontinuous polymer walls, the work presented in this chapter also explored several concepts looking towards future applications. To demonstrate the potential for tunable electro-optic devices that employ pi-cell defects, a disclination line control system was designed and implemented. A control loop was designed, which used image analysis techniques to determine the real-time position of a disclination line from a live-feed from a microscope camera. As a proof-of-concept, a disclination line was controlled and moved to desired positions over a 100 µm range with 1 µm accuracy.

It has been shown that colloidal microparticles can be picked-up and towed by these tunable defects. This is of interest because LC defects have shown promise as versatile scaffolds for the self-assembly of nano and microparticles. However, existing demonstrations of this concept have typically been static structures, with limited or no tunability. Introducing tunability into such systems may enable more advanced applications in tunable metamaterials and functional plasmonic nanomaterials.

The final section of this chapter has demonstrated several advanced concepts for controlling defects in pi-cells via rapid prototyping with 2PP-DLW. It was found that topology T2 can be preserved and stabilised indefinitely within square regions enclosed by polymer walls written in the V-state. This could be critical for future applications of pi-cells that exploit the fast-switching V-state and cannot tolerate the long warm-up time with which it is usually associated.

Lastly, the concept of LC defect microfluidics was introduced, where a growing state appears to 'flow' down a channel created by topologically discontinuous polymer walls. Several structures were shown, highlighting a high degree of control over the dynamic behaviour of the defects. The ability to confine topologically discontinuous states presents a way forward to develop complex electro-optic devices employing defects. This concept could be particularly powerful when combined with pixelated backplane electronics to produce next-generation spatial light modulators with topological pixels[137–139]. It may also find use in lab-on-chip applications that require particles to be sorted and moved in a controlled way within a liquid crystal matrix.

It is clear that LC defects are a rich area of study within soft matter photonics, with interest coming from both a fundamental and engineering perspective. This chapter has shown that a wealth of new behaviour and functionality can be unlocked with laser-based microfabrication inside LC devices, bringing unprecedented control over the processes governing of state nucleation and defect growth inside LC pi-cells.

# Chapter 7

# Switchable Diffractive Optical Elements

This chapter describes the fabrication of switchable diffractive optical elements (DOEs) including diffraction gratings and computer-generated holograms with 2PP-DLW in LC materials. The devices can be switched with the application of a uniform electric field and complex behaviour can be engineered by employing the 3D capabilities of the laser microfabrication technique. A finite-element model of a laser-written diffraction grating is developed in order to link together a continuum theory simulation of the LC director, and the propagation of light through the grating, and is successful in predicting diffractive behaviour. Laser-written bilayer switchable LC-DOEs are demonstrated, as well as switchable computer-generated holograms. These devices may find use in applications where greater flexibility than a fixed DOE is desirable, but a fully-programmable spatial light modulator is excessive.

*"Laser light flickered all over him as if he was a packet of biscuits at a supermarket check-out."*

**Douglas Adams**

## 7.1 Introduction and Background

As we have seen in Chapters 5 and 6, 2PP-DLW is a powerful technique for fabricating birefringent polymer structures inside liquid crystal devices on a micron scale. In Chapter 5, polymer pillars and walls with dimensions $\sim$1 µm were written into LC devices to produce optical patterns that could be viewed with a polarising optical microscope. By applying the same voltage magnitude to the device as that which was used during the fabrication of the polymer structure, the structure became invisible. In this chapter, this switchable-invisibility concept is extended to create diffractive optical elements (DOEs) that can be turned on and off with the application of a voltage.

The strength of this approach lies in the ability of 2PP-DLW to fabricate 3D polymer architectures, thereby enabling next-generation DOE designs with advanced functionality. Furthermore it allows fabrication of polymer structures with an arbitrary spatial distribution, such that complex diffraction patterns can be produced from phase holograms fabricated into an LC device. These switchable devices have the potential to sit in-between fully programmable but expensive spatial light modulators and cheap but inflexible static DOEs.

### 7.1.1 Diffractive Optical Elements (DOEs)

Diffractive optical elements are optical components that manipulate the spatial distribution of light intensity when illuminated with coherent light. They range from diffraction gratings that split a beam into a number of diffracted beams to complex computer-generated holograms that diffract light into a recognisable image[153] (see Section 7.1.2). Applications of DOEs span across a vast number of industries and include holographic displays[154, 155], augmented reality/virtual reality[156, 157], spectroscopy[158, 159], aberration correction[160, 161], beam steering[162], beam shaping[163, 164] and 3D depth sensing[165–167].

Diffraction gratings are periodic arrays of structures that produce a periodic modulation in the amplitude or phase of a wavefront incident on the grating. The result of this is that coherent light incident on a diffraction grating will be split into one or more diffracted beams travelling in different directions. An amplitude grating consists of an array of apertures, and the classic Young's double slit can be considered an example of a very simple amplitude grating. A major downside of amplitude gratings is low optical efficiency because, by definition, a large fraction of the light is absorbed or reflected by the grating and not transmitted. In contrast, phase gratings produce a modulation in the phase of light incident on the grating, due to a periodic modulation in the refractive index and can theoretically diffract light with 100% efficiency.

DOEs are generally fabricated by diamond tool machining[168] or conventional lithographic methods such a photolithography, e-beam lithography and holographic interference lithography[169]. While these methods have proven successful for fabricating DOEs, there are significant drawbacks that limit their use in advanced DOE designs. In the case of diamond tool machining, designs are limited to circularly symmetric elements and the smallest possible feature sizes are several times larger than the diamond tool tip[169]. Lithographic methods are more flexible but generally restrict device design to planar structures and require complex multi-step cleanroom fabrication procedures. In contrast, in this chapter, we will see how 2PP-DLW can be used to fabricate novel 3-dimensional switchable DOEs, enabling novel device designs with enhanced switching functionality.

Due to the combination of their high birefringence and sensitivity to external fields, LCs have found use as switchable optical materials for a variety of diffractive optical elements, in particular switchable phase gratings and phase holograms (sometimes called kinoforms). In the following discussion LC-DOE (Liquid Crystal Diffractive Optical Element) will be used to describe any DOE that contains liquid crystal.

The earliest implementations of LC-DOEs have used a variety of conventional lithographic methods to pattern surface relief structures into standard negative photoresists before they were transformed into an active device by adding a layer of index-matched LC[77, 78, 170–173]. However, the fabrication of useful devices using this principle is limited by the complex multi-step fabrication processes required. Furthermore, some authors report challenges in controlling the alignment of the LC on the fabricated polymer structures, with unwanted defects inhibiting the device performance[170].

Arguably the most successful LC-DOE technology is based on a composite material known as holographic polymer dispersed liquid crystal (H-PDLC) which is formed by exposing an LC device containing a mixture of LC and photosensitive isotropic monomer to an interference pattern[174, 175]. The holographic interference pattern can be oriented transverse to the LC cell, such that the photopolymerization process forms a series of stratified layers across the thickness of the device with the grating vector perpendicular to the substrates. Alternatively, the interference pattern can be oriented such that a series of polymer "slices" forms across the device, with the grating vector parallel to the substrates. This causes the LC to diffuse into the layers in between the polymer-rich layers, creating an alternating profile of LC-rich and polymer-rich layers[176]. With appropriate index-matching between the polymer and the LC, H-PDLC devices can function as electrically-switchable Bragg gratings with a very high diffraction efficiency and have therefore found use in applications where Bragg spectral and spatial selectivity is desirable[177].

However, a significant disadvantage of H-PDLC is that, compared to bulk LCs, large electric fields (15 - 20 V/µm) are required to switch off the diffraction, due to the confinement of the LC into micro- or nano-meter sized droplets[175, 176]. In response to this, a variation of H-PDLC called POLICRYPS (POlymer LIquid CRYstal Polymer Slices) was developed by Caputo et al. that switches with external fields of just a few V/µm and provides diffraction efficiencies of up to 98%[178, 179]. Similar to H-PDLC, POLICRYPS gratings are fabricated by holographic interference lithography but are formed at a temperature above the clearing temperature, which dramatically improves the morphology of the gratings as compared to H-PDLC. The uniform morphology and lack of imhomegeneities in the structure of POLICRYPS gratings reduces losses due to scattering, which can be considerable in H-PDLC gratings[176, 180]. However, owing to the reduced confinement of the LC regions in POLICRYPS gratings, they typically have slower switching speeds than equivalent H-PDLC gratings[176].

Although the interference lithography fabrication process for H-PDLC/POLICRYPS is flexible and fast, it is limited to producing gratings that are on (i.e. produce a diffraction pattern) in the absence of an applied field. For some optical applications, including AR/VR, it is desirable to use gratings that do not consume power in the off-state and are therefore "hidden" and operate in "reverse-mode" (non-diffractive in the off state)[181]. H-PDLC/POLICRYPS technologies are unable to provide a solution for such applications.

Early attempts at reverse-mode LC-DOEs have been fabricated using interference of UV lasers to create a modulated intensity pattern that is encoded directly into a device containing a UV-sensitive polymerisable LC/reactive mesogen mixture[181, 182]. Applying a voltage to the device after fabrication causes the LC in the unpolymerised channels to reorient, producing a refractive index mismatch between the polymer structures and the LC. As the cell can be switched between diffractive and non-diffractive states, it can be considered an electrically-switchable PSLC (Polymer Stabilised Liquid Crystal) diffraction grating operating in reverse-mode. However, employing such holographic interference fabrication methods limits grating designs to simple periodic structures. Within these constraints, the most complex LC-DOEs created in this way have been 2D hexatic lattices of micropillars which produce hexatic diffraction patterns[182].

In this chapter, 2PP-DLW is used for the first time to engineer electrically-switchable 3D LC-DOEs with the ability to switch between two distinct diffractive modes. Due to the freedom over the design of the phase patterns comprising these DOEs, and the additional degree-of-freedom offered by voltage-dependent 3D fabrication, enabling both reverse-mode and conventional mode operation; they have considerable potential to be used in next-generation diffractive optics and rival the reigning switchable LC-DOE technology H-PDLC.

### Raman-Nath and Bragg Diffraction Regimes

In general there are two types of behaviour exhibited by diffraction gratings which leads to their classification into operating into one of two regimes: (i) the Raman-Nath regime and (ii) the Bragg regime. Gratings are classified according to a dimensionless parameter, Q,

$$Q = \frac{2\pi\lambda d}{n\Lambda^2} \tag{7.1}$$

where $d$ is the grating thickness, $n$ is the average refractive index of the grating, $\Lambda$ is the grating period and $\lambda$ is the incident wavelength[183, 184].

When $Q < 1$, a grating is considered "thin" and will operate in the Raman-Nath regime and will exhibit many orders of diffraction. Whereas, when $Q > 10$, a grating is said to be "thick" or a volume grating and will only exhibit diffraction when the Bragg condition is met, making them highly sensitive to the angle and wavelength of incident light. Gratings with $1 < Q < 10$ are said to operate in an intermediate regime with properties that are a mixture of the two extremes.

### 7.1.2 Holography

Holography (from the Greek 'holos'; 'whole') is the study of DOEs known as holograms that diffract light to form complex images in a diffraction pattern (or "replay field") and was first invented by Dennis Gabor in 1947 in his search for a method to improve the resolution of electron microscopes[185]. However, his discovery did not attract a great deal of attention from mainstream scientists at the time[186], and it was not until the invention of the laser in the 1960s that holography became a discipline in its own right. Holography is now a vast field, spanning across art, science and engineering with applications in information processing, security & authentication, data storage, 3D displays, sensors and microscopy[187].

The basic holographic principle as described by Gabor involves recording the light field scattered off an object onto a photographic recording medium. To accomplish this, a beam of coherent light is split into an 'object beam' and a 'reference beam'. The object beam is expanded and goes on to illuminate the object, scattering light onto a photographic plate, while the reference beam is expanded directly onto the plate. The two beams form an interference pattern on the plate that encodes the information about the light field produced by the object. When the hologram is illuminated by a reference beam identical to that used to record the hologram, a reconstruction of the light field is produced. Thus an observer will see an exact replica of the object scene, complete with parallax and occlusion[187].

Computer-generated holograms (CGHs) were first demonstrated by Brown and Lohmann in 1966[188] and used a radically different approach to the generation of holograms compared to Gabor's traditional holographic recording method. They employed a fully computer-generated approach to hologram design and used a numerical algorithm to calculate the hologram from an image of the target, removing the need for a physical target object[189].

In 1972, Gerchberg & Saxton invented a fast algorithm for generation of a phase-only CGH from a desired target image[190] which is now known as the Gerchberg-Saxton algorithm or the Iterative Fourier Transform Algorithm (IFTA). It is considered the easiest CGH optimisation algorithm to implement and is the fastest to converge towards a solution[184]. The iterative algorithm takes a target image as an input and aims to minimise the mean-squared error between the fourier transform of a hologram and the target image. The initial "guess" of the solution is simply a hologram of random phase. This hologram is fourier transformed and the phase of this result is extracted and multiplied by the amplitude of the target image. The inverse fourier transform is then taken and the phase of the result extracted to obtain an updated guess of the hologram solution. By running this process iteratively, the hologram converges to a solution with a low mean-squared error.

Femtosecond laser micromachining is well-suited to fabricating

CGHs due to the flexibility of the fabrication technique and the ability to write in a maskless fashion in 3-dimensions. Zhao et al. first described the fabrication of an amplitude-mode CGH manufactured in this way, using a regeneratively amplified femtosecond laser to ablate holes in a 200 nm thick layer of aluminium[191]. Subsequently, several groups reported the fabrication of amplitude-CGHs buried inside silica glass using femtosecond laser-induced microexplosions[192, 193]. Reflection mode CGHs have also been realised, with a similar laser ablation technique applied to the surface of a silicon wafer[194]. Laser-induced micro-ablation of mass-produced polymer materials including polycarbonate has also been reported for the manufacture of CGHs, fresnel zone plates and gratings[195]. More sophisticated results have been obtained by using techniques originally developed for laser writing of waveguides in borosilicate glass to fabricate phase-only CGHs[196–198], where such methods result in a slight change in the refractive index but do not cause void formation, as in microexplosion/ablation laser writing.

A significant limitation of these early efforts towards laser-writing of CGHs is that the structures fabricated were fixed optical elements, with no degree of switchability. In contrast, in this chapter the first use of 2PP-DLW in fabricating switchable binary CGHs in polymerisable LC devices is described. By exploiting the 3D fabrication capabilities of 2PP-DLW, it may be possible to fabricate multi-layer multiplexed CGHs in a single device that can be switched on and off with the application of a uniform electric field.

## 7.2 Methods

### 7.2.1 Fabrication Procedure

A number of methods were developed to fabricate the DOEs described in this chapter. These new methods were necessary due to the complexities of fabricating in 3D and over a large area of a device. This section describes (i) the basic fabrication procedure for simple diffraction gratings, (ii) the special methods developed for 3D fabrication, and (iii) the factors that need to be considered for fabrication over a large device area.

#### Fabrication of Diffraction Gratings

The simplest example of fabrication of a diffraction grating with 2PP-DLW is shown in Figure 7.1. The LC device is mounted on top of the translation stage stack in the 2PP-DLW system described in Section 4.2 and moved so that the focus of the fabrication laser traces a series of parallel polymer walls in the device. As the polymer walls appear $\sim$1 μm wide (as studied by polarised optical microscopy), the walls must be spaced at least 2 μm apart.

The mixture was a polymerisable nematic LC mixture containing E7 (70.7 wt%), reactive mesogen RM257 (Merck) (28.5 wt%) and photoinitiator Irgacure 819 (Merck) (0.8 wt%). This mixture was prepared following the procedure described in Section 4.1.1 before it was filled into anti-parallel rubbed LC cells manufactured by Instec Inc. These cells had planar ITO electrodes, allowing a uniform electric field to be applied to the LC mixture during and after fabrication. Cells with thicknesses of 5 μm, 9 μm and 20 μm were used in this study.

Although Figure 7.1 shows fabrication at zero volts (i.e. without an applied electric field), it is possible to apply a voltage during fabrication

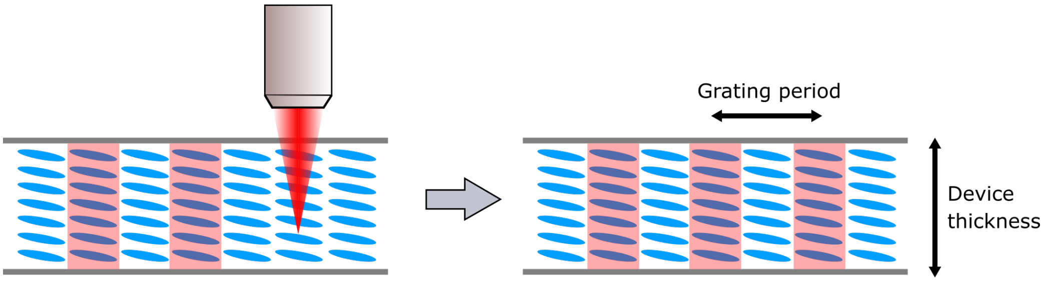

FIGURE 7.1: Schematic cross-sectional view of the fabrication process of a 1D diffraction grating inside a liquid crystal device. 2PP-DLW is used to write a series of parallel polymer walls inside the device. The grating period is of the order of the device thickness. Regions where a polymer network has formed are indicated by pink shaded regions.

and polymerise structures that preserve the voltage-dependent alignment of the LC at the moment of exposure, as seen in Chapters 5 and 6.

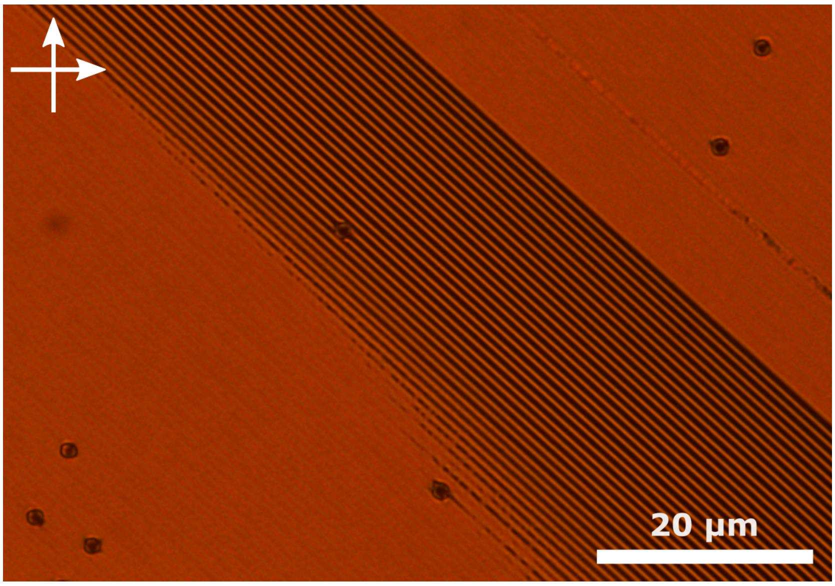

FIGURE 7.2: POM image of a grating with a 2.5 µm period where the fabrication laser power was changed during the fabrication. A voltage of 10 V has been applied to the device to observe the switching behaviour of the uncured regions. In the lower left and upper right of the image, the writing laser power was too high, resulting in polymerisation in between the polymer walls that inhibits the switching. In the centre of the image, the power was at an appropriate level to form polymer walls without curing surrounding regions.

For structures with a small spacing between the adjacent polymer features, the fabrication laser power is a critical experimental parameter. If the power is too high, the excess energy delivered to the sample causes curing of the regions in between the polymer walls. This restricts the uncured areas of the device from properly switching, preventing the generation of the refractive index contrast that is required for diffraction.

An example of a structure fabricated when the power was too high is shown in Figure 7.2. To address this issue, the laser power was carefully adjusted such that it was just above the polymerisation threshold, delivering the minimum necessary energy to the sample. This threshold power was found empirically to be 41 mW at a writing speed of 100 µm/s for the mixture containing E7, 30 wt% RM257 and Irgacure 819.

### Fabrication of 3D Structures

In this chapter, the 3D fabrication capabilities of 2PP-DLW are exploited to fabricate switchable multilayer DOEs. These consist of two separate DOEs that are fabricated in the same region of the device but at different heights. This has to be performed in a thicker device, so that the DOEs are spatially separated in the $z$-direction.

Fabricating 3D structures required that the fabrication method be adapted so that polymer structures could be reliably tethered to a desired substrate. To do this, a 'cell thickness scan' process was developed whereby a series of adjacent polymer lines were written in the device, with a lateral spacing of 5 µm and a known height-step between each wall. A schematic of the process is illustrated in Figure 7.3 where the staircase-like structure of the polymer walls can be seen.

By observing this laser writing process in-situ with the in-built microscope, information can be obtained about the position of the laser focus. An example of a microscope image of the cell thickness scan is shown in Figure 7.4. The polymer walls in the very centre of the cell are observed to float in the LC mixture as they are not tethered to a substrate. By initiating the cell thickness scan with the laser focus located within the bottom substrate, it is possible to establish the position of the bottom substrate by observing where the polymer structures begin to form.

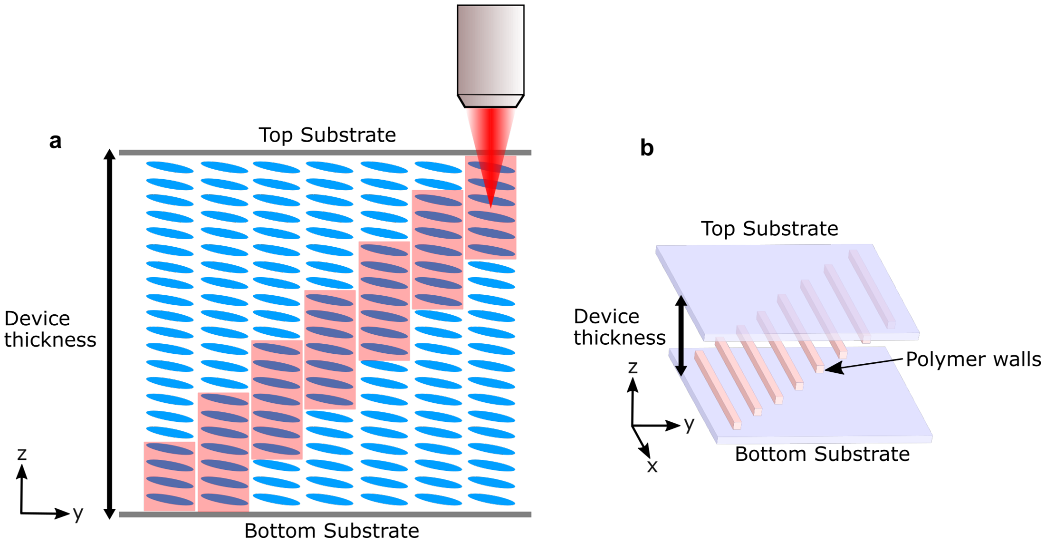

FIGURE 7.3: Schematic showing the process of performing a cell thickness scan across the thickness of an LC device. This procedure provides information about the height of the laser focus and allows 3D fabrication to be performed in an accurate manner. In this schematic, the polymer structures are not to scale and, in practice, there are gaps of 5 µm in the $y$-direction, between each wall.

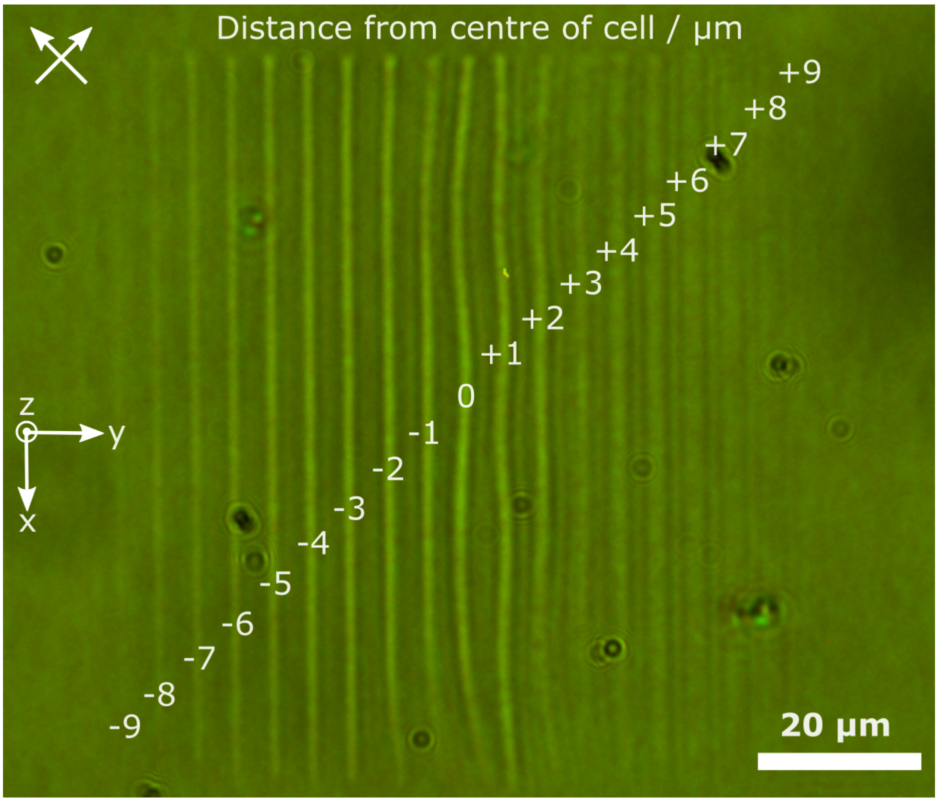

FIGURE 7.4: POM image of a cell thickness scan taken with the CCD mounted in the DLW system. The lines are fabricated with a separation of 5 µm in the $y$-direction and 1 µm in the $z$-direction. The walls that were fabricated in the centre of the cell are untethered and therefore have drifted from the position in which they were originally fabricated. Each line is labelled with its distance from the centre of the cell in µm and the labels are staggered for readability.

For 3D fabrication, it is important to consider the focal splitting phenomenon resulting from focussing a polarised laser beam through a birefringent material at high NA[199, 200]. As thicker LC devices are required for 3D fabrication, this effect becomes very pronounced because the laser travels a longer distance through the birefringent LC, resulting in a greater degree of splitting. The phenomenon is observed because, in general, the extraordinary refractive index seen by light passing through a birefringent material depends on the propagation direction. In the cone of light produced by tight focussing at high NA, the individual rays therefore have different optical path lengths, stretching the focus in the axial direction and producing spherical aberration.

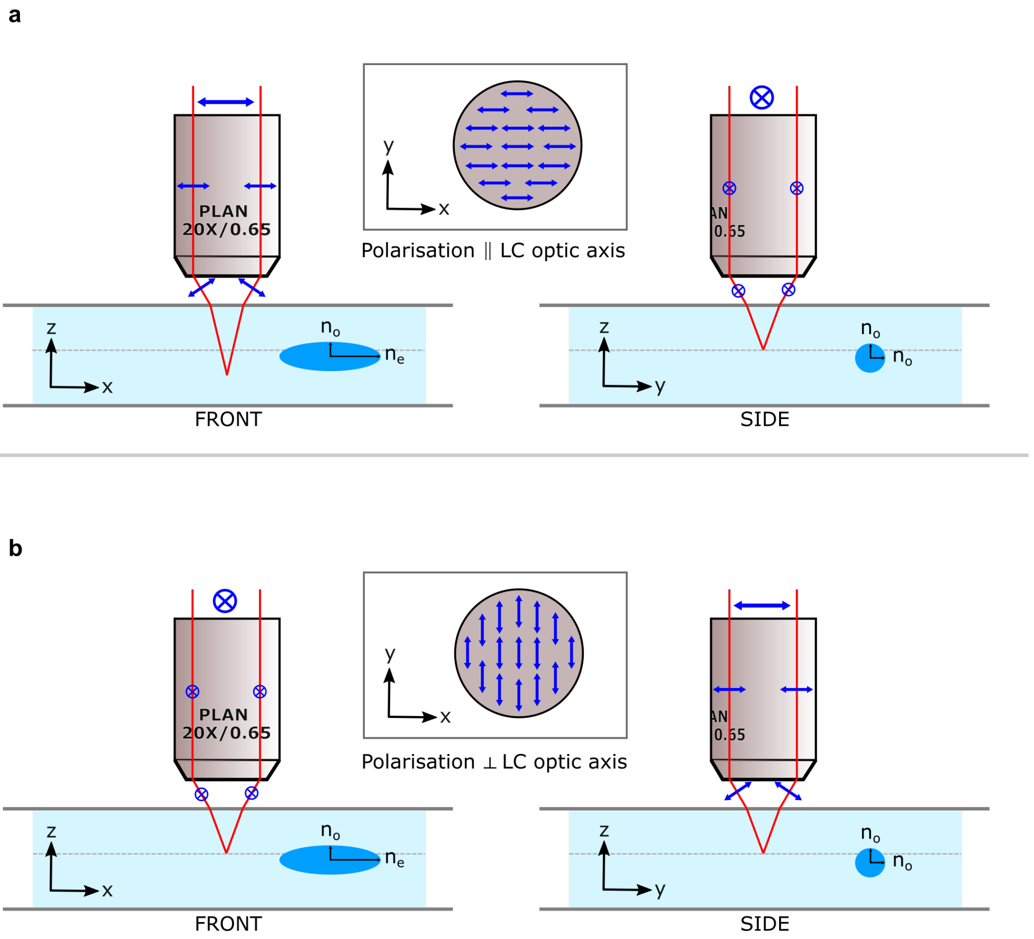

FIGURE 7.5: Spherical aberration induced by high NA focussing in an LC material. Blue arrows indicate the electric field vectors and red lines are showing path of light rays. (a) Writing laser polarisation parallel to the optic axis, which results in polarisation-related spherical aberration. (b) Writing laser polarisation perpendicular to the optic axis, with no polarisation-related spherical aberration. The optic axis of the LC is oriented along the $x$-axis in both cases and a front and side view for each geometry is shown.

This phenomenon is illustrated in Figure 7.5a, where the polarisation is parallel to the optic axis of the LC. In this experimental geometry, the focal depth of a light ray depends on its position in the cone of focussed light. Two viewing angles of the geometry are illustrated to highlight this and each show the extremes of this source of spherical aberration. Note that, in practice, the focus will be spread between these two extreme positions, with other focal depths resulting from the rays originating from other parts of the cone of light which enter the material at different angles. However, in one particular experimental geometry, where the polarisation is perpendicular to the optic axis of the LC (Figure 7.5b), then irrespective of the angle the light ray enters the material, it will always see the ordinary refractive index, $n_o$, removing this source of spherical aberration.

In all cases except when the polarisation is perpendicular to the optic axis and in addition to the spherical aberration, the polarisation eigenmode corresponding to the extraordinary mode possesses an additional phase aberration due to the dependence on the ray propagation direction. The aberration is complex but can be shown to have a significant difference in defocus from the ordinary mode (which does not depend on the propagation direction). This can lead to split foci, resulting in two distinct voxels spatially separated along the axial direction, reducing the resolution of the technique and prohibiting precise fabrication in a thin layer[201].

In general there are two approaches to compensating the birefringence-induced focal splitting and spherical aberration effect: (i) The fabrication laser must be polarised radially or azimuthally or (ii) the laser must be polarised linearly in an orientation perpendicular to the optic axis of the birefringent material (the case illustrated in Figure 7.5b). In this instance, the second option was chosen, as this could be straightforwardly implemented with a half waveplate in the optical setup. In this configuration, all rays in the tightly-focussed cone see the ordinary refractive index, eliminating the focal splitting effect. Producing a radially or azimuthally polarised beam would require q-plates, a spatial light modulator or another complex phase-control element. This was not investigated further, as the simpler approach using a half waveplate achieved the desired result.

### Fabrication of Structures Over a Large Area

In this chapter, the fabrication and characterisation of large diffraction elements called computer generated holograms (CGHs) are described. These structures consist of many thousands of polymer walls written over a large area (up to 2 × 2 mm). It was found that this type of process presented some unique problems which had to be overcome for successful fabrication. Namely, (i) limited controller memory, (ii) sample flatness and (iii) fabrication duration.

The first issue was related to the limited memory of the controller for the high-resolution translation stages. Due to the complexity of the structures, the AeroBasic fabrication scripts were up to 258,815 lines long, with a file size of up to 10,741 KB. This value is in excess of the memory of the controller, which is 2048 KB. Moreover, for some of the results described in this chapter, an older controller with a memory of just 32 KB was used, making the problem even more severe. To solve this issue, a LabVIEW program was written to process the large fabrication scripts, splitting each script into multiple sub-scripts smaller than the memory of the controller. The program sequentially passed each sub-script to the stage controller, appending the scripts with commands to open and close the laser shutter. These shutter commands were essential, as there is a delay of a few seconds while the stage controller reads and compiles the sub-script, during which time the laser would be fixed in one position.

The second issue emerges from the difficulty in mounting the sample to be perfectly flat (i.e. normal to the axis of the laser beam). For polymer structures written over a small area, this is not a significant issue as the deviation in the z-direction resulting from a slope in the sample is negligible over short distances. However, for large structures, such as the 2 × 2 mm CGHs described later in this chapter, even a very slight slope could lead to a significant deviation in the position of the focus of the laser as the fabrication proceeds. As can be seen in Figure 7.6, this resulted in larger structures "fading out" as the focus moved into the glass substrates as a fabrication routine progressed.

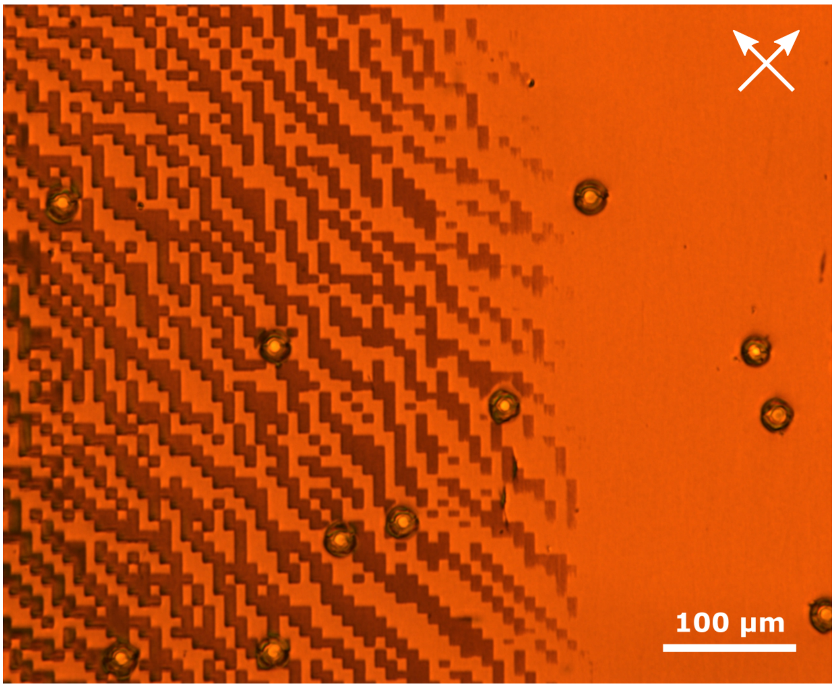

FIGURE 7.6: POM image of a large polymer structure "fading out" during a fabrication routine due to a large sample tilt. The fabrication started on the left hand side of the image and proceeded to the right. The structures become progressively more diffuse as the focus of the fabrication laser moves into the glass substrate, before fabrication ceases completely as seen on the right hand side. The white arrows indicate the orientation of the crossed polarisers and the scale bar is 100 µm.

A method to calibrate the slope in a sample was developed to compensate for this effect. Using the cell thickness scans described above, an estimate could be obtained for the slope by writing at three points just outside of the area in a cell designated for the fabrication of a large structure. As three points define a plane, these values were input to a MATLAB script that generates the AeroBasic fabrication script. The generation script was modified to compensate for the slope so that each linear move-command would also have a component in the z-direction.

The third problem was that the fabrication of such large structures initially took several days. Due to the narrowness of the polymer walls (∼1 µm), the size of the structures, and the high fill-factor of 50% (proportion of the fabrication area that is polymerised), the fabrication time will inevitably be much longer than smaller structures with a lower fill-factor. However, significant improvements to the writing speed were made by adopting a different approach to the laser writing process.

For much of the laser writing described in this thesis, the AeroBasic fabrication scripts incorporate commands that control an electronic optical shutter which modulates the exposure of the sample to the laser, as described in Section 4.2. For the fabrication of large-area structures, an alternative approach was developed that modulates the speed of the translation stages rather than the laser shutter. In this way, the laser could be continuously on and polymerisation was controlled by the speed of the stages. For regions where polymerisation was not desired, the stages were moved at 10 mm/s, as opposed to the usual speed for fabrication of 100 µm/s. Increasing the speed of the stages to this level effectively lowers the dose received by the polymerisable resin to be below the threshold dose for polymerisation. The MATLAB code that generated the AeroBasic fabrication scripts for this speed-modulation method was written by Hassan Daginawalla, a final-year undergraduate student in the Soft Matter Photonics group 2019-20.

The speed-modulation method reduced the fabrication time for a 2 × 2 mm CGH from ∼107 hours to ∼6 hours (a reduction of 94.4%), compared to previous laser writing methods. This was because in earlier methods, pauses had to be incorporated into the AeroBasic fabrication scripts in order to allow time for the mechanical shutter to open and close. Further reductions in fabrication time were attributed to the faster scanning speed over unpolymerised regions.

### 7.2.2 Characterisation Procedure

An optical setup was built to characterise the DOEs described in this chapter. A schematic optical layout of the setup can be seen in Figure 7.7 and an annotated photograph of the setup is shown in Figure 7.8.

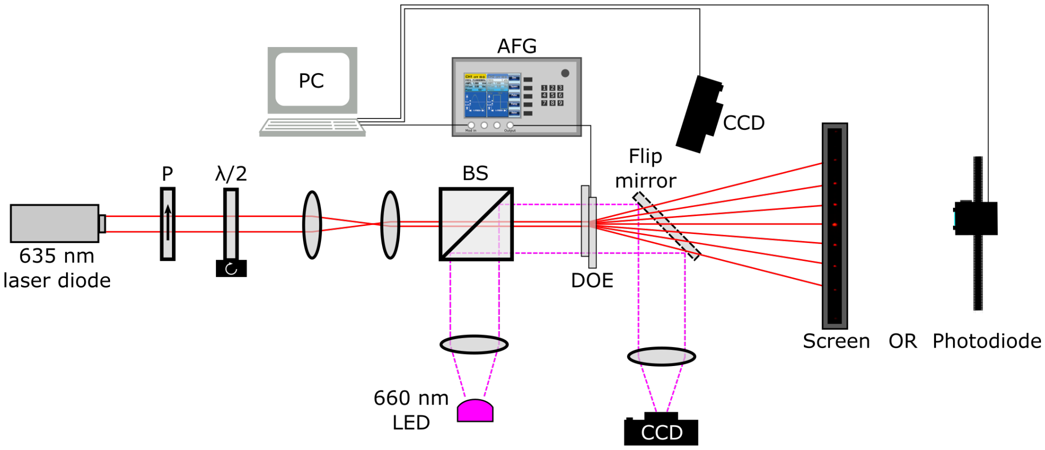

FIGURE 7.7: Schematic of the optical setup used for characterising diffractive optical elements. The optical path of the 635 nm laser diode is indicated by red lines and the 660 nm LED illumination path is indicated with purple dashed lines.

The coherent light source was a continuous wave 635 nm laser diode (Thorlabs PL202) which had a beam diameter of Ø3 mm and an optical power of 1 mW. The output power was reduced to 100 µW with a variable ND filter to provide a suitable power for the CCD and photodiode.

It was important to be able to change the input polarisation to the DOE and this was accomplished with a $\lambda/2$ waveplate. To selectively and

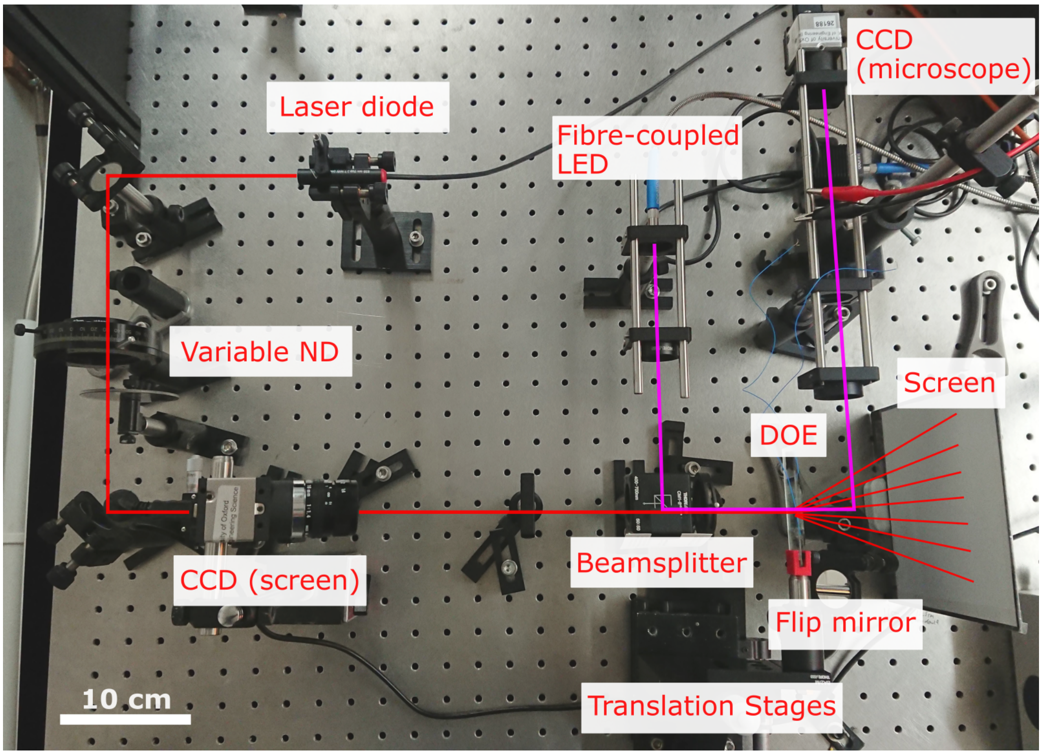

FIGURE 7.8: Photograph of the DOE characterisation setup. The path of the 635 nm laser diode is indicated by a solid red line and the path of the 660 nm fibre-coupled LED is indicated with a solid purple line. The CCD focussed on the white screen is mounted out-of-plane, above the path of the 635 nm characterisation beam.

precisely illuminate a particular DOE within a device, the beam had to be reduced from its Ø3 mm nominal diameter and so the beam was shrunk by two lenses in a keplerian telescope configuration. For some diffractive structures written over a very small area, the beam had to be focussed with a 300 mm lens in order to produce a beam size small enough to fit entirely within the area of a structure.

The setup had to flexible enough to accommodate LC devices where a number of different DOEs were fabricated across the active device area. To achieve this, precision targeting of the laser was enabled by mounting the sample on a stack of precise manual translation stages (Thorlabs PT1) with a travel range of 25 mm in X and Y.

To aid with locating and identifying DOEs in the device, a simple optical microscope was built, with illumination provided by a fibre-coupled 660 nm LED. This wavelength was chosen to remove any

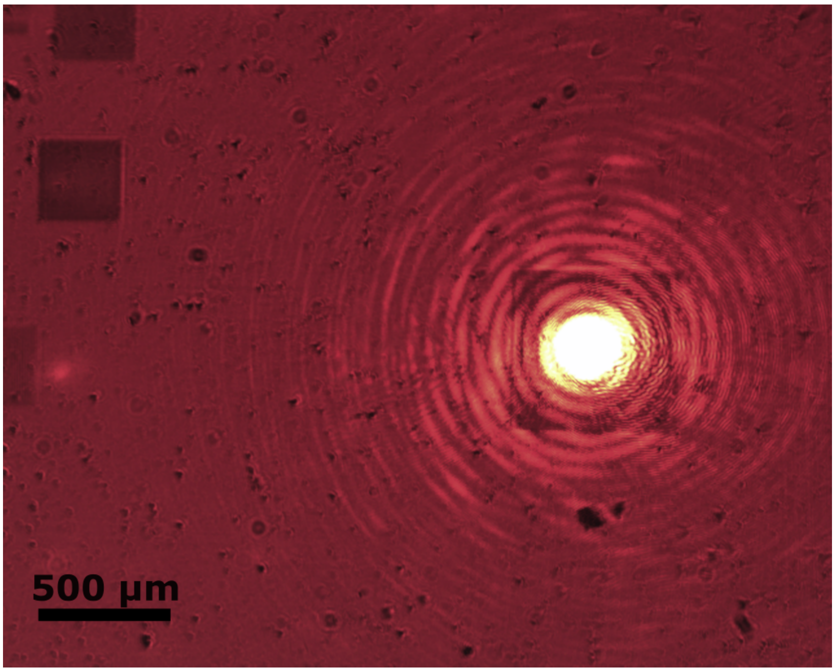

FIGURE 7.9: Image of a device containing a number of diffraction gratings, as seen by the microscope CCD in the characterisation setup. The 635 nm laser is passing through a large diffraction grating with dimensions 600 × 600 µm on the right side of the image. Other diffraction gratings present in the device can be seen on the left side of the image.

potential for further polymerisation occurring during the characterisation process. A full-colour CCD camera (Thorlabs DCC1240C) was used to provide a magnified image of the device so that it could be moved to the correct position for the laser to pass through a particular diffractive structure. An example of an image of a device taken with this CCD can be seen in Figure 7.9

The diffraction pattern could be recorded in one of two possible ways: (i) taking an image of the white screen using a full-colour CCD (Thorlabs DCU224C) with a camera lens attached or (ii) recording the diffraction intensity directly with a photodiode (Thorlabs PDA36A-EC). The CCD method had the advantage of quickly obtaining an image of the entire diffraction pattern, however, it required further image processing to establish quantitative values for diffraction intensity. An example of a recorded diffraction pattern is shown in Figure 7.10. In both cases, stray light was reduced by switching off the lights in the laboratory and blocking any other light sources. For the photodiode measurements, a 10 cm lens tube was mounted to the front of the photodiode to further reduce any unwanted stray light.

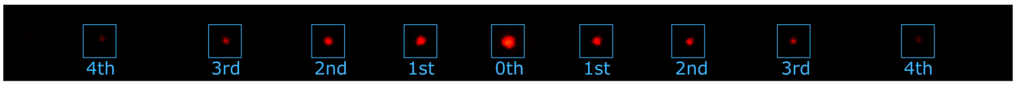

FIGURE 7.10: Example of a diffraction pattern recorded by the CCD focussed on the screen in the characterisation setup. The diffraction orders have been labelled.

An image processing method was developed to convert CCD images of diffraction patterns into intensity values. MATLAB was chosen to automate the process due to its powerful Image Processing Toolbox and data visualisation capabilities. Figure 7.11 illustrates the process in the form of a flowchart.

As shown on the left side of Figure 7.11, the CCD records large 1280 × 1024 pixel images of the screen. The diffraction pattern only occupies a small region of this image and so the first step is to crop the image using the MATLAB Image Processing Toolbox function *imcrop*. To compensate for unwanted rotation of the diffraction pattern with respect to the orientation of the camera, the image is also rotated so that the diffracted orders sit along a horizontal line using *imrotate*. Then the image is converted from full RGB colour to a greyscale image using *rgb2gray* before a threshold is applied (pixel value > 10) to form a thresholded mask. The function *regionprops* is used to obtain centroids of the spots and these coordinates are used to centre a series of 30 × 30 pixel crops on the greyscale image. To obtain the intensity of each diffracted order, a sum is then performed over all the pixels in each of these cropped images. This process can be repeated for a series of images of the diffraction pattern at different voltages to obtain the diffraction intensity as a function of voltage.

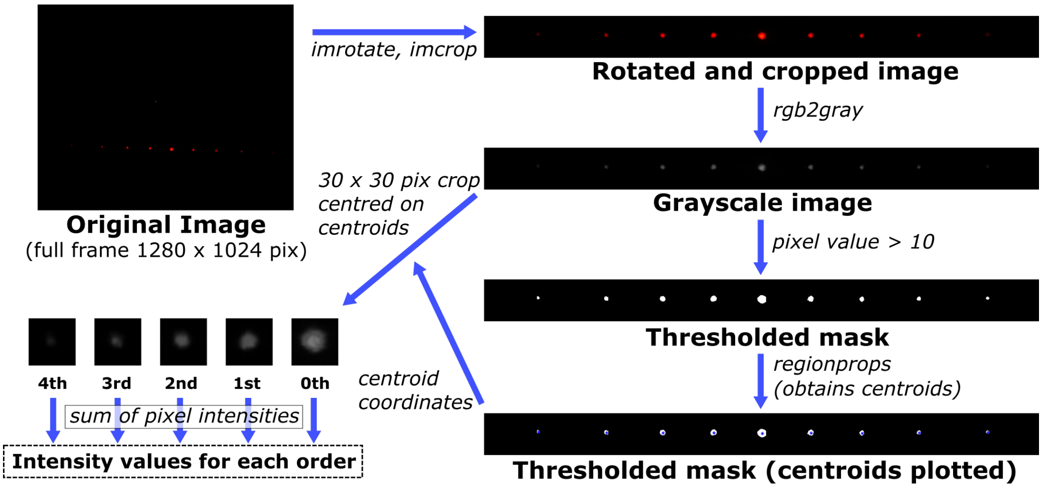

FIGURE 7.11: A flowchart showing the steps of the image processing method to obtain diffraction intensity from CCD images of diffraction patterns. The original image is cropped and rotated using the functions *imrotate* and *imcrop* before being converted to a greyscale image with *rgb2gray*. This is then made into a mask by applying a threshold of pixel value > 10. This thresholded mask is processed by *regionprops*, a MATLAB function to obtain centroids. The coordinates of the centroids are then used to centre a series of 30 × 30 pixel crops on the greyscale image. The pixel values are then summed for each image to obtain a relative measure of intensity for each diffracted order.

As an alternative to the CCD method for obtaining quantitative diffraction data, another method was developed where the intensity of the diffracted orders were recorded by using a photodiode. This process involved aligning the photodiode with the beam of a diffracted order and running a sweep of the voltage applied to the device, while recording the output of the photodiode. A comparison of data obtained using the each technique can be seen in the following section.

MATLAB scripts were written to run voltage sweeps and automate the experimental process of obtaining diffraction data from DOEs. An arbitrary function generator (Tektronix AFG 3021) was controlled to provide the AC driving voltage to the DOE, while data was recorded by either the CCD focussed on the screen or the photodiode. For the latter method, the voltage sweep had to be repeated for each diffracted order, realigning the photodiode between each measurement. The MATLAB script interfaced with the CCD camera via a .NET library, whereas the photodiode was connected to a digital oscilloscope (Tektronix

TDS2024C) which was read via SCPI commands to return the voltage signal from the photodiode.

## 7.3 Results and Discussion

### 7.3.1 1D Diffraction Gratings

This work began by testing the simplest possible diffractive optical element design, a 1D diffraction grating. Starting with a simple structure provides a useful foundational platform on which to test the method and evaluate characterisation methods before exploring more complex novel DOE designs.

Preparation of the mixture and device-filling followed the method described in Section 7.2.1, using a cell with a thickness of 5 µm. Following this, a 1D switchable diffraction grating was fabricated via 2PP-DLW, using the fabrication system described in Section 4.2 with a writing speed of 100 µm/s and a power of 41 mW. Polymer walls were written at 0 V so that the device would be in the off-state when no voltage was applied. The grating was written over an area of 1000 × 1000 µm and walls were spaced 5 µm apart.

Figure 7.12 illustrates the idealised principle of operation behind the switchable diffraction grating. With no voltage applied, there is expected to be no difference in the LC alignment between polymerised and unpolymerised regions. In this state, the device behaves as a uniform birefringent layer and no diffraction occurs. When a voltage is applied with a magnitude above the Fréedericksz threshold, the unpolymerised regions switch (Figure 7.12b), with the director tending towards vertical as the voltage is increased. In this switched state, light that is polarised parallel to the rubbing direction will see a modulation in the effective

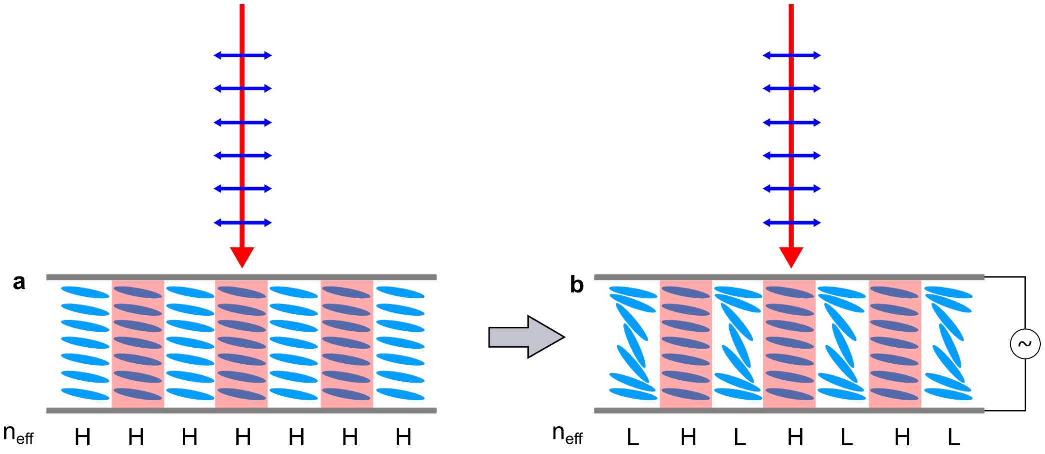

FIGURE 7.12: Schematic representation of a 1D diffraction grating switching under an applied voltage. (a) The diffraction grating in the off-state with no applied voltage. (b) The device under an applied voltage large enough to cause the unpolymerised regions to switch. The red arrow indicate the direction of light propagation through the grating, and the blue double-headed arrows show the electric field vectors. High values of $n_{eff}$ are indicated with an "H" and low values indicated with an "L". In this schematic the laser is polarised parallel to the rubbing direction and so experiences the largest possible modulation in the refractive index.

refractive index, with higher values of $n_{eff}$ in the polymerised regions and lower values of $n_{eff}$ in the unpolymerised switched regions. At infinite voltage, the unpolymerised regions will tend to $n_o$ when the director is completely vertical. If the light incident on the device is coherent (such as that from a laser), diffraction will occur as a result of this spatial modulation in the refractive index.

Note that diffraction should not occur for light polarised perpendicular to the rubbing direction. In this geometry, the light will see the ordinary refractive index, $n_o$, across the device, irrespective of the voltage applied. Thus there is no spatial modulation in the refractive index and no diffraction occurs.

The device was first investigated with polarised optical microscopy (POM), and micrographs at 50X magnification at a range of voltages can be seen in Figure 7.13. The spacing of the walls appears to be highly uniform, as does the width of the walls themselves and this was investigated with further image analysis. At 2 V, it can be seen that there are multiple stripes of different colours in the unpolymerised channels in between the polymer walls. This is due to the influence of the polymer walls on the unpolymerised LC. The lateral elasticity deriving from the walls lowers the free energy for adjacent LC that has the same director profile as the polymer walls.

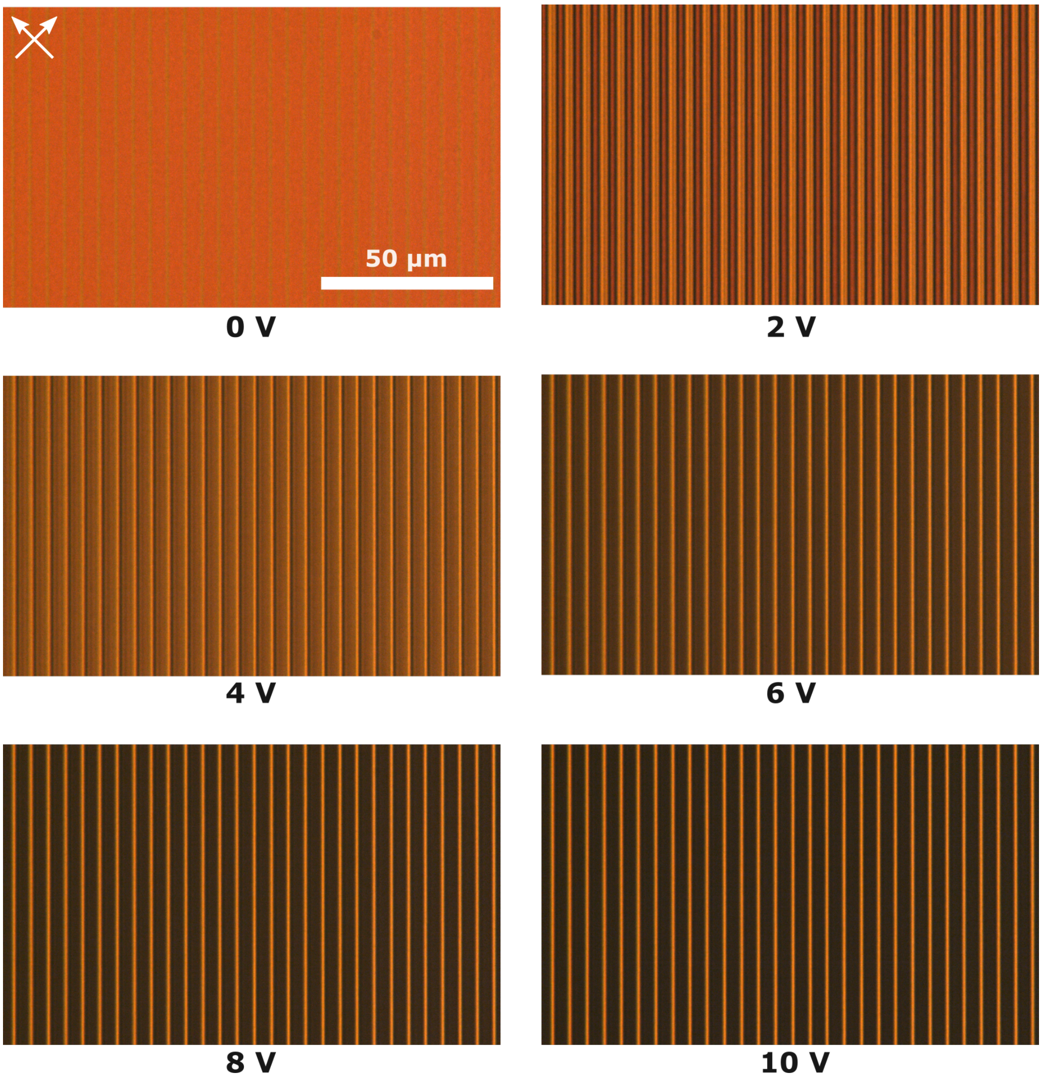

0 V
2 V
4 V
6 V
8 V
10 V

FIGURE 7.13: POM images of a 5 μm pitch diffraction grating at 50X magnification with applied voltages 0 - 10 V in 2 V steps. The polymer walls were written at 0 V. At an applied voltage of 2 V, the influence of the polymer walls on the adjacent unpolymerised LC is visible. At higher voltages, the anchoring of the polymer walls is overcome and the director is near vertical at 10 V. The walls remain bright as the director is locked-in and the walls therefore remain birefringent. The orientations of the crossed polarisers are indicated by white arrows in the first image.

Image analysis was performed to assess the uniformity of the wall-spacing and obtain an estimate of the width of the polymer walls. It should be noted that obtaining these values from microscope images is an estimate from an indirect measurement method and ideally scanning electron microscopy would be used to provide direct measurements. As the appearance of the polymer structures is influenced by the behaviour of the unpolymerised LC adjacent to the structures, analysis was performed using the POM image of the grating at 10 V. This is preferred because at higher voltages the dielectric coupling with the applied field dominates over the elastic influence of the polymer walls on the unpolymerised LC. Adopting this voltage for the analysis should provide the best estimate of the true width of the polymer walls that can be obtained with this type of microscopy.

The analysis was conducted by performing horizontal line-scans across a greyscale version of the POM image of the grating under an applied field of 10 V (shown in Figure 7.13). These line scans were averaged to reduce noise, and the result is plotted in Figure 7.14a where each wall is represented by a peak. The scale was calibrated using a microscope calibration slide with an etched scale. The MATLAB function *findpeaks* was used to find the location of the peaks and these values are plotted against the peak number in Figure 7.14b. The linearity of Figure 7.14b shows that there is a constant spacing between each polymer wall that comprises the grating. The mean of the distances between adjacent walls was found to be 5.00 µm exactly and the standard deviation was 0.08 µm which is of the order of the resolution of the image of 0.09 µm/pixel.

An estimate of the polymer wall width can be obtained with an optional output from the *findpeaks* function, which calculates the full-width of the peak at half-prominence. Averaging these widths gives a value of 0.87 µm and the standard deviation is just 0.02 µm, showing a very high polymer wall uniformity. It can be seen that there is a slight asymmetry in the base of the peaks in Figure 7.14a which could indicate that the polymer walls are not perfectly parallel to the rubbing direction of the device.

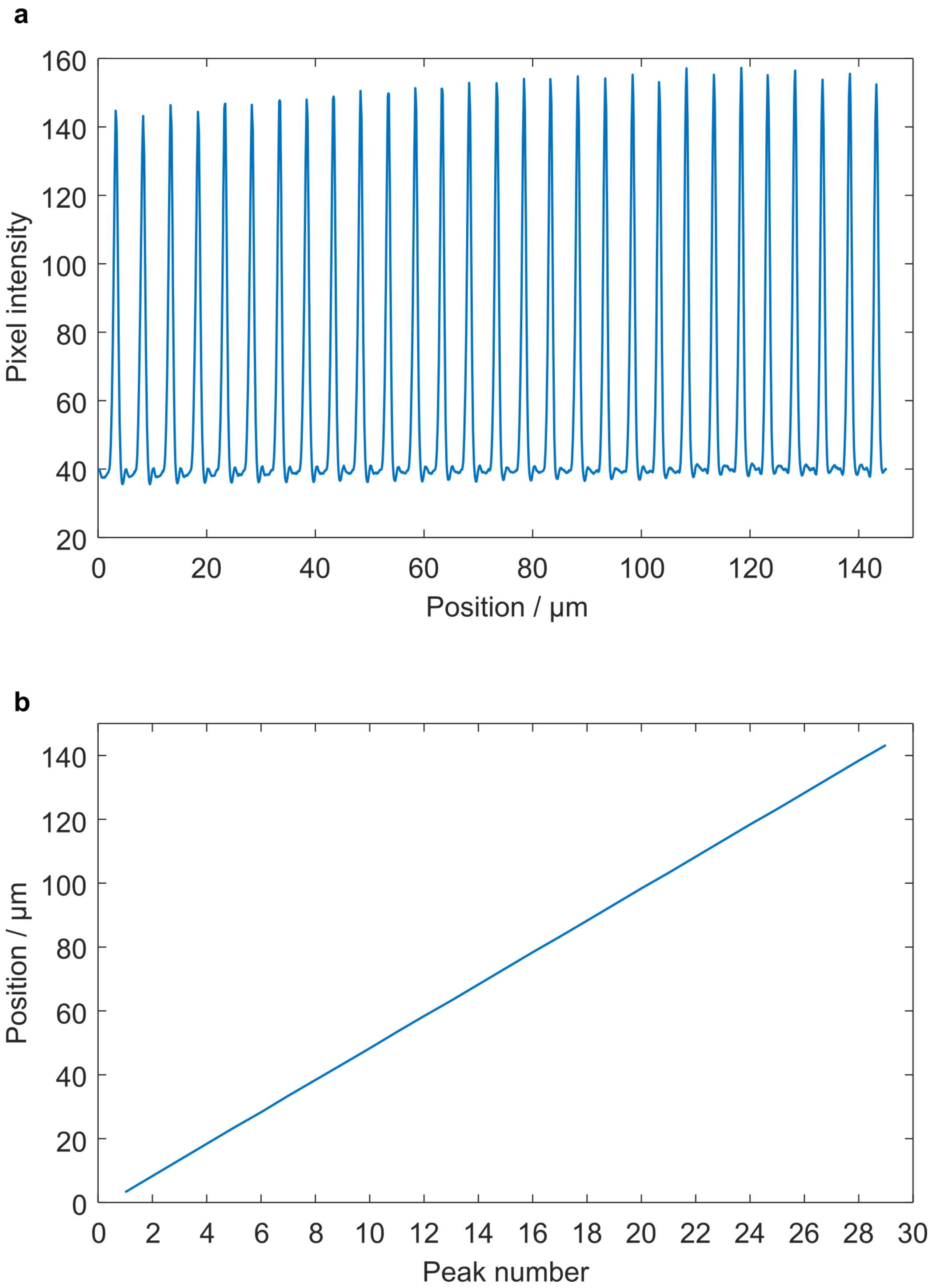

FIGURE 7.14: Image analysis of a POM image of the 5 μm period grating under an applied voltage of 10 V. (a) pixel intensity versus position in μm. (b) position in μm versus peak number. The regularity of the peak position shows there is a highly regular spacing between the walls. The uniformity of the peaks themselves shows the walls have a highly uniform structure.

Diffraction characterisation was performed using the DOE characterisation system described in Section 7.2.2, with the 635 nm laser diode polarised parallel to the rubbing direction of the device. A 300 mm lens was used to focus the beam to a spot ∼300 µm in diameter to ensure that the entire beam passed through the grating.

The diffraction pattern was recorded using the CCD method (see Section 7.2.2) for a range of voltages from 0 - 10 V in 0.1 V steps and for a range of exposure times. Figure 7.15 shows a subset of these images (0 - 10 V in 1 V steps, 40 ms exposure). In the off-state at 0 V, the polymer network is in the same state as the unpolymerised channels and so there is no refractive index contrast and almost no diffraction. As the voltage is increased, a diffraction pattern appears once the unpolymerised LC begins to switch, producing a refractive index contrast between the polymer walls and unpolymerised channels. The grating clearly produces multiple diffracted orders, as is characteristic of the Raman-Nath regime, and is in accordance with the Q-factor (see Section 7.1.1) for this grating of Q = 0.50. This diffraction behaviour is explored further in the following section on director and optical modelling in COMSOL.

Diffraction angles were measured by analysing an image of the diffraction pattern where all the orders were clearly visible, such as the image for 10 V in Figure 7.15. The scale of the images was obtained by measuring a known distance in a calibration image taken with the CCD. With knowledge of the distance from the device to the screen, the diffraction angles could then be calculated with basic trigonometry. A MATLAB script was written to obtain the centroids of the diffracted spots and automate this calculation. Figure 7.16 shows the experimental angles and the theoretical values derived from the standard diffraction grating

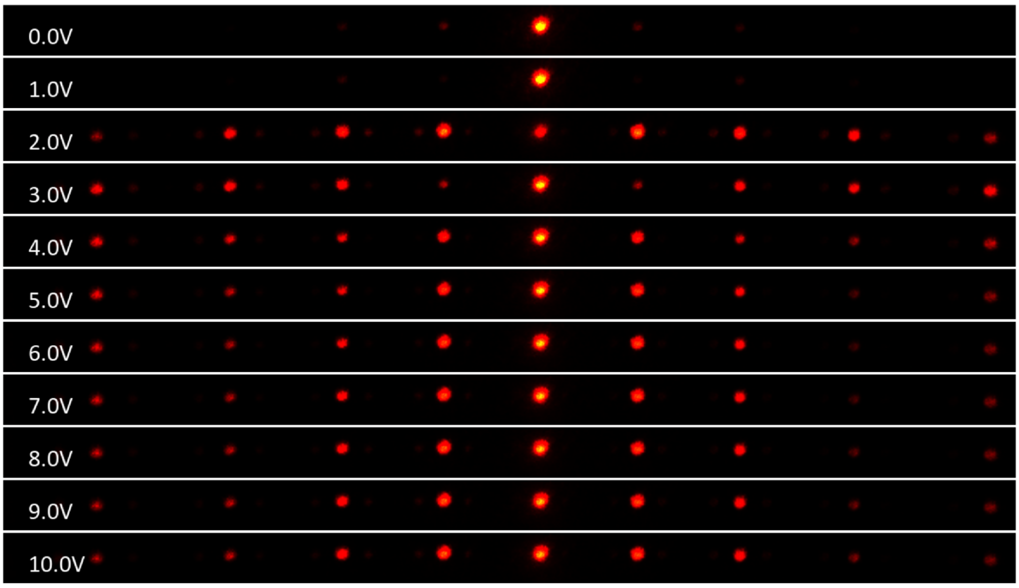

FIGURE 7.15: Images of the diffraction pattern from a 5 µm pitch diffraction grating as a function of voltage. A 40 ms exposure was used to record the images with the CCD. The voltage range is 0 - 10 V in 1 V steps. Below 2 V, only the zero order is visible as the unpolymerised regions of the grating in between the polymer walls have not switched.

equation for light at normal incidence,

$$n\lambda = d \sin \theta_n \tag{7.2}$$

where $n$ is the order of diffraction, $\lambda$ is the wavelength of light, $d$ is the grating pitch and $\theta_n$ is the angle of diffraction of order $n$.

As the grating pitch $d$ was obtained from the POM images in Figure 7.13 with an uncertainty of 0.09 µm, the dashed lines in Figure 7.16 show the maximum and minimum theoretical values corresponding to the uncertainty in the measurement of $d$. The errors in the experimental measurements are estimated from the experimental error in calibrating the image scale and measuring the distance from the device to the screen. Although the experimental data is within the uncertainty range of the theoretical predition, the fact that all of the experimental values are slightly lower than expected suggests there is a systematic error in the measurement. This is most likely to originate from an inaccurate measurement of the distance between the device and the screen.

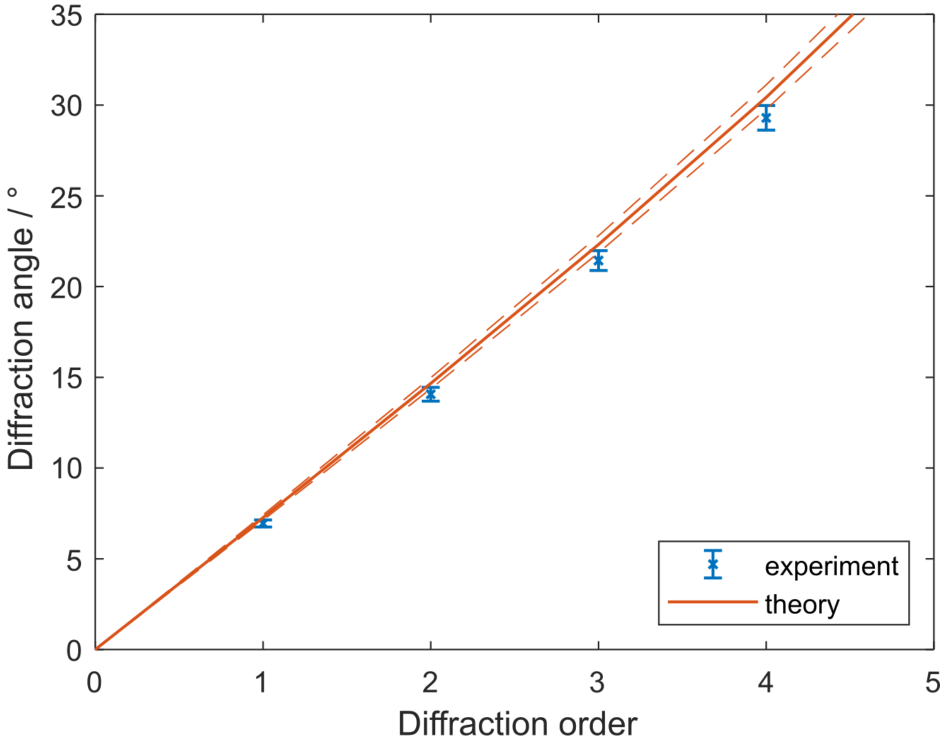

FIGURE 7.16: Diffraction angles for each diffracted order. Theoretical values are obtained from the grating equation $n\lambda = d \sin \theta_n$ and experimental values were obtained by measuring the distance between diffracted orders in an image of the diffraction pattern.

The images of the diffraction patterns were processed following the image analysis procedure described in detail in Section 7.2.2 to produce graphs of diffracted order intensity as a function of voltage which are presented in Figure 7.17. This process was repeated for CCD exposure times of 0.3 ms, 5 ms, 40 ms, 200 ms and 500 ms. The intensity data was normalised to the intensity of the zero order at 0 V.

For all exposure times except the lowest of 0.3 ms, the zero order was found to saturate the CCD. Saturation of the CCD significantly reduces confidence in the accuracy of the relative intensities of the diffracted orders. As Figure 7.17 indicates, the exposure time (and therefore degree of saturation) has a significant impact on the results. In particular, it is impossible to draw firm conclusions about the relationship between the intensity of the zero order and the other diffracted orders as the relationship varies depending on the exposure. As a key parameter for evaluating DOE performance is the diffraction efficiency, it is crucial to

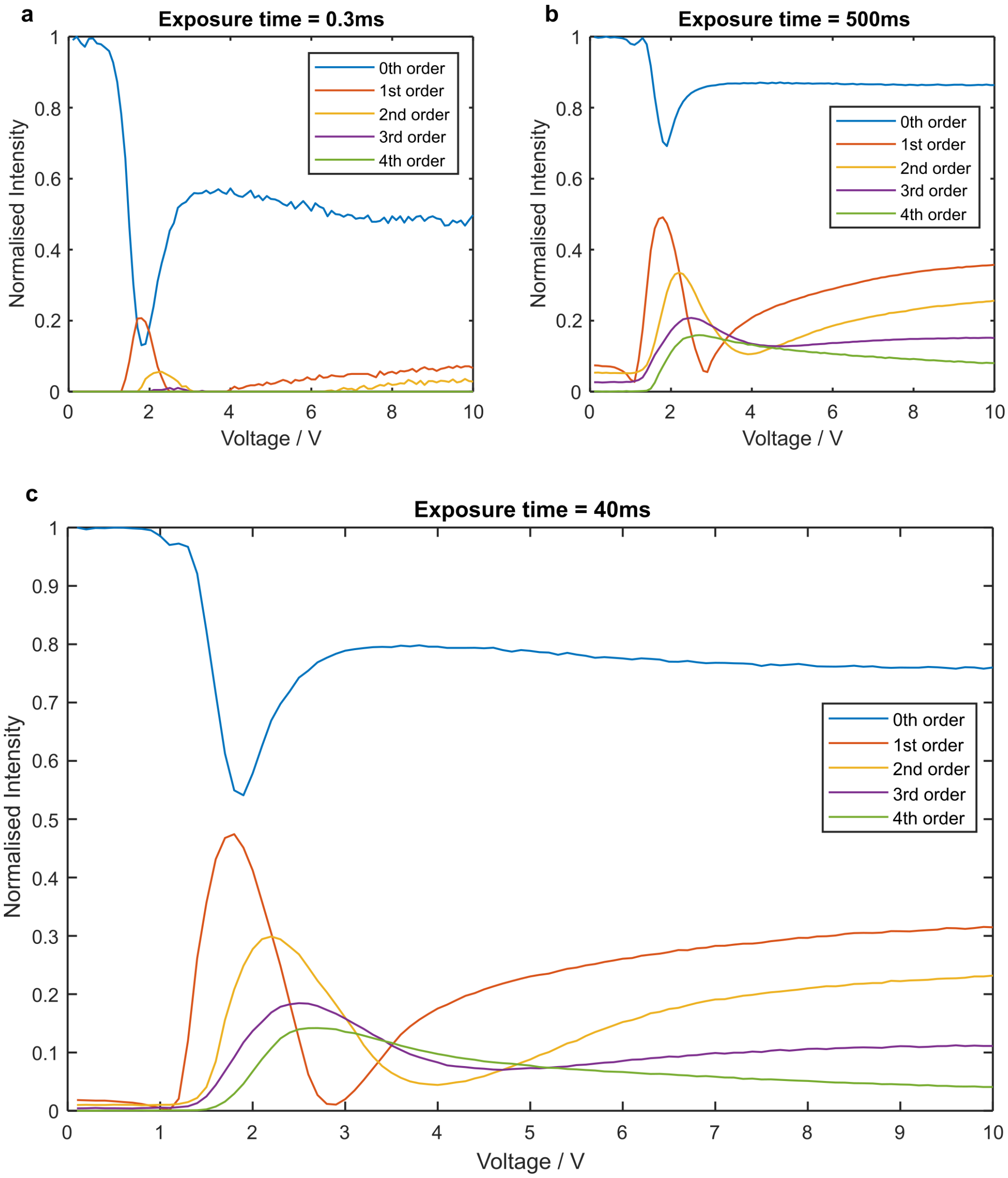

FIGURE 7.17: Diffracted order intensity as a function of voltage obtained using the CCD method. Three different CCD exposure times for each image capture are shown: (a) 0.3 ms exposure, (b) 500 ms exposure and (c) 40 ms exposure.

accurately measure these intensities.

In the case of an exposure of 0.3 ms, we have greater confidence in the relative intensity between the zero order and the first order, as no pixels were saturated on the CCD. However, using such a short exposure time leads to a poor signal/noise ratio, as can be seen in the noisy data at higher voltages. Furthermore, the lower intensity 3rd and 4th orders are not detected at all when using such a low exposure time.

It is clear that, while the CCD method can be used to obtain a qualitative indication of the diffractive behaviour, it is not suitable for obtaining accurate quantitative data of diffraction intensity. An alternative is to use a photodiode to directly record the intensity of the diffracted orders, as also described in Section 7.2.2. Figure 7.18 shows the result of such a measurement.

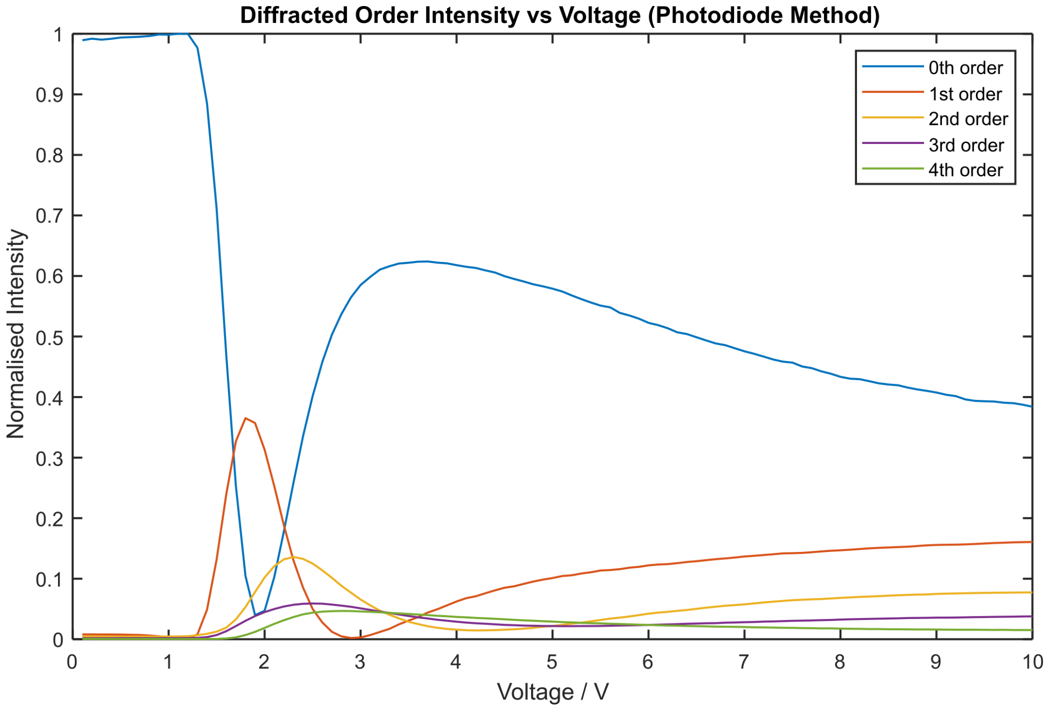

FIGURE 7.18: Diffracted order intensity as a function of voltage obtained using the photodiode method.

Examining the behaviour of the diffracted orders at low voltage (<1 V), it can be seen from Figure 7.18 that there is a low non-zero intensity associated with orders 1 and 2. Indeed, looking closely at Figure 7.15, faint 1st and 2nd order spots are visible at 0 V. This suggests that the formation of the polymer network slightly disturbs the alignment of the LC, changing the effective refractive index, resulting in weak diffraction at 0 V because of the difference in $n_{eff}$ between the polymer walls and the unpolymerised channels.

As the voltage is increased, the 1st order disappears at 1.2 V, which suggests that, as the unpolymerised regions begin to switch, they match the $n_{eff}$ of the polymer walls. This implies that the polymerisation process slightly reduces the $n_{eff}$ in the polymer walls. It therefore appears that in the formation process of the fibrils of the polymer network, the order parameter of the LC is slightly reduced, lowering the $n_{eff}$ in the walls.

Studying the Fréedericksz transition allows us to see the elastic influence of the polymer walls on the switching behaviour in the LC. The effective Fréedericksz threshold voltage is 1.2 V for the fabricated device, which is higher than the pre-polymerised value of 0.7 V. This shows that the influence of the polymer walls has increased the magnitude of the field required to reorient the director.

As the intensity data plotted in Figure 7.18 was measured directly, we have greater confidence in the intensity relationship between the different orders. This is critical because an important evaluation parameter for diffractive optical elements is the diffraction efficiency, which is defined for a diffracted order $n$ as,

$$DE_n = \frac{I_n}{I_{inc}} \tag{7.3}$$

where $I_n$ is the intensity associated with order $n$ and $I_{inc}$ is the incident light intensity.

| Diffracted order | Max. intensity voltage / V | Diffraction efficiency |
|---|---|---|
| 1 | 1.8 | 0.332 |
| 2 | 2.3 | 0.124 |
| 3 | 2.5 | 0.054 |
| 4 | 2.8 | 0.043 |

TABLE 7.1: Peak diffraction efficiencies for each order of diffraction.

Table 7.1 lists the extracted diffraction efficiencies for each order. As the diffraction efficiency of a given order varies with voltage, these values were calculated at the maximum intensity of each order. The voltage corresponding to this peak intensity is indicated in the table. The maximum diffraction efficiency in the first order of 33.2% is comparable to a value of ∼34% previously reported by Kossyrev et al. for a PSLC reverse-mode grating fabricated with a UV interference technique[182].

### Diffraction Grating Modelling

The simple 1D diffraction grating described in the previous section represents a useful experimental system to verify our understanding of the 2PP-DLW process as applied to DOEs. Through observations of the fabricated grating with polarised optical microscopy and studying the diffraction pattern, we have made reasonable hypotheses about the way the grating behaves on a microscopic level. However, verification of the microscopic phenomena is needed to complete our understanding of the system.

In this section, a multi-component model is described and used to validate our understanding of the 1D diffraction grating. The objective of this is to build a model that links LC continuum theory with wave-optics diffraction modelling, to better understand the microscopic behaviour in laser-written switchable diffraction gratings. Taking this approach produces a direct link between the director in the grating and the resulting diffraction pattern, allowing us to understand the implications of the experimental results. Thus there are two distinct components of the model: (i) LC director modelling and (ii) diffraction modelling, that are coupled in order to produce a full description of the system.

The finite element package COMSOL Multiphysics was used for this simulation and it was chosen for a number of reasons including its efficient FEM solver engine, Wave-Optics Module, Optimization Module, support for coupled partial differential equations (PDEs) and versatile post-processing and visualisation capabilities. The COMSOL interface supports arbitrary experimental geometries, 2D and 3D modelling and has many modules that simplify the implementation of simulations and models. For this simulation, however, a custom approach had to be employed as there is no liquid crystal modelling module available for COMSOL.

To model the LC director, the Euler-Lagrange equations for the elastic free energy had to be cast in the form accepted by the COMSOL custom PDE interface. The theory behind these equations and how they are codified for input into COMSOL is described in detail in Section 2.6.1. By instructing COMSOL to solve the Euler-Lagrange equations for the director, $\mathbf{n}$; the lowest energy state of the system can be found, giving a solution to the energy-minimisation problem and producing the equilibrium configuration of the director.

For wave optics modelling of diffractive structures, only a single unit cell of the DOE needs to be computed. COMSOL's wave-optics module can take this single unit cell and extrapolate to a periodic infinite structure by applying periodic boundary conditions. Therefore, the first part of the model, which models the director in the grating, also only required a single unit cell of the grating, significantly simplifying the task of simulating the device. The geometry of the model is illustrated in Figure

7.19, which shows the relationship between the grating schematics of the previous section and the geometry of the COMSOL director model.

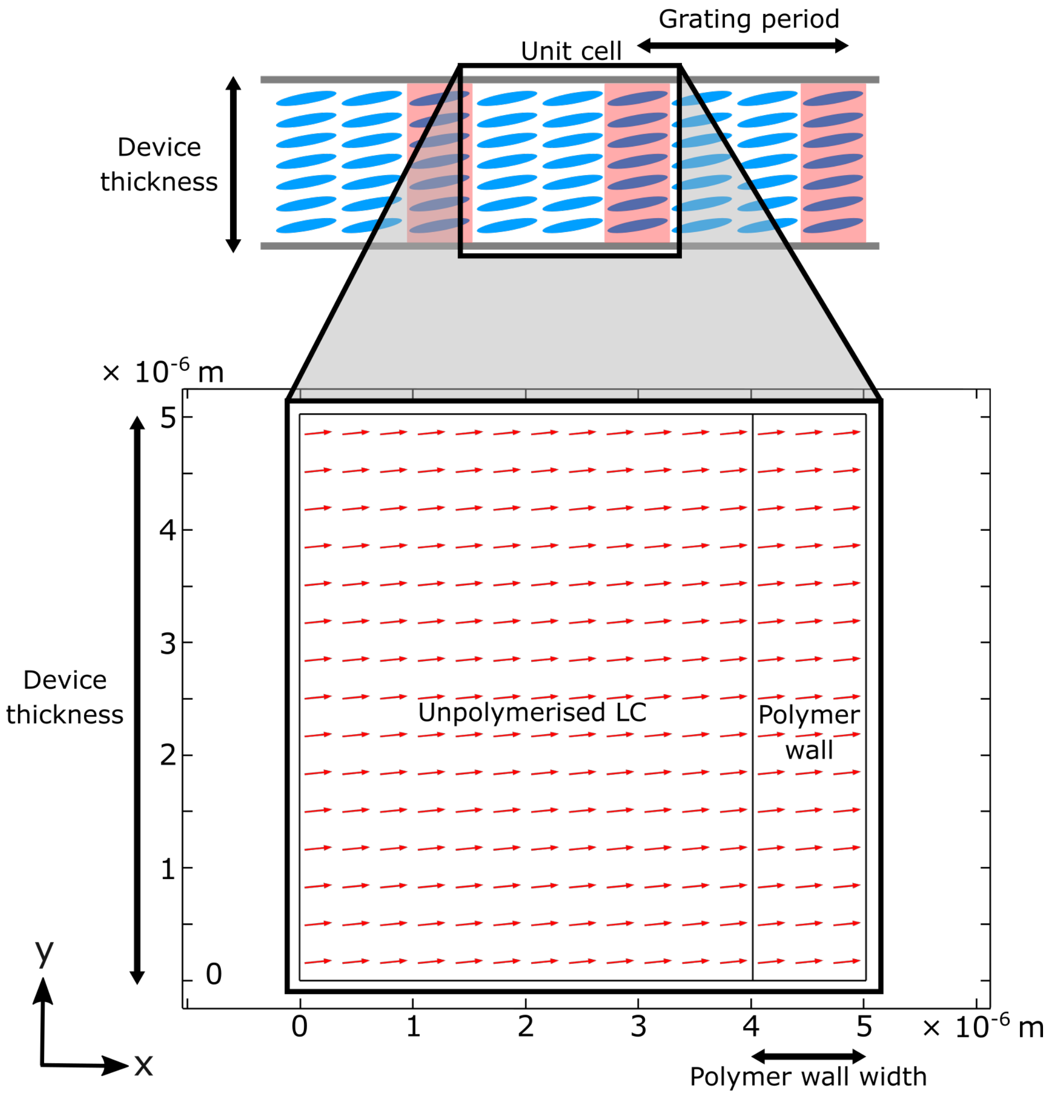

FIGURE 7.19: The geometry of the COMSOL model in relation to a schematic of a switchable diffraction grating. Red arrows represent the liquid crystal director. The model is a single unit cell of a 1D diffraction grating, with two regions: one representing the unpolymerised LC and the other representing the polymer wall. The director configuration shown here is the equilibrium state for no applied electric field.

The model geometry consists of a single unit cell of the grating, which is comprised of a wider region of unpolymerised LC and a narrower region representing the polymer wall. The geometry was built in a fully parametric manner, using global parameters that controlled the device thickness, grating period and polymer wall width. Built in this way, it is possible to easily change the geometry of the model by changing the value of these parameters, avoiding the need to use the geometry interface when modifying the model. This approach also allows the Optimization Module to be used where necessary in order to fit these parameters to the experimental data.

The two regions were governed by PDEs of the same form, but with different material parameters, such that the polymer wall could be modelled as a liquid crystal with a higher elastic constant than the unpolymerised region[202–204]. By running the model and studying the results, appropriate values were found for these material parameters by running an optimisation routine.

Arrow surface plots, such as those in Figure 7.19 were found to be an expedient way of visualising the results of the director simulation. This is a convenient COMSOL visualisation plot where each arrow has an x-component and a y-component that determines the length and orientation of the arrow. Therefore, the x-component was set to $n_x$ and the y-component was set to $n_y$, the x and y components of the director. To complete the visualisation, the arrows were placed in a $15 \times 15$ regular grid across the unit cell, and the 'base' (effectively the centre of rotation) of the arrows was set to centre.

In FEM modelling, after defining the geometry and the governing equations, the next steps before a solution can be calculated is to define the boundary conditions. Two types were employed: Dirichlet (fixed) boundary conditions and periodic boundary conditions, the locations of which are shown in Figure 7.20. Dirichlet boundary conditions specify the values that a solution must take along the boundary of a domain and were used in this model to represent the strong-anchoring of the alignment layers on the inside of the glass substrates. The rubbed polyimide alignment layers used in these devices had a pretilt, $\theta_{pt}$ = 1 - 3°, and so 2° was chosen as a first-approximation. As the model is in terms of the components of the director, this pretilt angle had to be specified as $n_x = \cos\theta_{pt}$ and $n_y = \sin\theta_{pt}$.

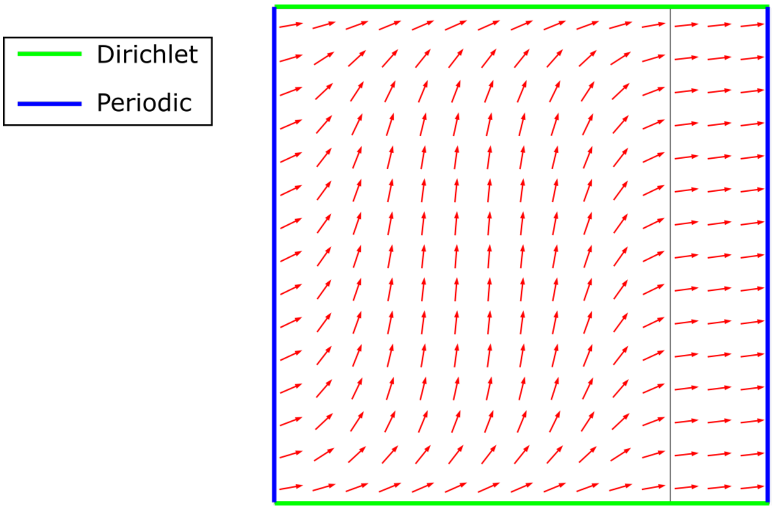

FIGURE 7.20: Types of boundary condition employed in the COMSOL FEM director model. There is a fixed (Dirichlet) boundary condition along the top and bottom of the geometry, to represent the strong anchoring of the rubbed polyimide alignment layer on the inside of the cell substrates. Periodic boundary conditions are used on the lateral boundaries of the unit cell, to represent the periodicity of the diffraction grating structure.

Periodic boundary conditions were used to represent the fact this model is just a single-unit cell of a larger periodic structure. Figure 7.20 shows where the boundaries were employed, namely the left and right lateral domain boundaries of the model. Imposing this condition means that the solution along these boundaries must be equal and thus this geometry faithfully represents the unit cell of a larger periodic structure.

The final step before running the FEM solver is to discretize the geometry by defining a mesh. This is integral to finite element analysis, which relies on subdividing a large system into smaller, simpler domains called finite elements. The mesh has a finite number of points and is a numerical approximation to the true solution. Therefore the accuracy of the solution depends on the granularity of the mesh. However, in practice, computation time increases with increasing mesh granularity and so a compromise is normally sought between granularity and computation time.

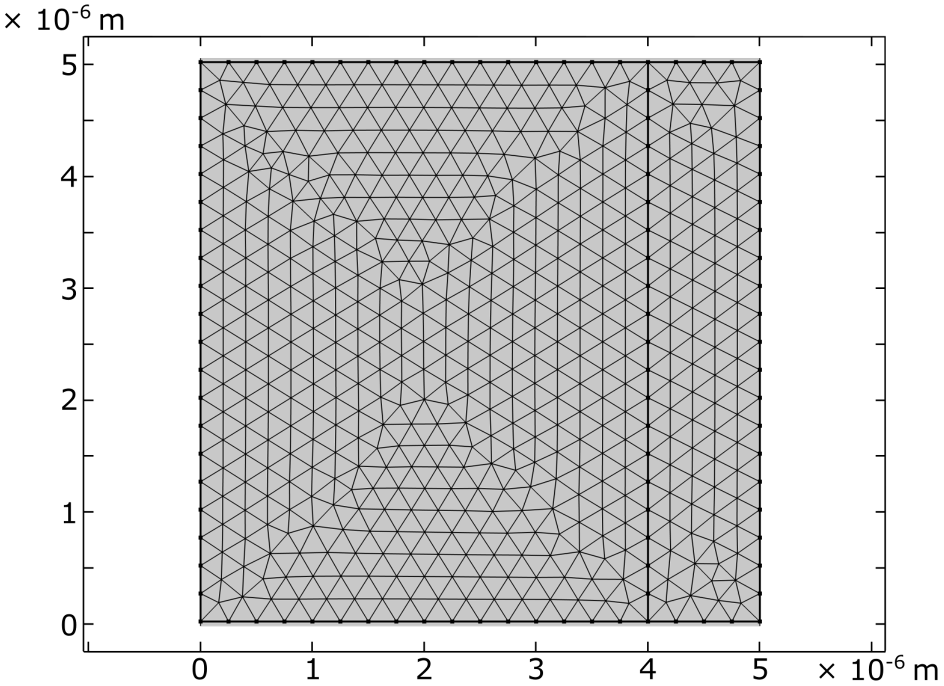

FIGURE 7.21: Mesh used for the continuum theory model of the LC director. The mesh size is 0.25 µm.

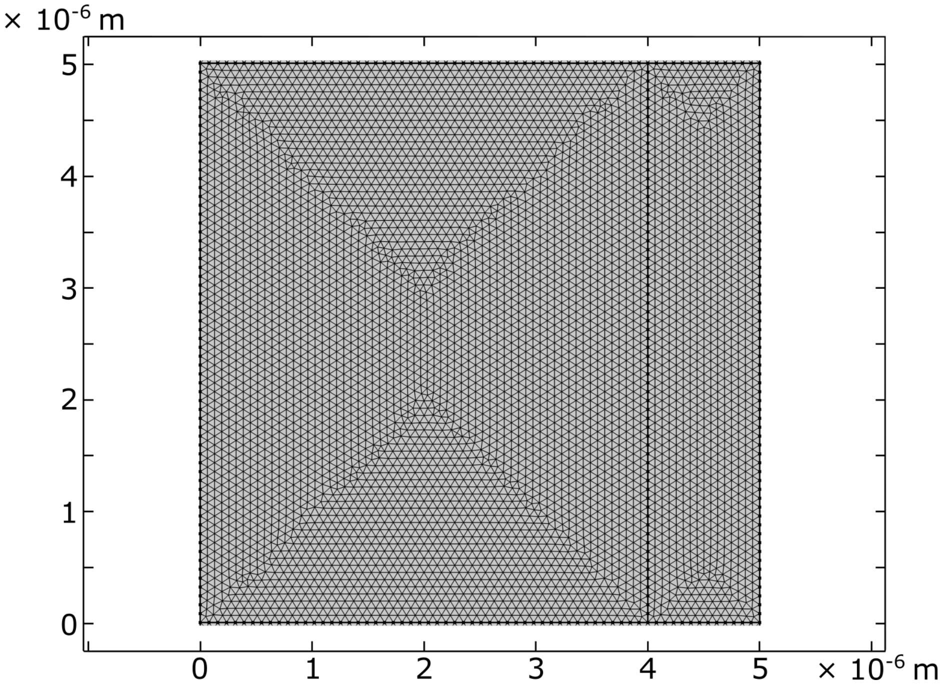

FIGURE 7.22: Mesh used for the wave-optics part of the diffraction grating model. The mesh size is approximately 0.08 µm.

For the continuum theory part of the model, a mesh size of 0.25 µm was chosen (Figure 7.21), as using finer elements produced no significant change in the solution, but had a considerable impact on the computational work required and the calculation time. For the wave-optics part of the model, the element size was chosen automatically by COMSOL, which takes into account the physics being simulated. A finer mesh was found to be necessary, with an element size of 0.08 µm selected by the FEM solver (Figure 7.22).

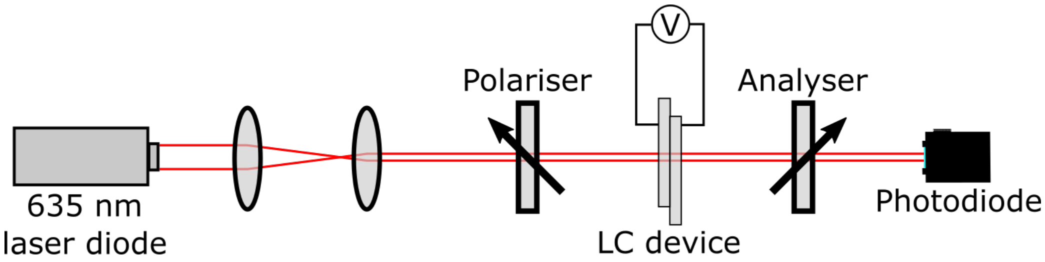

FIGURE 7.23: Optical layout for performing an LC device transmission experiment. The easy axis of the polariser and analyser are crossed at 90 ° to each other, while the optic axis of the device is 45° to the easy axes of the polariers.

To accurately simulate the switchable diffraction grating and provide a good match with the experimental data, it was necessary to obtain the material parameters that were input to the model. Although the mixture is ∼70 wt% E7, a well-characterised LC material, the addition of ∼30 wt% of reactive mesogen results in significant changes in the material properties.

| Material parameter | Value | Description |
|---|---|---|
| $\Delta\varepsilon$ | 12.0 | Dielectric anisotropy |
| $n_o$ (635 nm) | 1.5 | Ordinary refractive index |
| $n_e$ (635 nm) | 1.69 | Extraordinary refractive index |

TABLE 7.2: Material parameters derived from FDM modelling.

To obtain the material parameters, the transmissive behaviour of an uncured 5µm thick device was studied as a function of voltage between crossed polarisers, with the optic axis of the device at 45° to the polarisers, using a wavelength of 635 nm (Figure 7.23). The resulting

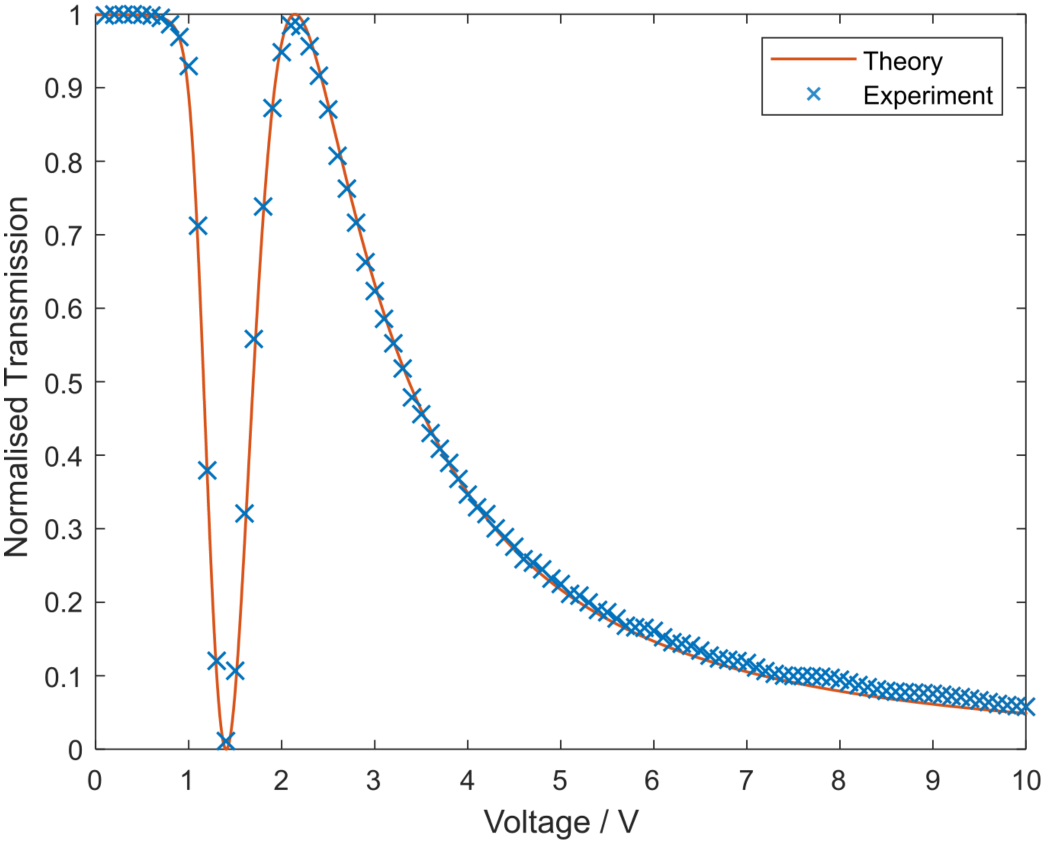

FIGURE 7.24: Transmission vs voltage for the polymerisable LC mixture in a cell of thickness 5 µm. Experimental data is plotted as orange crosses while the results from the modelling are shown as a blue line.

experimental data was fitted with a simple finite-difference method (FDM) director modelling program that incorporated a Jones matrix subroutine. The theory behind FDM is explained in Section 2.6.2 and the Jones matrix method is explained in Section 2.7.2. By adjusting the material parameters in the FDM model to fit the experimental data, an estimate could be obtained of the true material parameters. The experimental data and the fit are shown in Figure 7.24 and the derived material parameters are in Table 7.2.

The second major component of the model involved simulating the propagation of light through the LC diffraction grating. The COMSOL wave-optics module was used for this part of the model as it allows for solving electromagnetic wave problems at optical frequencies. To model the propagation of light through a material in COMSOL, we have to specify its refractive index. This was accomplished by taking the solution from the director modelling and mapping this onto a spatially varying refractive index via the equation for the effective refractive index,

$$n_{eff} = \frac{1}{\sqrt{\left(\frac{n_y}{n_o}\right)^2 + \left(\frac{n_x}{n_e}\right)^2}} \tag{7.4}$$

where $n_o$ and $n_e$ are the ordinary and extraordinary refractive indices respectively, and we have assumed the polarisation of the input light is parallel to the x-axis (the rubbing direction of the device).

The form of this equation can be understood by considering the limiting cases of $n_x$ and $n_y$. For example, when $n_x = 1$ and $n_y = 0$, the director is uniformly pointing along the x-axis, and therefore light polarised parallel to the x-axis would propagate according to an effective refractive index equal to $n_e$. Conversely, when $n_x = 0$ and $n_y = 1$, the director is oriented vertically and the input light would propagate according to a refractive index of $n_o$, as it is now travelling along the optic axis of the material.

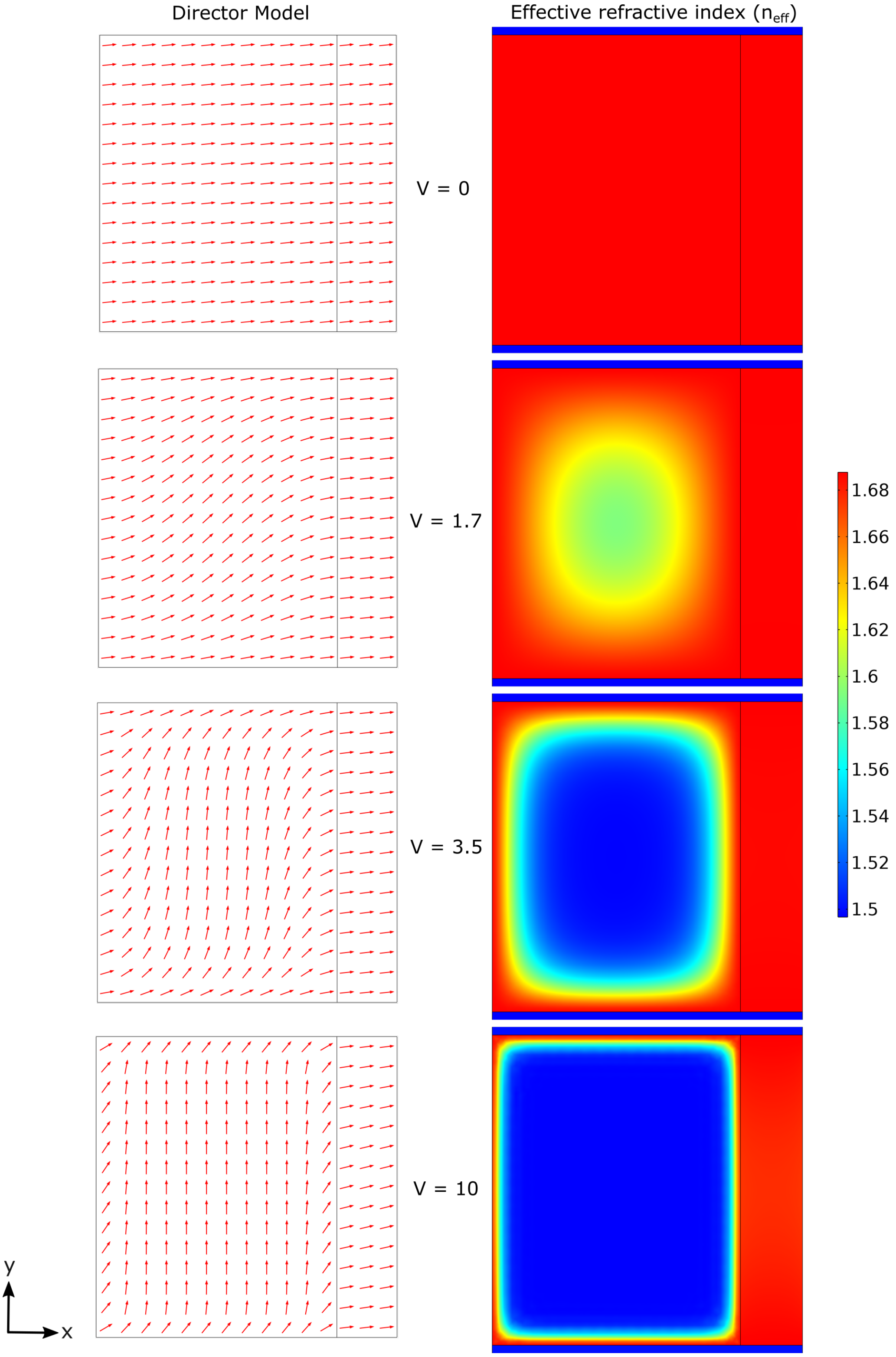

FIGURE 7.25: Director profiles and effective refractive index map for the diffraction grating at a range of different voltages.

Figure 7.25 illustrates the mapping between the director and the effective refractive index experienced by light polarised parallel to the y-axis, for a range of different applied voltages. Regions of the device where the director is oriented vertically have an effective index of $n_o = 1.5$ whereas regions where the director is oriented horizontally tend towards $n_e = 1.69$. As the voltage increases, more of the unpolymerised region is oriented vertically, and thus the area with an index of $n = 1.5$ increases. This effect can be seen as the increasing size of the blue area in Figure 7.25 as the applied voltage increases.

To properly represent the propagation of light through the diffraction grating, the geometry had to be extended to incorporate the glass substrates bounding the thin LC layer. Figure 7.26 shows the extended geometry, where the glass substrates have been represented by 10 µm thick layers of material with $n = 1.5$ either side of the LC layer. Although the bounding substrates are in reality approximately 700 µm thick, the results of the simulation did not change significantly when increasing the substrate thickness in the simulation above 10 µm. Therefore, to reduce computational complexity, these artificially-thin substrates were employed in the model.

To add electromagnetic wave propagation to the model, input and output 'ports' must be specified that instruct COMSOL where electromagnetic energy enters or exits the model. These ports must be along a boundary in the geometry and have been labelled in Figure 7.26. Furthermore, for this model, the ports must be specified as periodic ports, to represent the infinitely large repeating structure of the grating. Finally, a Floquet-type periodic condition is imposed on the lateral edges of the entire geometry, which instructs the wave-optics module that this geometry is a unit cell of a larger periodic structure.

Having set up the continuum theory director model and the

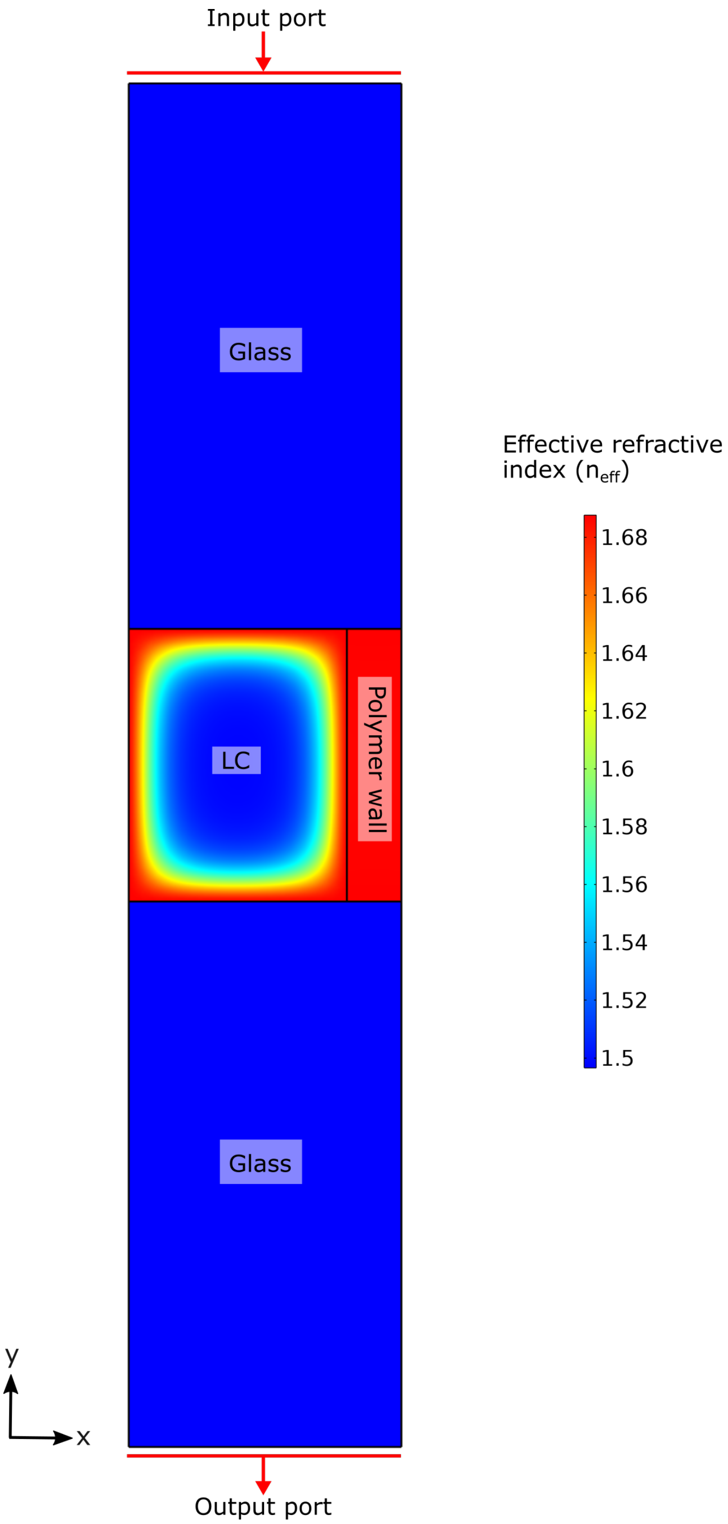

FIGURE 7.26: Overall geometry for wave-optics model. The effective refractive index is shown for an applied voltage of 3.5 V. Each domain has been labelled with the component of the diffraction grating that it represents. The input and output ports are shown at the top and bottom of the geometry and the propagating wave moves from the top to the bottom of the structure.

wave-optics model, and coupled them together such that the solution of the director model is used to define the refractive index for the wave-optics model, we can now evaluate the theoretical transmission for each diffracted order. Parametric sweeps of the voltage parameter were performed to study the transmission as a function of voltage and to compare with the experimental results from Figure 7.18.

The material parameter inputs to the model were tuned by running an optimisation routine using the COMSOL Optimization Module. A BOBYQA (Bound Optimization BY Quadratic Approximation) optimisation algorithm was used with a least-squares objective, comparing the simulation output with the experimental data shown in Figure 7.18.

The parameters tuned by the optimisation algorithm were:

- Elastic constant for the unpolymerised region - $K_{LC}$
- Elastic constant for the polymerised region - $K_{pol}$
- Width of the polymer wall - $d_{pol}$

The results from the optimised model are presented in Figure 7.27 where the experimental results from Figure 7.18 have been plotted again to provide a comparison. The optimised parameter values are $K_{LC} = 9.79$ pN, $K_{pol} = 1,500,000$ pN and $d_{pol} = 0.93$ µm. The results from the model show a good fit with experiment, with just a small deviation from the experimental data. Possible causes of the difference between experiment and the model are explored in the following discussion.

Director profiles superimposed onto a map of the effective refractive index at a selection of key voltages are shown in Figure 7.28. Studying the behaviour of the director in the grating allows us to obtain a greater understanding of the diffraction behaviour. At 0 V (Fig. 7.28a),

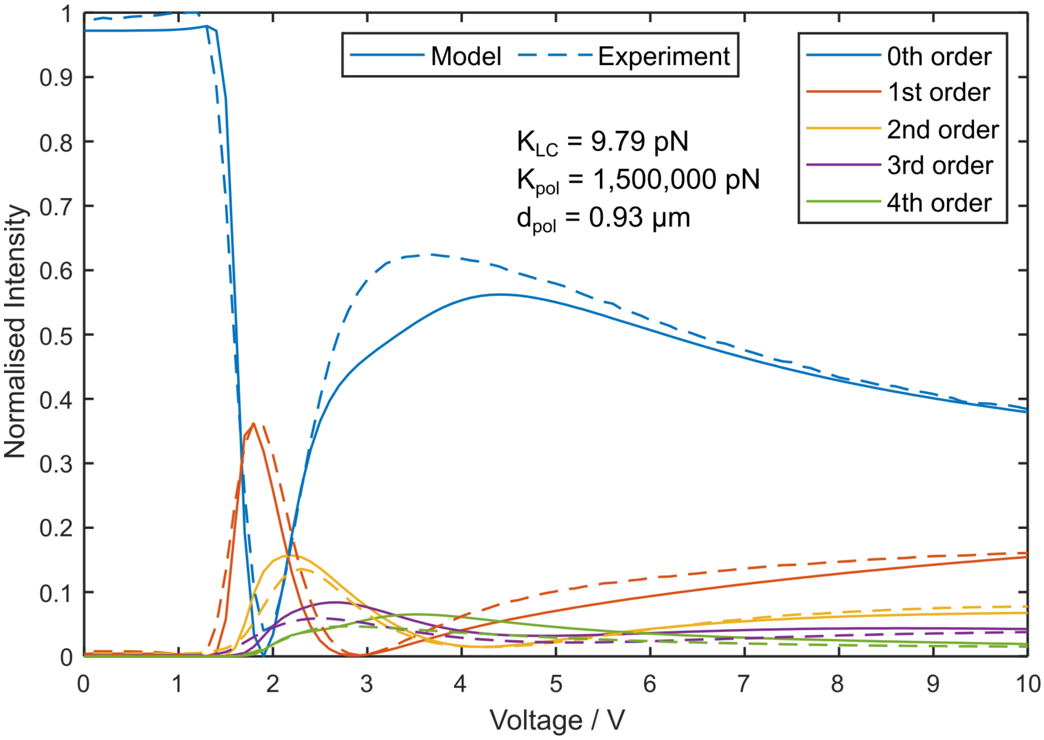

FIGURE 7.27: Optimised model transmission versus voltage for diffracted orders compared with experiment. Experimental data is plotted with dashed lines and model data is plotted with solid lines. Model parameters: $K_{LC} = 9.79$ pN, $K_{pol} = 1,500,000$ pN and $d_{pol} = 0.93$ µm.

the grating has a uniform effective refractive index of almost 1.69 (it is not quite equal to 1.69 due to the 2° pretilt of the cell) and consequently there is no diffraction. At ∼1.5 V (Fig. 7.28b), the director in the centre of the unpolymerised region begins to reorient, resulting in a decrease in the refractive index to ∼1.63. And, as there is now a difference between the refractive index in the polymer wall and in the unpolymerised region, diffraction begins to occur around this voltage, with most of the light being coupled into the first order at ∼1.8 V. As the voltage is increased further, the director in the centre of the unpolymerised region has an increasingly vertical orientation (Figs. 7.28c, d), enhancing the magnitude of the modulation in the refractive index. The result of this effect is that the light is increasingly coupled into higher orders, as the phase difference of the light passing through the unpolymerised and polymerised regions of the grating increases.

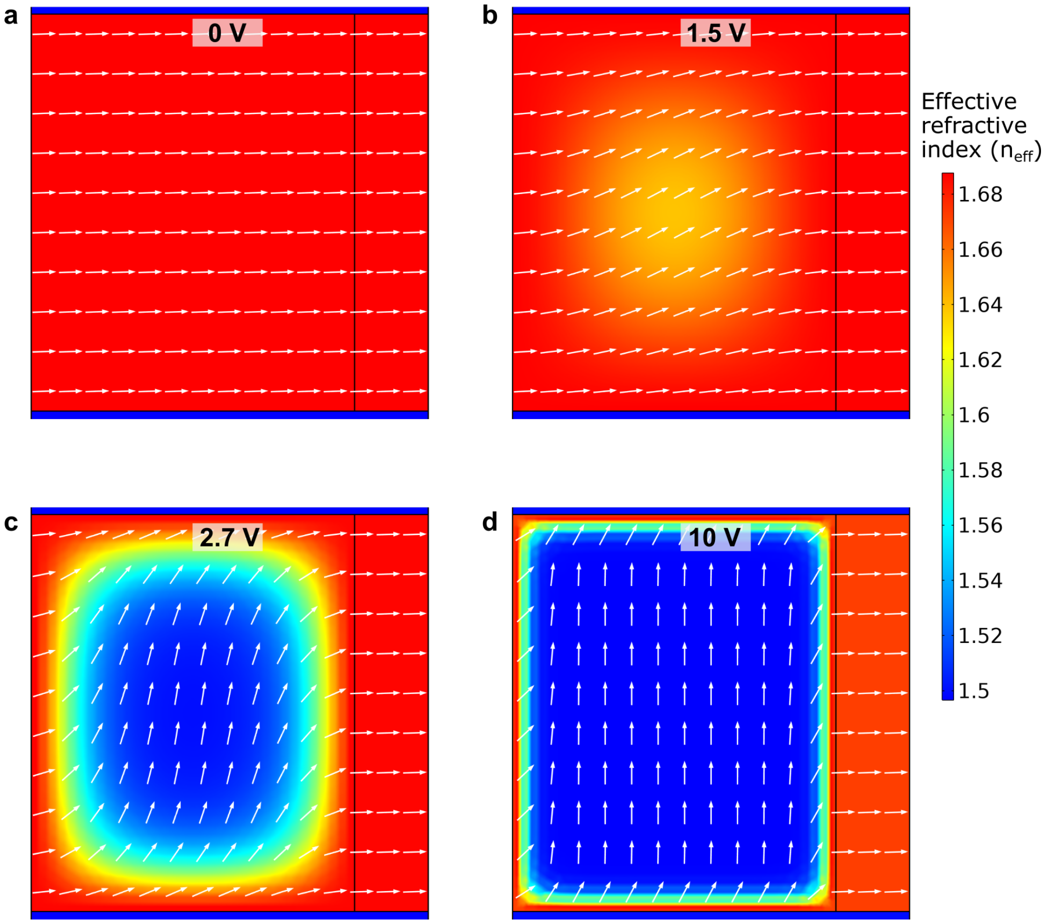

FIGURE 7.28: Director profiles and effective refractive index from the optimised model for voltages corresponding to (a) 0 V, (b) 1.5 V, (c) 2.7 V and (d) 10 V. The director is shown here with white arrows to enhance visibility on the multicoloured map of the refractive index. Model parameters: $K_{LC} = 9.79$ pN, $K_{pol} = 1,500,000$ pN and $d_{pol} = 0.93$ µm.

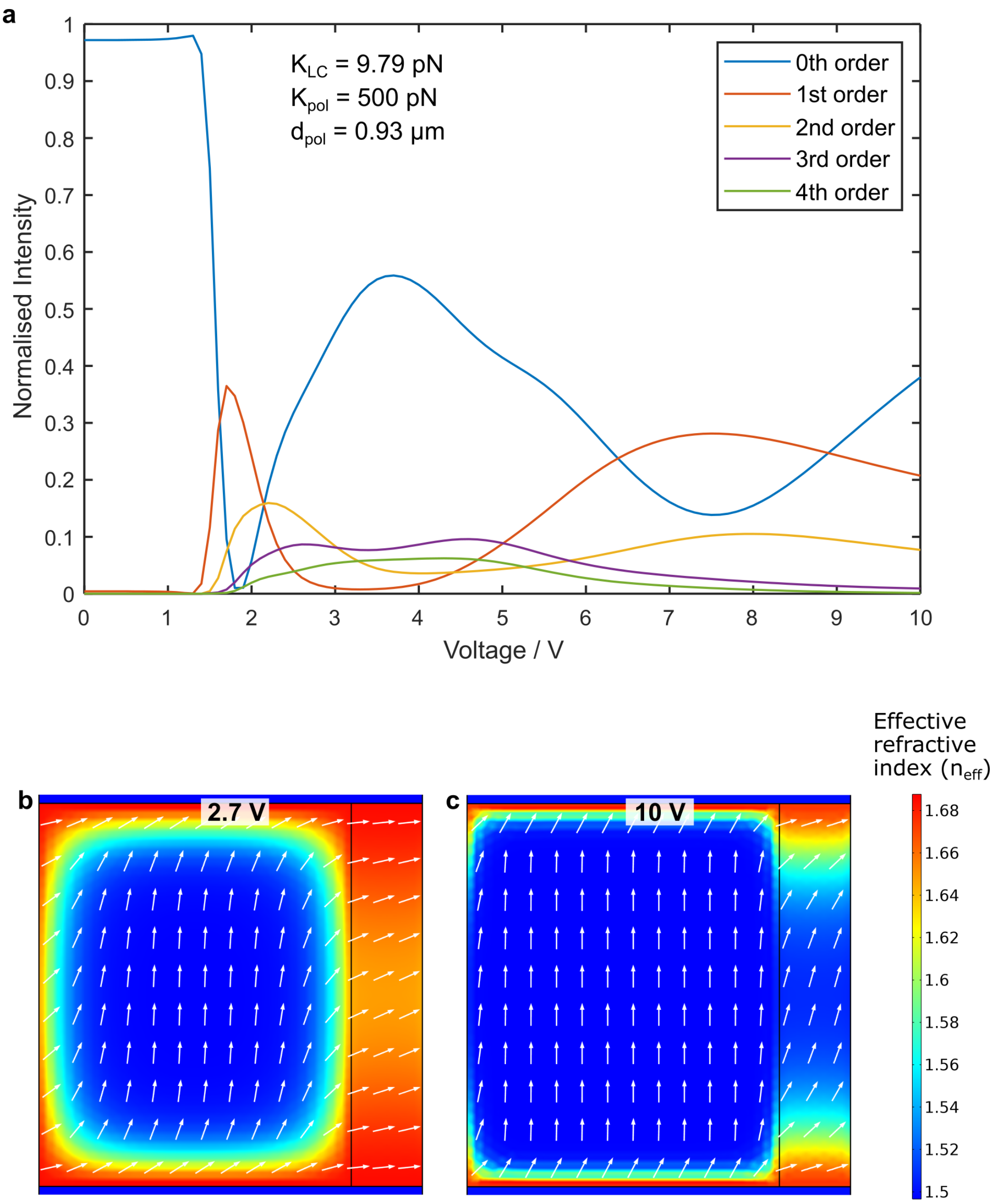

FIGURE 7.29: Model results for an artificially-low $K_{pol}$. (a) Transmission versus voltage for diffracted orders. Director profile and effective refractive index for (b) 2.7 V and (c) 10 V. Model parameters: $K_{LC} = 9.79$ pN, $K_{pol} = 500$ pN and $d_{pol} = 0.93$ μm.

It was found that the elastic constants for the unpolymerised ($K_{LC}$) and polymerised ($K_{pol}$) regions have a significant influence on the behaviour of the model. The nature of the influence can be understood by running the model for artificially low or high values of the parameters. Figure 7.29 shows the results of the model for $K_{pol} = 500$ pN, four orders of magnitude lower than the optimised value. By comparing with the optimised results in Figure 7.27, it can be seen that the value of $K_{pol}$ strongly affects the diffractive behaviour at higher voltages but has a minimal impact at lower voltages. For voltages from 0 V - 2.7 V, the low $K_{pol}$ model has almost identical results to the optimised model. Whereas, at voltages > 2.7 V, there is a strong deviation from the optimised model.

This effect can be understood by examining the director profiles for key voltages along the transmission versus voltage plot. At 2.7 V (Fig. 7.29b), this low $K_{pol}$ model begins to show reorientation in the polymerised region. At higher voltages, the polymer wall has a large area of vertically-oriented director with a refractive index of 1.5, illustrated in Figure 7.29c. The artificially-low value of $K_{pol}$ has effectively caused the grating to have a second Fréedericksz threshold at $\sim$2.7 V, corresponding to the polymerised region.

It is interesting that the optimisation algorithm found that the best parameter for $K_{pol}$ was such a high value of $1,500,000$ pN. This suggests that the polymer network fabricated by 2PP-DLW is strongly locking-in the LC, preventing it from switching even at reasonably high voltage. A value of $K = 1,500,000$ pN in a standard LC device would correspond to a Fréedericksz threshold of 373 V.

The elastic constant in the unpolymerised region, $K_{LC}$, predominantly influences the voltage at which the LC begins to switch and the diffracted orders appear. Figure 7.30 shows the effect of an artificially low and high $K_{LC}$. It can be seen that a low value of $K_{LC} = 1$ pN causes the LC in the unpolymerised region to switch at a voltage of ~0.4 V, compared to the optimised model which switches at ~1.5 V and has a $K_{LC} = 9.79$ pN. Whereas for a high value of $K_{LC} = 20$ pN, the LC switches at a higher voltage of ~2 V.

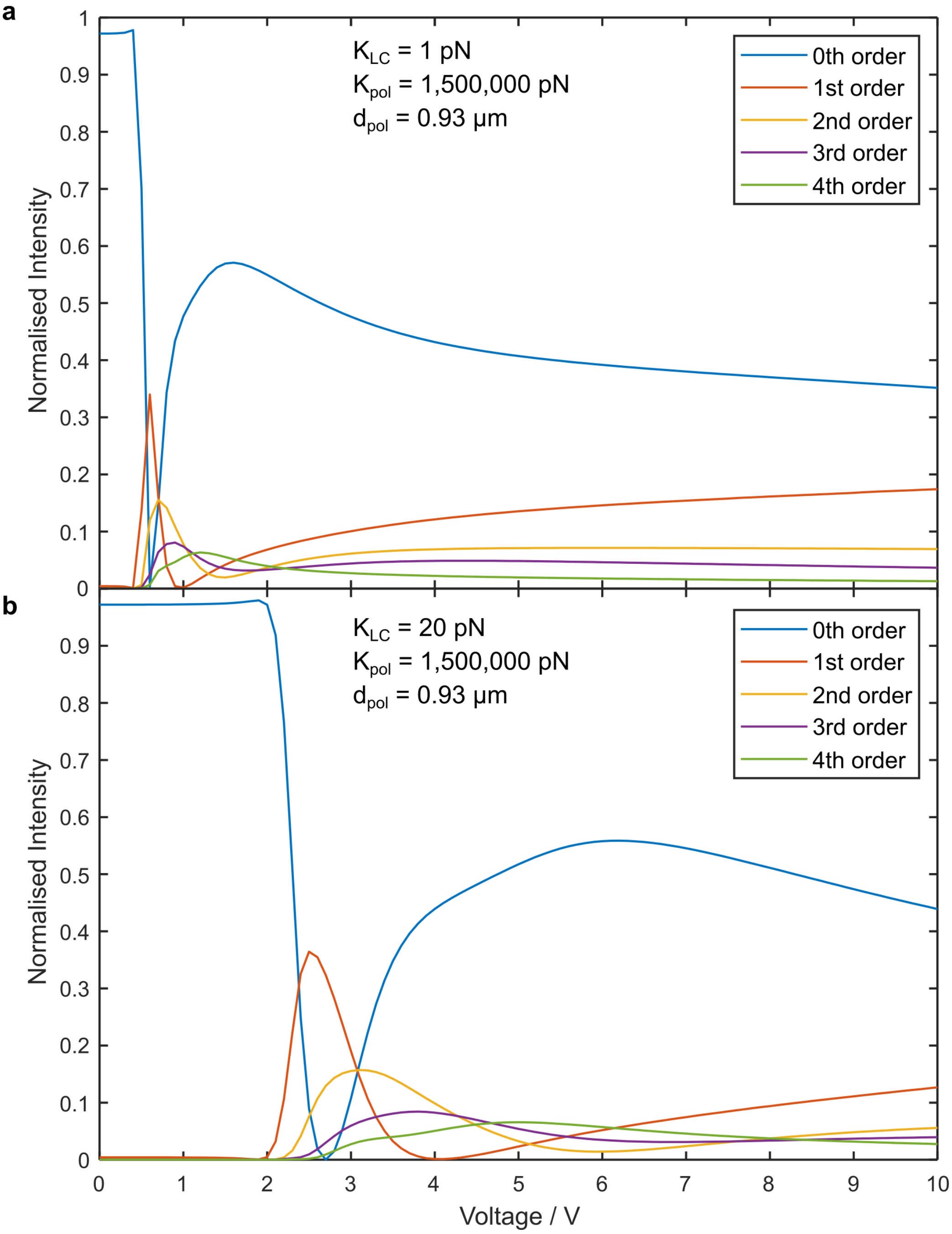

FIGURE 7.30: Model results for $K_{LC}$ set to a value that is (a) too low or (b) too high. Model parameters: $K_{LC} = 1$ or 20 pN, $K_{pol} = 1,500,000$ pN and $d_{pol} = 0.93$ μm.

It is notable that the optimised model value of $K_{LC} = 9.79$ pN is slightly lower than expected for a mixture predominantly consisting of E7, which has elastic constants of $K_{11} = 11.1$ pN, $K_{22} = 6.5$ pN and $K_{33} = 17.1$ pN[205]. Under the one-constant approximation used in this model, a value of $K = \sim 11.6$ pN would be expected to give appropriate results for E7[206].

A possible cause of this artificially-low $K_{LC}$ could be due to the assumption in modelling the polymer network as a region with a uniform elastic constant. Due to polymer diffusion during the laser writing process, it is expected that there will be a gradient in the polymer network density, with the strongest network in the centre of the fabrication laser focus. This gradient in polymer network density is likely to cause a gradient in the elastic constant, with the highest $K$ in the centre of the polymer wall and a lower $K$ towards the wall edges. However, in this simulation, the polymer wall is modelled as a region of uniform elastic constant. Therefore, the optimisation algorithm may be artificially lowering $K_{LC}$ to compensate for the uniformly rigid polymer network.

There are a number of other assumptions made in the model that could explain why the results do not perfectly match the experimental reality. The pretilt was assumed to be 2°, as the manufacturer of the LC cells gives a pretilt value of 1 - 3°, but no direct measurement of the pretilt was obtained. A lower pretilt would increase the Fréedericksz threshold of the device, causing the diffraction to switch on at a higher voltage.

Another possible cause of the inability to perfectly match the model to experiment could be the simplified device structure implemented in the model. The real device has an ITO layer and a rubbed polyimide alignment layer on both substrates, which were omitted from the model and could affect the measured diffraction efficiency by causing the diffracted orders to be partially reflected.

As this model was based on the one-constant approximation for the distortion free energy, the true nature of the elastic behaviour of the LC is markedly simplified. Implementing a full model with all three elastic constants would have significantly increased the mathematical complexity of the model, as well as the computational load on the FEM solver. As a result of this, a one-constant model was implemented, but this could be another cause of the failure to perfectly match the experimental data.

Finally, another notable weakness of the model is in the assumption of a uniform electric field across the device. This is a simplification because the local electric field actually depends on the coupling between the dipoles in the LC molecules and the external electric field. Thus the permittivity changes as the director reorients, which affects the magnitude of the local electric field. To properly model the electric field would require solving Laplace's equation for the electric potential with a dielectric permittivity tensor that depends on $n_x$, $n_y$ and $n_z$. Implementing this approach in the model is possible, but increases the computational load and significantly complicates the optimisation process.

Despite the clear limitations of this simple model, it has still provided a very reasonable fit to the experimental data. More importantly, it has shed light on the behaviour of the LC director in the grating and has allowed us to understand and relate this to the diffraction. The model shows that the polymer network strongly restricts the director in the polymer wall region, with an extremely high effective elastic constant of $1,500,000$ pN. Whereas the unpolymerised region has an elastic constant of 9.79 pN and, above a voltage of $\sim$1.5 V, the director reorients, producing a modulation in the refractive index between the two regions and the onset of diffraction. Finally, the model predicts a polymer wall width of 0.93 µm, which is in good agreement with the value of 0.87 µm obtained from the analysis of the POM images of the grating shown in Figure 7.14.

### 7.3.2 Multilayer Diffraction Gratings

One of the powerful advantages of 2PP-DLW, as compared to many other lithography techniques, is the ability to fabricate in 3-dimensions. In conventional photolithography, pseudo-3D structures can be built up slowly, in a layer-by-layer fashion with multiple processing steps in between the fabrication of each layer. This process is both time-consuming and technically challenging as each step in the process has to be tested and refined throughout the development of the fabrication procedure. In contrast, 2PP-DLW enables structures to be rapidly fabricated on multiple planes within a transparent material, without laborious intervening processing steps.

In this section, the 3D capabilities of 2PP-DLW are employed to rapidly-prototype multilayer switchable DOEs. The advantage of writing multiple diffractive structures within one device is to increase the functionality and utility of the device. Rather than just being able to switch a DOE on and off, as in the previous section, multilayer gratings enable switching between at least two different diffraction patterns.

The strength of these devices lies in the simplicity of their operation. The clear competition for mutlilayer switchable DOEs are phase-only LCOS (Liquid Crystal On Silicon) spatial light modulators (SLMs) which were commercialised in the early 2000s and are now a mature technology. They allow a user to switch between arbitrary pixellated DOE designs with a switching speed of a few ms[207]. However, these devices are quite costly as they require complex active-matrix CMOS backplane electronics to drive the pixels of the LC layer. In contrast, the multilayer DOEs described in this chapter allow switching between different phase patterns in an incredibly simple LC device with uniform ITO electrodes. These devices therefore have the potential to sit in-between fixed DOEs and fully-programmable pixellated SLMs.

A conceptual schematic of a multilayer switchable DOE consisting of two orthogonal gratings is presented in Figure 7.31. The polymer walls of grating A are fabricated such that they are tethered to the bottom substrate of the device and the polymer walls of grating B are tethered to the top substrate. Note that this simple schematic shows the gratings as having the same period but with orthogonal orientations of the polymer walls. In practice, any arbitrary structure could be written, ranging from 1D gratings with varying pitches, to 2D gratings, to totally arbitrary phase holograms.

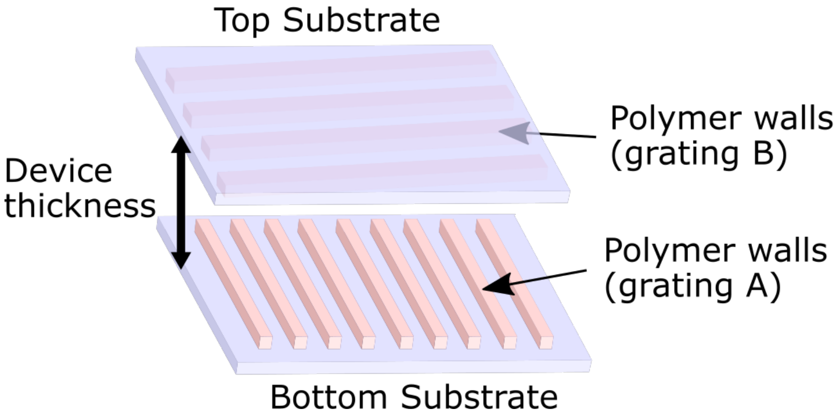

FIGURE 7.31: Schematic showing the configuration of a bilayer switchable diffractive optical element. Grating A has been tethered to the bottom substrate and grating B has been tethered to the top substrate of the device.

In order to fabricate a switchable DOE, where the device can switch between the two different diffraction gratings, the writing voltage for the polymer walls comprising each grating must be different. This is similar conceptually to the read-on-demand structures described in Chapter 5. There are particular similarities with the microbicycle structure (Fig. 5.10), where multiple voltage-dependent director profiles were stabilised in close proximity within an LC device. In contrast, for these multilayer DOEs, polymer walls with different director profiles are stabilised in precisely the same region of the device, but are spatially separated across the thickness of the device. Note that for the polymer structures in Chapter 5 the feature of interest was the appearance of the structures when viewed with polarised optical microscopy. Whereas for DOEs, it is the phase difference imparted on light passing through the structures that is the key phenomenon of interest.

Figure 7.32 illustrates a schematic cross-section of the fabrication process. The focus depth of the laser is changed during fabrication, such that one grating is tethered to the bottom substrate, and a second grating is tethered to the top substrate. In addition to the change in fabrication height, the voltage applied to the LC layer is also changed during the process so that the polymer walls comprising each grating are written at different voltages. Note that, for clarity in this schematic, grating A is shown being written at 0 V and grating B at an arbitrary voltage above the Fréedericksz threshold for the device. In practice, however, it is not required for one of the fabrication voltages to be 0 V. Other technical details regarding the techniques that were developed for fabrication in 3D are described in the Methods section of this chapter (Section 7.2.1).

The switching behaviour after fabrication of a bilayer grating device is conceptually illustrated in Figure 7.33. At the write-voltage for grating A (0 V), grating B is active, as the polymer structures comprising grating B have locked-in a non-zero voltage state. This creates a refractive index modulation for grating B, between the unpolymerised and polymerised regions, while for grating A the director alignment is uniform across both regions.

In order to switch to grating A, an applied voltage with a magnitude equal to the write-voltage for grating B is applied to the device, rendering grating B inactive and switching grating A to an active state.

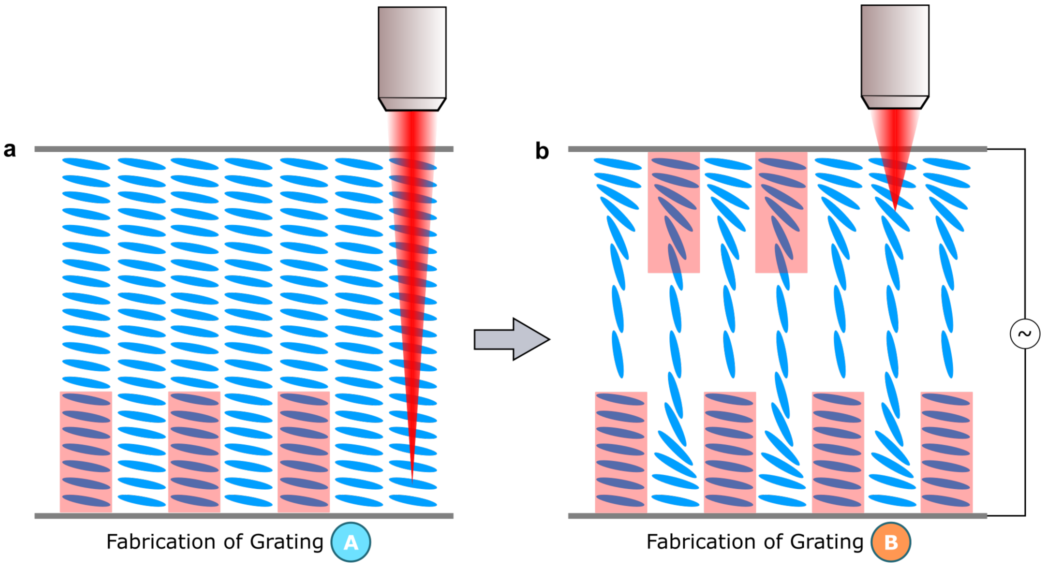

FIGURE 7.32: Schematic showing the fabrication procedure for a bilayer grating inside a liquid crystal device. (a) Grating A is fabricated such that the polymer structures are attached to the bottom substrate. During the fabrication there is no voltage applied to the device and the polymer structures lock-in the LC alignment at 0 V. (b) A voltage above the Fréedericksz threshold is then applied to the device, causing unpolymerised regions of the device to switch. Grating B is then fabricated in the same region of the device but attached to the top substrate (superstrate).

The unpolymerised regions of the cell are now in the same state as the state locked-in for grating B, so there is no refractive index modulation for grating B. However, there is a refractive index modulation for grating A, owing to the difference in the director profile between the polymer walls of grating A and the switched unpolymerised regions.

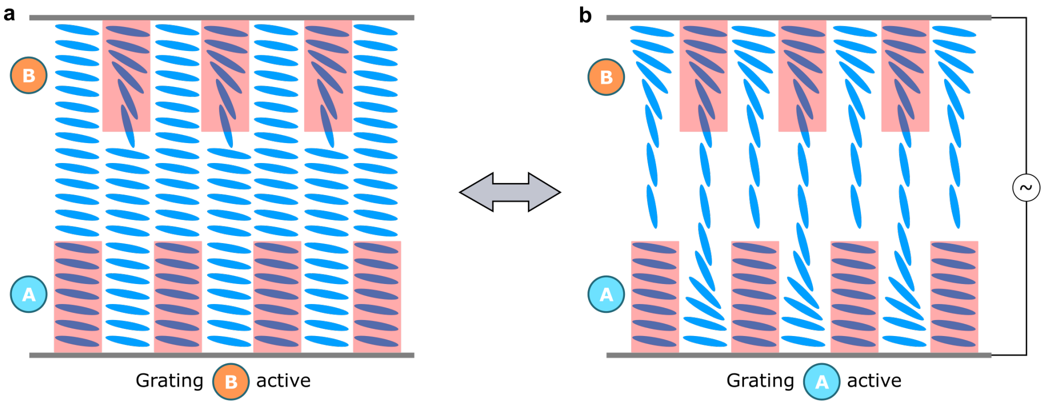

FIGURE 7.33: Schematic showing the effect of voltage when switching between two gratings in a bilayer diffraction grating written into a liquid crystal device. (a) In the absence of an applied voltage, grating B (which was written with the voltage on) is active. (b) Conversely, when the fabrication-voltage for grating B is applied to the device, grating A is active, as this was written with no voltage applied to the device.

The voltages used for fabricating each of the two gratings needs to be carefully selected to ensure maximum diffraction efficiency. For maximum diffraction efficiency in a binary phase grating, the phase difference should be equal to $\pi$[169]. Therefore we must find the relationship between phase and voltage for this device, so that the polymer structures of each grating can be written such that they have a phase difference equal to $\pi$. As the dependence of phase on voltage depends on the particular device and mixture, it is best established empirically by studying the transmissive behaviour of the device when oriented between crossed polarisers.

The optical layout in Figure 7.23 was used to obtain the transmission versus voltage between crossed polarisers for a 20 µm thick device containing the polymerisable LC mixture used in this study. It is necessary to use a larger cell thickness for bilayer DOEs in order to spatially separate the gratings in the z-direction. The result of this experiment is shown in Figure 7.34. There are many more oscillations in the transmission when compared to a 5 µm cell (Fig. 7.24), due to the increased effective birefringence resulting from the greater cell thickness.

To select suitable voltages for the fabrication of each grating we choose the voltages of a peak and a trough in the transmission-voltage graph. Peaks are where the device is effectively functioning as a half-waveplate, and the polarisation is rotated by 90° from the polariser axis to the analyser axis. Troughs are where the device is functioning as a full-waveplate (lambda plate) and the polarisation orientation is unchanged from the original orientation of the polariser, resulting in extinction after the analyser. The transmission of a birefringent layer between crossed polarisers, $T$, with its optic axis at 45° to the polariser axes, can be related to phase, $\phi$, through the equation[16],

$$T = \sin^2\left(\frac{\phi}{2}\right) \tag{7.5}$$

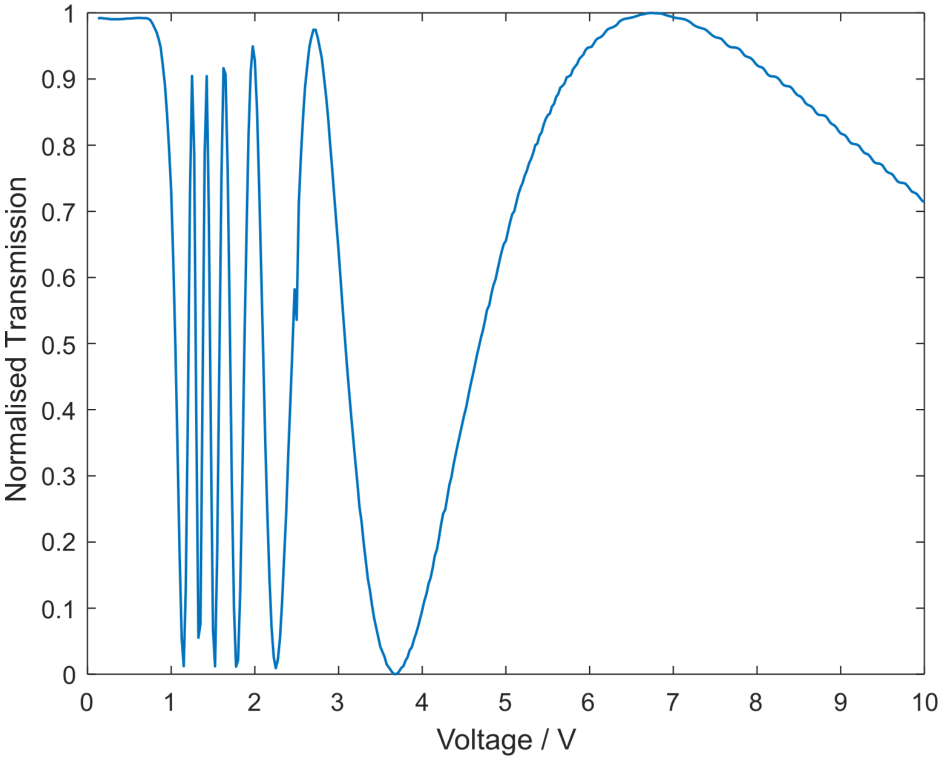

FIGURE 7.34: Transmission versus voltage between crossed polarisers for a 20 µm thick device containing the polymerisable LC mixture.

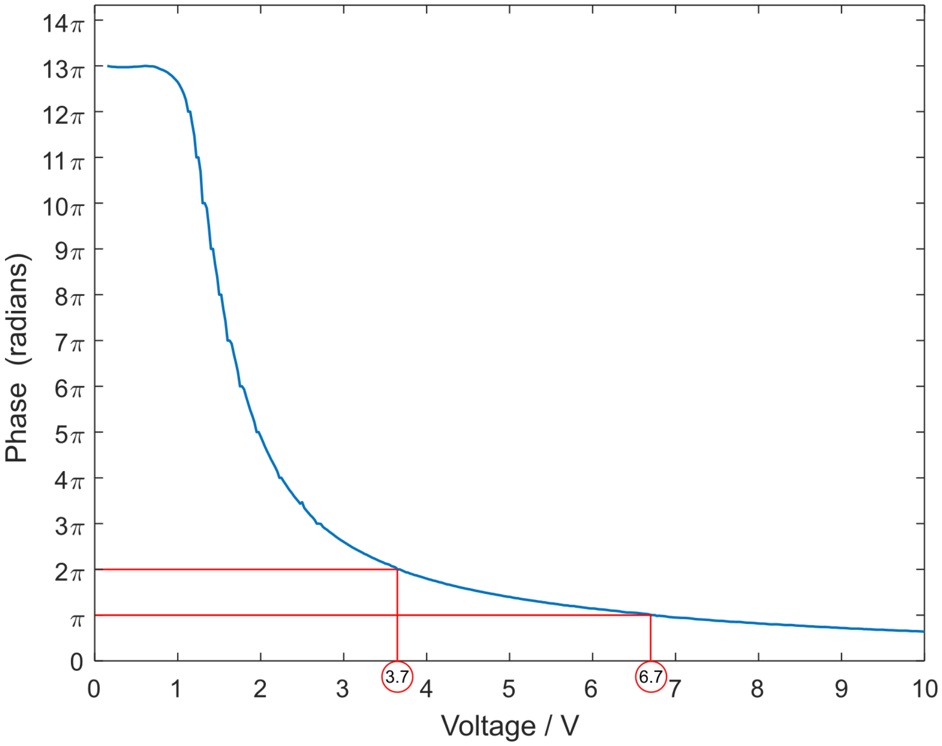

FIGURE 7.35: Phase versus voltage for light of wavelength 635 nm passing through a 20 µm thick device containing the polymerisable LC mixture.

Note that this relation is, strictly speaking, the transmission normalised to the maximum transmission through the device. See Section 2.7.2 for a complete description of the transmission through an LC device at an arbitrary angle to the polariser transmission axis.

Using the above equation, the phase can be extracted from the transmission versus voltage, and the result of this is shown in Figure 7.35. Although in theory any two voltages with a phase difference equal to $\pi$ could be selected, in practice it was most suitable to choose the highest-voltage peak and trough, because the period between oscillations in the transmission becomes longer at higher voltages. This is equivalent to the gradient of the phase versus voltage graph decreasing as the voltage increases. Therefore any small error in the applied voltage will be less likely cause a dramatic change in the phase. Following this approach, for 20 µm thick devices, 3.7 V and 6.7 V were chosen as the write voltages for the two gratings.

To initially test the multilayer diffraction grating concept, a relatively simple orthogonal grating design was chosen, where the polymer walls of the grating B were written perpendicularly to the polymer walls of grating A. This configuration is convenient because the diffraction patterns from each grating are easy to interpret and the orthogonality of the diffraction patterns should be highly apparent. Using the cell thickness scans described in Section 7.2.1, the polymer walls were fabricated as close to the substrates as possible, to ensure the gratings were both spatially separated in the z-direction and tethered to the substrates.

Figure 7.36 shows a sequence of polarised optical microscopy images of the DOE under different applied voltage conditions. This collection of microscope images were all taken in the exact same region in the cell, so changes in appearance between the images are due solely

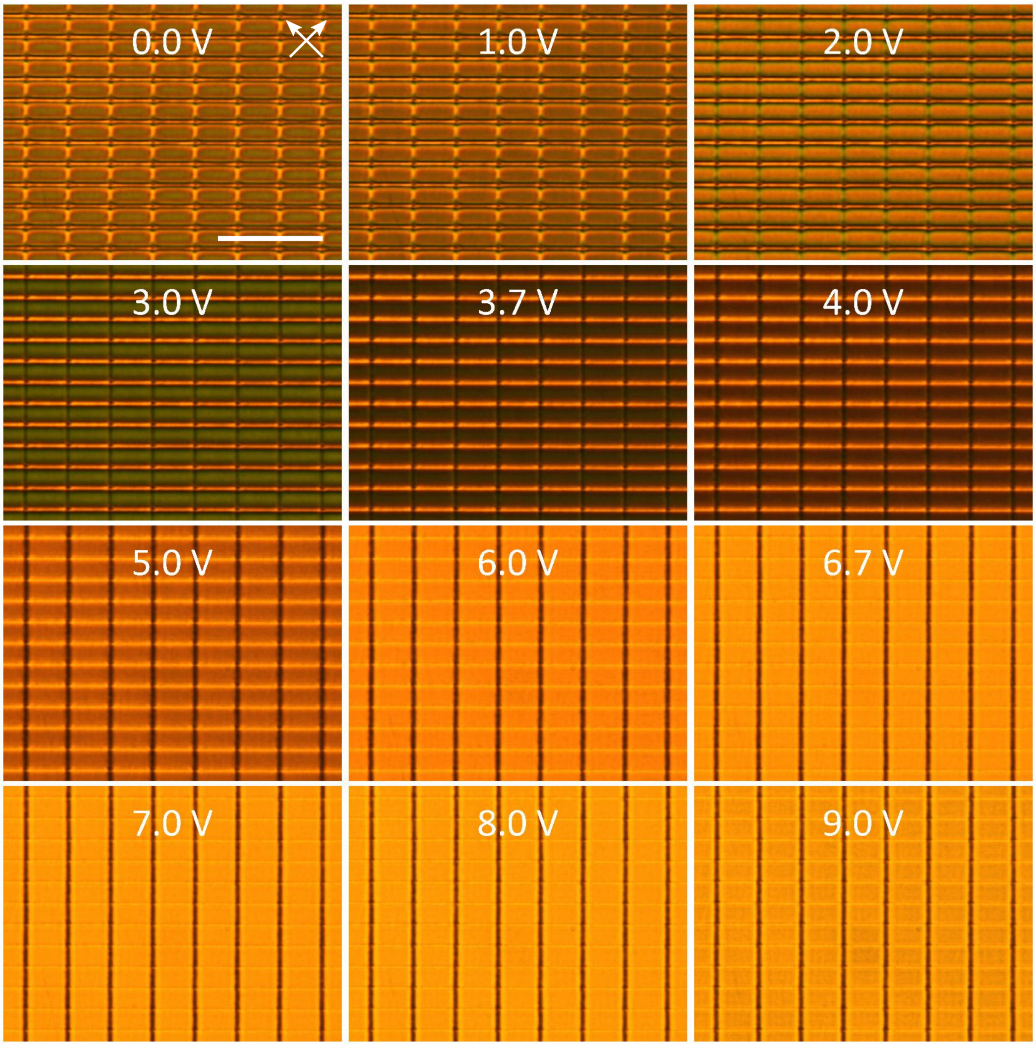

FIGURE 7.36: Polarised optical microscopy images of a bilayer orthogonal grating written in a 20 µm thick cell. The images shown were taken in the exact same position in the device, so that the only difference in the conditions under which each image was taken was the magnitude of the voltage applied to the LC cell. The white arrows indicate the orientation of the crossed polarisers and the scale bar is 50 µm.

to the change in the magnitude of the voltage applied to the device. The grating tethered to the bottom substrate, grating A, was written at 3.7 V with a grating period of 20 µm and is vertically oriented in these images. Whereas grating B was tethered to the top substrate, was written at 6.7 V with a period of 10 µm, and is horizontally-oriented.

At an applied voltage of 3.7 V, grating A is invisible in the POM images due to the homogeneity between the bulk director and the director of the polymer walls locked-in at 3.7 V. Thus, at this voltage, grating B is most visible because the polymer walls comprising this grating were locked-in at 6.7 V and therefore have a different director profile to the bulk. The horizontally oriented polymer walls of grating B are clearly visible in Figure 7.36 at 3.7 V.

Conversely, at an applied voltage of 6.7 V, grating B becomes invisible as the director in the bulk of the device is in the same director state as the polymer walls of grating B. Therefore, at this voltage, grating A is most visible due to the difference in the director in the bulk of the device and the polymer walls of grating A, as can be seen in Figure 7.36 at 6.7 V.

The diffraction patterns produced by this bilayer switchable DOE are presented in Figure 7.37 for the same applied voltage magnitudes shown in the POM images above in Figure 7.36. Note that the distances between diffracted orders in the vertically-oriented diffraction pattern are larger, as they are produced by grating B which has a smaller pitch than grating A. Below 3 V, a mixture of the horizontal and vertical diffraction patterns is clearly visible. As the voltage is increased, the horizontal diffraction pattern disappears near 3.7 V, the writing voltage for grating A. Increasing the voltage further, the vertical diffraction pattern completely disappears at 6.7 V, the writing voltage for grating B. In this way, the

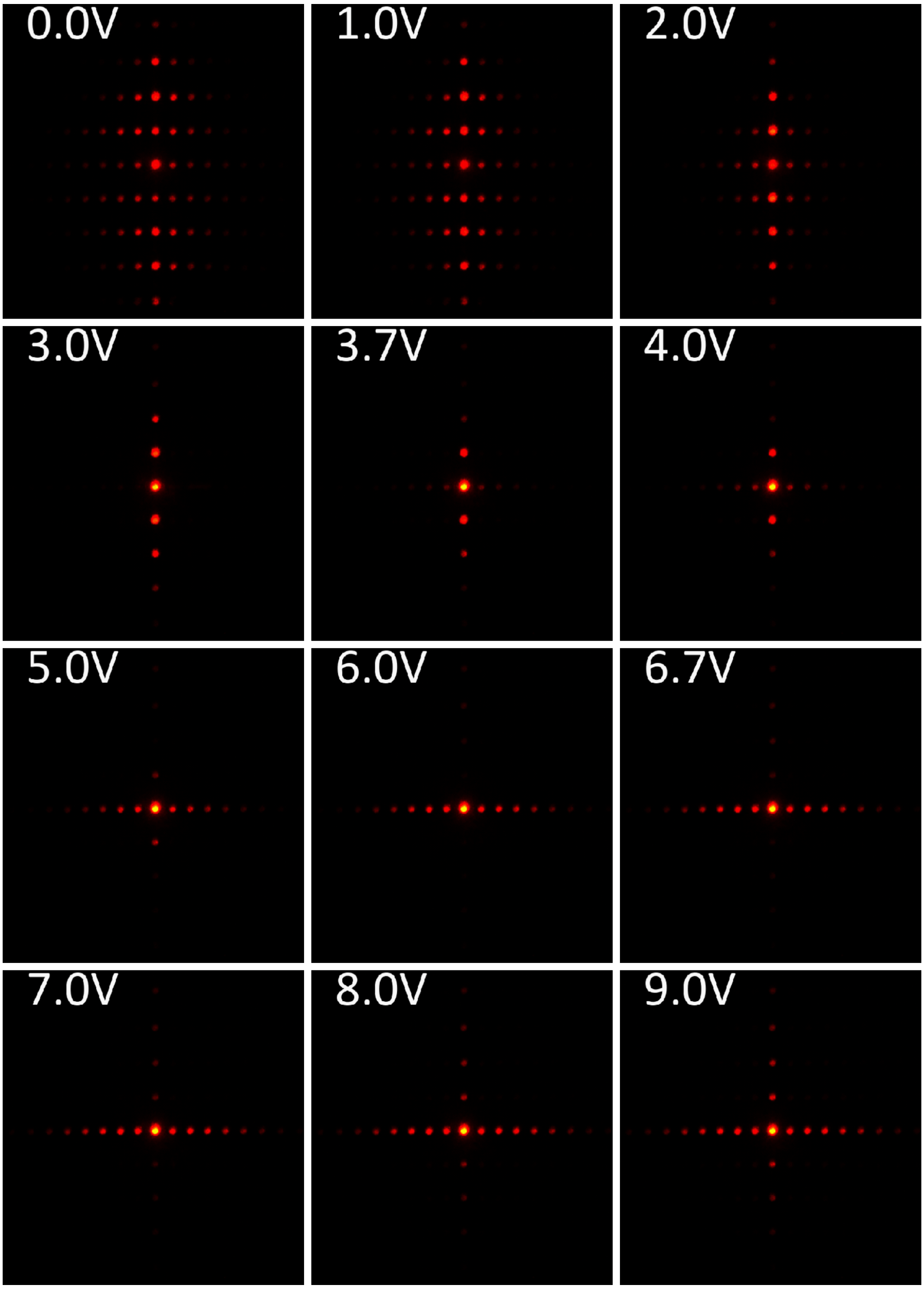

FIGURE 7.37: Diffraction patterns from a 20 μm thick switchable orthogonal grating. At the writing voltages of 3.7 V and 6.7 V, only one diffraction pattern is visible, while at other voltages a mixture of the two patterns is observed. For the diffraction pattern visible at 3.7 V, it appears actual index-matching occurs at 3.0 V, instead of 3.7 V.

diffraction pattern generated by the bilayer grating can be switched by applying a voltage of either 3.7 or 6.7 V to the device.

However, on closer inspection, it appears that the vertical diffraction pattern produced by grating B is in fact most visible at 3.0 V, rather than the writing voltage of 3.7 V. This effect could be caused by the polymer walls written at 6.7 V exerting an elastic influence on the unpolymerised LC in the device. Locking-in this higher voltage creates an anchoring surface in the cell that influences the bulk LC to be more tilted than the 0 V equilibrium state of the cell. This would effectively lower the correct index-matching voltage for grating A written at 3.7 V, as the LC in the bulk will switch at a lower voltage due to the influence of the polymer walls anchored at 6.7 V.

Having demonstrated a simple bilayer grating consisting of two spatially-superimposed orthogonal diffraction gratings that can be switched by applying a uniform voltage, we will now explore the fabrication of a bilayer grating that exploits some of the other unique capabilities of 2PP-DLW. For comparison, using interference lithography, the conventional method for making switchable LC gratings, it is straightforward to create simple 1D gratings. However, there is a significant challenge in creating more complex structures, as this requires interference of multiple beams. Furthermore, to fabricate completely aperiodic gratings (such as computer generated holograms) requires holographic masks, further adding to the complexity of the technique. In contrast, with 2PP-DLW, we can use free-form arbitrary patterning and fabricate highly aperiodic structures with ease, such that it is just as straightforward to fabricate a simple 1D grating or complex CGH.

Figure 7.38 shows a schematic of a bilayer grating where one of the two gratings in the device has a triangular structure. The fabrication

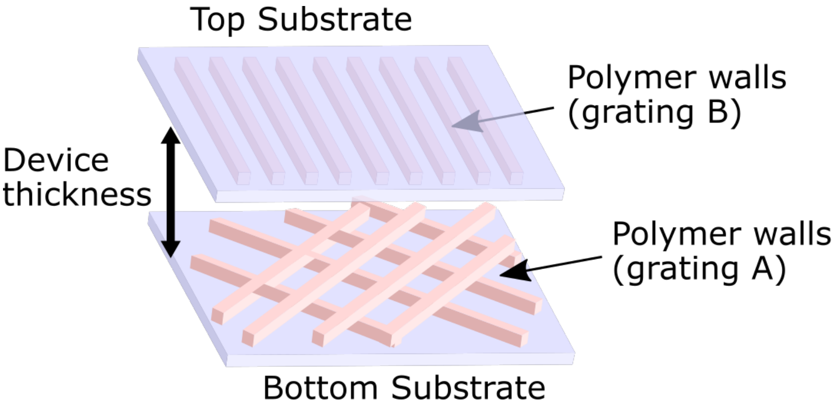

FIGURE 7.38: Schematic showing the configuration of a bilayer switchable DOE where one grating is a triangular grating. Grating A, the triangular grating, has been tethered to the bottom substrate and grating B, a conventional 1D grating, has been tethered to the top substrate of the device. Note that the specific gratings shown are representative structures only.

of this device is conceptually similar to the orthogonal bilayer grating described above but with a more complex grating design. A device of the same cell thickness used for the orthogonal grating, 20 µm, was used, which meant that the relationship between phase and voltage was the same as in Figure 7.35. Therefore, the same voltages, 3.7 V and 6.7 V were used as writing-voltages for the fabrication of this bilayer DOE, as that ensures a phase difference equal to $\pi$ between the two gratings.

POM images of the triangular bilayer grating at a range of applied voltages are shown in Figure 7.39. Grating A was comprised of periodic triangular elements with a pitch of 5 µm written at 3.7 V, while grating B was a 1D diffraction grating with a pitch of 5 µm written at 6.7 V. Therefore, at an applied voltage of 3.7 V, grating A is invisible and only grating B, the 1D grating is visible. Conversely, at an applied voltage of 6.7 V, grating B is invisible and only grating A, the triangular grating, can be seen.

The diffraction patterns generated by this DOE are shown in Figure 7.40 for the same range of voltages as shown in the POM images above in Figure 7.39. Similarly to the bilayer orthogonal grating, at an applied voltage of 3.7 V, only the 1D diffraction pattern produced by

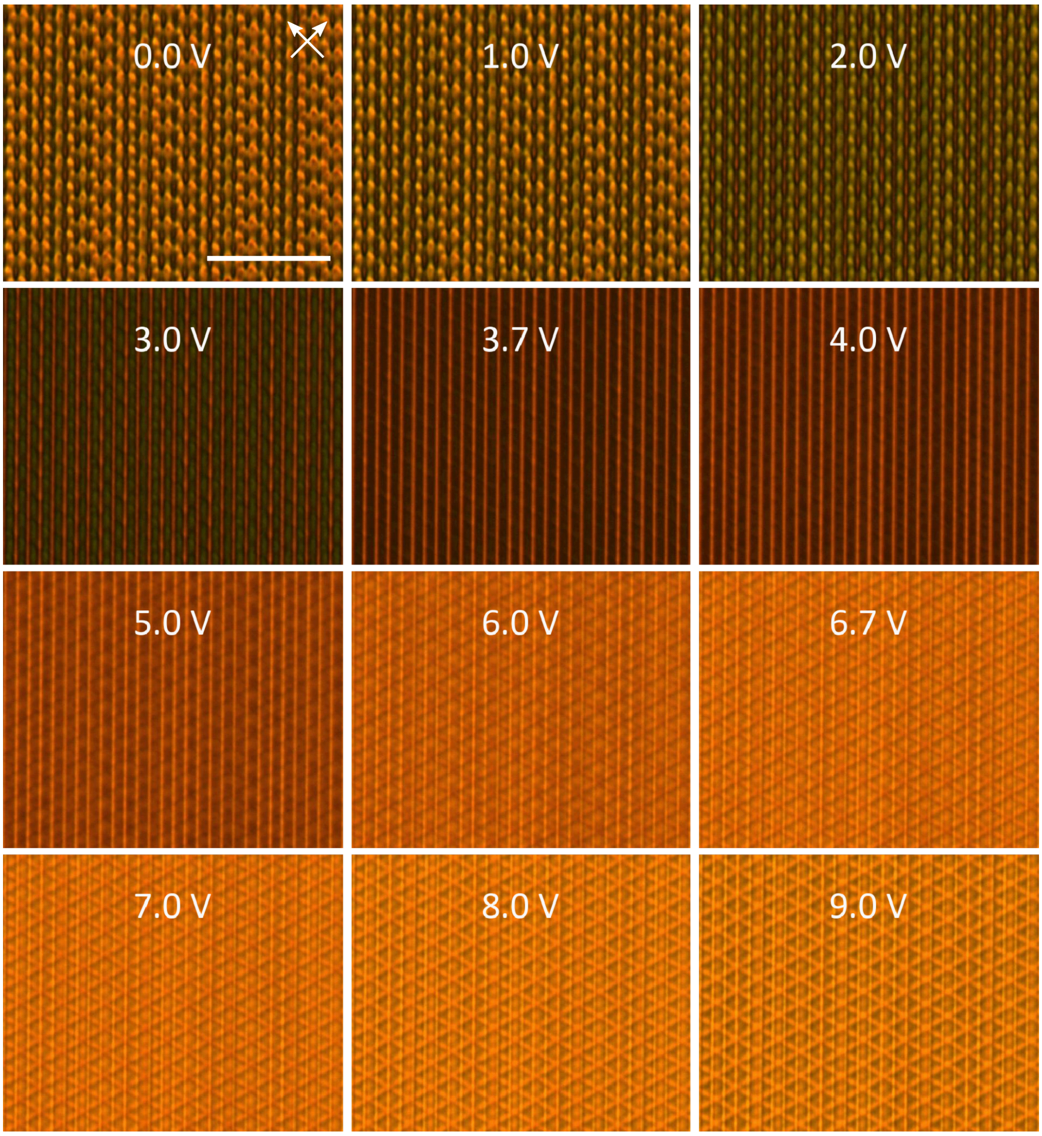

FIGURE 7.39: POM images of a bilayer DOE where one layer is a triangular grating. The images shown were taken in the exact same position in the device, so that the only difference in the conditions under which each image was taken was the magnitude of the voltage applied to the LC cell. The focus of the microscope is in the centre of the cell. The white arrows indicate the orientation of the crossed polarisers and the scale bar is 50 µm.

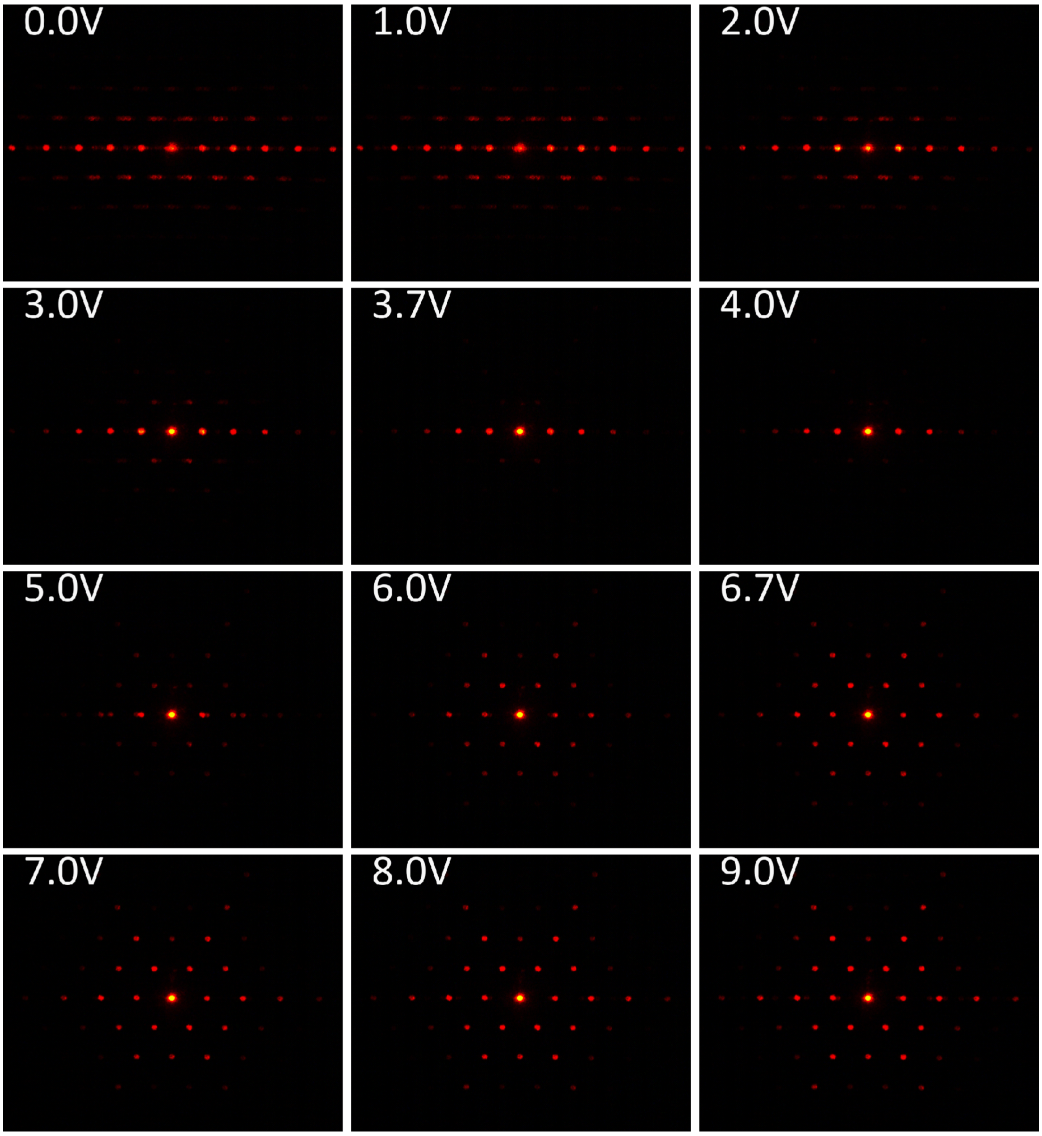

FIGURE 7.40: Diffraction patterns from a 20 µm thick switchable bilayer DOE where one layer is a triangular grating. At an applied voltage of 3.7 V, only a horizontal diffraction pattern is visible, while at other voltages a mixture of the two patterns is observed. At 6.7 V, the hexatic diffraction pattern resulting from the triangular grating is visible.

grating B is visible. As the voltage is increased to the writing voltage of grating B, 6.7 V, the pattern changes to the hexatic diffraction pattern produced by grating A, the triangular grating.

The bilayer DOEs described in this section are the first demonstration of a new type of switchable LC diffraction grating. Although LCs have been used in switchable diffractive optics, these previous technologies can typically only be switched between being on or off (i.e. producing a diffraction pattern, or not producing a diffraction pattern). In contrast, bilayer DOEs engineered with 2PP-DLW can be switched between two totally different diffractive states by exploiting the ability to laser write polymer structures at different voltages and on different layers within a device.

Furthermore, with many existing LC-DOE technologies, there is no flexibility to choose the mode of operation of the grating. POLICRYPS and H-PDLC gratings are completely restricted to operating in the conventional mode, where the diffraction is on by default (default meaning when no voltage is applied). On the other hand, existing demonstrations of PSLC gratings have operated in reverse-mode, where the diffraction is off by default[181, 182]. In contrast, gratings engineered here with two-photon polymerisation can be fabricated to operate in either conventional or reverse-mode by simply changing the voltage used to fabricate the polymer structures. If the polymer structures are fabricated at 0 V, the grating will operate in reverse-mode and be off at 0 V. However, if the polymer structures are fabricated at an applied voltage above the Fréedericksz threshold, the grating will operate in the conventional mode and be on at 0V.

### 7.3.3 Computer Generated Phase Holograms

As shown throughout this thesis, 2PP-DLW can be used to fabricate arbitrary patterns inside transparent materials. In this section, we extend the discussion from diffraction gratings to computer-generated holograms that produce recognisable images in the far-field diffraction pattern.

The arbitrary patterning capabilities of 2PP-DLW represent a significant advantage over conventional high-resolution microfabrication methods. An example of such a method is interference lithography, where the periodicity of a diffraction grating is dictated by the distance between fringes in an interference pattern. Consequently, it is possible to produce gratings with a very small period, but impossible to produce structures that are aperiodic.

Computer generated holograms are optical elements that produce a recognisable image, in the far-field diffraction pattern (in holography, this is sometimes called the replay field). The phase maps that define a hologram are highly aperiodic and so 2PP-DLW is well-suited to the task of fabricating a CGH, due to the ability to arbitrarily control the exposure pattern of the writing laser.

The optical system for capturing data from CGHs was slightly different from the characterisation system used to obtain data from the diffraction gratings described in the previous section. A schematic of the optical layout is shown in Figure 7.41, which highlights the use of a Fourier transform lens to bring the far-field diffraction pattern to the focus of the lens where it can be captured with a screen or a CCD. In practice, it was found that the image quality resulting from capturing a replay field directly onto a CCD was vastly superior than images taken of a replay field projected onto a screen.

CGHs were generated using the Gerchberg-Saxton

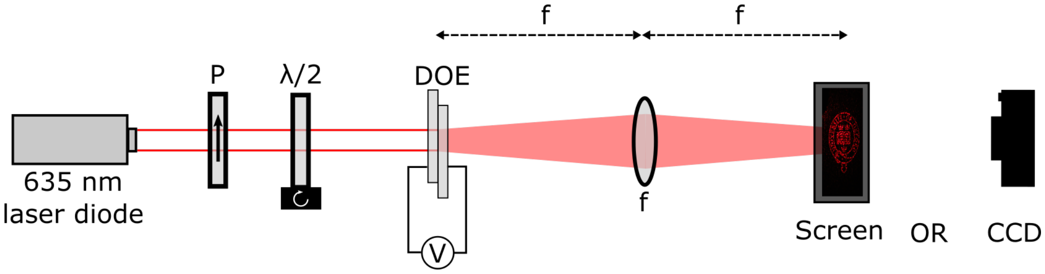

FIGURE 7.41: Schematic of the optical layout for capturing diffraction patterns produced by computer generated holograms. A Fourier lens is used to bring the far-field diffraction pattern to the focus of the lens for capture by a CCD or screen.

algorithm[190] described in detail in Section 7.1.2 and implemented in MATLAB. The target image was a 512 × 512 pixel binary image of the Oxford University crest that was resized to a 128 × 128 pixel image before being placed in the upper left corner of a black 256 × 256 pixel image. The reason for placing the desired target in the upper corner of the image input to the GS algorithm is to prevent overlap in the replay field with the zero order spot and the conjugate image. The output of the GS algorithm was a 256 × 256 pixel binary hologram.

The binary CGH was fabricated in a 5 µm thick LC cell following the method described in Section 7.2.1, using the same anti-parallel rubbed polyimide LC cells and same mixture as those used for all DOEs described thus far. Also described in Section 7.2.1 are the modifications to the fabrication procedure that are required for fabricating CGHs over a large area. The hologram was written over an area of 2048 × 2048 µm, such that each pixel of the hologram was a size of 8 × 8 µm.

A MATLAB script converted the hologram design into an AeroBasic fabrication routine that wrote the hologram line-by-line with a spacing of 1 µm between adjacent lines. The speed modulation method (see Section 7.2.1) was employed to considerably reduce the fabrication time. The writing voltage for the fabrication was 0 V, as the DOE was intended to operate in reverse-mode and be off in its default state with no voltage is applied.

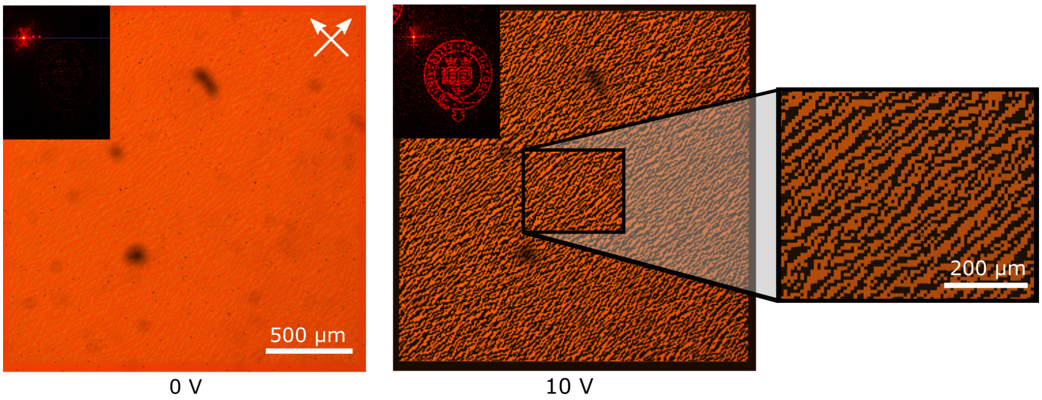

FIGURE 7.42: POM images at an applied voltage of 0 V and 10 V of a 256 × 256 pixel binary CGH designed to produce an image of the Oxford University crest in the replay field. The inset images show the first order of the replay field at 0 V and 10 V. A zoomed-in image is shown for the device under an applied field of 10 V. The white arrows indicate the orientation of the crossed polarisers in all the images.

Figure 7.42 shows POM images of the switchable CGH taken with a magnification of 10X. At 0 V, the hologram is largely invisible, due to index-matching between the unpolymerised and polymerised regions of the structure which were written at 0 V. At an applied voltage of 10 V, the unpolymerised regions have switched, highlighting the polymerised pixels of the CGH that have locked-in the 0 V state. The unpolymerised pixels are therefore free to switch, while the polymerised pixels have been locked-in. The inset zoomed image was taken at 20X magnification and shows the detail of the structure of the hologram.

The inset images in Figure 7.42 show the first order of the diffraction pattern produced by the hologram at 0 V and 10 V. The zero order spot is visible in the upper left of the images. Similarly to the 1D diffraction grating described in Section 7.3.1, the 1st order is faintly visible at 0 V. This effect can likely be attributed to the formation of the polymer network disturbing the equilibrium alignment of the LC, slightly decreasing the order parameter in the polymerised region.

Figure 7.43 shows the first order of the replay field at voltages from 0 V to 5.5 V in 0.5 V steps. It can be seen that the replay field becomes completely invisible at 1 V and goes through another minimum

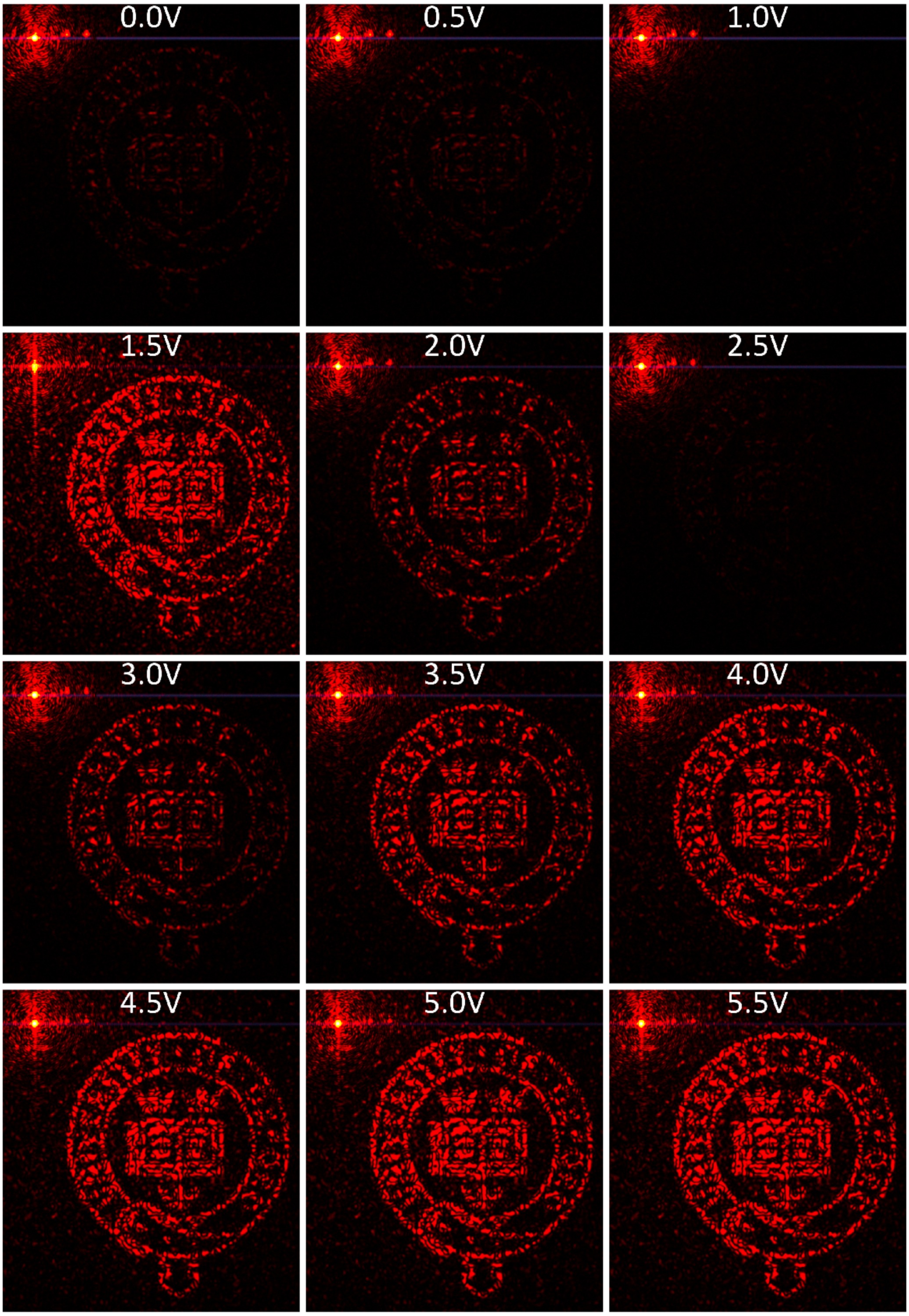

FIGURE 7.43: Images of the first order of the replay field produced by a CGH designed to create an image of the Oxford University crest. The voltages range from 0 V to 5.5 V in 0.5 V steps. There are minima in visibility at 1 V and 2.5 V.

of visibility around 2.5 V. We can assume that at these minima, the phase of polymerised and unpolymerised pixels must be equal and therefore no diffraction occurs. Furthermore, the fact that the actual phase-matching condition occurs at 1 V rather than 0 V supports the hypothesis that the formation of the polymer network slightly lowers the order parameter of the LC and decreases the $n_{eff}$ of the polymerised pixels. At 1 V, the LC has just begun to switch and therefore $n_{eff}$ in this state is slightly lower than the equilibrium state at 0 V, showing that the $n_{eff}$ of the polymerised pixels is slightly lower than the $n_{eff}$ of the unpolymerised mixture.

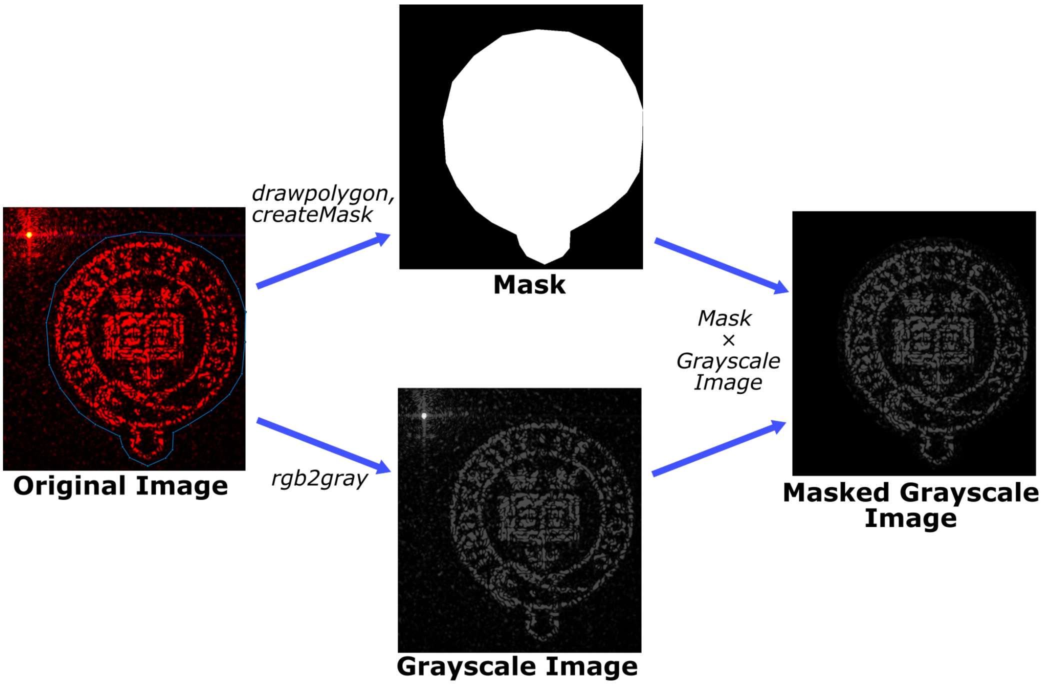

FIGURE 7.44: Flowchart showing the image analysis process for obtaining an estimate of intensity from images of the diffraction pattern.

To further analyse the effect of voltage on the intensity of the replay field, an image analysis routine was performed on images of the type shown in Figure 7.43. A schematic flowchart of this process is shown in Figure 7.44. The images were first masked by drawing a polygon around the Oxford University crest. This mask was applied to a greyscale version of the original RGB images to produce greyscale images of the replay field that excluded the zero order and surrounding optical noise.

The pixels in these masked greyscale images were then summed to obtain an estimate of the intensity of the image for each applied voltage.

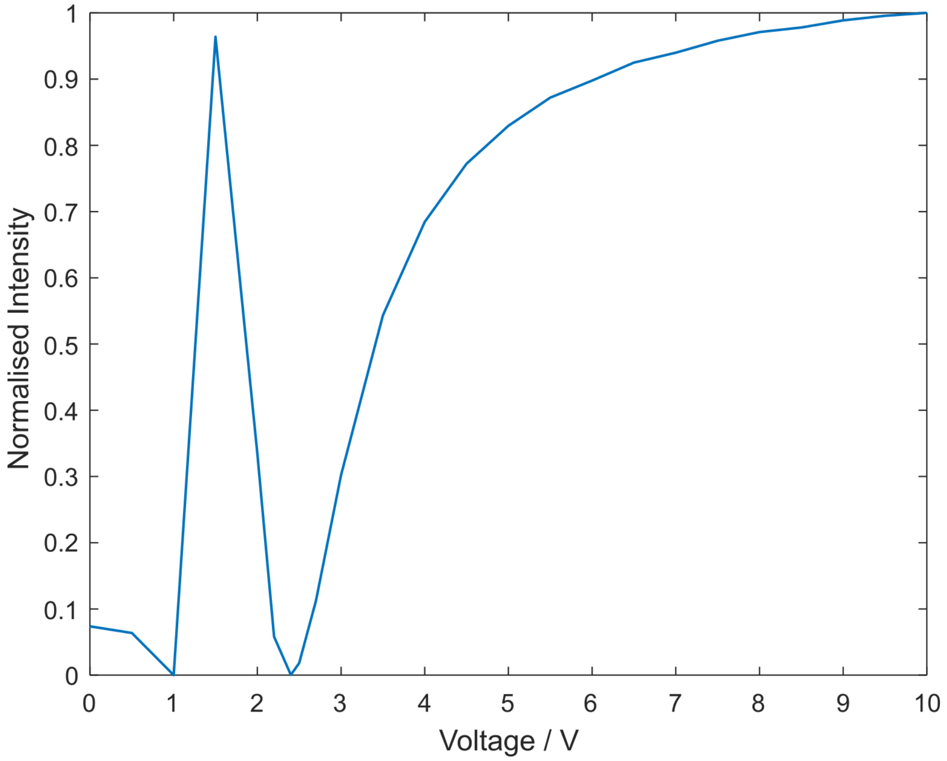

FIGURE 7.45: Normalised intensity of the first order against voltage for a CGH designed to produce an image of the Oxford University crest in the replay field.

The relationship between the first order intensity and voltage is shown in Figure 7.45. The overall shape of this graph including the minima in intensity at 1 V and 2.4 V as well as the maximum in intensity at ∼1.5 V can be understood by considering the dependence of phase on voltage for this polymerisable mixture in a 5 µm thick device (Figure 7.46). This can be obtained from studying the dependence of transmission versus voltage in between crossed polarisers, in the same way as described previously for a cell of thickness 20 µm.

Red vertical lines have been drawn on the graph in Figure 7.46 at a voltage of 1 V and 2.4 V, corresponding to the intensity minima. Horizontal red lines show the phase at these voltages. At 1 V, where the unpolymerised pixels and polymerised pixels are perfectly phase-matched, it can be seen that the phase is slightly decreased from the

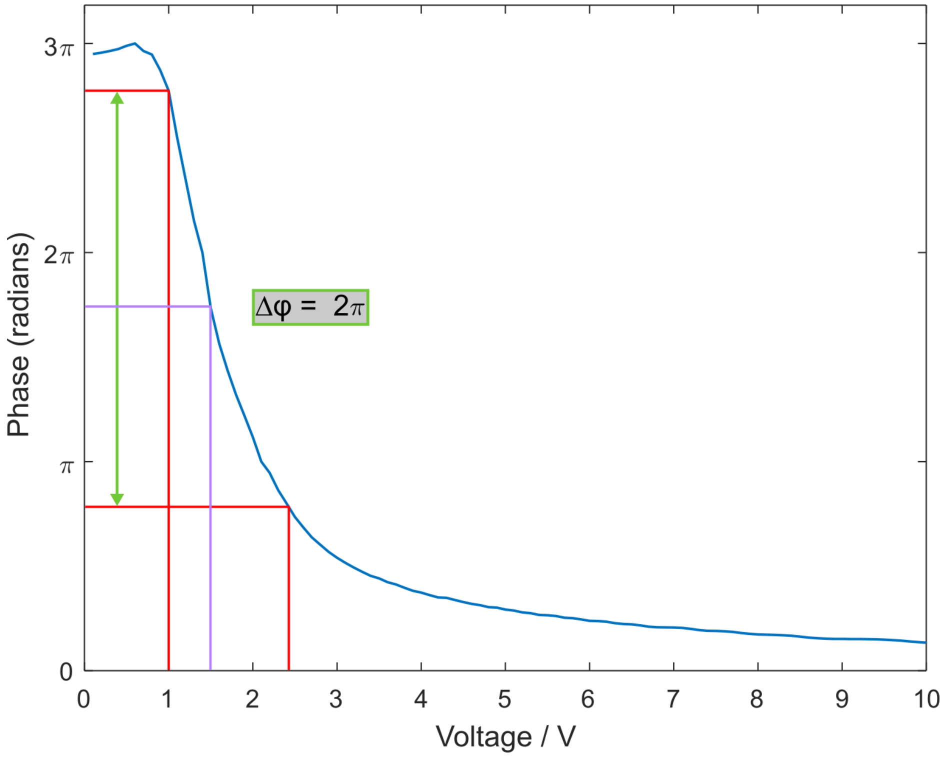

FIGURE 7.46: Phase against voltage for the polymerisable mixture in a device of thickness 5 µm for light of wavelength 635 nm. Red lines have been drawn from the minima in intensity at 1 V and 2.4 V for a laser written CGH, to show the phase of the device at these voltages. Purple lines have been drawn from the intensity maximum at 1.5 V to show that the phase difference from the intensity minima is equal to $\pi$ at this point.

phase at 0 V. This further supports the hypothesis that the polymerisation slightly decreases the $n_{eff}$ of the mixture, such that index-matching occurs at a slightly higher voltage than expected.

The minimum at 2.4 V in Figure 7.45 is shown in Figure 7.46 to have a phase difference of 2$\pi$ from the device at 1 V. Minima are expected to occur whenever the phase of the unpolymerised and polymerised pixels of the CGH are equal and at any 2$\pi$ multiple thereof. Conversely, maxima in a binary hologram should occur when there is a $\pi$ phase difference between unpolymerised and polymerised pixels. Purple lines show the phase of the device at the intensity maximum of 1.5 V, which is indeed separated by $\pi$ from the phase at each intensity minima; explaining the existence of the maximum at 1.5 V in the intensity versus voltage graph in Figure 7.45.

## 7.4 Summary

This chapter has described the first application of the 2PP-DLW fabrication technique to manufacturing LC-DOEs using a tunable LC resin. The process is remarkably flexible, whereby the switching behaviour of DOEs can be programmed during the fabrication by simply changing the write-voltage of the polymer structures that comprise the DOE. These devices have favourable properties that mean they are well-positioned to compete with existing switchable DOE technologies. The key findings of this chapter are presented below along with discussion, comparisons with other technologies and potential avenues to explore in future work.

Firstly, parallel polymer walls were written in an LC device at 0 V, to form a 1D switchable diffraction grating. The switching properties of this DOE were studied and compared with a COMSOL wave-propagation model of the LC director in the grating. This model provided a good match with the experimental data and increased our understanding of the switching behaviour inside the grating by showing that the polymer walls very strongly anchor the director, with an effective elastic constant of $1,500,000$ pN.

Following this, bilayer switchable diffraction gratings were demonstrated by exploiting the 3D patterning capabilities of 2PP-DLW. Initial work was in the form of a bilayer orthogonal grating, where the device could be switched between producing vertically and horizontally oriented diffraction patterns with the application of voltages used during the fabrication. To further explore the unique possibilities offered by 2PP-DLW, a bilayer grating was fabricated where one grating had a triangular structure. In order to create such a grating with interference lithography would require interference of multiple beams or multiple separate exposures. Whereas, with 2PP-DLW, not only can this structure be easily fabricated in a single step, it can also be fabricated on a specific plane of the device in order to create a multilayer DOE.

Finally, a switchable computer generated hologram that produced an image of the University of Oxford crest in the replay field was fabricated inside an LC device, and its switching properties were studied. The voltage-dependence of the intensity of the first order of the replay field was examined and explained by considering the voltage-dependent phase of the pixels comprising the CGH.

One of the most significant benefits of this approach to switchable DOEs is that the 2PP-enabled fabrication process supports multiple modes of operation. In many previously-reported LC diffraction gratings, including the industry-leading H-PDLC technology, fabricated devices are optically active by default (when no voltage is applied), such that a voltage is required to switch the device off. This limitation means that H-PDLC devices consume power in the off-state, which can be an undesirable characteristic for many applications where power consumption is of importance. In contrast, with LC-DOEs made via 2PP-DLW, gratings can be engineered to operate in reverse-mode and be optically inactive with the voltage off, by simply writing the polymer structures at 0 V during fabrication.

Although the simple 1D grating described in this chapter was fabricated such that it operated in reverse-mode, it could also be designed to work in conventional mode (with the diffraction on by default). To fabricate such a grating would simply require that the polymer walls be fabricated while a voltage above the Fréedericksz threshold is applied to the device. This would create a grating that was optically active when the voltage was off, and could be switched to an optically inactive state by applying a voltage equal to the write voltage. Therefore, in employing this fabrication technique for LC-DOEs, the grating designer is free to easily chose the mode of operation depending on the specific application and the desired switching properties of the DOE.

There are a number of contemporary applications of DOEs that could exploit some of the switchable LC-DOEs described in this chapter. LC-DOE gratings manufactured with 2PP-DLW could find use in 3D depth mapping technologies where gratings are used to create structured light illumination patterns. Versions of this technology, where DOEs are referred to as "dot projectors", are found in Apple's Face ID system and Microsoft's Kinect, but are limited to producing a fixed dot grid to illuminate a scene. For the high-resolution depth sensing required to process the movements of individual fingers and subtle changes in facial expression, illumination grids of thousands of infrared dots are projected onto a scene of interest and processed by cameras and dedicated ASICs[208].

There are several methods disclosed in the prior art for optical 3D depth mapping using time-coded illumination[209], beam steering[210] and switchable DOEs[211]. The bilayer LC-DOEs described in this chapter may find use in such applications as a switchable dot projector, able to project two different illumination patterns onto a scene. Alternatively, the simpler 1D switchable diffraction gratings may be similarly useful, as being able to switch the light source between flood illumination and dot projection may allow different sensors to collect multiple types of optical information with a single light source[211]. As many applications that use 3D depth mapping technology, including head-mounted displays, require extensive miniaturisation and have stringent power consumption requirements, there may be an advantage in combining multiple optical functions in one switchable device.

## 7.5 Future Work

As this chapter represents the first demonstration of switchable LC-DOE technology enabled by 2PP-DLW in an LC resin, there are many potential areas to explore in future work. These include some extensions of the existing experiments already described, and totally new concepts that have not yet been empirically explored. The following discussion presents some of these ideas for future work.

### 1D Conventional-Mode Gratings

The versatility of this approach to LC-DOEs should be tested by writing simple 1D diffraction gratings at write-voltages above the Fréedericksz threshold. By doing this, the grating should operate in the conventional mode where the diffraction is on at 0 V, as seen in H-PDLC and POLICRYPS devices. Although the reverse-mode grating described in this chapter is arguably more useful, there are some applications where conventional mode operation may be preferred. Therefore, it is essential to establish the versatility of the fabrication process and study the switching behaviour of a variety of gratings manufactured via 2PP-DLW.

### Blazed Gratings

3D fabrication is a clear advantage that 2PP-DLW holds over other microfabrication approaches, and this capability was used to manufacture the bilayer gratings described in this chapter. This work could be extended by attempting the fabrication of 3D switchable blazed gratings. This would involve fabricating a 3D grating, with a sawtooth-like cross section, in a layer-by-layer fashion tethered to the bottom substrate of a thick polymerisable LC device. The unpolymerised LC above the grating could then be switched to produce a contrast in the refractive index and switch the diffraction grating on. The blazed structure could be designed to diffract the majority of the incident light into one particular order. Gratings of this type are commonly used as input and output couplers in augmented reality waveguide technology[212] and the single-order diffraction efficiency is therefore a critical performance indicator to measure and evaluate.

### Multilayer Cascaded CGHs

Multilayer 3D laser writing could be extended to more-complex diffractive structures by combining bilayer gratings with computer generated holograms. There is considerable interest in stacked or "cascaded" CGHs for applications including multiplexed information display[213, 214], colour images[215] and multiwavelength optical interconnects[216]. Furthermore, stacked CGHs have been employed to improve image resolution[217] and diffraction efficiency[218] over conventional single-layer CGHs. Therefore there is considerable potential in using 2PP-DLW to pattern two different CGHs in the same area of a cell in order to manufacture a switchable bilayer LC-CGH device. As in the bilayer DOEs demonstrated in this chapter, the CGHs would be fabricated at two different write-voltages with a phase difference equal to $\pi$ to produce the highest possible diffraction efficiency, while preserving the ability to switch between the CGHs.

### Chiral Gratings

One of the additional advantages of using LC materials in the manufacture of DOEs is their ability to self-organise into structures with complex microstructures that exhibit unusual physical and optical properties. This is observed in chiral LCs where the constituent LC molecules spontaneously assemble into microscopic helices that collectively behave as a 1D photonic crystal. If the pitch of the chiral helices is of the order of the wavelength of light, a photonic bandgap is observed for a range of wavelengths whereby circularly polarised light is forbidden from propagating through the material unless it has the same handedness as the chiral helices.

The spontaneous self-organisation of chiral LCs could be employed to manufacture chiral diffraction gratings with unique polarisation-sensitive behaviour. This would involve doping a small quantity of chiral dopant into a polymerisable LC mixture such that a uniform standing helix structure forms inside a standard LC cell with a pitch on the order of the wavelength of light. A diffraction grating could then be written in the cell with 2PP-DLW, to lock-in this chiral structure in a series of parallel polymer walls. After fabrication, the grating could be made optically active by applying a large voltage to unwind the chiral helix, causing the unpolymerised regions of the device to switch to a vertically oriented director profile. Due to the flexibility of 2PP-DLW, the fabricated structure could be a hologram or another complex DOE, leading to the interesting possibility of the device being able to split light into separate replay fields with different circular polarisations.

### Tunable LC-DOEs

It is notable that the LC-DOEs fabricated with 2PP-DLW in this chapter, have been switchable, but not tunable. That is, their switching behaviour is inherently discrete rather than continuous. For many applications of DOEs, such as in beam steering and adaptive optics, it is essential that a device have a tunable phase profile. In the case of beam steering applications, this is required so that a beam can be steered continuously over a given range, and in adaptive optics it is critical that the strength of an aberration mode can be adjusted smoothly to precisely correct for aberrations in an optical system.

One potential solution to this is found by observing that it is possible to obtain an approximation to tunable behaviour by using a series of binary switchable elements. This was employed by Facebook Reality Labs in their recent demonstration of a cascaded switchable LC lens device developed to solve the pernicious vergence-accommodation conflict in head-mounted displays[219]. In a similar manner, it would be interesting to stack a series of multilayer laser written DOEs to obtain an approximation to continuous switching behaviour.

Another possible solution to the manufacture of tunable LC-DOEs with 2PP-DLW could be to use the anchoring strength of the laser written polymer network as another degree-of-freedom in the fabrication process. By varying the power of the fabrication laser, a gradient of network-strength could be formed in the device such that weakly locked-in regions still switch, but to a lesser extent than strongly locked-in regions. This would create a device with a phase pattern that could be tuned with the application of a simple uniform voltage. Note that it would not be possible to completely reconfigure the phase pattern of the device, as in bilayer DOEs, but the magnitude of the phase variation across the pattern could be adjusted. This would be particularly suited for applications in adaptive optics where aberrations can be decomposed into a series of distinctive aberration modes. A tunable LC-DOE device could be patterned to correct for a particular aberration mode, and the magnitude of the correction could be adjusted simply by varying the voltage applied to the device.

### Slanted/Tilted Gratings

There is a growing need for slanted gratings that function as beam combiners in emerging AR/VR technology, as they typically have high diffraction efficiencies and greater spectral bandwidth than Bragg gratings[220]. The LC-DOE fabrication methods described in this chapter could be adapted to create such gratings in a relatively straightforward way by tilting the sample plane with respect to the propagation direction of the fabrication laser. This would create polymer structures that are tilted relative to the device substrates by an angle equal to the tilt of the sample plane. Future work in this area could proceed by fabricating some DOEs of this type with a simple 1D grating design in order to assess the impact on the diffraction efficiency and the switching of the device.

#### Greyscale Gratings and Holograms

The ability to write LC-DOEs at a range of voltages opens up the possibility of writing gratings and holograms with greyscale phase. That is, where the phase is not purely binary, but takes a range of quantised values between 0 and $2\pi$. Using this approach, the unit cell of a blazed grating could be fabricated by writing a series of parallel polymer walls, varying the write voltage for each wall, such that together they form a linear phase-ramp. Repeating this unit cell across a large area of an LC device would engineer a fixed blazed grating. Due to the influence of lateral elasticity of the locked-in walls, it is likely that the nominal write voltages would need to be adjusted to take into account the anchoring introduced by the walls during the fabrication.

In addition to blazed gratings, this greyscale phase technique would enable multi-level phase holograms with significantly improved diffraction efficiency over the binary holograms discussed in this chapter. Theoretically, the maximum diffraction efficiency for a 4 phase level hologram is 81%, which is vastly improved from the theoretical value of 40.5% for a binary phase hologram. Increasing this further to 8 phase levels should result in a theoretical diffraction efficiency of 94.9%[169, 184]. However, a downside of writing greyscale phase in this manner is that it is not immediately obvious how these devices can be switchable and they are likely to be fixed elements, unless an as yet unforeseen innovation in the fabrication process can be discovered. Therefore, the approach described above for fabricating 3D phase gratings, where the grating is written in the off-state and the height of the polymer structures determine the phase depth, may be a better solution for creating switchable greyscale DOEs.

### Switching Speed

For any switchable device, the switching speed is clearly an important figure of merit. Thus far, no measurements have been undertaken of the switching speed in any of the LC-DOEs described in this chapter. A clear direction for future work would be to obtain such measurements and understand any structure-property relationships that exist in this area. For example, would changing the height of the fabricated polymer structures in a bilayer device affect the speed of switching between the two gratings? Questions like this could be answered by fabricating a range of devices with altered design parameters and characterising their performance.

### Locking-in Isotropic Polymer Structures

The LC-DOE devices discussed so far were written at room temperature, with the polymerisable LC mixture in the nematic phase. Drawing inspiration from POLICRYPS, which is a fabrication technique that differs from H-PDLC only in that the process is performed at a temperature above the clearing point, gratings could be fabricated in the isotropic phase. In POLICRYPS devices, vastly improved grating morphology results from avoiding the formation of nematic droplets during the curing process, allowing complete phase-separation between the polymer and the LC[176, 178, 179]. Therefore, it would be interesting to explore laser writing at an elevated temperature with LC-DOEs to evaluate the impact on grating morphology and performance.

### Non-switchable LC-DOEs

Possibly the largest impediment to developing the switchable LC-DOEs described in this chapter into a useful technology is the presence of unreacted monomer in the device post-fabrication. This limits the usable wavelengths to those longer than the absorption spectrum for the photoinitiator. For applications of DOEs in AR/VR displays, blue light at 450 nm and green light at 520 nm are critical wavelengths, both of which are likely to cause further photopolymerisation and destroy the switchability of the device. Future development of this technology should therefore involve optimisation of the mixture composition such that the minimum quantity of unreacted monomer remains in the device post-fabrication.

An alternative approach would be to deliberately sacrifice the device's switchability and post-cure the laser-written structure with UV flood illumination. This would produce high-quality fixed DOEs that can be used with any wavelength (because there is no possibility of further polymerisation). This method offers the intriguing possibility of tuning the unpolymerised regions to give the maximum diffraction efficiency before curing the device but this would require using a laser with a wavelength longer than the absorption spectrum of the photoinitiator to characterise the device before the final curing step.

### Tunable LC Defect Gratings

There is potential in combining the tunable defect concepts discussed in Chapter 6 with switchable LC-DOEs. Recently, Serra et al. demonstrated tunable defect arrays in an LC device that could produce diffraction patterns[221]. Using an array of pillars fabricated on a substrate with photolithography, they could control the nucleation of an array of umbilical defects which spontaneously form in a negative dielectric anisotropy LC mixed with ionic dopants and filled into a homeotropic cell. Furthermore, they demonstrated a degree of tunability in the array spacing by changing the voltage and frequency of an applied AC electric field. They demonstrated that this could cause changes in the diffraction pattern, but the method was somewhat crude and only provided a tunability range of 13.1 - 26.2 µm in the array spacing.

The method described by Serra et al. is refining a random nucleation process, exploiting the self-organisation properties of LCs and obtaining some degree of control with voltage. However, as shown in Chapter 6, 2PP-DLW allows complete control over the nucleation points of defects in pi-cells and could therefore be used to fabricate a tunable defect-based diffraction grating with a much wider tunability range. This could involve fabricating an array of tunable channels inside a pi-cell and varying the voltage to change the position of the defect trapped within the channels. With appropriate structure design, it may be possible to change the effective period of a grating in this way and obtain wide tunability by simply varying the voltage magnitude applied to the device.

## 7.6 Conclusions

The results described in this chapter are the very first demonstration of 2PP-DLW enabled fabrication of switchable LC-DOEs using a tunable LC resin. At each stage of the development process, the unique capabilities and properties of 2PP-DLW have been explored and utilised to design novel devices that are challenging or impossible to fabricate with other methods.

There is clearly a vast array of potential avenues to explore with 2PP-DLW in LC-DOEs. It should be noted that the list of future work areas above is not exhaustive and that the proposals could be combined to form hybrid concepts. For example, the fabrication of slanted gratings could be combined with the concept of bilayer DOEs to manufacture next-generation waveguide coupler devices that could be switched between two different slanted gratings.

These switchable LC-DOEs have the potential to fill a gap that exists between fully-programmable SLM devices and fixed diffractive optical elements. They may fail to match the versatility of SLMs but do provide simple electronic control of diffraction in an inexpensive and compact package. Therefore they could excel in an application where some degree of switchability/tunability is required but a fully programmable device is excessive and wasteful. They may first find use as aberration correction devices, where switching between different phase-profiles with a uniformly applied voltage significantly simplifies the operation of such a device compared to the complex active-matrix backplane electronics needed to drive an SLM.

# Chapter 8

# Conclusion

This chapter summarises the key findings of this DPhil thesis and charters a route forwards by detailing possible future work in the area of two-photon polymerisation in liquid crystal materials.

> *"All of this has happened before, and all of this will happen again."*
>
> **Leoben Conoy, Battlestar Galactica**

This thesis describes a significant exploration of two-photon polymerisation direct laser writing (2PP-DLW) in liquid crystal (LC) materials. The fabrication of microscale polymer structures was studied in a number of different LC device geometries and several potential applications were considered including authentication markings, microparticle manipulation and switchable diffractive optical elements. This chapter summarises the key findings of this thesis and suggests some areas that could be explored in future work.

As this thesis concerns the use of LCs as a resin material in 2PP-DLW, Chapter 2 presented a review of the theory and background of these fascinating anisotropic materials. Modelling approaches for LCs were discussed, and critical reviews of advanced alignment technologies and polymer stabilisation were provided such that the work described in thesis can be appreciated in a broader context.

In Chapter 3, the physics of two-photon absorption was elucidated in order to explain the unique attributes of two-photon polymerisation direct laser writing. Following this, the existing limited research on 2PP-DLW in LC materials was summarised and reviewed. The vast majority of this research has involved the use of 2PP-DLW to pattern negative photoresists which function as alignment surfaces when used as part of an LC device assembly. There have been some studies of polymer stabilisation using reactive mesogens and 2PP-DLW but, unlike the work conducted in this thesis, they have not exploited the stimuli-responsive characteristics of LCs.

As part of the work described in this thesis, a bespoke two-photon polymerisation system was designed and built which was specifically tailored to fabrication in LC materials. The experimental setup is described in Chapter 4 and detailed consideration was given to future development of the system. Incorporating adaptive optics in the form of a spatial light modulator into the setup would enable future experiments to be conducted in parallelisation of fabrication processes. Additional gains in fabrication speed could also be made by augmenting the system with a pair of galvanometer mirrors to steer the beam in the LC resin. This thesis did not address the scalability or throughput of 2PP-DLW in LCs but this is a critical area to consider for use in future manufacturing applications.

A spatial light modulator would also enable experiments to be conducted on the impact of aberrations and aberration-correction on 2PP-DLW in LC devices. Due to the mismatch in refractive index between the glass substrates and the LC mixture, focussing the fabrication laser into an LC device will introduce spherical aberration to the optical system that results in a lengthening of the polymerised voxel. This effect was not a significant limiting factor for the work described in this thesis, however, any future work that relies on fabrication of smaller voxels may require aberration correction to precisely localise the polymerisation to the smallest possible volume.

It was shown throughout this thesis that applying an electric field to LC devices during 2PP-DLW fabrication opens up the possibility of creating devices with spatially-varying properties. However, LCs respond to a variety of external stimuli, including temperature and magnetic fields. A fruitful area for future work could therefore be to investigate the effect of varying the temperature of the device during fabrication, which would allow the nematic order of the fabricated polymer features to be tuned. It would be particularly interesting to fabricate polymer structures in the isotropic phase and study the effect they have on surrounding LC molecules after the device is cooled back into the nematic phase. The custom-built 2PP-DLW system described in Chapter 4 was designed such that a hot stage could be added to the three-axis translation stage stack without interfering with any other components of the system.

The stabilisation of voltage-dependent states of the nematic Fréedericksz cell was explored in Chapter 5, where the flexible patterning capabilities of 2PP-DLW were used to create reconfigurable microscale images formed using polymer stabilised pillars. The voltage-dependent visibility of the structures relied on electrically-tunable refractive index matching between the unpolymerised mixture and the polymer-stabilised structures. The mechanism behind this effect was explored with the use of director modelling which confirmed the hypothesis that the polymer structures 'memorise' or stabilise the director profile at the moment of fabrication. Therefore, when the read-voltage was made equal to the write-voltage, the polymer structure would disappear due to the director profile of the bulk LC matching the stabilised director profile of the structure itself. This was used to demonstrate a concept for next-generation authentication devices using LCs, in the form of a microscale switchable QR code that could only be read when a voltage was applied to the device.

Future work on voltage-dependent visibility could explore the impact of other variables on the efficacy of this effect. For example, the lateral spacing of the polymer micropillars is likely to affect the switching of the unpolymerised LC mixture. Experiments could be performed by laser-writing micropillar arrays at a range of spacings and analysing the visibility using the image analysis techniques described in Chapter 5. The dimensions of the polymer structures may also have an impact on the switching characteristics, and the effect of this could be investigated in a similar manner by writing micropillars with a range of dimensions and studying their electro-optic properties and voltage-dependent visibility.

Chapter 6 extended the results of the previous chapter to the stabilisation of director states with topological discontinuities. States of the nematic LC pi-cell were stabilised in microscale polymer structures with 2PP-DLW, and control over the nucleation of topologically discontinuous states and the movement of defects by tailoring the design of the structures was demonstrated. The fundamental behaviour of disclination lines was explored by studying the defect speed as a function of applied voltage and by changing the orientation of the line relative to the device rubbing direction. Furthermore, a disclination line control system was developed which represents a proof-of-concept for electro-optic devices that employ electrically-tunable defects. As many emerging applications of defects in LCs concern the interaction of defects with colloidal inclusions; microparticle cargo-towing was demonstrated in which a silica bead was trapped by a defect and moved across an LC cell.

Chapter 6 also explored some more advanced concepts for controlling defect nucleation and growth via confinement of defects with laser-written topologically discontinuous polymer walls. In work that was inspired by developments in microfluidics, the movement of a defect along a bifurcated channel was demonstrated, showing a remarkable degree of control over defect dynamics.

Future work in this area could be to lay the foundations for emerging next-generation spatial light modulators that consist of arrays of 'topological pixels'. In order for laser-written tunable defects to find use in such applications, it will be essential to characterise the repeatability and any hysteresis present in the voltage-dependent behaviour of defects generated with 2PP-DLW. Experiments to investigate this could proceed by fabricating an array of the tunable defect structures described in Chapter 6 over a large area of a pi-cell device. The structures could be characterised simultaneously by adapting and extending the tunable disclination line control system developed for control of just a single structure. Image analysis techniques could be devised to detect the position of each defect in an array, such that statistical analysis can be performed in order to assess the repeatability of the defect behaviour. Developing such a system would also enable systematic investigation of the effects of other fabrication parameters, including the voltage amplitude used to lock-in topologically discontinuous states and the height of the polymer structures within the cell.

Chapter 7 described the fabrication and characterisation of switchable LC diffractive optical elements (DOEs) enabled by 2PP-DLW. Starting with a demonstration of a simple 1D diffraction grating created by laser-writing of parallel polymer walls, a wide exploration of the possibilities of fabrication of LC-DOEs with 2PP-DLW was conducted. A modelling approach was developed that connected a simulation of the LC director in a grating to the propagation of light through the grating, and showed that polymer structures strongly lock-in the director.

Using the ability of 2PP-DLW to write in 3D, bilayer switchable DOEs were demonstrated that could be switched between producing different diffraction patterns with the application of a voltage across the device. In addition, complex grating designs that produced hexatic diffraction patterns were demonstrated in order to highlight the flexibility of fabricating DOEs with 2PP-DLW compared to conventional lithography techniques. Finally, a computer-generated hologram (CGH) was fabricated and the voltage-dependence of the intensity of the replay field was analysed and understood in terms of the phase of the pixels comprising the structure.

A large number of potential concepts for future work in the area of LC-DOEs written with 2PP-DLW were described in Section 7.5, with key ideas including the fabrication of blazed gratings, multilayer CGHs, chiral nematic gratings and tunable (rather than switchable) gratings. There are a vast range of topics to explore in this area that are interesting both from a fundamental and applications perspective. An intriguing possibility lies in combining the tunable defects described in Chapter 6 with the switchable diffraction gratings of Chapter 7 to fabricate tunable defect arrays which produce diffraction patterns.

A key drawback of all of the switchable laser-written devices that are described in this thesis is their vulnerability to undergo further polymerisation after the completion of the fabrication process. It should be noted that devices had to be characterised on a microscope with a filtered illumination source to block wavelengths that could be absorbed by the photoinitiator and might cause further polymerisation. In the case of the LC-DOEs demonstrated in Chapter 7, the devices were characterised with the use of a low-power red laser diode in order to avoid causing any further polymerisation and destroying the switchability of the device.

Therefore, a crucial area of future work is to improve the ruggedness of the devices, such that they are stable when exposed to ambient lighting conditions. A possible approach to this would be to remove the LC resin after fabrication with the use of a solvent such as acetone, sometimes referred to as 'washing-out' the LC cell. Following this, the cell could be refilled with a standard nematic LC mixture containing no reactive mesogens. However, this approach is known to cause damage to polymer-stabilised liquid crystal networks, sometimes resulting in shrinkage and other structural modifications and therefore may not be suitable. It also significantly increases the number of steps involved in fabrication of a device and is therefore unlikely to find use as part of a manufacturing technique.

Another approach to ruggedisation with respect to ambient light exposure may be to optimise the reactive mesogen concentration of the polymerisable mixture. By calculating the total polymerised volume of a structure, it may be possible to dope only the required amount of RM and photoinitiator into a host LC. However, this may result in a decrease in the network density such that the polymer stabilised structures do not adequately anchor the LC in the alignment at the moment of polymerisation. Comprehensive studies employing imaging techniques including scanning electron microscopy and atomic force microscopy may be useful for providing information on the density and structure of the polymer stabilised LC network in the course of mixture optimisation.

Further development of the polymerisable LC resin with the goal of improving the index-matching between the polymer and the host LC would also enhance the performance of devices that rely on the voltage-induced invisibility phenomenon introduced in Chapter 5 and the switchable LC-DOEs demonstrated in Chapter 7. This would enhance the invisibility of the polymer features when viewed under a microscope and would minimise or eliminate any diffraction from laser-written diffraction gratings designed to be off at 0 V. There are a vast range of LC materials, photoinitiators and reactive mesogens that could be used in 2PP-DLW and optimising the polymerisable mixture is a crucial piece of future work. This would be a complex optimisation process as there are a large number of parameters to consider, including the refractive indices of the RM and the LC, the absorption of the photoinitiator, the clearing point and the effective elastic constants of the mixture. The proprietary negative photoresists used in commercial 2PP-DLW have undergone considerable development to optimise their two-photon absorption characteristics and this is one of the key reasons that it is possible to fabricate features smaller than the optical diffraction limit in such materials.

In summary, the work in this thesis has involved the fabrication and manipulation of polymer-stabilised liquid crystal networks using 2PP-DLW for new applications in photonics. Due to its focus on LC materials, this work is an important contribution to the development of advanced alignment and control technologies in LC devices, as many of the engineered alignments are challenging or impossible to produce with conventional methods. However, it also represents a contribution to the development of 2PP-DLW, in particular in the area of smart/multifunctional resists, where a device is engineered by applying external stimuli to alter the properties of the resist during fabrication. Liquid crystals are an excellent candidate for further development of smart resists due to their ability to self-organise and to respond to a range of external stimuli including temperature, electric fields and magnetic fields.

# Bibliography

1. Hahn, V., Mayer, F., Thiel, M. & Wegener, M. 3-D Laser Nanoprinting. *Optics and Photonics News* **30,** 28 (2019).
2. De. Gennes, P. G. & Prost, J. *The Physics of Liquid Crystals* (Clarendon Press, 1993).
3. Wang, L. & Li, Q. Stimuli-directing self-organized 3D liquid-crystalline nanostructures: from materials design to photonic applications. *Advanced Functional Materials* **26,** 10–28 (2016).
4. Lee, Y.-H. *et al.* Two-photon polymerization enabled multi-layer liquid crystal phase modulator. *Scientific Reports* **7,** 16260 (2017).
5. Ho, C.-H. *et al.* Controllable light diffraction in woodpile photonic crystals filled with liquid crystal. *Applied Physics Letters* **106,** 021113 (2015).
6. Serra, F. *et al.* Nematic liquid crystals embedded in cubic microlattices: Memory effects and bistable pixels. *Advanced Functional Materials* **23,** 3990–3994 (2013).
7. Tartan, C. C. *et al.* Read on demand images in laser-written polymerizable liquid crystal devices. *Advanced Optical Materials* **6,** 1800515 (2018).
8. Sandford O'Neill, J. J., Salter, P. S., Booth, M. J., Elston, S. J. & Morris, S. M. Electrically-tunable positioning of topological defects in liquid crystals. *Nature Communications* **11,** 2203 (2020).
9. Dunmur, D. & Sluckin, T. *Soap, Science and Flat-Screen TVs: A History of Liquid Crystals* (Oxford University Press, 2010).

10. *Pierre-Gilles de Gennes - Nobel Lecture: Soft Matter - NobelPrize.org* `https://www.nobelprize.org/prizes/physics/1991/gennes/lecture/` (01/07/2021).
11. Li, Q. *Liquid Crystals Beyond Displays: Chemistry, Physics and Applications* (John Wiley & Sons, NJ, 2012).
12. Wu, S.-T. & Yang, D.-K. *Fundamentals of Liquid Crystal Devices* 2nd ed. (Wiley-VCH, 2014).
13. Frank, F. C. I. Liquid crystals. On the theory of liquid crystals. *Discussions of the Faraday Society* **25,** 19 (1958).
14. Oseen, C. W. The theory of liquid crystals. *Transactions of the Faraday Society* **29,** 883 (1933).
15. Zocher, H. The effect of a magnetic field on the nematic state. *Transactions of the Faraday Society* **29,** 945 (1933).
16. Yeh, P. & Gu, C. *Optics of Liquid Crystal Displays* 1st (John Wiley & Sons, Ltd, 1999).
17. Jones, R. C. A New Calculus for the Treatment of Optical Systems. *Journal of the Optical Society of America* **31,** 488 (1941).
18. Takatoh, K. *Alignment Technologies and Applications of Liquid Crystal Devices* 263 (Taylor & Francis, 2005).
19. Pidduck, A. J., Haslam, S. D., Bryan-Brown, G. P., Bannister, R. & Kitely, I. D. Control of liquid crystal alignment by polyimide surface modification using atomic force microscopy. *Applied Physics Letters* **71,** 2907–2909 (1997).
20. Kim, J. H., Yoneya, M., Yamamoto, J. & Yokoyama, H. Surface alignment bistability of nematic liquid crystals by orientationally frustrated surface patterns. *Applied Physics Letters* **78,** 3055–3057 (2001).

21. Kim, J. H., Yoneya, M. & Yokoyama, H. Tristable nematic liquid-crystal device using micropatterned surface alignment. *Nature* **420,** 159–162 (2002).
22. Seki, T. New strategies and implications for the photoalignment of liquid crystalline polymers. *Polymer Journal* **46,** 751–768 (2014).
23. Chigrinov, V. G., Kozenkov, V. M. & Kwok, H.-S. *Photoalignment of Liquid Crystalline Materials* (John Wiley & Sons, Ltd, Chichester, UK, 2008).
24. Ichimura, K., Suzuki, Y., Seki, T., Hosoki, A. & Aoki, K. Reversible change in alignment mode of nematic liquid crystals regulated photochemically by command surfaces modified with an azobenzene monolayer. *Langmuir* **4,** 1214–1216 (1988).
25. Yaroshchuk, O. & Reznikov, Y. Photoalignment of liquid crystals: basics and current trends. *J. Mater. Chem.* **22,** 286–300 (2012).
26. Miyachi, K., Kobayashi, K., Yamada, Y. & Mizushima, S. 41.1 : Distinguished Paper: The World's First Photo Alignment LCD Technology Applied to Generation Ten Factory. *SID Symposium Digest of Technical Papers* **41,** 579 (2010).
27. Slussarenko, S. *et al.* Tunable liquid crystal q-plates with arbitrary topological charge. *Optics Express* **19,** 4085 (2011).
28. Provenzano, C., Pagliusi, P. & Cipparrone, G. Highly efficient liquid crystal based diffraction grating induced by polarization holograms at the aligning surfaces. *Applied Physics Letters* **89,** 1–4 (2006).
29. Cheng, K.-T., Liu, C.-K., Ting, C.-L. & Fuh, A. Y. Electrically switchable and optically rewritable reflective Fresnel zone plate in dye-doped cholesteric liquid crystals. *Optics express* **15,** 14078–85 (2007).
30. Miskiewicz, M. N. & Escuti, M. J. Direct-writing of complex liquid crystal patterns. *Optics Express* **22,** 12691 (2014).

31. Xiang, X., Kim, J. & Escuti, M. Far-field and Fresnel Liquid Crystal Geometric Phase Holograms via Direct-Write Photo-Alignment. *Crystals* **7,** 383 (2017).
32. De Haan, L. T., Sánchez-Somolinos, C., Bastiaansen, C. M. W., Schenning, A. P. H. J. & Broer, D. J. Engineering of Complex Order and the Macroscopic Deformation of Liquid Crystal Polymer Networks. *Angewandte Chemie International Edition* **51,** 12469–12472 (2012).
33. McConney, M. E. *et al.* Topography from topology: Photoinduced surface features generated in liquid crystal polymer networks. *Advanced Materials* **25,** 5880–5885 (2013).
34. Zhao, W. *et al.* Photopolymerization-Enforced Stratification in Liquid Crystal Materials. *Progress in Polymer Science* **114,** 101365 (2021).
35. Broer, D. J. On the History of Reactive Mesogens: Interview with Dirk J. Broer. *Advanced Materials* **32,** 1905144 (2020).
36. Broer, D. J., Boven, J., Mol, G. N. & Challa, G. In-situ photopolymerization of oriented liquid-crystalline acrylates, 3. Oriented polymer networks from a mesogenic diacrylate. *Die Makromolekulare Chemie* **190,** 2255–2268 (1989).
37. Hikmet, R. A. M. Anisotropic gels and plasticized networks formed by liquid crystal molecules. *Liquid Crystals* **9,** 405–416 (1991).
38. Broer, D. J., Crawford, G. P. & Žumer, S. *Cross-linked liquid crystalline systems : from rigid polymer networks to elastomers* 586 (CRC Press, 2011).
39. Dierking, I. Recent developments in polymer stabilised liquid crystals. *Polymer Chemistry* **1,** 1153 (2010).
40. Dierking, I. Polymer Network-Stabilized Liquid Crystals. *Advanced Materials* **12,** 167–181 (2000).

41. Hikmet, R. & Lub, J. Anisotropic networks and gels obtained by photopolymerisation in the liquid crystalline state: Synthesis and applications. *Progress in Polymer Science* **21,** 1165–1209 (1996).
42. Lub, J., Broer, D. J., Wegh, R. T., Peeters, E. & Van Der Zande, B. M. I. Formation of optical films by photo-polymerisation of liquid crystalline acrylates and application of these films in liquid crystal display technology. *Molecular Crystals and Liquid Crystals* **429,** 77–99 (2005).
43. Camacho-Lopez, M., Finkelmann, H., Palffy-Muhoray, P. & Shelley, M. Fast liquid-crystal elastomer swims into the dark. *Nature Materials* **3,** 307–310 (2004).
44. Hikmet, R. A. M. & Kemperman, H. Electrically switchable mirrors and optical components made from liquid-crystal gels. *Nature* **392,** 476–479 (1998).
45. Liu, D. & Broer, D. J. Liquid crystal polymer networks: Preparation, properties, and applications of films with patterned molecular alignment. *Langmuir* **30,** 13499–13509 (2014).
46. Gelebart, A. H. *et al.* Making waves in a photoactive polymer film. *Nature* **546,** 632–636 (2017).
47. Zeng, H., Wani, O. M., Wasylczyk, P., Kaczmarek, R. & Priimagi, A. Self-Regulating Iris Based on Light-Actuated Liquid Crystal Elastomer. *Advanced Materials* **29,** 1701814 (2017).
48. Malinauskas, M., Farsari, M., Piskarskas, A. & Juodkazis, S. Ultrafast laser nanostructuring of photopolymers: A decade of advances. *Physics Reports* **533,** 1–31 (2013).
49. Kawata, S., Sun, H. B., Tanaka, T. & Takada, K. Finer features for functional microdevices. *Nature* **412,** 697–698 (2001).

50. Soukoulis, C. M. & Wegener, M. Past achievements and future challenges in the development of three-dimensional photonic metamaterials. *Nature Photonics* **5,** 523–530 (2011).
51. Vaezi, M., Seitz, H. & Yang, S. A review on 3D micro-additive manufacturing technologies. *International Journal of Advanced Manufacturing Technology* **67,** 1721–1754 (2013).
52. Gan, Z., Cao, Y., Evans, R. A. & Gu, M. Three-dimensional deep sub-diffraction optical beam lithography with 9 nm feature size. *Nature Communications* **4,** 1–7 (2013).
53. Fischer, J. & Wegener, M. Three-dimensional optical laser lithography beyond the diffraction limit. *Laser and Photonics Reviews* **7,** 22–44 (2013).
54. Göppert-Mayer, M. Über Elementarakte mit zwei Quantensprüngen. *Annalen der Physik* **401,** 273–294 (1931).
55. Kaiser, W. & Garrett, C. G. Two-photon excitation in CaF2: Eu2+. *Physical Review Letters* **7,** 229–231 (1961).
56. Yu, T. *et al.* Chemically amplified positive resists for two-photon three-dimensional microfabrication. *Advanced Materials* **15,** 517–521 (2003).
57. Maruo, S., Nakamura, O. & Kawata, S. Three-dimensional microfabrication with two-photon-absorbed photopolymerization. *Optics Letters* **22,** 132 (1997).
58. Nanoscribe GmbH. *Photonic Professional GT2* `https://www.nanoscribe.com/en/products/photonic-professional-gt2` (02/18/2021).
59. Femtika. *Nanofactory* `https://www.femtika.lt/nanofactory/` (02/18/2021).
60. Misawa, H. & Juodkazis, S. *3D laser microfabrication : principles and applications* 388 (Wiley-VCH, 2006).

61. Kawata, S., Tanaka, T. & Takeyasu, N. *Two-Photon Fabrication of Three-Dimensional Metamaterials* in *Conference on Lasers and Electro-Optics/International Quantum Electronics Conference* (OSA, Washington, D.C., 2009), IThL1.
62. Bückmann, T. *et al.* Tailored 3D mechanical metamaterials made by dip-in direct-laser-writing optical lithography. *Advanced Materials* **24,** 2710–2714 (2012).
63. Rill, M. S. *et al.* Photonic metamaterials by direct laser writing and silver chemical vapour deposition. *Nature Materials* **7,** 543–546 (2008).
64. Raimondi, M. T. *et al.* Two-photon laser polymerization: from fundamentals to biomedical application in tissue engineering and regenerative medicine. *Journal of Applied Biomaterials & Functional Materials* **10,** 56–66 (2012).
65. Baldacchini, T. *Three-Dimensional Microfabrication using Two-Photon Polymerization : Fundamentals, Technology, and Applications* (Elsevier B.V, 2016).
66. Hecht, E. *Optics* 5th ed. (Pearson, New York, 2016).
67. Zhou, X., Hou, Y. & Lin, J. A review on the processing accuracy of two-photon polymerization. *AIP Advances* **5** (2015).
68. Haske, W. *et al.* 65 nm feature sizes using visible wavelength 3-D multiphoton lithography. *Optics Express* **15,** 3426 (2007).
69. Salter, P. S. & Booth, M. J. Adaptive optics in laser processing. *Light: Science and Applications* **8,** 1–16 (2019).
70. Simmonds, R. D., Salter, P. S., Jesacher, A. & Booth, M. J. Three dimensional laser microfabrication in diamond using a dual adaptive optics system. *Optics Express* **19,** 24122 (2011).

71. Jesacher, A. & Booth, M. J. Parallel direct laser writing in three dimensions with spatially dependent aberration correction. *Optics Express* **18,** 21090 (2010).
72. Lin, H., Jia, B. & Gu, M. Dynamic generation of Debye diffraction-limited multifocal arrays for direct laser printing nanofabrication. *Optics Letters* **36,** 406 (2011).
73. Salter, P. S. *et al.* Adaptive slit beam shaping for direct laser written waveguides. *Optics Letters* **37,** 470–472 (2012).
74. Kim, K. Laser Scanner-Stage Synchronization Method for High-Speed And Wide-Area Fabrication. *Journal of Laser Micro/Nanoengineering* **7,** 231–235 (2012).
75. Malinauskas, M., Jonušauskas, L., Gailevičius, D., Rekštyte, S. & Juodkazis, S. Optical 3D printing in mesoscale. *Laser 3D Manufacturing V,* 36 (2018).
76. Kawata, Y., Takatoh, K., Hasegawa, M. & Sakamoto, M. The alignment of nematic liquid crystals on photolithographic micro-groove patterns. *Liquid Crystals* **16,** 1027–1036 (1994).
77. Xie, A., Ito, T. & Higgins, D. A. Fabrication and Characterization of Polymer/Liquid Crystal Composite Diffractive Optics by Multiphoton Methods. *Advanced Functional Materials* **17,** 1515–1522 (2007).
78. Lee, C. H., Yoshida, H., Miura, Y., Fujii, A. & Ozaki, M. Local liquid crystal alignment on patterned micrograting structures photofabricated by two photon excitation direct laser writing. *Applied Physics Letters* **93,** 1–4 (2008).
79. Ji, Z. *et al.* Compartmentalized liquid crystal alignment induced by sparse polymer ribbons with surface relief gratings. *Optics Letters* **41,** 336 (2016).

80. He, Z. *et al.* Polarization-independent phase modulators enabled by two-photon polymerization. *Optics Express* **25,** 33688 (2017).
81. Yoshida, H., Lee, C. H., Miura, Y., Fujii, A. & Ozaki, M. Optical tuning and switching of photonic defect modes in cholesteric liquid crystals. *Applied Physics Letters* **90,** 071107 (2007).
82. Yoshida, H., Lee, C. H., Matsuhisa, Y., Fujii, A. & Ozaki, M. Bottom-Up Fabrication of Photonic Defect Structures in Cholesteric Liquid Crystals Based on Laser-Assisted Modification of the Helix. *Advanced Materials* **19,** 1187–1190 (2007).
83. Yoshida, H. Functionalisation of cholesteric liquid crystals by direct laser writing. *Liquid Crystals Today* **21,** 3–19 (2012).
84. Ito, K. & Kimura, M. Optically induced rotation of microcylinders made of photopolymerizable nematic liquid crystal. *Japanese Journal of Applied Physics* **49,** 0402081–0402083 (2010).
85. Tartan, C. C. *et al.* Generation of 3-dimensional polymer structures in liquid crystalline devices using direct laser writing. *RSC Advances* **7,** 507–511 (2017).
86. Tartan, C. C., Salter, P. S., Booth, M. J., Morris, S. M. & Elston, S. J. Localised polymer networks in chiral nematic liquid crystals for high speed photonic switching. *Journal of Applied Physics* **119,** 183106 (2016).
87. Outram, B. I. & Elston, S. J. Spontaneous and stable uniform lying helix liquid-crystal alignment. *Journal of Applied Physics* **113,** 043103 (2013).
88. Miller, D. S., Carlton, R. J., Mushenheim, P. C. & Abbott, N. L. Introduction to Optical Methods for Characterizing Liquid Crystals at Interfaces. *Langmuir* **29,** 3154–3169 (2013).

89. *Dynamic Optics and Photonics Group, Department of Engineering Science, University of Oxford* `https://eng.ox.ac.uk/dop/` (03/05/2021).
90. Chen, Y.-C. *et al.* Laser writing of coherent colour centres in diamond. *Nature Photonics* **11,** 77–80 (2017).
91. Mertelj, A., Spindler, L. & Čopič, M. Dynamic light scattering in polymer-dispersed liquid crystals. *Physical Review E* **56,** 549–553 (1997).
92. Amundson, K. Electro-optic properties of a polymer-dispersed liquid-crystal film: Temperature dependence and phase behavior. *Physical Review E* **53,** 2412–2422 (1996).
93. Doane, J. W., Vaz, N. A., Wu, B. G. & Žumer, S. Field controlled light scattering from nematic microdroplets. *Applied Physics Letters* **48,** 269–271 (1986).
94. Ondris-Crawford, R. *et al.* Microscope textures of nematic droplets in polymer dispersed liquid crystals. *Journal of Applied Physics* **69,** 6380–6386 (1991).
95. Drzaic, P. S. Reorientation dynamics of polymer dispersed nematic liquid crystal films. *Liquid Crystals* **3,** 1543–1559 (1988).
96. Higgins, D. A. Probing the Mesoscopic Chemical and Physical Properties of Polymer-Dispersed Liquid Crystals. *Advanced Materials* **12,** 251–264 (2000).
97. Jain, S. C. & Rout, D. K. Electro-optic response of polymer dispersed liquid-crystal films. *Journal of Applied Physics* **70,** 6988–6992 (1991).
98. Lampert, C. Large-area smart glass and integrated photovoltaics. *Solar Energy Materials and Solar Cells* **76,** 489–499 (2003).
99. Murray, J., Ma, D. & Munday, J. N. Electrically Controllable Light Trapping for Self-Powered Switchable Solar Windows. *ACS Photonics* **4,** 1–7 (2017).

100. Drzaic, P. S. Polymer dispersed nematic liquid crystal for large area displays and light valves. *Journal of Applied Physics* **60,** 2142–2148 (1986).

101. Craighead, H. G., Cheng, J. & Hackwood, S. New display based on electrically induced index-matching in an inhomogeneous medium. *Applied Physics Letters* **40,** 22–24 (1982).

102. Bunning, T. J., Natarajan, L. V., Tondiglia, V. P. & Sutherland, R. L. Holographic Polymer-Dispersed Liquid Crystals (H-PDLCs). *Annual Review of Materials Science* **30,** 83–115 (2000).

103. Amundson, K., van Blaaderen, A. & Wiltzius, P. Morphology and electro-optic properties of polymer-dispersed liquid-crystal films. *Physical Review E* **55,** 1646–1654 (1997).

104. Bouteiller, L. & Barny, P. L. Polymer-dispersed liquid crystals: Preparation, operation and application. *Liquid Crystals* **21,** 157–174 (1996).

105. Doane, J. W., Golemme, A., West, J. L., Whitehead, J. B. & Wu, B.-G. Polymer Dispersed Liquid Crystals for Display Application. *Molecular Crystals and Liquid Crystals Incorporating Nonlinear Optics* **165,** 511–532 (1988).

106. Coates, D. Polymer-dispersed liquid crystals. *Journal of Materials Chemistry* **5,** 2063 (1995).

107. Vaz, N. A., Smith, G. W., VanSteenkiste, T. H. & Montgomery, Jr., G. P. *Droplet-size polydispersity in polymer-dispersed liquid-crystal films* in *Liquid-Crystal Devices and Materials* (eds Drzaic, P. S. & Efron, U.) **1455** (1991), 110–122.

108. Ferrari, J. A. *et al.* Effect of size polydispersity in polymer-dispersed liquid-crystal films. *Journal of Applied Physics* **103** (2008).

109. Bansal, D. Anti-Counterfeit Technologies: A Pharmaceutical Industry Perspective. *Scientia Pharmaceutica* **81,** 1–13 (2013).

110. Guin, U., Forte, D. & Tehranipoor, M. *Anti-counterfeit Techniques: From Design to Resign* in *2013 14th International Workshop on Microprocessor Test and Verification* (IEEE, 2013), 89–94.
111. OECD. *The economic impact of counterfeiting and piracy* 1–395 (Organisation for Economic Cooperation and Development (OECD), 2007).
112. Frontier Economics. *The Economic Impacts of Counterfeiting and Piracy* tech. rep. (2017).
113. Bush, R. F., Bloch, P. H. & Dawson, S. Remedies for product counterfeiting. *Business Horizons* **32,** 59–65 (1989).
114. Soon, J. M. & Manning, L. Developing anti-counterfeiting measures: The role of smart packaging. *Food Research International* **123,** 135–143 (2019).
115. Tuyls, P. & Batina, L. *RFID-Tags for Anti-counterfeiting* in *Topics in Cryptology - CT-RSA 2006* **LNCS 3860** (Springer Verlag, 2006), 115–131.
116. Devadas, S. *et al. Design and Implementation of PUF-Based "Unclonable" RFID ICs for Anti-Counterfeiting and Security Applications* in *2008 IEEE International Conference on RFID* (IEEE, 2008), 58–64.
117. You, M. *et al.* Three-dimensional quick response code based on inkjet printing of upconversion fluorescent nanoparticles for drug anti-counterfeiting. *Nanoscale* **8,** 10096–10104 (2016).
118. Lee, R. Micro-technology for anti-counterfeiting. *Microelectronic Engineering* **53,** 513–516 (2000).
119. *The Physics of Soft and Partially Ordered Matter - Theory and Simulation Group, University of Ljubljana* `https://softmatter.fmf.uni-lj.si/main.php` (03/05/2021).

120. Ravnik, M. & Žumer, S. Landau-de Gennes modelling of nematic liquid crystal colloids. *Liquid Crystals* **36,** 1201–1214 (2009).
121. Mottram, N. J. & Newton, C. J. P. Introduction to Q-tensor theory (2014).
122. *Soft Matter Photonics Group, Department of Engineering Science, University of Oxford* `https://eng.ox.ac.uk/smp/` (03/08/2021).
123. Li, W.-S. *et al.* Demonstration of patterned polymer-stabilized cholesteric liquid crystal textures for anti-counterfeiting two-dimensional barcodes. *Applied Optics* **56,** 601–606 (2017).
124. Volovik, G. E. *Exotic Properties of Superfluid Helium 3* (World Scientific Publishing Co Pte Ltd, 1992).
125. Chaikin, P. & Lubensky, T. in *Principles of Condensed Matter Physics* 495–589 (1995).
126. Moore, J. E. The birth of topological insulators. *Nature* **464,** 194–8 (2010).
127. Vilenkin, A. & Shellard, E. P. S. *Cosmic Strings and Other Topological Defects* New ed (Cambridge University Press, 2000).
128. Chuang, I., Durrer, R., Turok, N. & Yurke, B. Cosmology in the Laboratory: Defect Dynamics in Liquid Crystals. *Science* **251,** 1336–1342 (1991).
129. Friedel, G. Les états mésomorphes de la matière. *Annales de Physique* **9,** 273–474 (1922).
130. Kleman, M. Defects in liquid crystals. *Reports on Progress in Physics* **52,** 555–654 (1989).
131. Fleury, J. B., Pires, D. & Galerne, Y. Self-Connected 3D architecture of microwires. *Physical Review Letters* **103,** 1–4 (2009).
132. Blanc, C., Coursault, D. & Lacaze, E. Ordering nano- and microparticles assemblies with liquid crystals. *Liquid Crystals Reviews* **1,** 83–109 (2013).

133. Li, Y. *et al.* Periodic assembly of nanoparticle arrays in disclinations of cholesteric liquid crystals. *Proceedings of the National Academy of Sciences* **114,** 2137–2142 (2017).
134. Peng, C., Turiv, T., Guo, Y., Wei, Q. H. & Lavrentovich, O. D. Command of active matter by topological defects and patterns. *Science* **354,** 882–885 (2016).
135. Liu, Q. *et al.* Self-alignment of plasmonic gold nanorods in reconfigurable anisotropic fluids for tunable bulk metamaterial applications. *Nano Letters* **10,** 1347–1353 (2010).
136. Senyuk, B. *et al.* Shape-Dependent Oriented Trapping and Scaffolding of Plasmonic Nanoparticles by Topological Defects for Self-Assembly of Colloidal Dimers in Liquid Crystals. *Nano Letters* **12,** 955–963 (2012).
137. Brasselet, E. & Loussert, C. Electrically controlled topological defects in liquid crystals as tunable spin-orbit encoders for photons. *Optics Letters* **36,** 719 (2011).
138. Marrucci, L., Manzo, C. & Paparo, D. Optical spin-to-orbital angular momentum conversion in inhomogeneous anisotropic media. *Physical Review Letters* **96,** 1–4 (2006).
139. Ghadimi Nassiri, M. & Brasselet, E. Multispectral Management of the Photon Orbital Angular Momentum. *Physical Review Letters* **121,** 213901 (2018).
140. Yoshida, H., Asakura, K., Fukuda, J. & Ozaki, M. Three-dimensional positioning and control of colloidal objects utilizing engineered liquid crystalline defect networks. *Nature Communications* **6,** 1–8 (2015).
141. Migara, L. K. & Song, J.-K. Standing wave-mediated molecular reorientation and spontaneous formation of tunable, concentric

defect arrays in liquid crystal cells. *NPG Asia Materials* **10,** e459–e459 (2018).

142. Wang, M., Li, Y. & Yokoyama, H. Artificial web of disclination lines in nematic liquid crystals. *Nature Communications* **8,** 388 (2017).

143. Bos, P. J. & Koehler/beran, K. R. The pi-Cell: A Fast Liquid-Crystal Optical-Switching Device. *Molecular Crystals and Liquid Crystals* **113,** 329–339 (1984).

144. Nakamura, H. & Noguchi, M. Bend Transition in Pi-cell. *Japanese Journal of Applied Physics* **39,** 6368–6375 (2000).

145. Salter, P. *Flexoelectricity and Chirality in Complex Liquid Crystal Systems* PhD thesis (University of Oxford, 2010).

146. Jung, J., Denniston, C., Orlandini, E. & Yeomans, J. M. Anisotropy of domain growth in nematic liquid crystals. *Liquid Crystals* **30,** 1455–1462 (2003).

147. Acosta, E. J., Towler, M. J. & Walton, H. G. The role of surface tilt in the operation of pi-cell liquid crystal devices. *Liquid Crystals* **27,** 977–984 (2000).

148. Smalyukh, I. I., Kuzmin, A. N., Kachynski, A. V., Prasad, P. N. & Lavrentovich, O. D. Optical trapping of colloidal particles and measurement of the defect line tension and colloidal forces in a thermotropic nematic liquid crystal. *Applied Physics Letters* **86** (2005).

149. Sasaki, Y. *et al.* Large-scale self-organization of reconfigurable topological defect networks in nematic liquid crystals. *Nature Communications* **7,** 1–13 (2016).

150. Bisoyi, H. K. & Kumar, S. Liquid-crystal nanoscience: an emerging avenue of soft self-assembly. *Chemical Society reviews* **40,** 306–319 (2011).

151. Lavrentovich, O. D. Transport of particles in liquid crystals. *Soft matter* **10,** 1264–83 (2014).

152. Kikuchi, H. *et al.* Bend-mode liquid crystal cells stabilized by aligned polymer walls. *Japanese Journal of Applied Physics* **44,** 981–989 (2005).
153. O'Shea, D. C., Suleski, T. J., Kathman, A. D. & Prather, D. W. *Diffractive Optics: Design, Fabrication, and Test* (SPIE, 2003).
154. Goncharsky, A., Goncharsky, A. & Durlevich, S. Diffractive optical element for creating visual 3D images. *Optics Express* **24,** 9140 (2016).
155. Li, G., Lee, D., Jeong, Y., Cho, J. & Lee, B. Holographic display for see-through augmented reality using mirror-lens holographic optical element. *Optics Letters* **41,** 2486 (2016).
156. Levola, T. Diffractive optics for virtual reality displays. *Journal of the Society for Information Display* **14,** 467 (2006).
157. Xiong, J., Yin, K., Li, K. & Wu, S.-T. Holographic Optical Elements for Augmented Reality: Principles, Present Status, and Future Perspectives. *Advanced Photonics Research* **2,** 2000049 (2021).
158. Kneubühl, F. Diffraction Grating Spectroscopy. *Applied Optics* **8,** 505 (1969).
159. Loewen, E. G. Diffraction gratings for spectroscopy. *Journal of Physics E: Scientific Instruments* **3,** 201 (1970).
160. Wulff, K. D. *et al.* Aberration correction in holographic optical tweezers. *Optics Express* **14,** 4169 (2006).
161. Dymale, R. C. Compensated telescope system with programmable diffractive optic. *Optical Engineering* **44,** 023201 (2005).
162. He, Z. *et al.* Liquid Crystal Beam Steering Devices: Principles, Recent Advances, and Future Developments. *Crystals* **9,** 292 (2019).
163. Račiukatis, G. Laser Processing by Using Diffractive Optical Laser Beam Shaping Technique. *Journal of Laser Micro/Nanoengineering* **6,** 37–43 (2011).

164. Katz, S., Kaplan, N. & Grossinger, I. Using Diffractive Optical Elements: DOEs for beam shaping – fundamentals and applications. *Optik & Photonik* **13,** 83–86 (2018).
165. Salvi, J., Pagès, J. & Batlle, J. Pattern codification strategies in structured light systems. *Pattern Recognition* **37,** 827–849 (2004).
166. Batlle, J., Mouaddib, E. & Salvi, J. Recent progress in coded structured light as a technique to solve the correspondence problem: A survey. *Pattern Recognition* **31,** 963–982 (1998).
167. Shpunt, A. S. & Zalevsky, Z. *US8050461B2: Depth-varying light fields for three dimensional sensing* 2007.
168. Blough, C. G., Rossi, M., Mack, S. K. & Michaels, R. L. Single-point diamond turning and replication of visible and near-infrared diffractive optical elements. *Applied Optics* **36,** 4648 (1997).
169. Kress, B. C. & Meyrueis, P. *Applied Digital Optics* 1–617 (John Wiley & Sons, Ltd, Chichester, UK, 2009).
170. Lester, G., Strudwick, A. & Coulston, S. Electronically switchable diffractive optical elements. *Opto-Electronics Review* **12,** 313–316 (2004).
171. Slinger, C. *et al.* Electrically controllable multiple, active, computer-generated hologram. *Optics letters* **22,** 1113–5 (1997).
172. Wang, X., Wilson, D., Muller, R., Maker, P. & Psaltis, D. Liquid-crystal blazed-grating beam deflector. *Applied Optics* **39,** 6545 (2000).
173. Fleisch, M. *et al.* Laser-written polymeric scaffolds for micro-patterned liquid crystal alignment. *Liquid Crystals* **46,** 2075–2084 (2019).
174. Tanaka, K., Kato, K., Tsuru, S. & Sakai, S. Holographically formed liquid-crystal/polymer device for reflective color display. *Journal of the Society for Information Display* **2,** 37 (1994).

175. Crawford, G. P. Electrically Switchable Bragg Gratings. *Optics and Photonics News* **14,** 54 (2003).
176. Liu, Y. J. & Sun, X. W. Holographic Polymer-Dispersed Liquid Crystals: Materials, Formation, and Applications. *Advances in OptoElectronics* **2008,** 1–52 (2008).
177. Wang, K. *et al.* Tri-color composite volume H-PDLC grating and its application to 3D color autostereoscopic display. *Optics Express* **23,** 31436 (2015).
178. Caputo, R., De Sio, L., Veltri, A., Umeton, C. & Sukhov, A. V. Development of a new kind of switchable holographic grating made of liquid-crystal films separated by slices of polymeric material. *Optics Letters* **29,** 1261 (2004).
179. Caputo, R. *et al.* POLICRYPS: A liquid crystal composed nano/microstructure with a wide range of optical and electro-optical applications. *Journal of Optics A: Pure and Applied Optics* **11** (2009).
180. D'Alessandro, A. *et al.* Electro-optic properties of switchable gratings made of polymer and nematic liquid-crystal slices. *Optics Letters* **29,** 1405 (2004).
181. De Sio, L., Lloyd, P. F., Tabiryan, N. V. & Bunning, T. J. Hidden Gratings in Holographic Liquid Crystal Polymer-Dispersed Liquid Crystal Films. *ACS Applied Materials and Interfaces* **10,** 13107–13112 (2018).
182. Kossyrev, P., Sousa, M. E. & Crawford, G. One- and two-dimensionally structured polymer networks in liquid crystals for switchable diffractive optical applications. *Advanced Functional Materials* **14,** 1227–1232 (2004).

183. Moharam, M., Gaylord, T. & Magnusson, R. Criteria for Bragg regime diffraction by phase gratings. *Optics Communications* **32,** 14–18 (1980).
184. Kress, B. C. *Field Guide to Digital Micro-Optics* (SPIE, 2014).
185. Gabor, D. A New Microscopic Principle. *Nature* **161,** 777–778 (1948).
186. Johnston, S. *Holographic Visions: A History of New Science* 1–540 (Oxford University Press, 2010).
187. Hariharan, P. *Basics of Holography* (Cambridge University Press, 2002).
188. Brown, B. R. & Lohmann, A. W. Complex Spatial Filtering with Binary Masks. *Applied Optics* **5,** 967 (1966).
189. Brown, B. R. & Lohmann, A. W. Computer-generated Binary Holograms. *IBM Journal of Research and Development* **13,** 160–168 (1969).
190. Gerchberg, R. W. & Saxton, W. O. A practical algorithm for the determination of phase from image and diffraction plane pictures. *Optik* **35,** 237–246 (1972).
191. Zhao, Q.-Z. *et al.* Direct writing computer-generated holograms on metal film by an infrared femtosecond laser. *Optics Express* **13,** 2089 (2005).
192. Li, Y., Dou, Y., An, R., Yang, H. & Gong, Q. Permanent computer-generated holograms embedded in silica glass by femtosecond laser pulses. *Optics Express* **13,** 2433 (2005).
193. Guo, Z., Qu, S. & Liu, S. Generating optical vortex with computer-generated hologram fabricated inside glass by femtosecond laser pulses. *Optics Communications* **273,** 286–289 (2007).
194. Wædegaard, K. J. & Balling, P. High-resolution computer-generated reflection holograms with three-dimensional effects written directly

on a silicon surface by a femtosecond laser. *Optics Express* **19,** 3434 (2011).

195. Alqurashi, T. *et al.* Femtosecond laser ablation of transparent microphotonic devices and computer-generated holograms. *Nanoscale* **9,** 13808–13819 (2017).
196. Cai, W., Reber, T. J. & Piestun, R. Computer-generated volume holograms fabricated by femtosecond laser micromachining. *Optics Letters* **31,** 1836 (2006).
197. Berlich, R., Richter, D., Richardson, M. & Nolte, S. Fabrication of computer-generated holograms using femtosecond laser direct writing. *Optics Letters* **41,** 1752 (2016).
198. Chabrol, G. R. *et al.* Investigation of diffractive optical element femtosecond laser machining. *Applied Surface Science* **374,** 375–378 (2016).
199. Stallinga, S. Axial birefringence in high-numerical-aperture optical systems and the light distribution close to focus. *Journal of the Optical Society of America A* **18,** 2846 (2001).
200. Karpinski, P., Shvedov, V., Krolikowski, W. & Hnatovsky, C. Laser-writing inside uniaxially birefringent crystals: fine morphology of ultrashort pulse-induced changes in lithium niobate. *Optics Express* **24,** 7456 (2016).
201. Zhou, G. *et al.* Axial birefringence induced focus splitting in lithium niobate. *Optics Express* **17,** 17970 (2009).
202. Dessaud, N., Raynes, P. & Bonnett, P. Dielectric behavior of polymer-stabilized-liquid-crystal cells made from hosts with different ultraviolet absorptions. *Journal of Applied Physics* **96,** 4366–4371 (2004).

203. Hoke, C., Xu, F. & Bos, P. *Modeling of polymer stabilized liquid crystals* in *Proceedings of the 5th International Display Workshop* (1998), 101–104.

204. Hoke, C. *Multi-Dimensional Alignment of Liquid Crystals and its Application to the Bistable Twist Cell* PhD thesis (Kent State University, 1999).

205. Ewings, R. A., Kischka, C., Parry-Jones, L. A. & Elston, S. J. Measurement of the difference in flexoelectric coefficients of nematic liquid crystals using a twisted nematic geometry. *Physical Review E - Statistical, Nonlinear, and Soft Matter Physics* **73,** 1–6 (2006).

206. Wild, J. H., Bartle, K., O'Neill, M., Kelly, S. M. & Tuffin, R. P. Synthesis and mesomorphic behaviour of wedge-shaped nematic liquid crystals with flexoelectric properties. *Liquid Crystals* **33,** 635–644 (2006).

207. Zhang, Z., You, Z. & Chu, D. Fundamentals of phase-only liquid crystal on silicon (LCOS) devices. *Light: Science & Applications* **3,** e213–e213 (2014).

208. Freedman, B., Shpunt, A., Machline, M. & Arieli, Y. *US8150142B2: Depth mapping using projected patterns* 2007.

209. Shpunt, A. *US9066087B2: Depth mapping using time-coded illumination* 2011.

210. Niclass, C. L. *et al. US10324171B2: Light detection and ranging sensor* 2015.

211. Zhu, L., Lyu, F. & Wang, B. *US10585194B1: Switchable diffuser projection systems and methods* 2019.

212. Mattelin, M.-A., Radosavljevic, A., Missinne, J., Cuypers, D. & Van Steenberge, G. Design and fabrication of blazed gratings for a waveguide-type head mounted display. *Optics Express* **28,** 11175 (2020).

213. Borgsmüller, S., Noehte, S., Dietrich, C., Kresse, T. & Männer, R. Computer-generated stratified diffractive optical elements. *Applied Optics* **42,** 5274 (2003).

214. Kämpfe, T., Kley, E.-B. & Tünnermann, A. *Creation of Multicolor Images by Diffractive Optical Elements, Arranged in a Stacked Setup* in *Adaptive Optics: Analysis and Methods/Computational Optical Sensing and Imaging Topical Meetings* (OSA, Washington, D.C., 2007).

215. Kämpfe, T., Kley, E.-B., Tünnermann, A. & Dannberg, P. Design and fabrication of stacked, computer generated holograms for multicolor image generation. *Applied Optics* **46,** 5482 (2007).

216. Deng, X. & Chen, R. T. Design of cascaded diffractive phase elements for three-dimensional multiwavelength optical interconnects. *Optics Letters* **25,** 1046 (2000).

217. Buckley, E., Cable, A., Lawrence, N. & Wilkinson, T. Viewing angle enhancement for two- and three-dimensional holographic displays with random superresolution phase masks. *Applied Optics* **45,** 7334 (2006).

218. Chambers, D., Nordin, G. & Kim, S. Fabrication and analysis of a three-layer stratified volume diffractive optical element high-efficiency grating. *Optics Express* **11,** 27 (2003).

219. Jamali, A., Yousefzadeh, C., McGinty, C., Bryant, D. & Bos, P. LC lens systems to solve accommodation/convergence conflict in three-dimensional and virtual reality displays. *Optical Engineering* **57,** 1 (2018).

220. Lee, Y.-H., Zhan, T. & Wu, S.-T. Prospects and challenges in augmented reality displays. *Virtual Reality & Intelligent Hardware* **1,** 10–20 (2019).

221. Kim, M. S. & Serra, F. Tunable Dynamic Topological Defect Pattern Formation in Nematic Liquid Crystals. *Advanced Optical Materials* **8,** 1–8 (2020).